MARIA JOÃO PORTELA DE SÁ PEREIRA

ESTUDO MICROSCÓPICO LOCAL DOS EFEITOS MAGNETO, ELETRO E ELASTOCALÓRICO

LOCAL MICROSCOPIC STUDY OF THE MAGNETO, ELECTRO AND ELASTOCALORIC EFFECTS

Universidade de Aveiro
2021

MARIA JOÃO PORTELA DE SÁ PEREIRA

ESTUDO MICROSCÓPICO LOCAL DOS EFEITOS MAGNETO, ELETRO E ELASTOCALÓRICOS

LOCAL MICROSCOPIC STUDY OF THE MAGNETO, ELECTRO AND ELASTOCALORIC EFFECTS

Tese apresentada à Universidade de Aveiro para cumprimento dos requisitos necessários à obtenção do grau de Doutor em Engenharia Física, realizada sob a orientação científica do Doutor Vitor Brás de Sequeira Amaral, Professor Catedrático do Departamento de Física da Universidade de Aveiro e co-orientação do Doutor Armando António Cardoso dos Santos Lourenço, Professor Auxiliar no Departamento de Física da Universidade de Aveiro e da Doutora Franca Albertini, Investigadora Principal no Istituto dei Materiali per l'Elettronica e il Magnetismo - Consiglio Nazionale delle Ricerche (IMEM-CNR, Parma).

o júri

presidente

Prof. Doutor Nuno Miguel Gonçalves Borges de Carvalho
Professor Catedrático da Universidade de Aveiro

vogais

Prof.ª Doutora Luana Caron
Professora da Universidade de Bielefeld

Prof. Doutor Luís Humberto Viseu Melo
Professor Associado da Universidade de Lisboa

Prof. Doutor João Pedro Esteves de Araújo
Professor Associado da Universidade do Porto

Doutor Andrei Leonidovitch Kholkine
Equiparado a Investigador Coordenador da Universidade de Aveiro

Prof. Doutor Vitor Brás de Sequeira Amaral (Orientador)
Professor Catedrático da Universidade de Aveiro

Ao Doutor João Amaral, por todos as conversas extremamente produtivas que tivemos e pelos conselhos que me dispensou, que se revelaram sempre muito acertados e úteis.

À minha coorientadora, Doutora Franca Albertini, pelo entusiasmo com que aceitou fazer parte da equipa de orientação e pela forma inexcedível como sempre cumpriu o seu papel. Foi sempre de uma enorme generosidade com o seu tempo, na partilha do seu imenso conhecimento científico. É, sem dúvida, um exemplo de excelência na liderança na ciência. Tenho por ela um enorme carinho e grande admiração, como cientista e como ser humano.

Ao meu coorientador, Professor Armando Lourenço, pelo apoio incondicional que dele recebi desde o primeiro dia em que começamos a trabalhar em conjunto na Universidade de Aveiro. Valorizo profundamente todo o conhecimento científico e técnico que sempre partilhou comigo e toda a disponibilidade que demonstrou, quer para produzirmos as amostras necessárias para a realização do trabalho, quer para a execução de qualquer tarefa experimental que pudesse beneficiar da sua participação. Além de tudo isto, tenho ainda a agradecer o pragmatismo contagioso que o caracteriza, e que fez várias vezes com que o trabalho prosseguisse em momentos cruciais.

Ao meu orientador, Professor Vitor Amaral, começarei por agradecer o fato de me ter concedido o privilégio e a responsabilidade de levar a cabo este trabalho sob a sua orientação. Igualmente, por ter conduzido a orientação do trabalho e do meu crescimento científico pautando-se por equilíbrios que são, na minha opinião, extremamente difíceis de atingir: primeiro, permitindo-me sempre explorar os meus caminhos e buscar a minha independência sem me fazer sentir desacompanhada em momento algum; depois, sendo extremamente exigente sem deixar nunca de ser amável. É uma fonte de conhecimento inesgotável e preserva, fazendo questão de a transmitir, uma óbvia paixão pela Ciência, com a qual me identifico. Do Professor Vitor Amaral destaco ainda a ética absolutamente irrepreensível que está presente em tudo a que se dedica e a capacidade sobre-humana com que gere todas as suas atribuições, que tantas vezes me motivou a continuar quando me sabia assoberbada. A reverência com que é tratado por todos os que com ele privam é o reflexo da justeza e afabilidade com que nos trata. É o principal responsável pelo meu amadurecimento científico e uma forte referência no meu amadurecimento pessoal. Será sempre para mim um modelo a seguir. Juntamente com os restantes membros da equipa de orientação, independentemente de onde as circunstâncias nos levarem, faço questão que esteja sempre presente no meu percurso, se assim o desejar.

Aos meus amigos: sabem que o são há demasiados anos para que seja necessário elucidar-vos quanto às razões pelas quais vos agradeço.

À minha família:

São a razão da minha resiliência. Não há circunstância adversa que eu não encare como quase natural e ultrapassável. Acredito ser uma questão de justiça relativa: ter uma família como a minha e navegar pela vida apenas em águas calmas seria uma afronta para todos os que não têm direito a pais e irmãos como os meus. Quando se faz parte, desde sempre e para sempre, de uma tripulação tão valorosa, os adamastores da vida inevitavelmente se tornam cabos da boa esperança.

À minha irmã Ana Sofia e ao meu irmão António Manuel:

É-me impossível expressar aqui toda a gratidão e afeto que vos tenho. É com uma pontinha de constrangimento que sempre vos vejo suspender tudo nas vossas vidas absurdamente ocupadas quando, por algum motivo, solicito a vossa ajuda ou, apenas, a vossa atenção. Resta-me a consolação de acreditar que não deixo de fazer o mesmo por vós.

Aos meus pais:

Tenho a agradecer-vos tudo. Desde sempre e para sempre.

Durante todo este processo, não mediram esforços para, de forma proativa, facilitar a minha vida em tudo o que estava ao vosso alcance, enquanto continuaram, como sempre, a gerir a vossa vida com a precisão de um relógio suíço. Vocês "inventaram" tempo que eu não tinha, sem que eu necessitasse de o pedir. O tremendo respeito e a profunda afeição são imutáveis.

À memória dos meus avós, porque a trago sempre comigo e procuro sempre honrá-la.

palavras-chave

Magnetocalórico, electrocalórico, elastocalórico, ligas heusler, memória de forma, transformação martensítica, gestão térmica, microscopia de sonda de varrimento, microscopia de varrimento térmico, microscopia de termografia de infravermelhos.

resumo

Determinar e atuar nas propriedades termofísicas à nanoescala é essencial para compreender/gerir a distribuição térmica de calor em materiais e dispositivos miniaturizados. Técnicas de nanocaracterização térmica são necessárias para analisar e controlar o comportamento térmico de dispositivos, evitando prejuízos à performance desejada. Neste contexto, a microscopia de varrimento térmico (SThM) é uma técnica de sondagem e atuação de elevada resolução espacial baseada na microscopia de força atómica (AFM), utilizando uma nano-sonda como termómetro e elemento resistivo de aquecimento. Permitindo a observação direta e o mapeamento de propriedades térmicas, esta é uma ferramenta poderosa em várias áreas, desde a ciência de materiais até à gestão térmica em dispositivos. Os mecanismos responsáveis pela transferência de calor à nano/microescala são essenciais para desenvolver e otimizar dispositivos, particularmente aquando da utilização de materiais que sofrem transições de fase de primeira ordem, que exibem efeitos ferrocalóricos (magnetocalórico, eletrocalórico e elastocalórico) e estruturais acoplados, tais como o Ni-Mn-Ga, o BaTiO3 e o Ni-Ti, investigados para aplicações de atuação, deteção e tecnologias de gestão térmica em estado sólido (arrefecimento).

Este trabalho pretende aumentar a compreensão da interação destes efeitos através da sondagem local das propriedades térmicas, combinada com estudos magnéticos, eletricos e estruturais:

- fenómenos termomagnéticos, termoeletricos e termoelasticos locais por microscópio de varrimento térmico (SThM) e termografia de infravermelhos.

- atuação local por aquecimento levada a cabo pela sonda SThM para avaliar condutividade térmica, contraste de mudança de fase e mapeamento de inomogeneidades dinâmicas de amostras.

- dependência temporal de fenómenos térmicos locais correlacionados com processos de difusão térmica através de transformações de fase para o Ni-Mn-Ga, o BaTiO3 e o Ni-Ti.

- sondagem local de "memória de ponto de retorno térmica" e efeitos de avalanche em filmes de Ni-Mn-Ga provocados por ciclagens térmicas.

Um dos resultados mais significativos consistiu na constatação de que a indução local da transformação estrutural em filmes finos de Ni-Mn-Ga resulta em intervalos muito mais alargados de temperaturas de transformação martensítica do que no caso de indução global da transformação estrutural, numa mesma área microscópica do material. Observámos ainda grandes diferenças no comportamento do efeito magnetocalórico no Ni-Mn-Ga dopado com Co, em aquecimento e arrefecimento, à escala microscópica, na vizinhança da transformação estrutural. Foi realizado com sucesso o mapeamento da contribuição para o efeito de cada área microscópica da amostra.

keywords

Magnetocaloric, electrocaloric, elastocaloric, heusler alloys, shape memory, martesitic transformation, thermal management, scanning probe microscopy, scanning thermal microscopy, infrared microscopy thermography.

abstract

Determining and acting on thermo-physical properties at the nanoscale is essential for understanding/managing heat distribution in micro/nanostructured materials and miniaturized devices. Adequate thermal nano-characterization techniques are required to control device thermal behavior and address thermal issues deterrent to their desired performance. In this context, Scanning Thermal Microscopy (SThM) is a high spatial resolution probing and acting technique based on Atomic Force Microscopy (AFM) using a nano-probe as thermometer and resistive heater. Enabling direct observation and mapping of thermal properties, it is becoming a powerful tool in several fields, from material science to device thermal management. The mechanisms driving heat transfer at the nano/microscopic-scale are essential for device development and optimization, particularly when using first-order phase transition materials exhibiting coupled structural and ferrocaloric effects, as Ni-Mn-Ga, BaTiO3 and Ni-Ti (magnetocaloric, electrocaloric, elastocaloric), researched for multifunctional actuating, sensing and solid-state heat-management technologies (cooling) applications.

This work aims to raise the understanding of the interplay of these effects by local probing of thermal properties, combined with magnetic, structural, and electric studies:

- local thermomagnetic, thermoelectric and thermoelastic phenomena by scanning thermal microscopy (SThM) and microscopic-infrared-thermography

- local actuation by heating performed by SThM-tip to evaluate thermal conductivity, phase change contrast and map sample dynamic inhomogeneities.

- time-dependence of local thermal phenomena correlated with thermal diffusion processes across phase transformations for Ni-Mn-Ga, BaTiO3 and Ni-Ti.

- local probing of "thermal return-point-memory" and avalanche effects on Ni-Mn-Ga films produced by temperature cycling.

One of our most significant results consisted in finding that locally inducing the structural transformation in Ni-Mn-Ga thin films results in much wider martensitic transformation temperatures (TM) intervals than for overall structural transformation inducing, within a same micrometric area of the material. We also observed large differences in the behavior of the magnetocaloric effect in bulk Co-doped Ni-Mn-Ga on heating and cooling, at the microscopic scale, in the vicinity of the structural transformation. Mapping of the contribution of each microscopic area of the sample to the effect was achieved.

INDEX

LIST OF FIGURES

LIST OF TABLES

ABSTRACT

Determining and acting on thermo-physical properties at the nanoscale is essential for understanding/managing heat distribution in micro/nanostructured materials and miniaturized devices. Adequate thermal nano-characterization techniques are required to control device thermal behavior and address thermal issues deterrent to their desired performance. In this context, Scanning Thermal Microscopy (SThM) is a high spatial resolution probing and acting technique based on Atomic Force Microscopy (AFM) using a nano-probe as thermometer and resistive heater. Enabling direct observation and mapping of thermal properties, it is becoming a powerful tool in several fields, from material science to device thermal management.

The mechanisms driving heat transfer at the nano/microscopic-scale are essential for device development and optimization, particularly when using first-order phase transition materials exhibiting coupled structural and ferrocaloric effects, as Ni-Mn-Ga, $BaTiO_3$ and Ni-Ti (magnetocaloric, electrocaloric, elastocaloric), researched for multifunctional actuating, sensing and solid-state heat-management technologies (cooling) applications.

This work aims to raise the understanding of the interplay of these effects by local probing of thermal properties, combined with magnetic, structural, and electric studies:

- local thermomagnetic, thermoelectric and thermoelastic phenomena by scanning thermal microscopy (SThM) and microscopic infrared thermography
- local actuation by heating performed by SThM-tip to evaluate thermal conductivity, phase change contrast and map sample dynamic inhomogeneities.
- time-dependence of local thermal phenomena correlated with thermal diffusion processes across phase transformations for Ni-Mn-Ga, $BaTiO_3$ and Ni-Ti.

- local probing of "thermal return-point-memory" and avalanche effects on Ni-Mn-Ga films produced by temperature cycling.

One of our most significant results consisted in finding that locally inducing the structural transformation in Ni-Mn-Ga thin films results in much wider martensitic transformation temperatures (T_M) intervals than for overall structural transformation inducing, within a same micrometric area of the material. SThM, with its simultaneously heated and temperature measuring tip, successfully undertook the role of thermal actuator by inducing the local transformation.

We observed large differences in the behavior of the magnetocaloric effect in bulk Co-doped Ni-Mn-Ga on heating and cooling, at the microscopic scale, in the vicinity of the structural transformation. Mapping of the contribution of each microscopic area of the sample to the effect was achieved.

1 – INTRODUCTION

Knowledge of heat transfer and thermal transport phenomena in materials is critical for scientific, engineering, and industrial development. Such knowledge will mark the difference between "making or breaking" nano-device implementation and development concerning the referred materials. Materials significantly responsive to changes in external magnetic, electric and stress fields, when subjected to a sudden change of said fields, experience thermal changes resulting in a variation of the material's temperature or heat exchange [1-2]. These caloric effects (magnetocaloric, electrocaloric and elastocaloric, respectively) are related to a change in entropy when the field is isothermally applied and are pronounced near magnetic, ferroelectric and structural transformations. The ferrocaloric effects have been widely used in applications associated with refrigeration purposes mainly at the macroscopic scale, but they are also highly promising in the quest to meet the needs in microelectronic and microelectromechanical devices for energy-efficient and environmental friendly solid-state refrigeration, a major research topic nowadays. There is, however, the need for more detailed studies in order to ascertain the true potential of these materials. The intrinsically atomic-scale nature of such phenomena renders necessary their understanding from a local, small scale perspective beyond the realm of macroscopic thermodynamic phenomenology and processes. The technological demand for development and optimization of systems at ever decreasing scales also sheds a modern light into this research field, claiming for the exploration of thermal measurement techniques to study localized phenomena at such reduced scales. This is not easily achieved and thus it is not yet sufficiently addressed in literature [3]. The research of local thermal effects on caloric nanomaterials possesses now an essential role in the path towards efficient thermal management and device development and optimization.

Several materials are being investigated in this research field, but in each case, some examples are prominent for their unique properties. In the thesis we

consider three types of ferroic materials: Shape memory alloys (SMAs), Ferromagnetic shape memory alloys (MSMA) and ferroelectrics. SMAs, such as NiTi, have received considerable fundamental and technological attention for possessing unique thermo-mechanical properties. They perform temperature induced recovering from very large deformations (~10%) (shape memory effect) and exhibit pseudoelastic behavior since the recovery stands for successive sample loading and unloading cycles. These properties are linked to the occurrence of a first-order structural transition from a high-temperature phase (higher symmetry) to a low-temperature phase (lower symmetry): the martensitic transformation [4]. When the first-order martensitic transition is induced by uniaxial stress, the entropy change associated with the latent heat of the transformation originates the elastocaloric effect [5-9][10], making SMAs promising candidates for mechanical refrigeration [4][11].

Ni-Mn-Ga is a ferromagnetic shape memory alloy (FSMA) belonging to the family of Heusler alloys [12]. The higher than 10% giant reversible magnetic-field-induced strain [13] is highly attractive for application into micro-electromechanical systems (MEMS). The magnetic behavior of the alloy can be controlled by temperature, magnetic field, and stress. [14-17]

As any shape memory alloy, Ni-Mn-Ga undergoes a martensitic transformation, in the vicinity of which the magnetocaloric effect is enhanced due to a strong difference in magnetization of both phases involved. Ni-Mn-Ga allows for martensitic transition temperature (T_M) and Curie temperature (T_C) of the material to be controlled by engineering the alloy's composition. The Curie temperature (T_C) is the temperature above which the material loses its spontaneous magnetization and becomes paramagnetic [18]. When magneto-structural coupling occurs, the effect is further increased, making Ni-Mn-Ga a highly attractive candidate for magnetic refrigeration.

BaTiO$_3$ is considered to be the ferroelectric of reference where the electrocaloric effect is concerned, due to the large amount of latent heat involved in the paraelectric to ferroelectric transition, but the study of the electrocaloric effect in this material is particularly challenging in thin films. [19-21]

LOCAL MICROSCOPIC STUDY OF MAGNETO, ELECTRO AND ELASTOCALORIC EFFECTS

The main goals of this work consist in the study of local thermal phenomena at the micrometric and nanometric scale (combined with other microscopic characterization techniques) of nanostructured systems of Ni-Mn-Ga (FSMA), Ni-Ti (SMA) and ferroelectric $BaTiO_3$.

From sample preparation, encompassing the use of bulk materials, going through structural (SEM,TEM, AFM and XRD) and magnetic characterization of samples, we strive to study local thermomagnetic and thermoelastic phenomena using infrared thermography and scanning thermal microscopies, with resolutions of 3 µm/pixel and 50nm/pixel, respectively, in a broad temperature range:

- thermal mapping of modifications experienced by the samples under external applied fields and electrical currents (by varying temperature, phase transformations will be locally induced and the materials' response will be measured);

- studies of local actuation by SThM (Scanning Thermal Microscopy) heated tip, which simultaneously measures temperature and heats selected sample areas, allowing the evaluation of features such as lack of sample homogeneity and promoting deeper understanding on thermal (structural, magnetocaloric, electrocaloric and elastocaloric) phenomena at small scales.

- Local nano-thermometry studies in Ni-Mn-Ga [22] will be held for clarification of "thermal return point memory" [20] and avalanche effects on Ni-Mn-Ga thin films.

2 – EXPERIMENTAL TECHNIQUES AND INSTRUMENTATION

In this chapter we will name the experimental techniques employed to characterize the properties of the samples studied in this dissertation and briefly describe the instrumentation used to that effect.

2.1 – X-Ray diffraction (XRD) analysis

X-ray diffraction measurements on thin films were performed at LCA (laboratório central de análises) at the University of Aveiro (UA) on a Philips PANalytical X'Pert MRD System (Fig. 2.1).
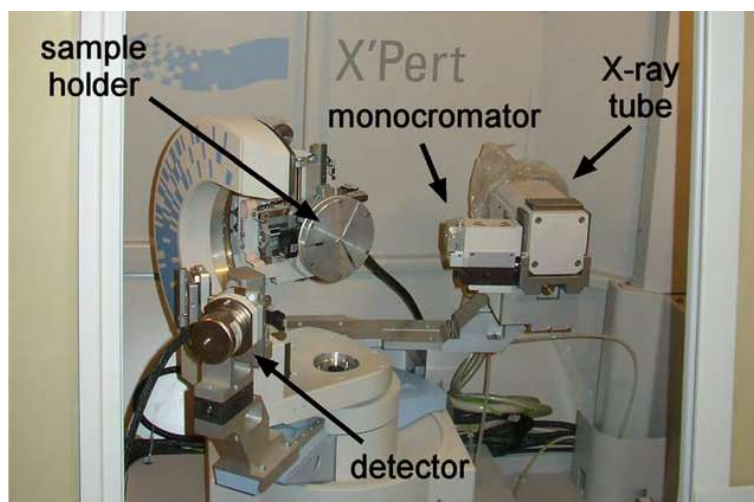
Fig. 2.1 - Reproduction of the model of Phillips PANalytical X'Pert-MRD X-Ray Diffractometer used in LCA at UA. [23].

X-ray diffraction temperature dependent measurements on bulk samples were performed at CICECO – Aveiro Institute of Materials facilities, located at the Materials Engineering and Ceramics Department at the University of Aveiro. The equipment used is a Rigaku Geigerflex X-ray diffractometer with a PW3050/60 (Theta/Theta) Goniometer and a 45 kV and 40 mA Cu-Kα radiation.

2.2 – Transmission Electron Microscopy (TEM)

TEM images where obtained with CICECO's filtered energy FE-TEM JEOL JEM-2200FS of atomic resolution with (FE) mapping located at the Materials Engineering and Ceramics Department at the University of Aveiro.

2.3 – Scanning Electron Microscopy (SEM) and Energy-Dispersive X-ray Spectroscopy (EDS) analysis

SEM images and EDS analysis performed were obtained with the following equipment:

- analytical and high-resolution Hitachi SU-70 scanning electron microscopy (SEM) equipment, with a Bruker QUANTAX 400 system of microanalysis by energy-dispersive X-ray spectroscopy (EDS)

Fig. 2.2 - Hitachi SU-70 SEM equipment from CICECO – Aveiro Institute of Materials [24].

- SEM Hitachi S4100

2.4 – Superconducting Quantum Interference Device (SQUID) and Vibrating Sample Magnetometer (VSM)

Samples were magnetically characterized using a Quantum Design MPMS3 SQUID-VSM at 2–400K range and using magnetic fields ranging from -70 kOe–70 kOe. M(H) measurements performed on VSM (vibrating sample magnetometer) mode and M(T) measurements performed on DC (direct current) extraction mode.

2.5 – Experimental setup for the measurement of electrical resistivity

Electrical resistivity measurements were performed on a setup built at the CICECO Magnetic Properties Laboratory, at UA. All measurements were done using the four-contact method. This method consists in aligning four electrical contacts along the sample. The outward contacts are used to provide the electrical current to the sample and the inward contacts are used to measure the sample's voltage.

The system used to perform these measurements is described in further detail elsewhere [25]. Here we will highlight the aspects deemed relevant for the work developed for the thesis.

Fig. 2.3 shows, on the left, the part of the electrical resistivity measurement setup where the sample holder belongs and on the right we can see (from top to bottom) the Lakeshore 325 temperature controller, the Agilent 34420A Nanovolt/micro-ohm Meter, and the Keithley 6221 current source. Fig. 2.4 depicts the copper sample holder with sample NiTi_1 mounted on it. The sample is glued with GE varnish to a piece of thin natural gum rolling paper that in turn is also glued with GE varnish to the copper sample holder. This montage assures very good thermal conductivity and electrical insulation between sample and sample holder. The temperature of the system is altered by a closed cycle helium cryostat allowing it to go from about 10 K to 450 K. The copper sample holder is thus designed for high temperature usage. The magnetic field, up to 10 kOe (1 T) is provided by an

Hallback system from Magnetic solutions, with automated rotation in horizontal plane.
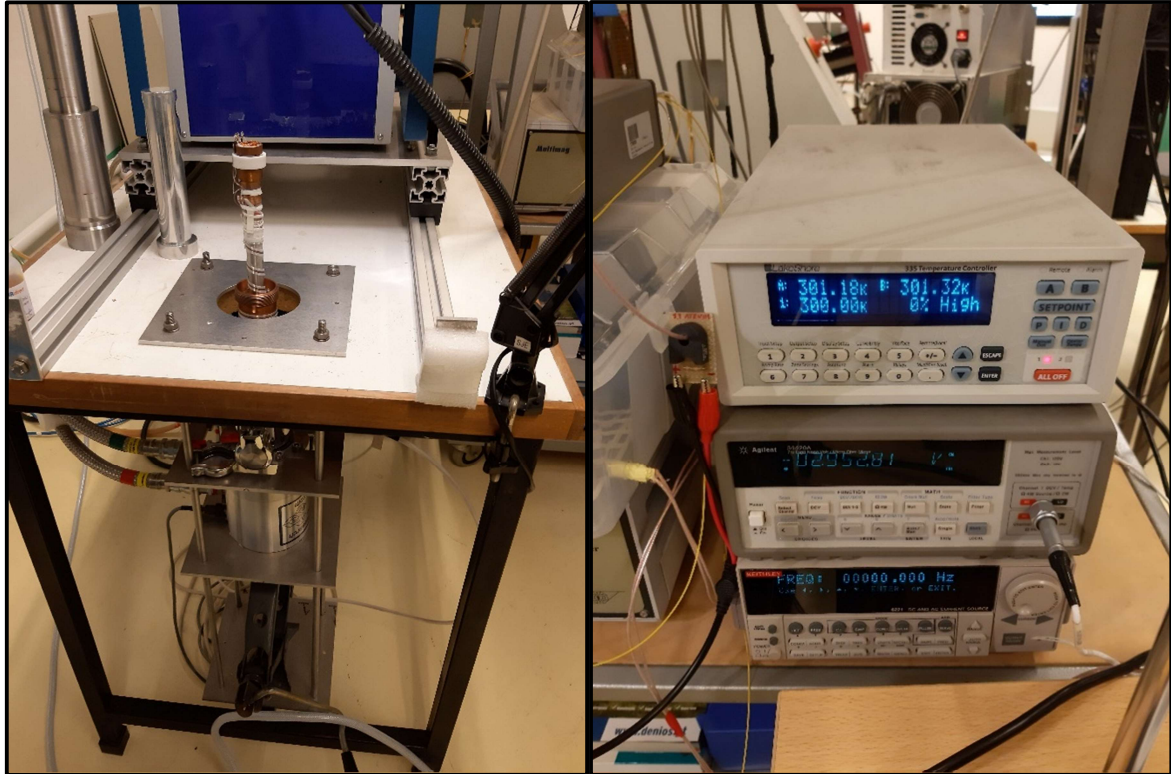
Fig. 2.3 - Electrical resistivity measurement setup at the Magnetic Properties Laboratory at UA.

Fig. 2.4 - Image of the copper sample holder with sample NiTi_1 mounted.

3 – CALORIC EFFECTS AND MATERIALS

Current conventional refrigeration solutions, which are based on the vapor compression system, present critical disadvantages when compared to magnetic refrigerators. Reports have magnetic refrigerators reach an efficiency of 60% [26] of the theoretical limit in contrast with the 40% reached by the vapor-based cooling solutions [27]. Also, vapor compression-based refrigeration devices resort to gases which are considered to be highly contributing to global warming, such as HFC (hydrofluorocarbon). The fact that they are evermore considered a cause for serious environmental concerns make them a relevant issue in terms of environmental ethics [28-29]. In spite of the use of new coolant fluids, the development of such technologies borders the danger of becoming saturated. Cooling technologies based on the vapor compression cycle explore the entropy change in a material caused by a change in pressure, which will ultimately result in a variation of the material's temperature. New solutions based on different caloric effects such as the magneto, electro and elastocaloric effects are being considered by researchers who are looking for more environmentally friendly alternatives. These caloric effect - based potential applications for refrigeration are not only more deferent to current environmental concerns but can also certainly be more efficient than their predecessors [28] [30].

The description of the caloric phenomena will be further developed by discussing the magnetocaloric effect. The remaining electrocaloric and elastocaloric effects can be then understood by replacing the magnetic field by electrical and mechanical fields, respectively. Specific information concerning each effect will be then added.

3.1 – Magnetocaloric effect and Ni-Mn-Ga

The magnetocaloric effect is a result of coupling that occurs between the materials' magnetic subsystem and an applied external magnetic field [36]. It

manifests through a variation in the material's temperature when the magnetic field is applied under adiabatic conditions, ΔT_{ad} (Fig. 3.1) [32].
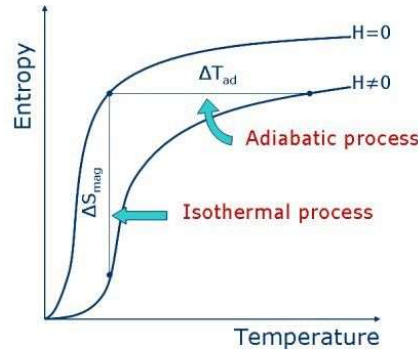
Fig. 3.1 - Entropy variation of a material under isothermal and adiabatic conditions in the presence and absence of applied magnetic field [33].

Under adiabatic conditions, the total entropy of the magnetic material is maintained. Since the applied magnetic field promotes order in the electronic and magnetic subsystem, it decreases the entropies of these subsystems. In order for the total entropy to be maintained, another form of entropy in the system must be increased. Such entropy is connected to phonons (lattice vibrations). An increase in lattice vibration entropy will lead to an increase in the material's temperature. This relationship is represented in Fig. 3.2, where S_{total} is the entropy of the system, S_m is the entropy of the magnetic subsystem, S_e is the entropy of the electronic subsystem and S_r is the lattice vibrational entropy [34-28].

$$S_{total}\ (H,T) = S_m\ (H,T) + S_e\ (T) + S_r\ (T)$$

Fig. 3.2 - Relationship between the entropies of the magnetic material in the magnetocaloric effect [28].

As can be understood from Fig. 3.1, the width of the temperature variation depends on the material and the magnitude of the applied field [34].

The removal of the applied magnetic field will retrieve the system's initial state, which means that the values of magnetic and electronic entropies increase and the lattice vibrational entropy decreases in order to maintain the total entropy of the system

imposed by the adiabatic nature of the process. This promotes a cooling of the material [32].

Magnetocaloric materials can be classified according to the order of the phase transition that they undergo [35]. First-order phase transition (FOPT) materials exhibit large magnetic entropy change and adiabatic temperature change. However, they also present thermal hysteresis. Second-order phase transition (SOPT) materials do not possess the disadvantage of thermal hysteresis, but the magnitude of their magnetocaloric effect is considerably smaller.

Although the magnetocaloric effect was first observed by Warburg in 1881 [36], the clarification of the involved physical mechanisms came only in 1918 by the hand of Weiss and Picard [37], to whom the authorship of the effect's discovery is attributed.

Since then, different magnetocaloric materials have been investigated and different values of temperature variation have been found, depending on the applied magnetic field. The highest value reached was a -13 K variation, with an applied magnetic field of 2T for FeRh [38].

The first applications of the magnetocaloric effect in low temperature physics (T < 2 K) were discussed and presented between the mid 20s and mid 30s of the previous century using paramagnetic salts [39].

However, it was only in 1976 that a prototype for a magnetic refrigerator near room temperature was indicated as an actual application of the magnetocaloric effect, with a material (Gd) undergoing a magnetic phase change [40].

Current research focuses mainly in exploring the magnitude of the magnetocaloric effect in different magnetic materials, since it is considered to be well understood as a phenomenon at the macroscopic scale. Although there are some prospects for this effect in terms of large scale applications, mainly in the refrigeration field, a strong focus lies currently in exploring the phenomenon and its achievable applications in smaller (micro-nano) scales [32].

The magnetocaloric effect also finds applicability in the medical field, in the context of hyperthermia applications for cancer cells treatment and targeted drug

release, both of which are usually based on the use of magnetic nanoparticles that require localized nano-thermal characterization [32][41].

Ni-Mn-Ga

Heusler alloys were first mentioned in 1903 and take the general compositional formula X_2MnY, where X and Y represent elements from the d and p blocks of the periodic table. In most cases, these alloys crystallize in well-ordered structures based upon the fcc lattice [4][42].

Heusler alloys have attracted great interest as a subject of study due to their interesting diverse magnetic behavior. Among these alloys is the Ni-Mn-Ga system, regarded as a class of smart materials investigated in recent years because of their unique magneto-mechanical properties, such as giant magnetic field-induced strain (MFIS) up to 10%, and potential applications, from a technological point of view, as actuator/transducer as well as sensor. The Ni-Mn-Ga system belongs to the category of the ferromagnetic shape memory alloys (FMAs) [42][43].

Ni-Mn-Ga exhibits two main structural phases: the austenitic (cubic) phase and the martensitic (tetragonal) phase, also known as the high and low temperature phases, respectively. The martensitic deformation characteristic of this structural transformation causes stress in the material, which can be released by the introduction of twin boundaries appearing on the sample's surface as a set of almost parallel waves [44][45][7][46-49]. Ni-Mn-Ga presents not only a displacive and diffusionless martensitic transition from high symmetry cubic structure (austenitic phase) to low symmetry tetragonal/orthorhombic structure (martensitic phase), but also several phase transitions between different crystallographic structures within the martensitic phase, induced by a change of composition, temperature or stress, or by a combination of these parameters. In the ternary Ni-Mn-Ga system, the temperatures at which these structural transitions and the magnetic transition occur are extremely sensitive to stoichiometry [50].

The martensitic transition temperature (T_M) is the temperature at which the material transforms from the austenitic to the martensitic phase.

The Ni-Mn-Ga alloys' applicability to micro-electromechanical systems (MEMS) led to an increased interest in the study of Ni-Mn-Ga thin films, where magnetic properties vary, to a certain extent, as a function of the film thickness [51]. This magnetic behavior can be controlled by temperature, moderate magnetic fields, stress and their combination [14].

The martensitic transformation has been well covered in bulk Ni-Mn-Ga, as well as the effect of composition on the temperature at which this transformation occurs. [50] [16]

In the specific case of stoichiometric Ni_2MnGa, the martensitic transformation temperature (T_m) is around 200 K, and the ferromagnetic behavior occurs below the Curie temperature (T_C) of approximately 370 K.

A study of the phases involved in the martensitic transformation in bulk stoichiometric Ni_2MnGa was first reported in 1984 by Webster et al. [44]. The parent cubic phase (austenite), stable at high temperature, belongs to Fm-3m space group, with a L21 structure with a lattice parameter of a_a = 5.833 Å. The thermo-elastic transformation occurs when the material is cooled below 220 K. This homogeneous deformation starts following the mechanism described by Bain in 1924, generally called "Bain strain" (Fig. 3.3) [54]. It consists of a contraction of the c-axis accompanied by the elongation of the other two vectors. The cell parameters of the Ni_2MnGa martensitic structure (referred to the austenite L21) lattice are a_m=5.920 Å and c_m=5.566 Å [54]. It is known for shape memory alloys that different martensitic structures exhibit diverse structural modulations, depending on the alloy's composition [54].
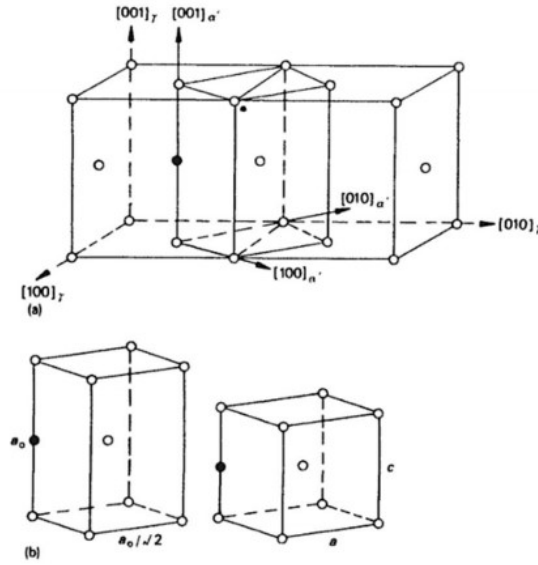
Fig. 3.3 - The lattice correspondence for the formation of martensite from austenite: (a) tetragonal unit cell outlined in austenite, (b) lattice deformation [52].

While most current applications of SMAs explore temperature/stress driven martensitic transformation, Ni-Mn-Ga, being a FSMA, allows the faster and more efficient magnetic control of such transformations [54]: the application of a magnetic field influences the martensitic transformation temperature of the system and can induce a martensitic transformation from austenite to martensite.

Another important effect that can be exploited in the applications is the magnetic-field-induced reorientation of twin variants (MIR) in the martensitic phase. It occurs in twinned martensites with high magneto-crystalline anisotropy energy.

The mechanism is sketched in Fig. 3.4. This phenomenon is usually referred as "magnetic shape memory effect".
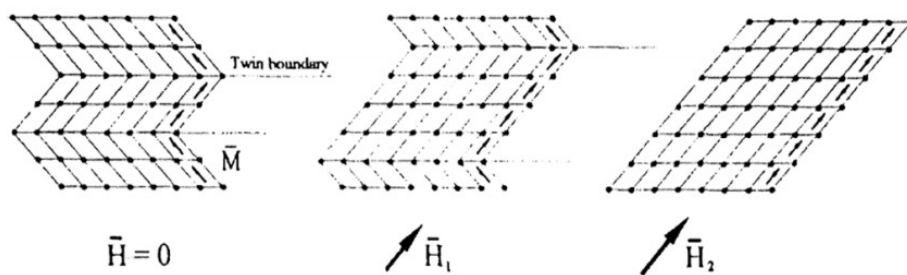
Fig. 3.4 - Schematic illustration of the magnetic shape memory effect (H2 > H1) [55].

It is known that strong magnetic and structural coupling of subsystems in the material leads to the existence of hysteresis in the magnetization, when the temperature or applied magnetic field are varied. [56].

Ni-Mn-Ga composition does not only strongly influence the martensitic transformation temperature, but also its crystalline structure or specific structural modulation, as well as the magnetic behavior of the alloy. For instance, for a composition of $Ni_{2+x}Mn_{1-x}Ga$ (excess of Ni over Mn) three different regions can be distinguished on the plot of T_m and T_C versus x (Fig. 3.5) [50].
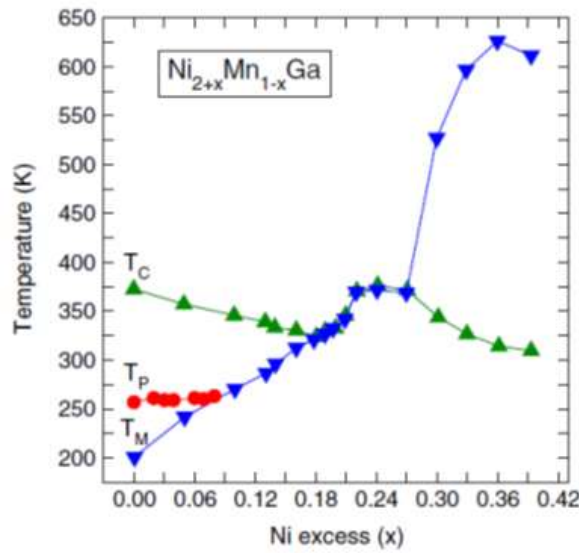
Fig. 3.5 - Ferromagnetic (T_C), martensitic (T_M) and premartensitic (T_P) transition temperatures determined from DSC and low-field magnetization measurements as a function of the Ni excess concentration x in $Ni_{2+x}Mn_{1-x}Ga$ alloys. [50].

When $x \leq 0.18$, $T_C > T_m$ and the martensitic transformation takes place when in the ferromagnetic state. Alloys for which $0.18 \leq x \leq 0.27$ are characterized by a coupled magnetostructural transition, i.e., $T_m \approx T_C$. Finally, the third region, where $x \geq 0.27$, is characterized by a sharp increase in the martensitic transformation temperature, which reaches $T_m \approx 625$ K. In this region the martensitic transformation takes place when in the paramagnetic state. The occurrence of the high temperature martensitic transformation makes alloys from this region attractive for application as high temperature shape memory alloys. Studies performed for films with a composition of $Ni_{2+z}MnGa_{1-z}$ related that the martensitic transformation temperature

(T_m) increases linearly with increasing z and the Curie temperature (T_C) decreases almost linearly with increasing z : for z = 0 (stoichiometric Ni_2MnGa), T_C is approximately 370 K, whereas for z = 0.18-0.19, T_C matches the value of T_m. For z > 0.19, T_C shows a sharp increase. [56]

The magnetocaloric effect is enhanced for Ni-Mn-Ga near the martensitic transformation. When T_m and T_C coincide, which can be achieved by tuning the alloy's composition, this enhancement of the effect is even more accentuated. Coupling the two transitions means that the change in entropy is the result of both the magnetic and structural contributions. In addition, the much larger magnetization change in the transformation from a para-austenite to a ferro-martensite makes the magnetic field more effective in changing the transformation temperature, thus demanding a lower field to induce the transformation. A vast portion of the research work being developed nowadays on the magnetocaloric effect on Ni-Mn-Ga is focused on tuning the alloy's composition to the enhancement of this effect. [57]

High values of the magnetic entropy change (ΔS_M) are exhibited by $Ni_{55}Mn_{20}Ga_{25}$ single crystals (86 $JKg^{-1}K^{-1}$ for a field variation of 5 T [58]), but these are not economically favorable in terms of production which is a drawback for their applicability. Polycrystalline samples are cheaper to produce, but the occurring defects decrease ΔS_M values to about one tenth of those presented by the single crystals [59].

The different properties presented by the two different structural phases of the Ni-Mn-Ga system, namely the different values in their magnetization (ΔM), make them promising in their magnetoelastic behavior, and, in the magnetocaloric effect. The last decade brought considerable attention to Co-added Ni-Mn-based systems due to reports on values of the MCE comparable to the best performances of systems deemed relevant in this context, such as La-Fe-Si-H or Gd-Si-Ge. [60][61]. Specifically, the addition of Co into Mn-rich Ni-Mn-Ga systems revealed an increase in the ΔM between two ferromagnetic phases [62]: it attributes higher magnetization to austenite than to martensite, unlike what normally happens in the Ni-Mn-Ga parent phase [63], leading to the so-called inverse MCE. This particular member of the

Heusler family became thus an item of interest within the field of study of the magnetocaloric effect.

3.2 – Elastocaloric effect and NiTi

The elastocaloric effect is especially enhanced when a material undergoes first order structural transformations [31]. A specific class of such materials are the shape memory alloys (SMAs). The shape memory effect exhibited by SMAs originates in the first order diffusionless transformation between two different solid phases. As mentioned, this transformation is called the martensitic transformation (Fig. 3.6a) [31][64]. This phase transition consists in the material changing from a phase with higher symmetry, austenite, to a phase with lower symmetry, martensite. The term direct martensitic transformation refers to the austenitic phase transforming into the martensitic phase. This is an exothermic process and can be induced by applying stress to the material. The transformation from martensite to austenite is called the reverse martensitic transformation, which takes place when stress is no longer applied to the material SMA. It is an endothermic process, heat being absorbed by the material undergoing the transformation.
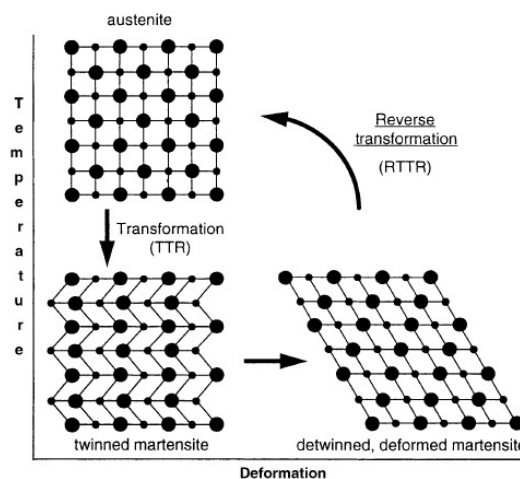
Fig. 3.6a - Martensitic transition and shape memory effect [30].
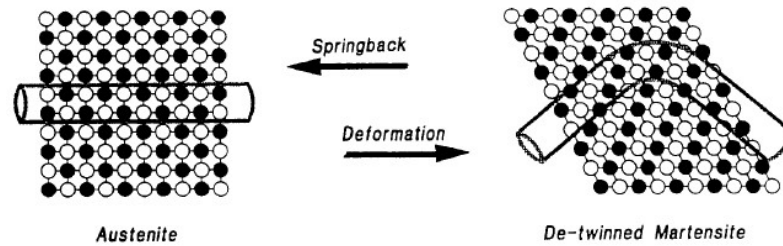
Fig. 3.6b - Pseudoelasticity in NiTi alloy [70].

The elastocaloric effect is associated to the applied stress inducing the martensitic transformation [31]. In the martensitic phase transformation taking place in SMAs, the material reacts reversibly to any applied stress due to the material's phase boundaries showing reversible motion. This characteristic is called pseudoelasticity [65-66] (Fig. 3.6b) and it is strongly desirable for the cycling process required for most refrigeration processes. Currently, local studies of this caloric effect are interesting especially near the martensitic transition, and furthermore when the transformation drives the material to a metastable state. Metastable paths are deeply connected to the transformation driving mechanism, and constraints in the moving of interfaces in the material can cause fluctuations in the applied stress, as shown by E. Bonnot *et al.* in 2007 [67].

NiTi

NiTi is a SMA, presenting a reversible structural transformation that makes it attractive for engineering applications. NiTi alloys were initially explored in the 1960s by Buehler [68] and their most singular trait was presenting the shape memory effect when given the adequate heat treatment [30]. In this case, they are known as austenitic/martensitic activated alloys. NiTi alloys that do not exhibit the shape memory effect are generally designated as martensitic-stabilized Nitinol, which is the commercial designation for these materials [69]. NiTi alloys are currently one of the most used shape memory alloys for technological applications, furthermore due

to their great biocompatibility [1], and can exist in the form of a binary compound, exhibiting a Ni_3Ti_4 phase within the NiTi matrix [69].

The shape-memory effect can be observed by applying stress or by varying the material's temperature.

The predicted stable crystalline structure for the NiTi austenitic phase agreeing with data collected from different characterization techniques such as XRD, differential scanning calorimetry (DSC), and neutron scattering is similar to the B2 structure (Pm-3m) (Fig. 3.7a), but with deviations (Fig. 3.7b) [70] . On the other hand, the martensitic phase presents a monoclinic structure (Fig. 3.8) [71]. The different crystalline structures of the two phases presented by NiTi are responsible for dramatic differences between their properties, such as rigidity, brittleness, and electrical resistivity. Austenitic NiTi is higher in rigidity and not as plastically deformable as the martensitic NiTi, which is more ductile, easier to deform.
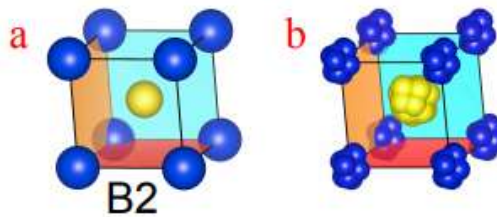
Fig. 3.7 - (a) B2 structure (b) Projection of Ni27Ti27 atomic positions on a B2 cell; Ni (yellow) and Ti (blue) [70].
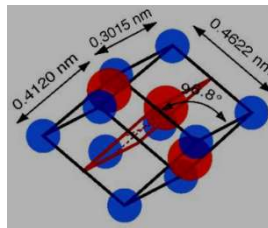
Fig. 3.8 - Monoclinic crystalline structure of the NiTi martensitic phase [72].

Concerning caloric effects associated to the transition in NiTi SMA, $Ni_{50}Ti_{50}$ wires with different diameters were used to demonstrate elastocaloric cooling, with $\Delta T = - 17K$ [6]. Measurements performed with infrared microscopy (IR) on

magnetron sputtered $Ni_{50,4}Ti_{49,6}$ 20 μm films exhibiting room temperature pseudo-elastic stress-strain behavior presented a maximum temperature decrease of about 16 K during the reverse martensitic transformation [73].

In 2014, Ossmer et al. found a large effect size similar to bulk during load cycling in magnetron sputtered binary NiTi films, but fatigue related issues appeared, which led to further investigation in the subsequent year on other strategies based on NiTi to circumvent this limitation [74]. Also in 2015, $Ni_{50,375}Ti_{49,625}$ single crystals showed a $\Delta T_{máx}$ = 14 K [75].

Ni-Mn-Ga is also a SMA. All aspects discussed here concerning the relationship between the martensitic transformation and the elastocaloric effect are also valid for this material. However, since Ni-Mn-Ga is more specifically a ferromagnetic shape memory alloy (FSMA), it is used widely in the context of the magnetocaloric effect, and that is why it was discussed on the previous section.

3.3 – Electrocaloric effect and BaTiO$_3$

The electrocaloric effect was first brought to light when it was experimentally demonstrated by Kobenko and Kurtschatov on Rochelle salt in 1930 [76].

Later, in the 60s, Wiseman and Kuebler achieved an actual quantified measurement of the effect in the order of mK accompanied and suggested the temperature variation observed to be dependent on the squared electrical polarization [77]. The small magnitude of the temperature variation intervals exhibited in the electrocaloric effect seriously diminished the interest on the research in this field, since applicability was seen as an unlikely scenario [78].

Only in the 2000's the research on this subject resurged, after the work of Mischenko et al reported the giant electrocaloric effect ($\Delta T \sim 12K$), near the ferroelectric Curie temperature, of 300 nm sol-gel $PbZr_{0.95}Ti_{0.05}O_3$ films. This finding gave this field of research a considerable boost [21][21][79][80].

The presently observed tendency for device miniaturization requires effective heat dissipation solutions with particular characteristics. The dimensional

compactation allowed by electrocaloric-based technologies is a great plus in this context [81].

Although the macroscopic mechanism of the electrocaloric process is fairly well understood, performing local studies in electrocaloric materials will clarify the effect at the micro and nanoscales, e.g., the role of domains. [82]

BaTiO₃

BaTiO₃ is a material that has been thoroughly studied mainly due to its interesting ferroelectricity. BaTiO₃ has different structures depending on the material's temperature, with each of these phases possessing specific properties like crystallographic structure, electrical polarization, among others.

At high temperatures BaTiO₃ belongs to the family of the perovskites, with the general formula ABO_3, where A corresponds to Ba^{2+} (larger cation) and B to Ti^{4+} (smaller cation) [83].

The structure is cubic with Ba^{2+} in the corners and Ti^{4+} in the center of the cube and O^{2-} in the center of the cube's faces (Fig. 3.9).
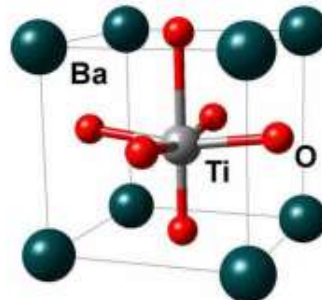
Fig. 3.9 - BaTiO3 perovskite structure cubic, at high temperatures [84].

The perovskite cubic structure holds for temperatures above 393 K, temperature at which the material transforms from a paraelectric state to a ferroelectric state. For lower temperatures, BaTiO₃ shows different structural phases, each a distortion of the cubic symmetry. As temperature decreases, BaTiO₃ subsequently goes through the tetragonal (393 K > T > 278 K), orthorhombic (278

K > T > 183 K), and rhombohedral (T < 183 K) crystalline structures (Fig. 3.10) [83][85]. Fig. 3.11 shows the pressure versus temperature phase diagram for BaTiO₃, based on low-pressure experiments and classical extrapolation.
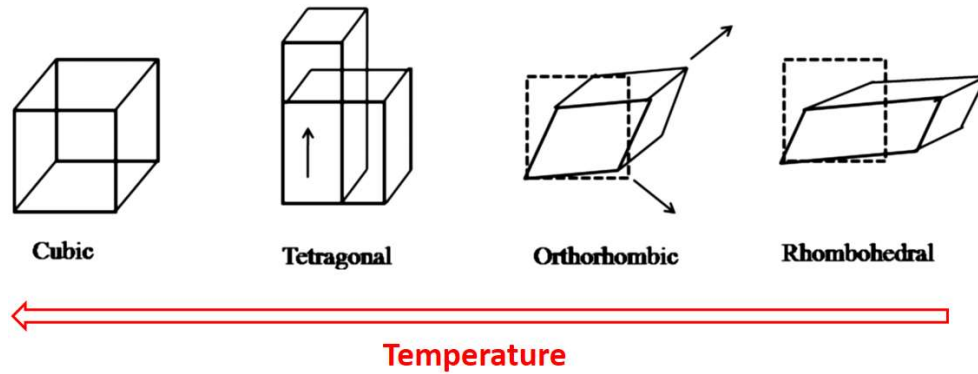
Fig. 3.10 - Structural phases of BaTiO3 [86].
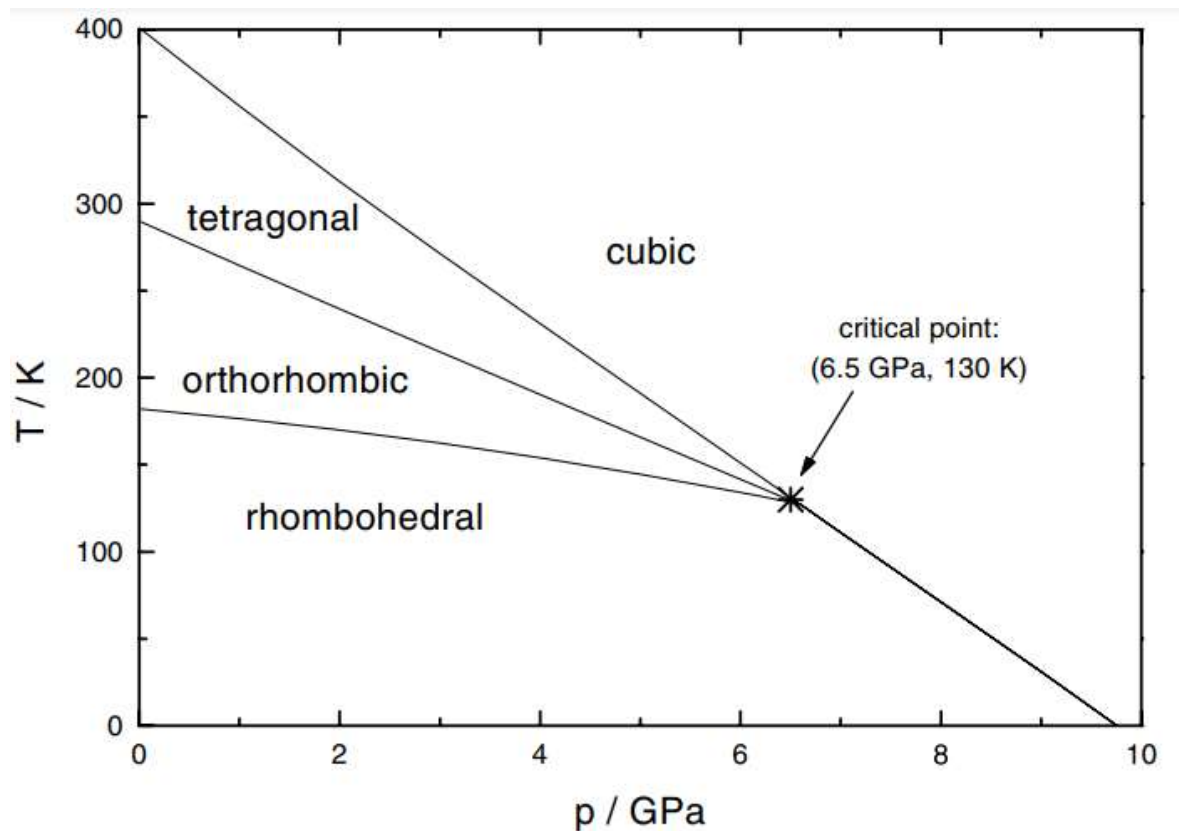
Fig. 3.11 - Pressure versus temperature phase diagram for BaTiO3, based on low-pressure experiments and classical extrapolation (Samara 1966, 1971, Decker and Zhao 1989) [87].

BaTiO$_3$ is the most studied material in the context of the electrocaloric effect, because of its giant manifestation which is due to the large amount of latent heat involved in the paraelectric to ferroelectric transition.

The electrocaloric effect was studied in BaTiO$_3$, bulk and thin film form by Akcay et al. in 2007 [88], and in dense nanoceramics form by Qiu et al. in 2009 [89].

In terms of thin films, the small working volume implies a low heat absorption capacity and a hindrance for application purposes in refrigeration solutions based on the electrocaloric effect [90]. In this context, research developed on BaTiO$_3$ multilayers such as that of Kar-Narayan *et al.* [91], showing a relevant temperature change of ~ 1.3 K, has drawn the field's attention.

4 – THERMAL CHARACTERIZATION TECHNIQUES

4.1 – Scanning Thermal Microscopy

The characterization of temperature dependent processes and the exploitation of existing and new technologies require heat transfer management. Miniaturization in modern devices to the order of few tens of nanometers has turned the study of physical phenomena at reduced length and time scales into an area of intense research [92-101].

The need for thermal nano-characterization techniques that enable measuring and controlling temperature with nanoscale spatial resolution and high temporal resolution has led to new developments in scanning probe microscopies enabling direct observation of physical phenomena with the desired spatial and temporal resolutions. These have had great impact on experimental research [102-103] and they have been applied to the investigation of thermal properties of materials at scales never before achieved. The use of nano-probes in Scanning Thermal Microscopy (SThM) [93][104-108] is a good example of such improvements.

SThM performs scans across a sample surface with a thermal sensor containing a thermally conductive tip that is often also used as a heater [109] . The tip, mounted on a force sensitive cantilever, is connected to a feedback loop used to maintain a constant tip-surface force while scanning line by line across a given area of the sample surface. This approach is based on the well-known Atomic Force Microscopy (AFM) technique used in contact and constant force modes and containing a thermal probe.

The core feature of SThM is the probe acting as a nanoscopic temperature sensor and a source of heat, which can be external (incident electromagnetic radiation), internal to the sample (a buried hot region inside a chip) or may consist of the probe itself [110]. Besides desiring and needing thermal nano-characterization

technical solutions [108] with adequate spatial resolution for miniaturized devices and materials [111], the development of nano-sensors which also act as local micro/nano-scaled heating devices is required [112].

The fact that most conventional thermal analysis techniques are limited to measuring the thermal response of the whole sample raises the importance of thermal mapping, enabling the study of local thermo-physical effects arising from location of centers, whose temperature changes due to nucleated modifications.

This stands in the way of ascertaining the origin of a broad change in behavior on heating a specimen, whether it arises from a genuine effect in a homogeneous system or it is due to a series of overlapping responses from a heterogeneous system, where there may be a gradation in properties throughout the sample. Alternatively, a weak effect observed in the entire sample could constitute a strong response from a minority component (e.g. an impurity) within the material [113]. The thermal nano-probe is a fast response system with a low mass/thermal capacity ratio, which is a significant contribution in achieving the time resolution below 1 ms that is sought for in thermal analysis techniques [94][97][104].

Displaying the ability to act as a local nano-heater on the material(s) of the sample, the recently developed SThM thermal nano-probes have raised intense scientific interest.

4.1.1 – SThM specific considerations concerning the present work

It is appropriate to begin this section by stressing that an open issue in the use and development of the SThM technique is the present unavailability of quantitative thermal conductivity measurements by commercial equipment [114]. Since each probe-sample system is thermally complex, changing considerably for different probes and even between successive measurements with the same probe (or within a single scan on a rough heterogeneous surface), obtaining quantitative data from SThM thermal conductivity measurements is still problematic. Despite

relevant progress achieved towards a solution in this matter [115][116][102], it is still necessary to search for ways to completely overcome these limitations [117].

Another well-established difficulty in scanning thermal microscopy is the existing correlation between the topography and the thermal signal. The thermal conductivity contrast measurement obtained by scanning thermal microscopy is an image heavily influenced by changes in tip-sample thermal contact area arising from any surface roughness of the sample [94]. When the probe scans a depression on the surface the tip-sample contact area increases, increasing also the heat flux from the tip to the sample. A natural consequence of this occurrence is that it is necessary to provide more power to the tip in order to keep its temperature constant. This increase in power provided to the tip will show on the image resulting from the measurement as an apparent increase in the local thermal conductivity of the sample. When the probe encounters some sharpness, the opposite occurs. When there is little thermal contrast between different areas of a heterogeneous surface, it can be particularly difficult to interpret the thermal results. A thorough sample preparation by fine polishing, for instance, might help soothe the effect. Current approaches towards a solution for this issue consist in the development of a complex neural net algorithm [118] where for each pixel the local topography is characterized by subtracting its height from the heights of surrounding pixels to ascertain whether the probe stays on a depression, a flat surface or a sharp feature. Such algorithm requires lengthy training of the neural net with a variety of specimens. Other methods apply pixel statistical analysis distribution to enhance image contrast [119]. These issues have been limiting the potential of SThM as a technique and their resolution will account for a greatly claimed extension of SThM applications.

All SThM measurements in this work were performed in ambient conditions using the PARK SYSTEMS XE7 Scanning Thermal Microscopy equipment (Fig. 4.1). Fig. 4.2 presents a schematic representation of the basic principle of operation for this system. We used standard first-generation thermal probes from KELVIN Nanotechnology [120]. These are nanofabricated thermoresistive probes where a palladium resistive element is lithographically patterned on the AFM tip apex mounted on a silicon nitride cantilever (400 nm thick) (Fig. 4.3). The electrical

connection is made to two Au pads on the probe's base. The thermal tip, with a radius of approximately 100 nm, has a sensitivity of ~ 1 Ω / °C and provides a 50 nm spatial resolution ("NanoAndMore KNT-SThM-1an", n.d.).

The thermal probe can also obtain topographic information in the conventional contact AFM mode. In this case the tip is scanned across the sample using a pair of piezoelectric elements orthogonally aligned in the horizontal plane. As the height of the sample changes, the tip in contact with the surface is deflected, which translates in a change in direction of the laser beam reflected by the tip. The reflected beam is then detected by a set of photodiodes and the tip is vertically controlled by a feedback loop connected to a z-axis piezo element which provides the height of the sample for each x-y plane position [121].

Fig. 4.1 - PARK XE7 system.
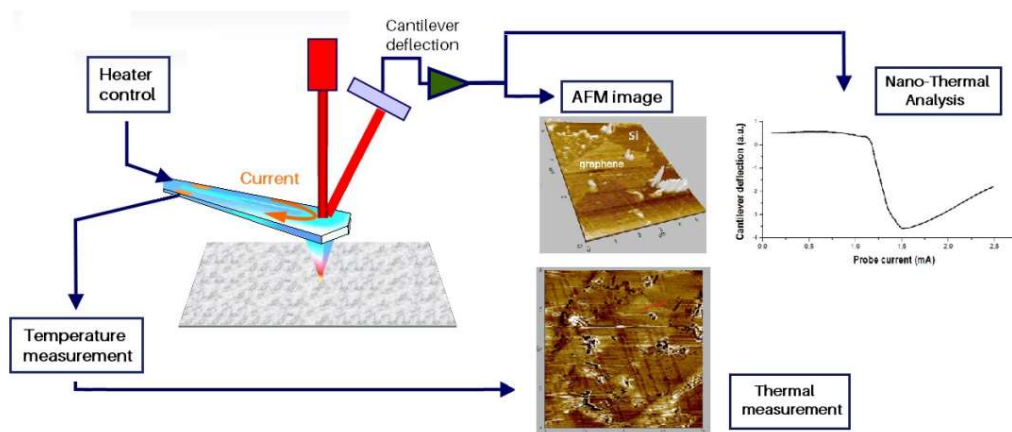
Fig. 4.2 - Schematic representation of the SThM XE7 PARK SYSTEMS operating principle.
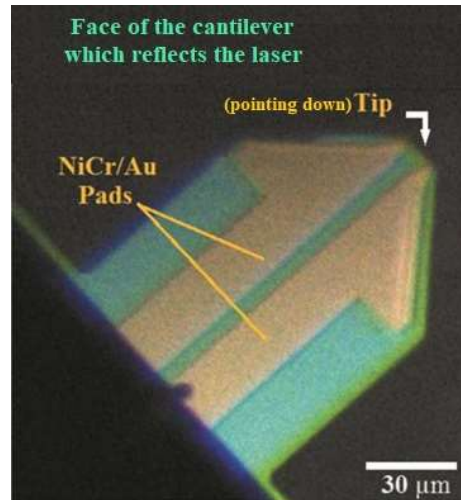
Fig. 4.3 - Kelvin Nanotechnology thermal nanoprobe.

The electrical current flowing through the thermal probe allows to measure topography while the sample is being heated at different temperatures, depending on the sample's thermal conductivity. The SThM tip serves thus as a nanoheater as well as a resistance thermometer, while also performing as an AFM tip. The resistivity of the SThM tip changes depending on the temperature of the surface with which it is in contact. This resistance is read from the Wheatstone bridge which can be seen in the schematic representation of the SThM circuit provided by PARK (Fig. 4.4).
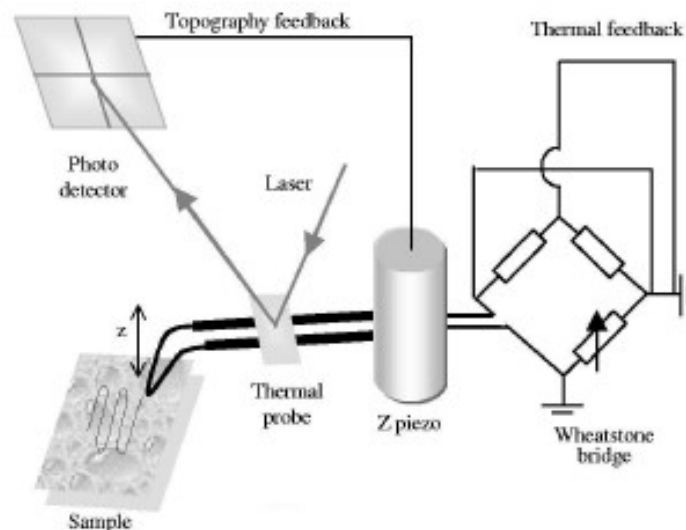
Fig. 4.4 - SThM diagram showing the Wheatstone bridge circuit [122].

The PARK XE7 SThM module system thermal calibration is accomplished using known melting points and glass transition points of polymers. The calibration of the SThM system is a standardized procedure accomplished using known melting points of polymers [111][101]. Semi-crystalline polymer melting standards provided with the equipment (polycaprolactone, high-density polyethylene and polyethyleneterephthalate, with melting points ranging from 323K to 523K) are used in the calibration [123].

In thermal conductivity contrast measurements, the bridge circuit is used to keep the probe's temperature (determined by its electrical resistance) constant. During this type of measurement, the tip is kept in contact with the sample. By electrically feeding the tip and monitoring the electrical current (output of the system in this mode) needed to keep the probe's temperature constant during a scan (using the bridge feedback circuit), it is possible to map the material's thermal response with sub-micrometric resolution. Areas of the sample with higher thermal conductivity are signaled by higher values of current needed to maintain constant the tip's temperature [124][125]. We have also performed measurements in the local nano-thermal analysis mode in which the thermal probe heats at a specific spot of the sample and obtains the local thermal response of that sample confined site [126]. While the probe is in contact with the sample surface, cantilever deflection is measured as a function of the tip's temperature (or the current that is being fed to the probe in order to heat it). The determination of the temperatures at which changes in sample topography occur enables the assessment of the temperature signaling structural transformations due to the resulting deflection of the cantilever [124].

Localized structural transformations induced by thermal probe heating are therefore easily accomplished in the case of low thermal conductivity samples, such as polymers [127][128]. Despite the ability of the probe to heat selected sample areas locally up to 433 K, for metallic thin films with transition temperatures well above room temperature, attaining high enough temperature to induce structural transitions with a nano-probe is difficult. In fact, heat diffusion limits the temperature at the sample surface. To overcome this limitation we have developed an approach

for the study of local structural transition temperatures in Ni_2MnGa thin films by heating the sample externally with a thermoelectric element, bringing it to a temperature just below the interval of transition temperatures of the sample, leaving to the probe the remaining heating needed to achieve the transition temperature. This process will be described in detail in section 5.1.2.

It is now indispensable to draw the reader's attention to the core of the SThM as a technique from the point of view of the user, which is a good understanding of how the probe interacts thermally with the sample according to the thermal properties involved. This is a complex endeavor which should be taken with a step by step approach.

An experiment was designed and conducted to bring us closer to a fuller understanding of such phenomena. Several materials with different thermal conductivities were selected, which can be seen on Table 4.1, along with the values for their thermal conductivities near room temperature, obtained from tabulated values in bulk materials. It was assured that all the probed surface areas of each material had a similar degree of roughness. This was achieved by making topography scans with the SThM tip of the areas to be probed and using the XEI software (developed by PARK Systems) to estimate the average roughness of the area to be acted on by the probe in each measurement. We were thus able to minimize differences in topographical features which could influence the thermal measurements by introducing differences in contact area between probe and probed material. Limitations in SThM measurements resulting from sample topography were already discussed in detail.

This study consisted in measuring the probe electrical current needed to keep the different materials at the same local temperature measured by the SThM probe in a steady state. It was performed for two different temperatures: 308 K and 318K.

Table 4.1 - Thermal conductivity values used in Fig. 4.5

Material	K (Wm^{-1}K^{-1})
Cork	0.044 [129]
PET	0.3 [130]
Quartz	3 [129]
Stainless steel	25 [131]
Aluminum	235 [132]
Silver 925	400 [131]

The plot showing the dependence of the probe's current on thermal conductivity for the considered temperatures is shown in Fig. 4.5. To maintain the sample's local temperature constant, the required probe current varies more significantly for materials with lower values of thermal conductivity. The knowledge on the behavior of the probe for higher values of thermal conductivities is relevant, since the samples where we propose to locally induce structural transformations are metallic alloys. Stoichiometric Ni$_2$MnGa has been reported to have a thermal conductivity of about 20 Wm^{-1}K^{-1} at 300 K with a significant increase near and during the structural transformation in heating [133]. For the range of thermal conductivities reported for Ni$_2$MnGa, significant variations in thermal conductivity do not demonstrably cause significant alterations in probe current needed for the tip to achieve a given temperature. It is important to stress that, whether the tip is in contact with a solid material or with air (Fig. 4.6), the temperature measured by the calibrated probe has, in general, a non-linear relationship with the current fed to the probe.
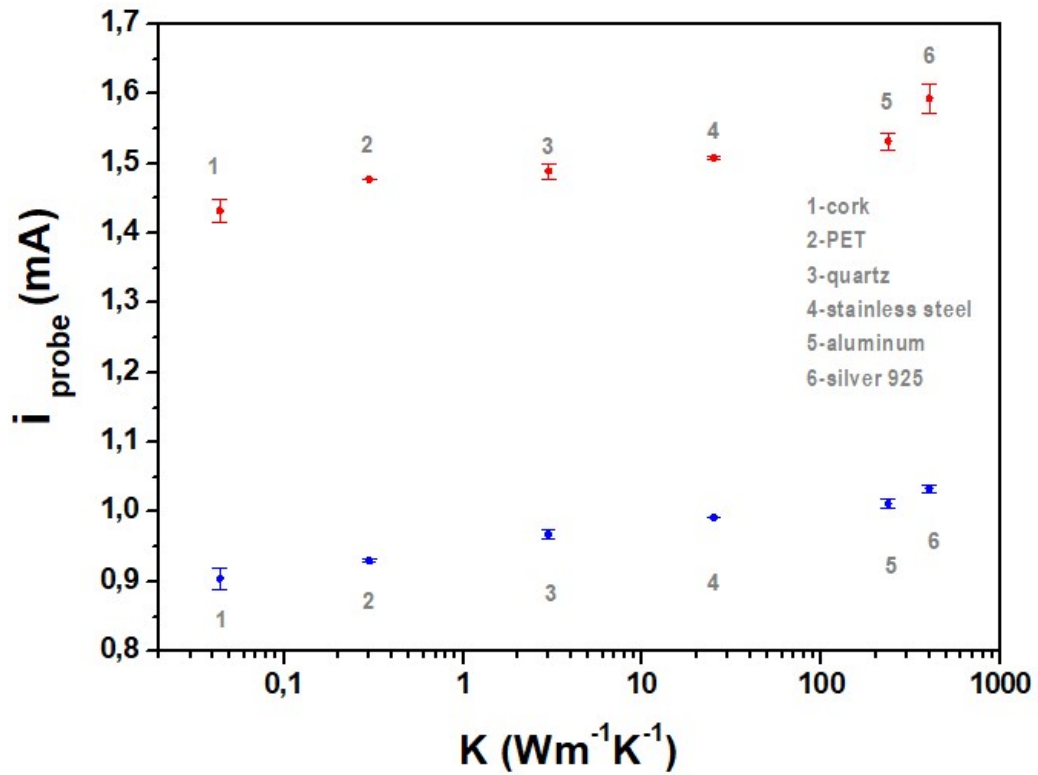
Fig. 4.5 - Probe current vs thermal conductivity (logarithmic scale) for the same probe temperature (308 K and 318 K).
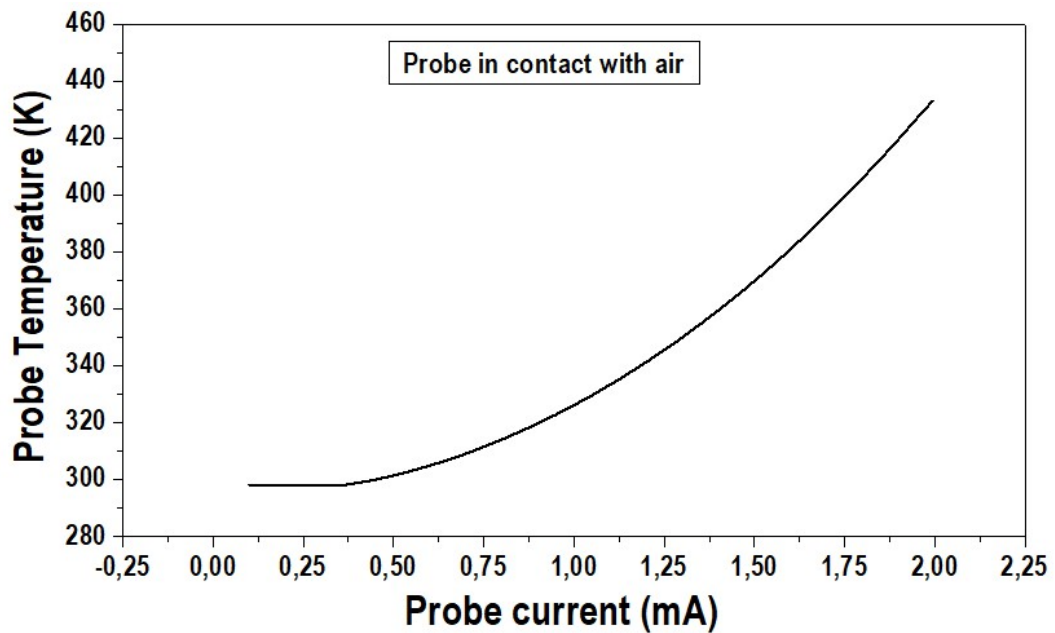
Fig. 4.6 - Plot showing the temperature measured by the SThM probe as a function of the current with which it is being supplied while the probe is in contact with air.

4.2 – Infrared Thermographic Microscopy

Thermography techniques consist in the translation of a scene's thermal status into digital data that can be used to produce a visible image (thermogram) or be fed into a computer for interpretation [134][135]. The infrared thermal imaging technology emerged in the 1960s, developed mostly for nighttime surveillance purposes and heat signature detection [136]. It is now used extensively in several fields, such as law enforcement, firefighting, engineering, building assessment, medical imaging, archaeology, as well as volcanology and biological and ecological applications [137-140]. As an imaging technology, infrared thermal imaging has the advantages of possessing a noninvasive and non-contact approach [141]. It is a convenient and effective tool for real-time temperature monitoring of objects or processes in a non-contact way, which is a valuable feature for most application fields. It is important to stress that infrared thermal imaging is subject to uncertainties requiring physical modeling, which can be accomplished by built-in software solutions [142-143]. Modern image processing tools on the acquired infrared thermal information along with artificial intelligence-based approaches can thus further increase the reliability and efficiency of this technique. Contrary to SThM which measures temperature changes in a single point at a time, an infrared thermography microscope measures the temperature changing in the area of observation with spatial resolution determined by the digital recording system used and the lens system of the microscope. The possibility of recording a video of the sample while the changes in temperature are taking place brings also time resolution to the measurement of whichever caloric effect is being studied.

All measurements obtained with this technique for this work were performed by a FLIR SC5600-M (Fig. 4.7), which is a large format infrared camera for R&D and thermography applications. It has an InSb sensor, a response spectral interval of 2.5 µm to 5.1 µm a 640 x 512 pixel resolution and a 0,02 ºC resolution in temperature. The frame rate can go from 1 Hz to 100 Hz. In the experiments performed, a 25 Hz frame rate was used. Temperature calibration range goes from -20 °C to 3000 °C and temperature measurement accuracy is ± 1°C or ± 1 %.

Fig. 4.7 - FLIR SC5600-M infrared camera for R&D and thermography applications.

The amplification provided by the infrared camera depends on the lens that is used. The real dimensions represented by one pixel depend on the distance at which the camera is placed in relation to the object under study. In our study, the field of vision used was such as to equate a pixel to an 85x85 μm^2 area. A suitable microscopy system can be attached, reaching a resolution of 3x3 μm^2 area. Due to the complexity of the experimental setup for the study of the magnetocaloric effect, it was not used.

5 – LOCALLY INDUCED TRANSFORMATIONS IN NMG AND NiTi

Device miniaturization required in a wide range of technological fields draws interest in the study of the martensitic transformation at the micro/nanoscale. It is known that structural transformations, in particular the martensitic transformation in shape memory alloys, depend on the dimensions of the material where the transformation is taking place. Research already existing on the behavior of the martensitic transformation at smaller scales contemplates mostly the analysis of micro and nanostructured materials [144-147]. Less is known about the behavior of the martensitic transformation when the volume of material being transformed is of nano/micrometric dimensions while incorporated in a sample with a much bigger overall volume. The main challenges for this kind of analysis consists in being able to only heat such a small volume of material, in order to induce the transformation locally, while being able to simultaneously evaluate the behavior of the transformation. The SThM thermal nanoprobe responds constructively to such challenges, in a way that will be explored in the present section.

5.1 – Mapping local martensitic transformations in NMG thin films

In this chapter we study the thermal effect of locally induced structural transformations by a combined temperature dependent cantilever deflection. For this purpose, two Ni-Mn-Ga thin films were used: NMG1537 and NMG1535, respectively, a 400 nm film and a 100 nm film, both prepared by sputtering deposition on MgO substrates, by Francesca Casoli at IMEM-CNR, Parma, in a sector of the Magnetic and Multiferroic Materials group led by Franca Albertini. The films were grown epitaxially on MgO(100) by RF sputtering. Deposition rate and Ar

pressure were fixed at 0.1 nm/s and 1.5 Pa, respectively. Growth temperature was 350 °C.

Firstly, the samples are characterized, namely in their magnetic properties, topographies and compositions. The concept of locally inducing and probing transformations is explored, and we elaborate on the method to determine local transformation temperatures used in this study, highlighting its most relevant aspects. Whenever considered appropriate, further considerations about the SThM probe are added, due to their significance in this particular context.

For the 400 nm sample NMG1537, we start by selecting a 2x2 μm^2 area and perform a series of temperature dependent AFM topography scans around the transformation temperature, where we can witness the evolution of the martensitic pattern on the selected area vs temperature. We then locally induce the transformation in 100 different points, one at a time within the same 2x2 μm^2 area. The distribution and mapping of the local transformation temperatures (T_Ms) for this area are presented, and these results are compared with the results from the AFM vs temperature measurements. The following step consists in extending the study of locally inducing and probing T_Ms for over 100 different points within the whole area of the film. Also within this chapter, the temperature dependent AFM scans are analyzed in terms of the martensitic twinning characteristics (martensitic "wave" height and width) as the transformation takes place, both in heating and cooling, namely by approaching the dependence of the estimated percentage of martensite with temperature in heating and cooling.

For the 100 nm NMG1535 sample, the characteristics of the film's surface were deterrent to the quality of the obtained AFM topography scans performed. For this reason, the broadness of our work for this film was limited when compared to the 400 nm NMG1537 film, namely excluding the analysis of martensitic features. We then present the choice of a 2,4x2,4 μm^2 area of the film to locally induce the transformation in over 100 points within the selected area. As a result, the distribution and mapping of the local T_Ms for this area are presented. The distribution of the obtained T_M values was analyzed to some detail.

5.1.1 – Sample Characterization

5.1.1.1 – Magnetic Measurements

a) Sample NMG1537 (400 nm thin film)

Magnetization vs temperature (20 Oe magnetic field) and magnetization vs magnetic field (Figs. 5.1 to 5.4) for three different temperatures: 5 K, 300 K and 380 K were measured. Fig. 5.1 shows the field cooled (FC) magnetization vs temperature curves (in cooling and heating). In heating, a rise in the magnetization of the sample is shown due to the structural transformation from the lower symmetry-lower temperature martensitic phase to the higher symmetry-higher temperature austenitic phase, with $T_A \sim$ 336 K. The decrease in magnetization that follows signals the magnetic transformation to the paramagnetic phase with $T_C =$ 346 K. When samples exhibit such behavior in magnetization vs temperature curves, it is unclear whether the magnetic transformation before or after the whole sample has finished the structural transformation. On cooling, the Curie temperature is confirmed as 346 K, this magnetic transformation showing no thermal hysteresis. The fall in magnetization (roughly from 5.5×10^7 to 1.5×10^7 emu/m^3) indicates the martensitic transformation at $T_M \sim$ 330 K. The structural transformation shows thus a thermal hysteresis of about 6 K (Fig. 5.1).
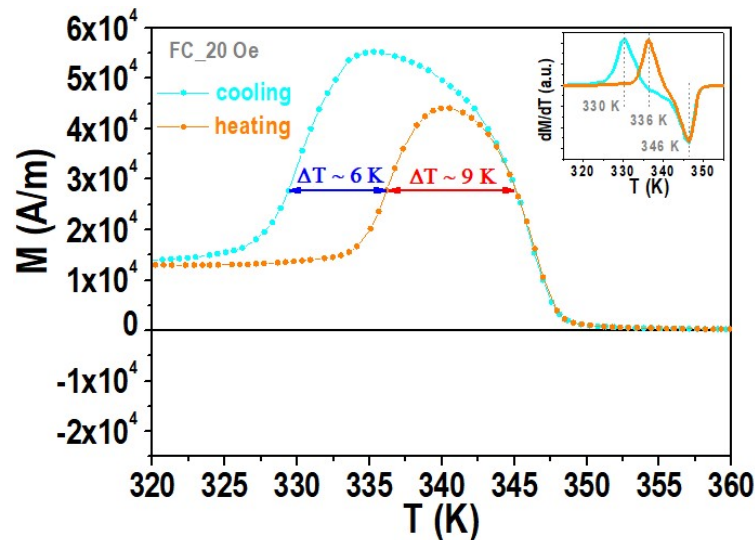
Fig. 5.1 - Field cooled (FC) magnetization vs temperature curves (cooling and heating) for the 400 nm film NMG1537.

Magnetization vs temperature curves (on heating) when the sample is subjected to a 20 Oe magnetic field after zero field cooling (ZFC) and 20 Oe field cooling (FC) (Fig 5.2) do not show significant differences in terms of the transformation temperatures and irreversibility is observed below T_C. Fig. 5.3 shows the plot of the expected linear variation of the reverse magnetization with temperature in the paramagnetic regime for of the NMG1537 film.

Magnetization vs magnetic field curves, in the range of -1000 Oe to 70000 Oe, taken at 5 K, 300 K and 380 K are plotted in Fig. 5.4. The sample shows a ferromagnetic behavior at 5 K and 300 K, both temperatures below T_C, according to the M vs T measurements. At 380 K, paramagnetic behavior is observed for this sample. The M(H) curves taken at 5K and 300K suggest the existence of the diamagnetic contribution from the MgO substrate, which is more noticeable in the 300K curve. At 380 K, the paramagnetic contribution overcomes the contribution from the substrate. The saturation magnetization, obtained by extrapolating the high field behavior to zero field give $M_{sat} = 5 \times 10^5$ A/m (500 emu/cm^3) and $M_{sat} = 3 \times 10^5$ A/m (300 emu/cm^3) at 5 K and 300 K, respectively. These values are comparable to those found in literature [50] [148].
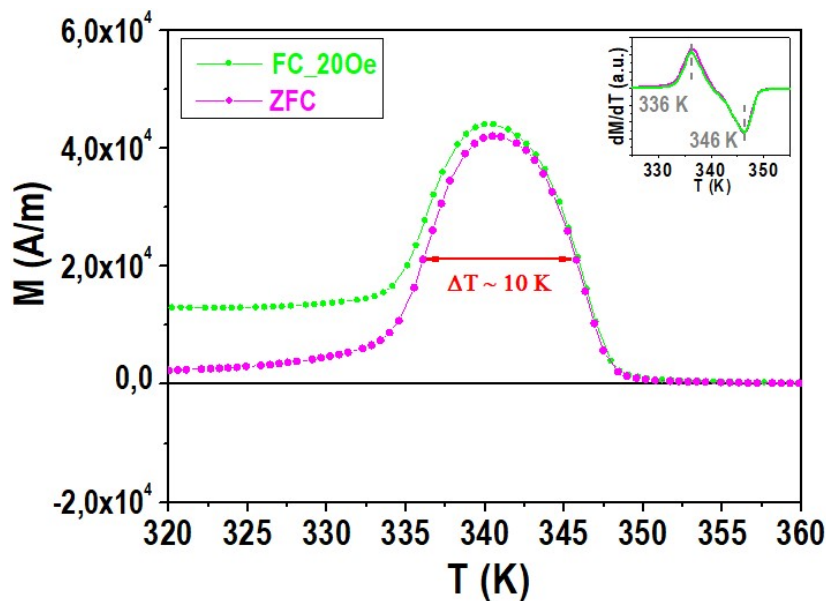
Fig. 5.2 - FC and ZFC magnetization vs temperature curves on heating for the 400 nm film NMG1537.
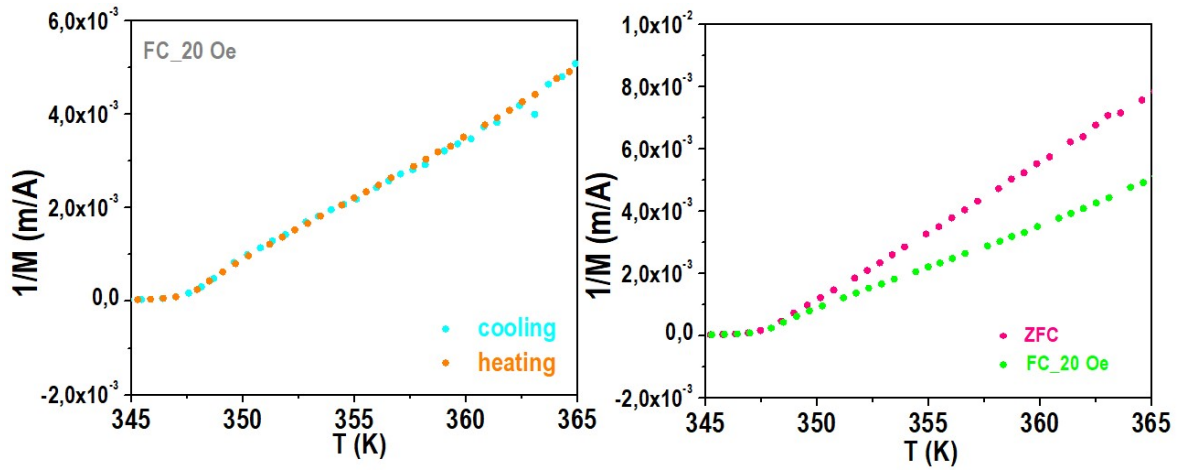
Fig. 5.3 - Expected linear behaviour of the reverse magnetization on temperature in the paramagnetic regime for the 400 nm film NMG1537.
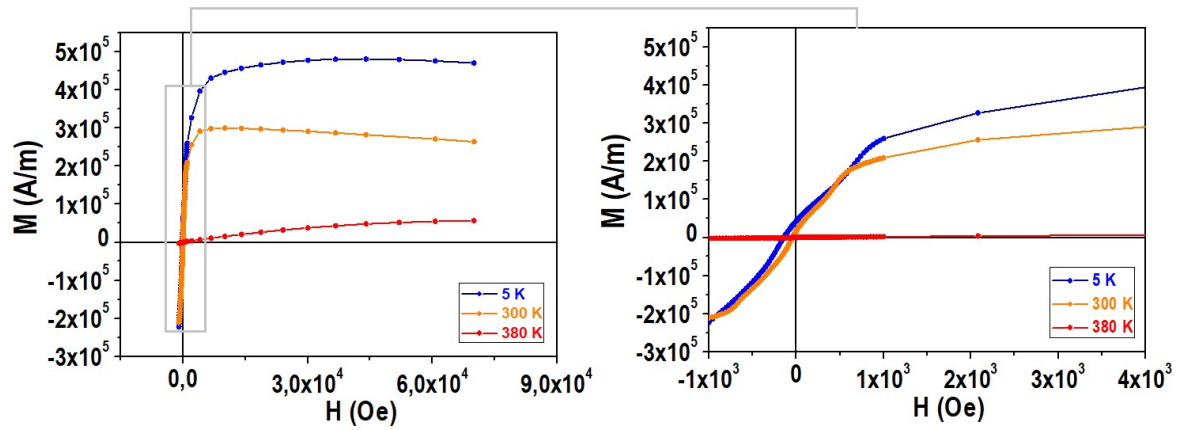
Fig. 5.4 - Magnetization vs magnetic field plots at different temperatures for the 400 nm film NMG1537; left: whole measurement; right: detail of measurement.

b) Sample NMG1535 (100 nm thin film)

Magnetic measurements performed on the 100 nm NMG1535 sample are presented in Figs. 5.5 to 5.8 In the field cooled curves (Fig. 5.5) there is no indication of the presence of the austenitic transformation. Only the magnetic phase transformation is present, with T_C = 339 K in heating and T_C = 337 K in cooling.

The ZF/FC hysteresis curve (Fig. 5.6) subtly shows the presence of the structural phase transformation. The rise in magnetization due to the austenitic

transformation is considerably smoother for this sample than it was for the 400 nm film NMG1537, in such a way that it becomes difficult to assess the temperature at which we should consider that the structural transformation has begun to occur. However, it can only be said that the increase in magnetization seems to become more evident at about 316 K as temperature rises and falls significantly roughly at the same temperature as T_C = 340 K. Fig. 5.7 shows the a plot of the variation of the reverse magnetization with temperature in the paramagnetic regime for of the 100 nm film NMG1535 where the linear dependency is not observed for higher temperatures.
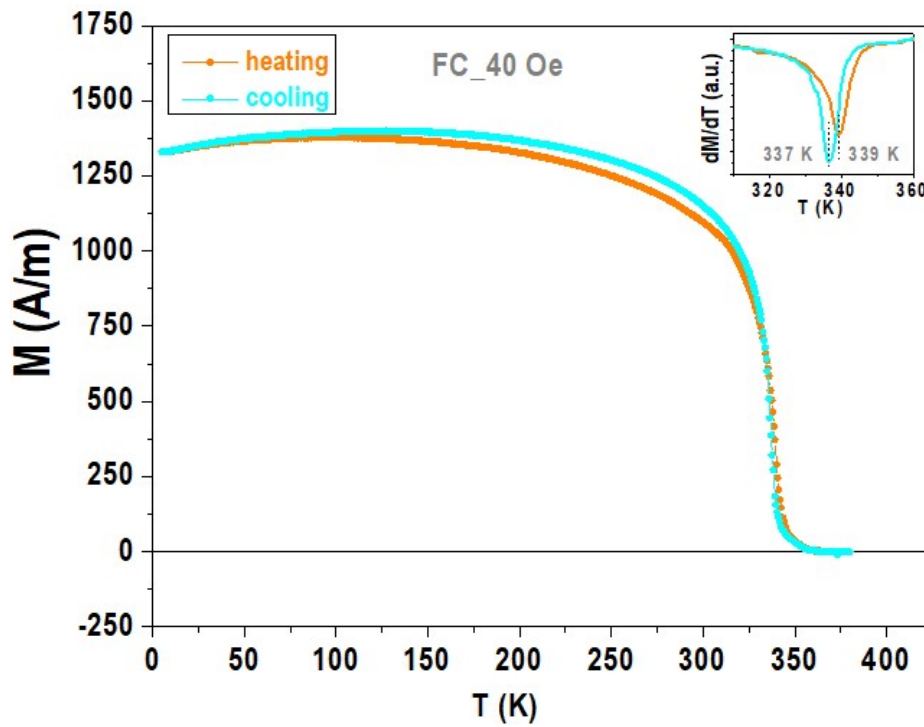
Fig. 5.5 - FC magnetization vs temperature curves (cooling and heating) for the 100 nm film NMG1535.

Magnetization vs magnetic field curves taken at 5 K, 300 K and 380 K are plotted in Fig. 5.9. The sample shows a ferromagnetic behavior at 5 K and 300 K, both temperatures below T_C, according to the M vs T measurements. At 380 K, the measured magnetic behavior is dominated by the diamagnetism from the MgO substrate.
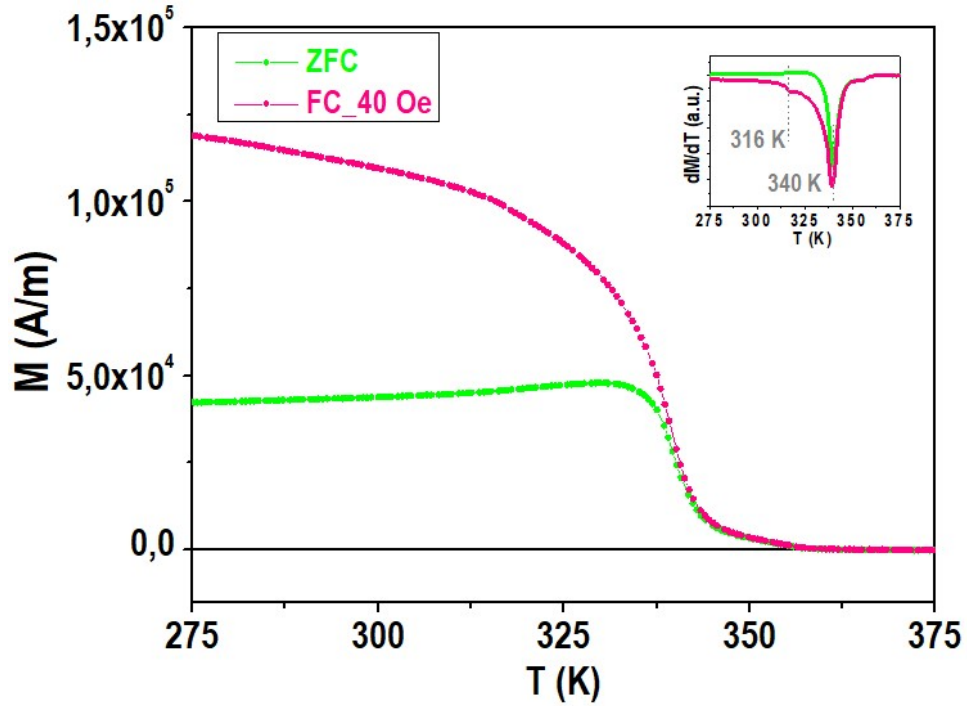
Fig. 5.6 - FC and ZFC magnetization vs temperature curves for the 100 nm film NMG1535.
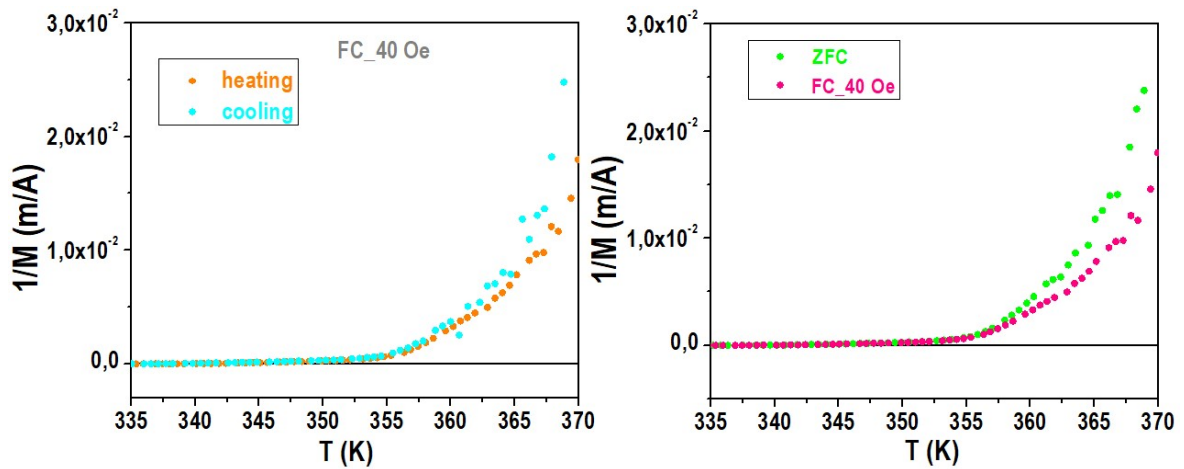
Fig. 5.7 - Linear behaviour of the reverse magnetization on temperature in the paramagnetic regime for the 100 nm film NMG1535; tendency for deviation from linearity for higher temperatures.

The diamagnetic contribution from the MgO substrate is also visible in both the 5 K and 300 K M(H) curves. The saturation magnetization, obtained by extrapolating the high field behavior to zero field give M_{sat} = 9.2X10^5 A/m (920 emu/cm^3) and M_{sat} = 3.8X10^5 A/m (380 emu/cm^3) at 5 K and 300 K, respectively.
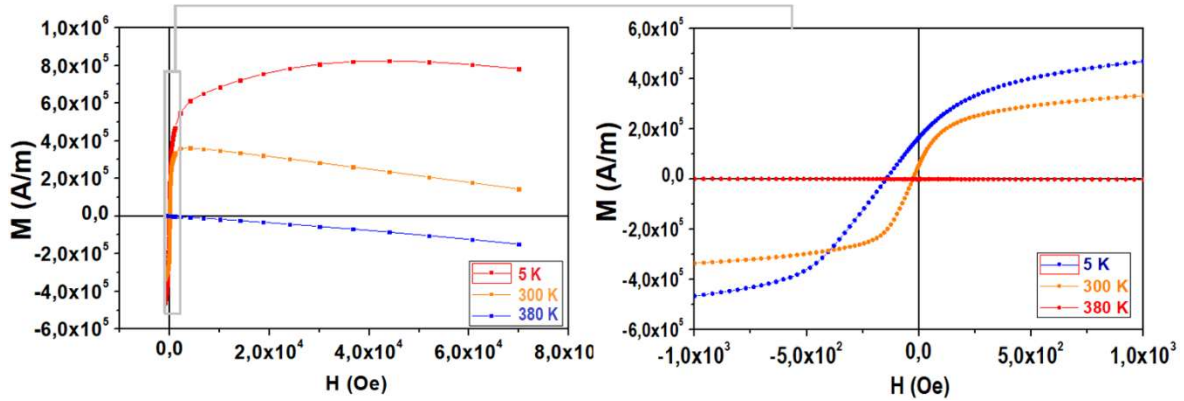
Fig. 5.8 - Magnetization vs magnetic field plots at different temperatures for the 100 nm film NMG1535; left: whole measurement; right: detail of measurement.

5.1.1.2 – Atomic Force Microscopy (AFM) studies

Topography scans were performed in both samples (Figs. 5.9 and 5.10). The measurements were performed with a PARK XE7 atomic force microscope, in contact mode, with CONTR probes [149]. These are standard shaped AFM probes, with radius: < 7 nm (< 10 nm guaranteed) and beam shaped cantilever. The force constant is 0.2 N/m, resonance frequency 25 kHz. The dimensions are 225 µm, 48 µm and 1 µm in length, width, and thickness, respectively. The cantilever has an approximately 30 nm thick aluminum reflex coating, enhancing the reflectivity of the laser beam. Bending of less than 2% of the cantilever length is provided by this virtually stress-free coating.

As can be seen from Figs. 5.9 and 5.10, both films show protrusions on their surfaces. In the 400 nm film NMG1537 these are located further apart from each other, allowing to obtain topography scans free from any protuberance with acceptable resolution. That is not the case for the 100 nm film NMG1535. Additional cleaning took place for the NMG1535 sample, missing the intended result of being able to obtain and identify an area which allowed for satisfying topography scans. In fact, after cleaning, topography scans for the NMG1535 film presented more

artifacts, further compromising the quality of the obtained measurement and making the distinction of martensitic features barely impossible.
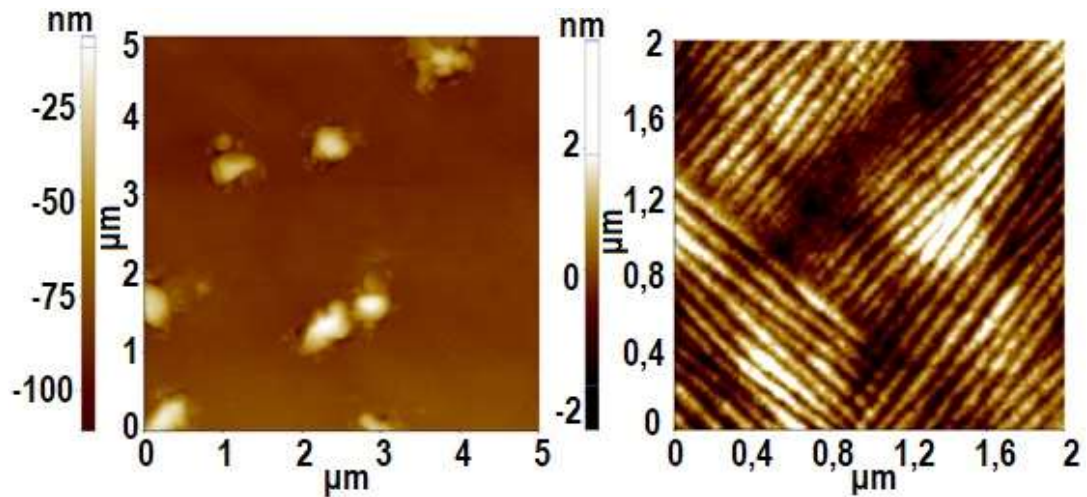
Fig. 5.9 - Representative topography scans of 400 nm film NMG1537 at room temperature; left) 5x5 um area, protuberances showing; right) 2x2 μm^2 area, protuberance free, well defined martensitic twinning.
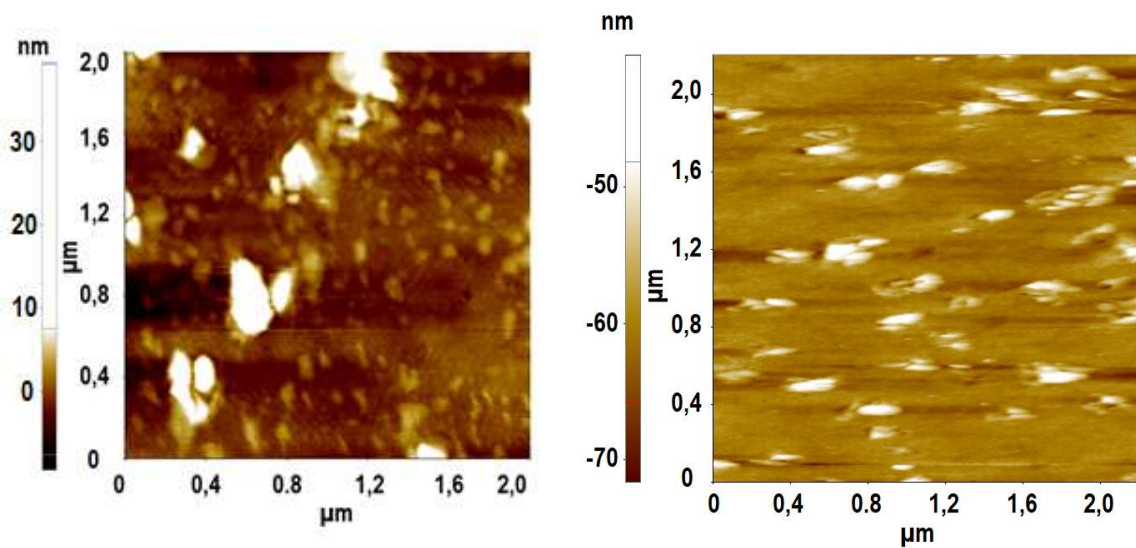
Fig. 5.10 - Representative 2x2 μm^2 topography scans of 100 nm film NMG1535 at room temperature: left) before cleaning; right) after cleaning.

5.1.1.3 – Energy-dispersive X-ray spectroscopy (EDS) analysis

Protuberances and protuberance-free areas of both films were analyzed (Fig. 5.11a to 5.11c). These analyses were performed on a S4100 Hitachi scanning electron microscope (SEM) equipment coupled with a RÖNTEC EDS spectrometer (described in chapter 2). The spectra were collected, and elements presence quantified with BRUKER Espirit 1.9 software. The results show that the protuberances are composed of the same elements as the protuberance free areas. As for the film composition, as expected, we see the peaks for Ni, Mn, and Ga, as well as C, since the sample had to be carbon coated on a carbon evaporator prior to the EDS analysis.

El	AN	Series	unn. C [wt.%]	norm. C [wt.%]	Atom. C [at.%]	Error (1 Sigma) [wt.%]
Mn	25	K-series	11,88	17,73	19,77	0,35
Ni	28	K-series	32,27	48,16	50,26	0,87
Ga	31	L-series	22,86	34,11	29,97	1,57
		Total:	67,01	100,00	100,00	
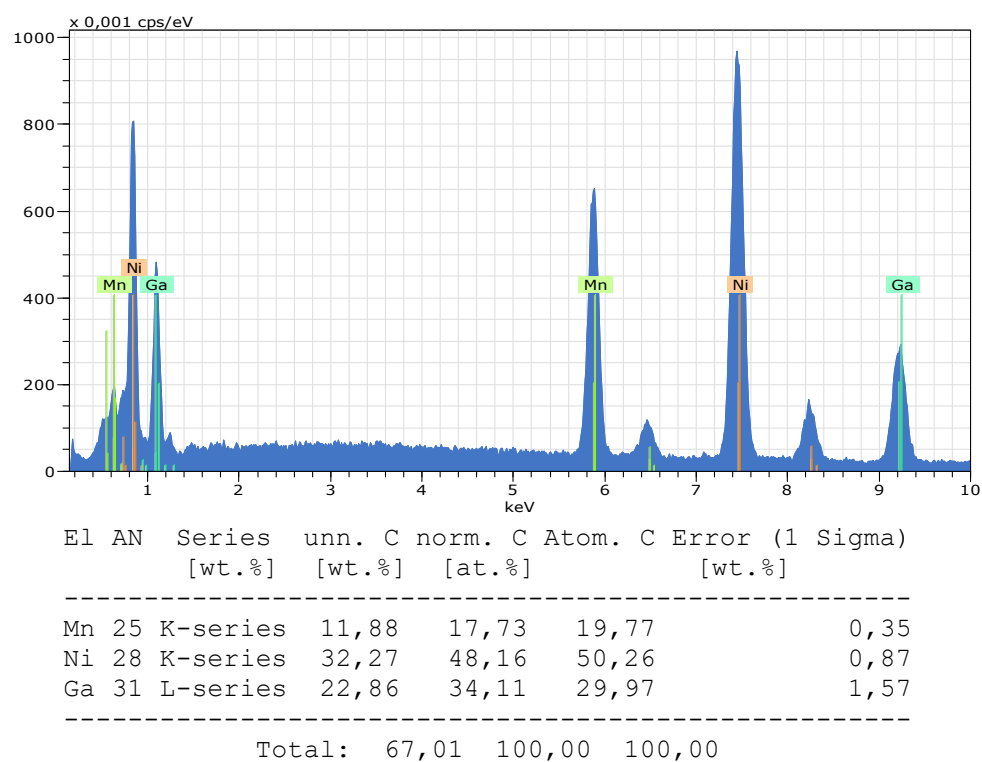
Fig. 5.11a - Representative plot of EDS analysis of 1.2 x 1 µm² area of the 400 nm film NMG1537.

El	AN	Series	unn. C [wt.%]	norm. C [wt.%]	Atom. C [at.%]	Error (1 Sigma) [wt.%]
Mn	25	K-series	11,44	17,83	19,88	0,34
Ni	28	K-series	30,88	48,14	50,23	0,83
Ga	31	L-series	21,82	34,02	29,88	1,51
		Total:	64,14	100,00	100,00	
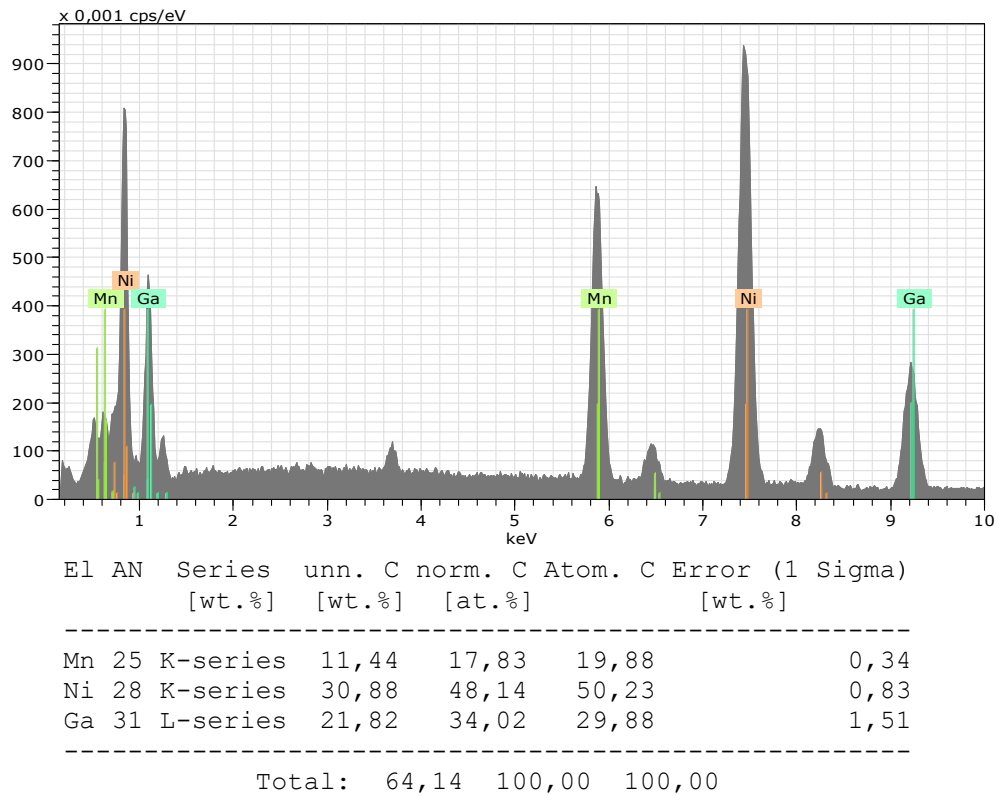
Fig. 5.11b - Representative plot of EDS analysis of 100 x 150 µm^2 area of the 400 nm film NMG1537.

El	AN	Series	unn. C [wt.%]	norm. C [wt.%]	Atom. C [at.%]	Error (1 Sigma) [wt.%]
Mn	25	K-series	13,50	20,42	22,51	0,40
Ni	28	K-series	33,84	51,19	52,83	0,91
Ga	31	L-series	18,77	28,39	24,66	1,34
		Total:	66,11	100,00	100,00	
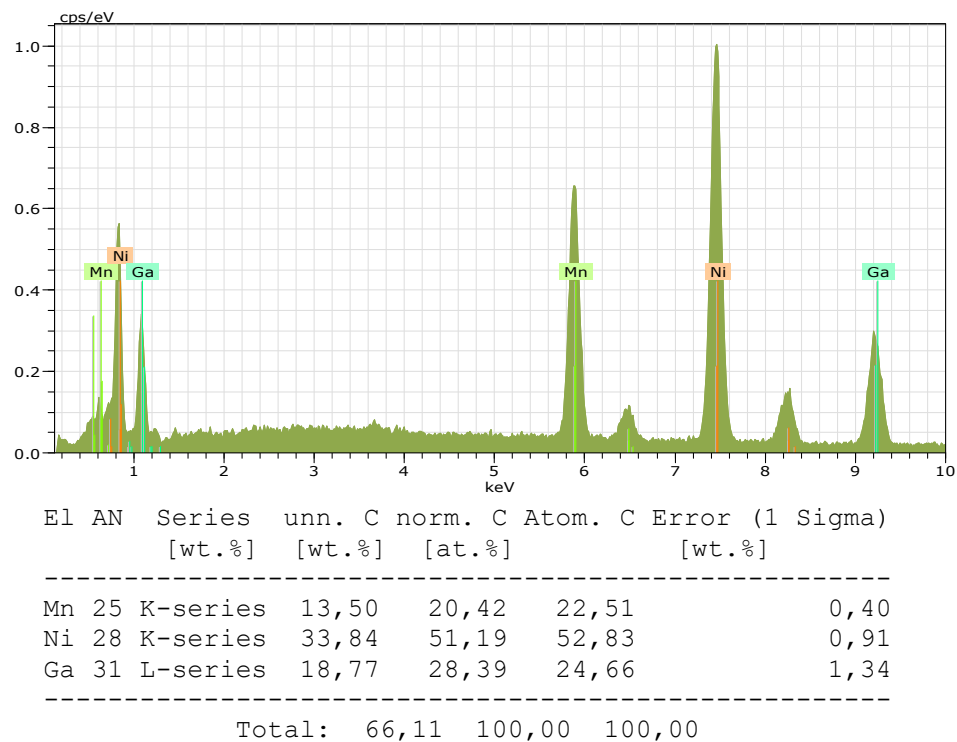
Fig. 5.11c - Representative plot of EDS analysis of a protuberance area of the 400 nm film NMG1537.

Element quantification presented on table 5.1 suggests that, in all protuberance free studied areas, the 400 nm film NMG1537 is richer in Ga, slightly lacking in Ni and considerably deficient in Mn, in relation to the Ni_2MnGa stoichiometric system. Wider and smaller areas of the film show very similar ratios of Ni, Mn, and Ga. In the protuberance, however, the same elements are present in different atomic percentages.

The uncertainties associated with these elemental quantifications make it a complex endeavor to comment on local compositional inhomogeneities, especially in the case of alloy systems such as this one, whose properties vary very sensitively with compositional changes, mainly for specific ranges of compositions. As mentioned before, for the $Ni_{2+x}Mn_{1-x}Ga$ system (Fig. 5.12 [9]), a 2.25% increase/decrease in Ni/Mn content (for compositions between $Ni_{2.27}Mn_{0.73}Ga$ and $Ni_{2.36}Mn_{0.64}Ga$) can cause changes of several hundred degrees (from ~ 375K to ~ 625K, respectively).
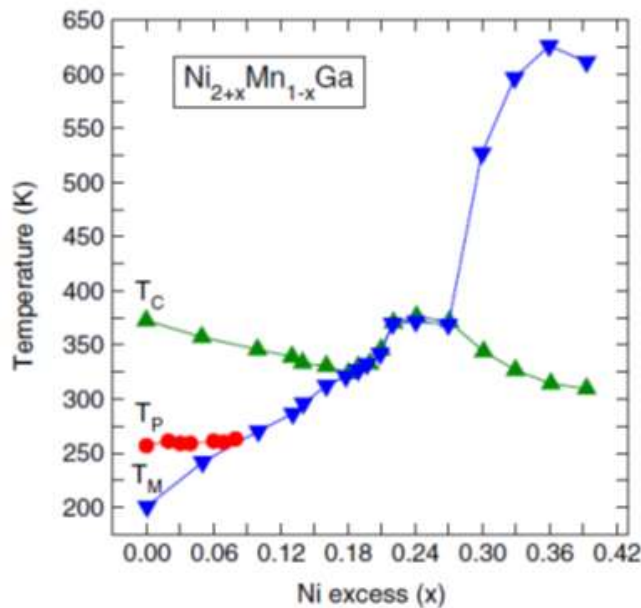
Fig. 5.12 - Ferromagnetic, TC, martensitic, TM and premartensitic, TP, transition temperatures determined from DSC and low-field magnetization measurements as a function of the Ni excess concentration x in $Ni_{2+x}Mn_{1-x}Ga$ alloys, for 0 < x < 0.4 [50].

The protuberances in 100 nm film NMG1535 are also composed by the same elements present in the rest of the film, as confirmed by EDS measurements performed for this sample (Fig. 5.13a and 5.13b) (with HITACHI S4100, described in chapter 2).

Like for 400 nm film NMG1537, we see the peaks for Ni, Mn, and Ga, as well as C, since this sample was also carbon coated.

Table 5.1 - Elements percentage quantification for different areas of the 400 nm film NMG1537 (obtained with HITACHI S4100)

Material	Area	Ni ± ΔNi (%)	Mn ± ΔMn (%)	Ga ± ΔGa (%)
film	1,2 x 1 µm^2	48.2 ± 0.9	17.7 ± 0.4	34.1 ± 1.6
	100 x 150 µm^2	48.2 ± 0.8	17.8 ± 0.3	34.0 ± 1.5
protuberance	200 x 300 nm^2	51.2 ± 0.9	20.4 ± 0.4	28.4 ± 1.3


```
El AN   Series   unn. C norm. C Atom. C Error (1 Sigma)
         [wt.%]   [wt.%]  [at.%]          [wt.%]
-------------------------------------------------------
Mn 25 K-series   3,53   12,65   14,62            0,14
Ni 28 K-series   9,56   34,28   37,07            0,31
Ga 31 L-series  14,79   53,06   48,31            1,04
-------------------------------------------------------
         Total:  27,88  100,00  100,00
```
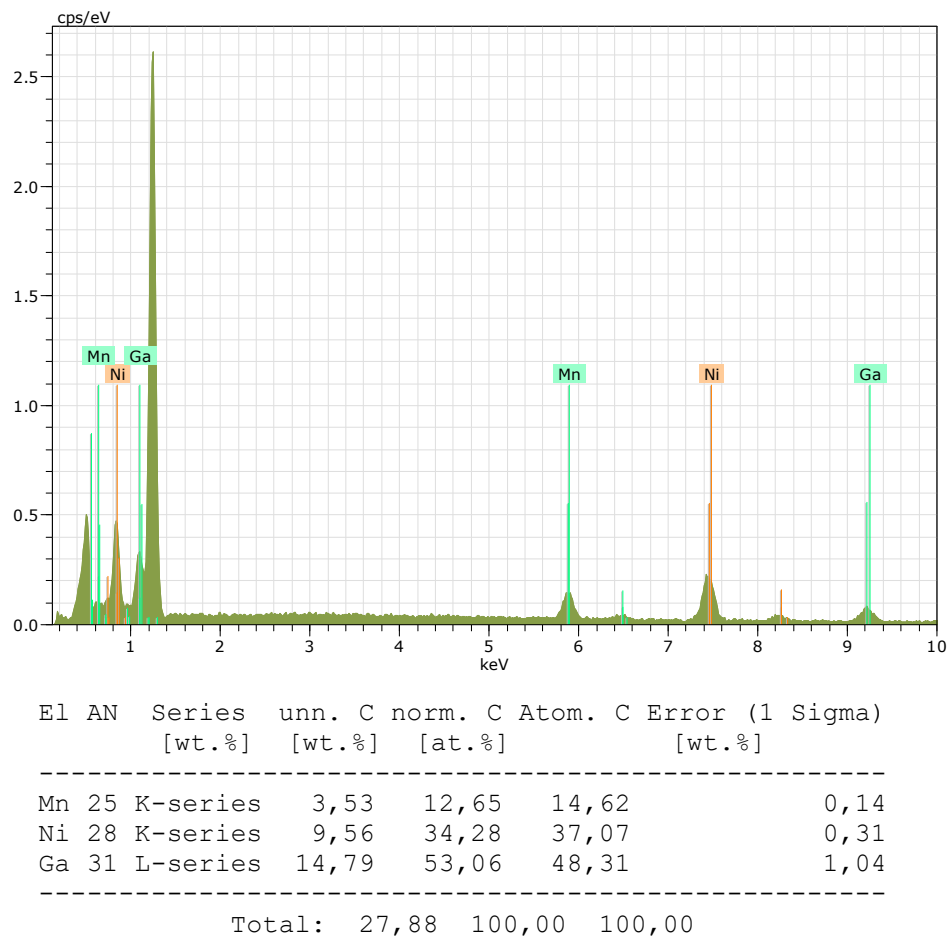
Fig. 5.13a - Representative result of EDS analysis for protuberance-free areas of the 100 nm film NMG1535.

```
El AN   Series   unn. C norm. C Atom. C Error (1 Sigma)
                 [wt.%]  [wt.%]  [at.%]        [wt.%]
--------------------------------------------------------
Mn 25 K-series    3,07   11,22   13,17          0,14
Ni 28 K-series    7,40   27,08   29,76          0,26
Ga 31 L-series   16,86   61,70   57,07          1,19
--------------------------------------------------------
              Total:  27,33  100,00  100,00
```
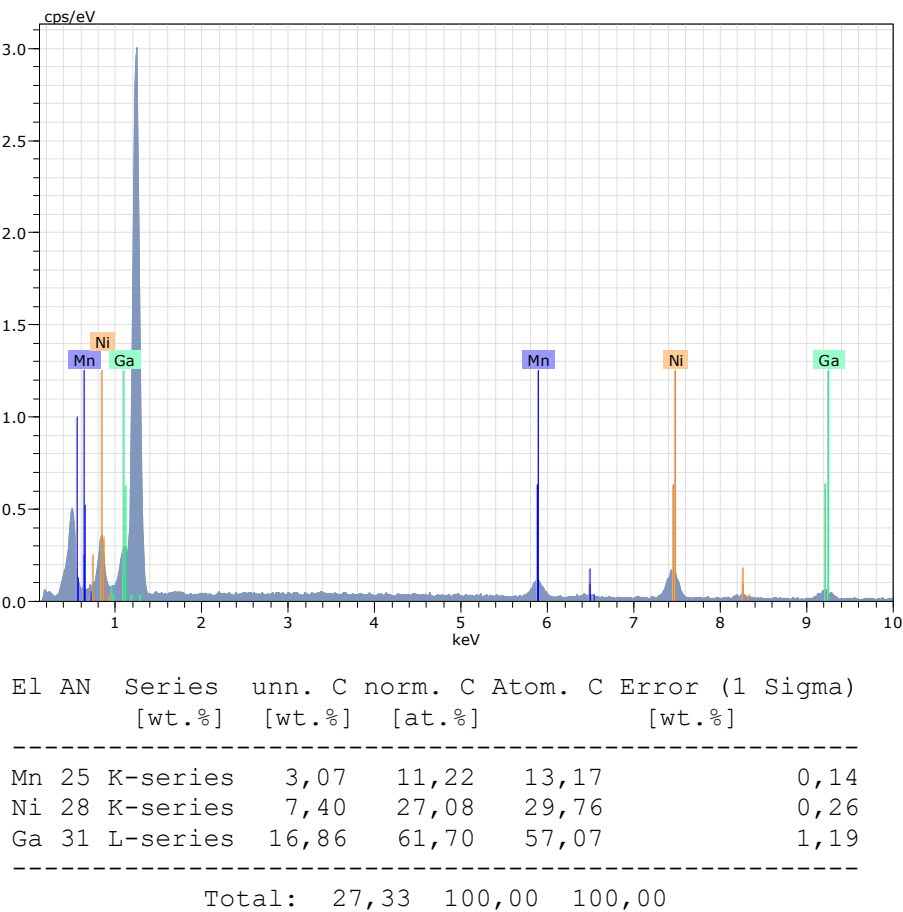
Fig. 5.13b - Representative result of EDS analysis for protuberance areas of the 100 nm film NMG1535.

Additional peaks present correspond to the elements Mg and O from the substrate, which appear in the measurements due to the very thin nature of the film (100 nm). Another similarity between films is that protuberances and protuberance free areas are composed of the same elements, and that in both areas, the elements are present in different weight percentages.

Element quantification for film NMG1535 provides a composition of $Ni_{34.3\pm0.3}Mn_{12.6\pm0.1}Ga_{53.1\pm1.0}$, very far from the stoichiometric Ni_2MnGa, pointing actually in the direction of a $NiMnGa_2$ type of alloy, with excess Ni and Ga, and Mn-deficient, both for protuberance and protuberance free areas.

5.1.2 – Locally inducing/probing temperature dependent structural transformations by an SThM probe

The process of locally inducing/probing temperature dependent structural transformations by an SThM probe (Nano-Thermal Analysis, Nano-TA) will be here described with all relevant details. The probe is first placed in contact with the surface of each sample. An electrical current is fed to the probe. By Joule effect, the palladium resistive element lithographically patterned on the tip of the probe is heated. As the heated tip is in contact with a material's surface which is, for instance, at room temperature, heat will be transferred from the tip to the material, locally increasing the material's temperature (Fig. 5.14).

The temperature of the material in contact with the heated probe is mainly dependent on two variables: the power dissipated at the tip (depending on the current being fed to it) transferred through the contact area between tip and material, and the material's thermal conductivity. For the same material (same thermal conductivity), the temperature will increase with increasing values of the electrical current fed to the probe. For the same value of the probe's electrical current, the temperature locally reached by the material, measured at the contact area between tip and material, will be higher for materials will lower values of thermal conductivity.
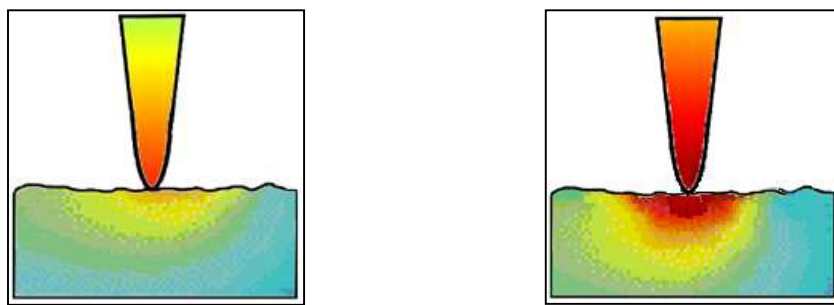
Fig. 5.14 - Heat being transferred from heated probe to the sample.

While probe and sample are in contact and the probe current is being increased, we can simultaneously register the probe's cantilever deflection. This

allows us to plot cantilever deflection vs probe current (Fig. 5.15). When calibrated by using the method described in section 4.1.1, the probe also allows us to plot cantilever deflection vs temperature.
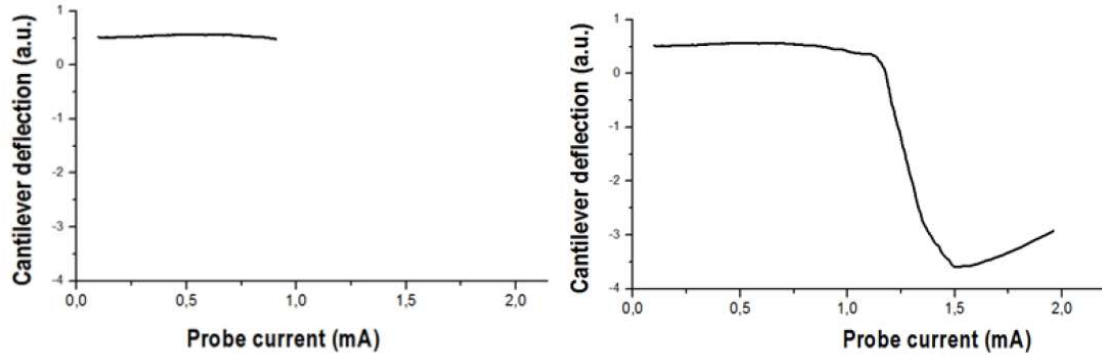
Fig. 5.15 - Effect on cantilever deflection before and after the local fusion of polycaprolactone (PCL) during a current sweep which heats the tip; The PCL sample used has a fusion temperature of 55 °C.

Any change occurring on the sample's surface during this local heating process will cause the cantilever deflection to change.

While performing the current sweep process in different locations of the NMG1537 thin film at room temperature, we found that no alteration in cantilever deflection was detected which could characterize a significant change in the sample's local structure. The heat locally provided by the probe, while the rest of the sample is at room temperature, flows too rapidly through the material, rendering it insufficient to significantly raise the temperature locally within the probe current range allowed by the system. This difficulty was overcome by simultaneously rising the global sample temperature using a Peltier element (RS 490-1339, 21.2W, 3.9A, 8.8V, 20x20mm) fed by an Agilent E3644A DC power supply source. The whole sample is heated to a temperature closer but below the value known from the magnetic measurements for the beginning of the structural transformation. The 400 nm film NMG1537 was thus placed at the base temperature of 313 K with the aid of the Peltier. Under the described conditions, several current sweeps performed on the NMG1537 thin film, on different points of the film's surface, allowed for the observation of a sudden discontinuity in cantilever deflection in each one of these

measurements. Fig. 5.16 shows a representative plot of this behavior. A topography scan of the NMG1537 film is shown on the left of the figure, while several curves taken for the points signaled in the topography scan are shown on the right. The flat horizontal line observed for higher temperatures means that the system's limit for detecting cantilever deflection was achieved.
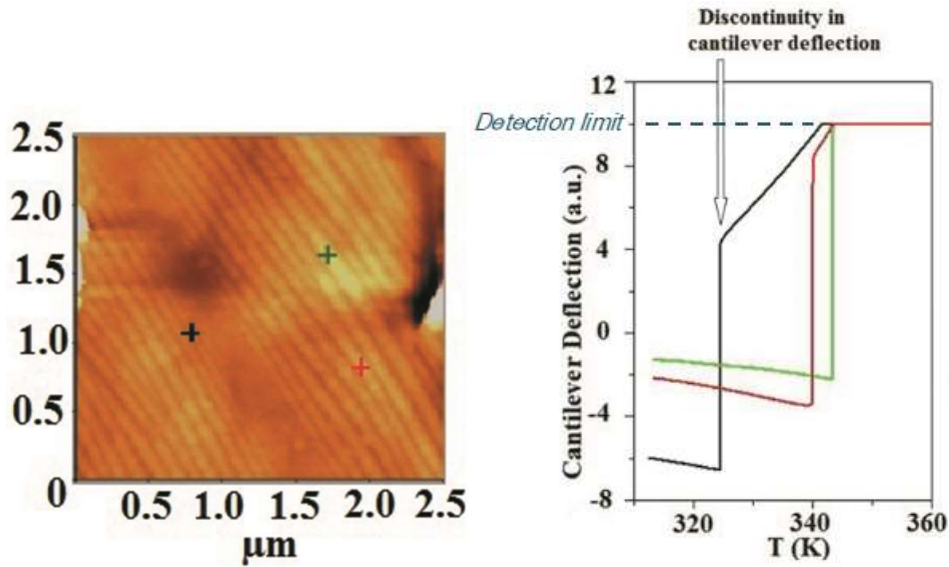
Fig. 5.16 - Topography scan of the NMG1537 film and cantilever deflection vs temperature curves for the signalled points.

To confirm this, the same current sweeps were performed when the sample was in contact with air (fig. 5.17a) and a Si wafer (fig. 5.17b). In fig. 5.17a, the flat horizontal line observed for higher temperatures means, once more, that the system's limit for detecting cantilever deflection was reached. In order to clarify what causes the discontinuity in cantilever deflection during the current sweeps, we also remark that there is no discontinuity in this curve and the observed cantilever deflection is caused by the upward bending of the cantilever due to the heating of its gold pad [122]. There is also no discontinuity in the plots presented in fig. 5.17b for the Si wafer, which is coherent with the known fact that the Si wafer does not exhibit any structural transformation within the interval of temperatures involved in this experiment. The behavior of cantilever deflection as a function of temperature when the probe is in contact with the Si wafer is reproducible in its linearity and

slope value, which gives us some insight on how the cantilever behaves when an electrical current is being fed to the tip while there is a solid-solid contact between probe and a given material which doesn't exhibit any structural change. It is reasonable to assume that, for other materials in this category, the linear behavior will be sustained, albeit with a different slope value, which should be related to the material's thermal conductivity. Thermal deformation of the cantilever is thus dismissed as a possible cause for the occurrence of the discontinuity observed in NMG1537, since it clearly does not manifest itself in the form of a discontinuity in cantilever deflection.
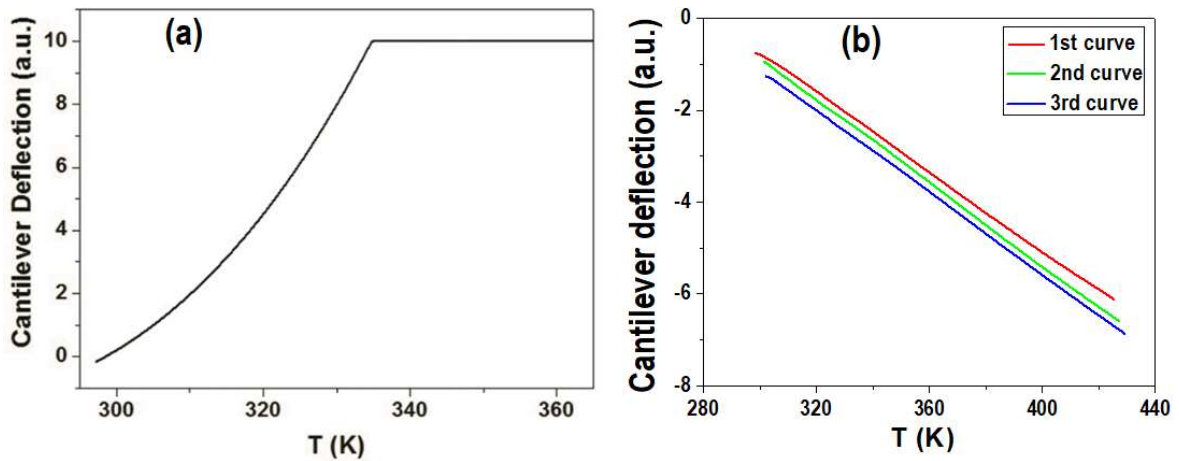
Fig. 5.17 - Cantilever deflection vs probe temperature for a current sweep performed in (a)air and (b) Si wafer.

When comparing curves of cantilever deflection vs probe current for the tip in air and two different locations of the NMG1537 film where the structural transformation was locally induced (Fig. 5.18), we can see that, after the discontinuity, the shape of cantilever deflection curve in air and in the NMG1537 points coincides. This means that the discontinuity must arise from loss of contact between the tip and the film's surface due to a sudden modification occurring in the material's topography, which we associate with the structural transformation.
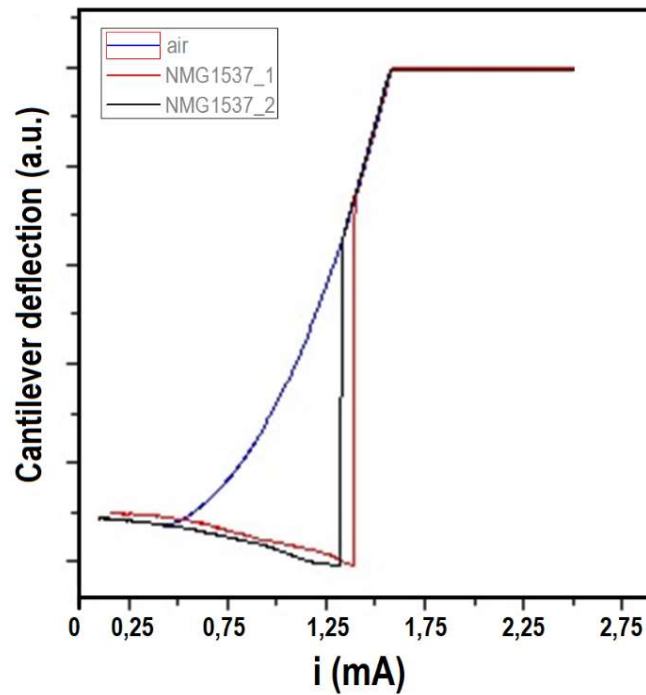
Fig. 5.18 - Comparison between curves of cantilever deflection vs probe current for the tip in air and two different locations of the NMG1537 where the structural transformation was locally induced.

We have proceeded to test the reproducibility of the transformation temperature measurement with the SThM probe by inducing the structural transformation in the same place several times after cooling back to the base temperature dictated by the Peltier. The result can be seen in Fig. 5.19 where the local measurements were shown to spread over a 2,2 K interval, being thus reproducible with an uncertainty of about 1,1 K. Each measurement was made using the same tip with the same calibration. Performing reproducibility tests with different calibrations of the tip is not be feasible, since calibration of the tip implies replacing the film with the calibration sample during that process. When returning to the NMG film, it would be extremely difficult to guarantee the probing of the very same formerly probed location.

This method for transformation temperature measurement through observation of changes in cantilever deflection can only be used in heating in the PARK XE7 with SThM system, since the software controlling the equipment (XEP)

does not allow the collection of data regarding cantilever deflection and temperature while the applied electrical current decreases and the tip temperature decreases.
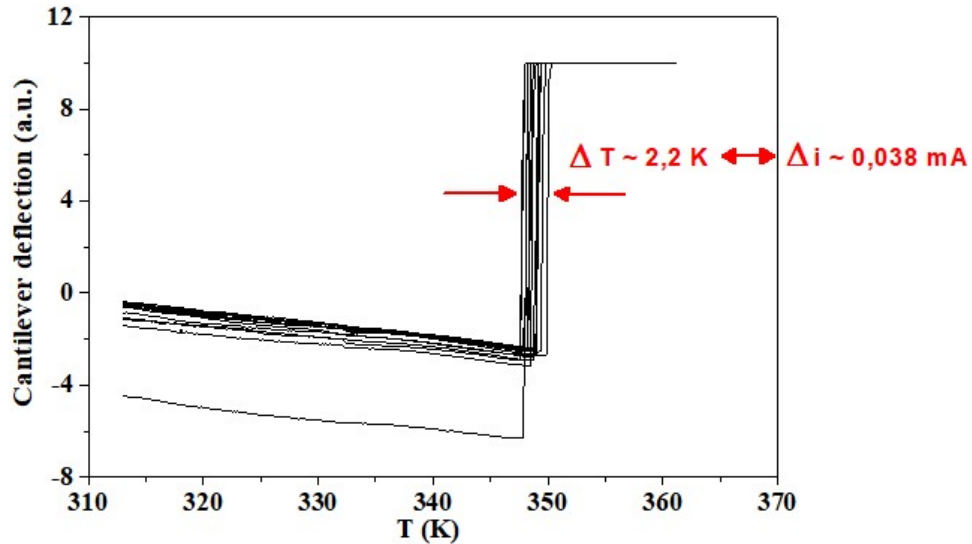
Fig. 5.19 - Reproducibility test and uncertainty determination for the transformation temperature measurement at the same location/position (400 nm NMG1537 sample).

a) NMG1537 (400 nm thin film)

Several topography scans were performed at room temperature on the surface of the 400 nm NMG1537 thin film with the SThM probe in order to analyze the surface features of the film. Fig. 5.20 shows a representative topography scan on a 2 µm x 2 µm area of the film, exhibiting a "wavy-like" surface characteristic of twinning in the martensitic phase. A line profile taken as an outline of a roughly perpendicular section of the twinning pattern on the film's surface shows that the characteristic "wave" height (topography modulation) and width (linear modulation) are, respectively, about 2 nm and 80 nm. Two line profiles were taken along two martensitic twinning directions (green and blue lines in Fig. 5.20) to evaluate their roughness, which we estimate to be below 1 nm. A "higher" modulation is observed, resulting from the "brighter larger spots" that partially compose the film's surface. The values on the horizontal axis "Line" represent positions in the AFM scan image in Fig. 5.20 along each colored line, 0 µm corresponding to the extremity of the line

marked with a small white dot, and the highest value corresponding to the other extremity of the line, marked with a small white arrowhead. For "Line" axis values lower than approximately 2.0 µm and 1.8 µm for the green and blue line plots, respectively, we are mainly observing the roughness of the sample along that martensitic twining direction, but the martensitic modulation. For "Line" axis values higher than 2.0 µm and 1.8 µm (green and blue lines, respectively) we observe the modulation corresponding to the martensitic twinning present on the bottom right corner of the AFM scan image.
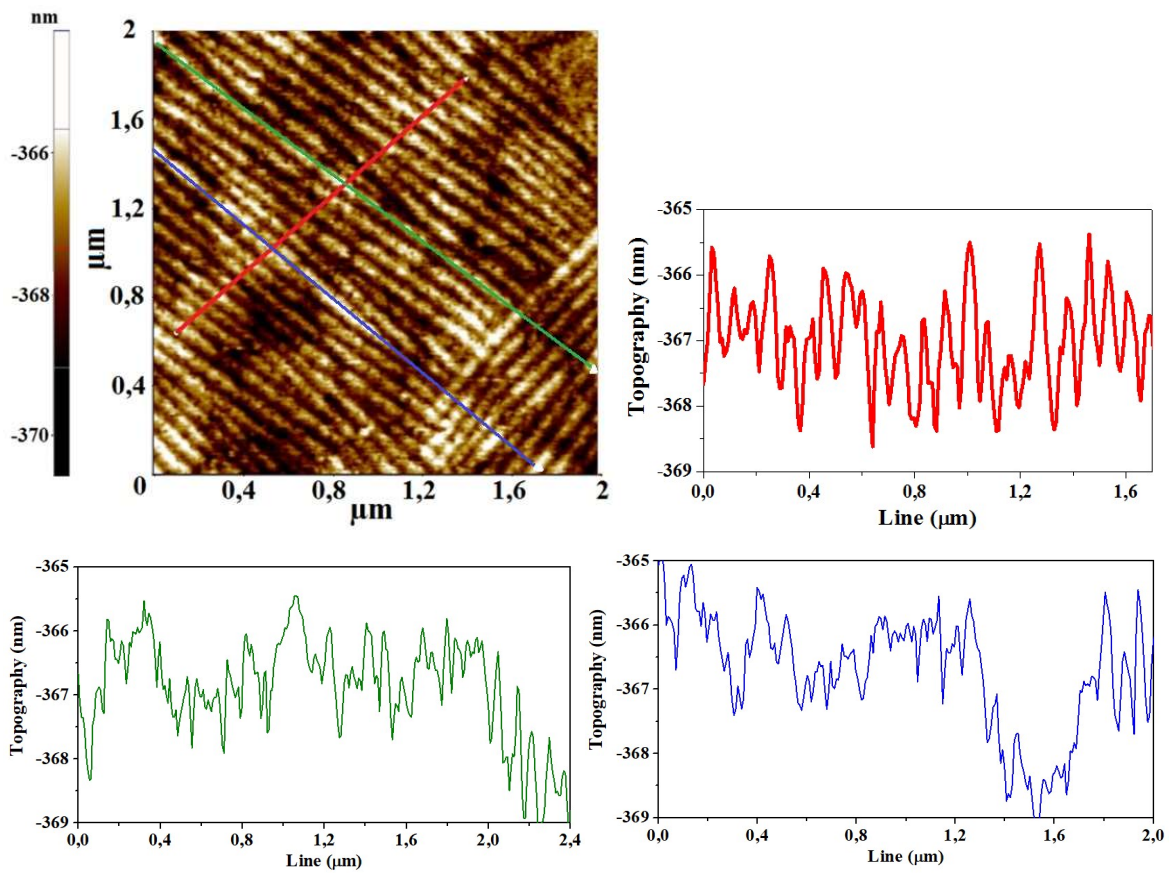
Fig. 5.20 - AFM image of the 400 nm Ni-Mn-Ga film deposited on MgO substrate, performed at room temperature – line profiles.

In Ni-Mn-Ga films, Kaufmann et al [150][151] reported the observation of twinning periods from 1.47 nm up to 0.1 mm. Diestel et al [152] stated the dependency of twinning period on the square root of the film thickness in a study

involving Ni-Mn-Ga films deposited onto MgO substrates (with a Cr buffer layer), with thicknesses between 30 nm and 2 μm. For this film, as demonstrated, we have obtained a twinning period of about 80 nm.

With the film kept at 313 K, transformation temperatures were measured in this same area, in 26 different locations, mapped with a color scale on the topography scan (Fig. 5.21). The measured transformation temperatures are found within an interval of 34 K, from 329K to 363 K, with a frequency distribution shown in Fig. 5.22.
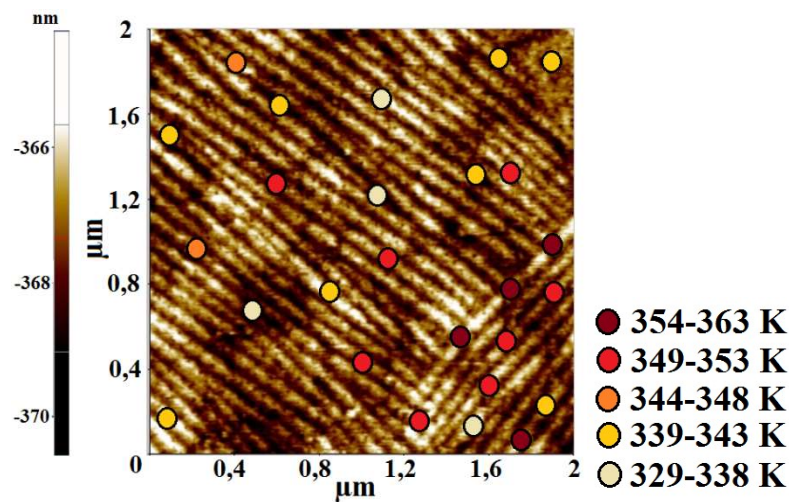
Fig. 5.21 - Mapping of transformation temperatures on an AFM scan of the NMG1537 film.
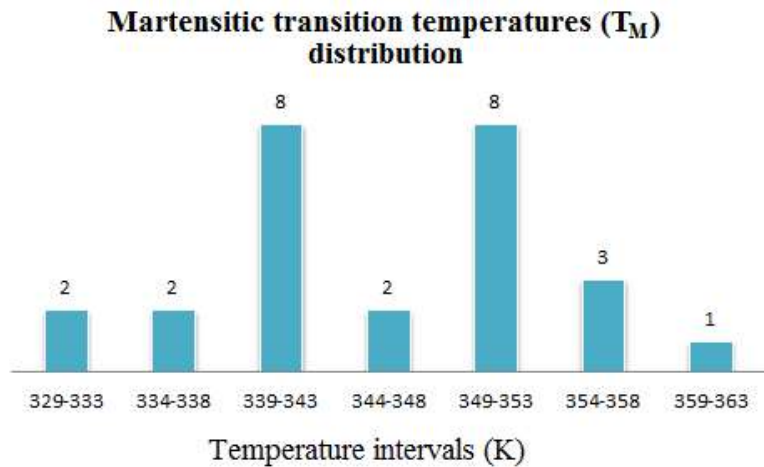
Fig. 5.22 - Transformation temperatures distribution for 26 points on the NMG1537 film of Fig. 5.21.

For comparison, a different 2 µm x 2 µm area of the NMG1537 film was selected and topography scans were taken at different temperatures. For each scan, the whole sample was kept at one specific temperature by the Peltier element, and the probe used was a standard contact mode probe, manufactured by NANOSENSORS [149], with reflex aluminum coating, tip with standard shape and radius < 7 nm (< 10 nm guaranteed). The first and last scans were taken, respectively, at 324,0 K and 327,5 K in heating. For this specific area, topography scans at different temperatures in cooling were not registered. At the end of the present section, we present a similar study for a different area of the film which includes topography scans taken at different temperatures in heating and cooling.

We can see in Fig. 5.23 that this specific area transforms almost completely within an interval of about 1,5 K.
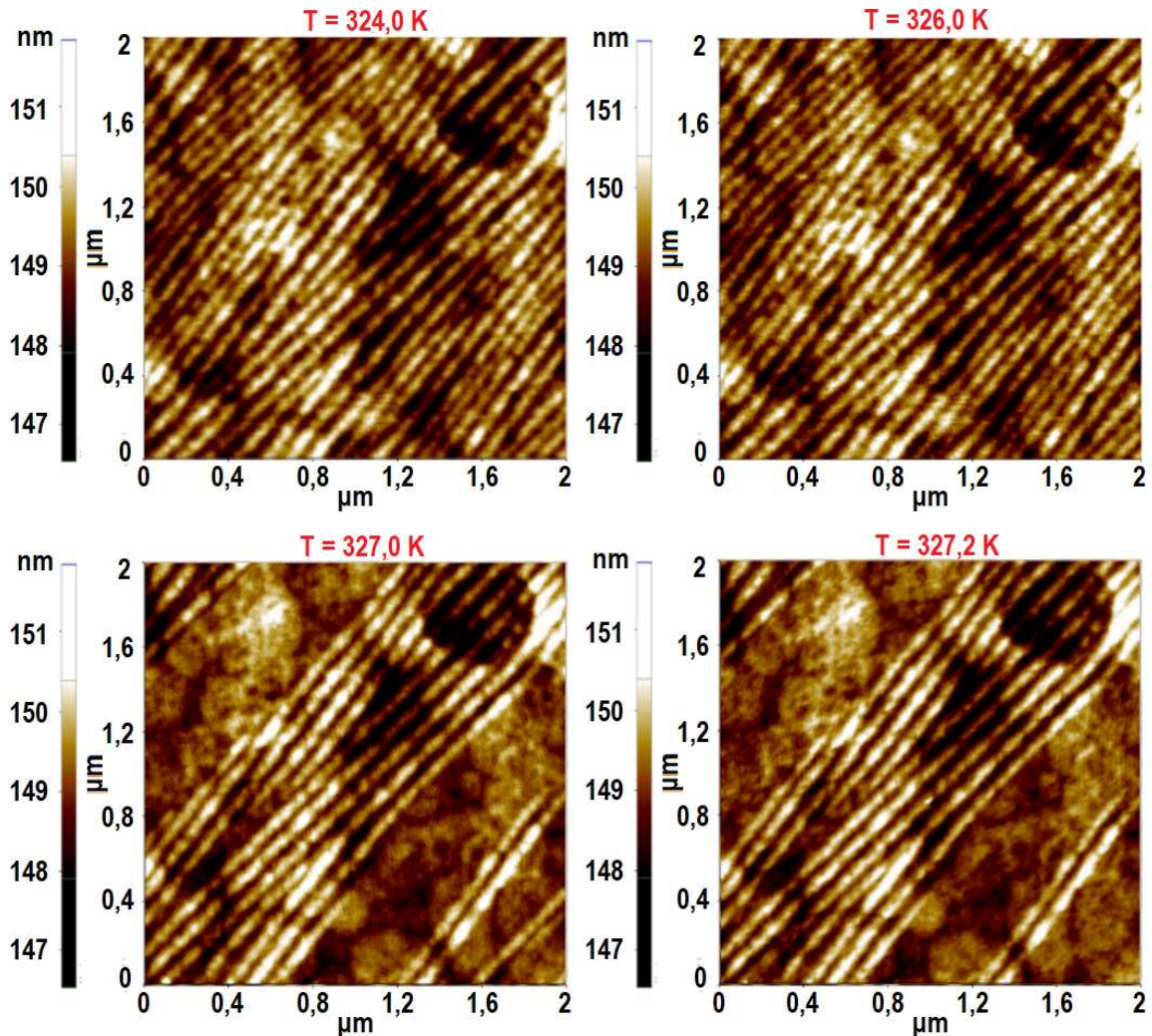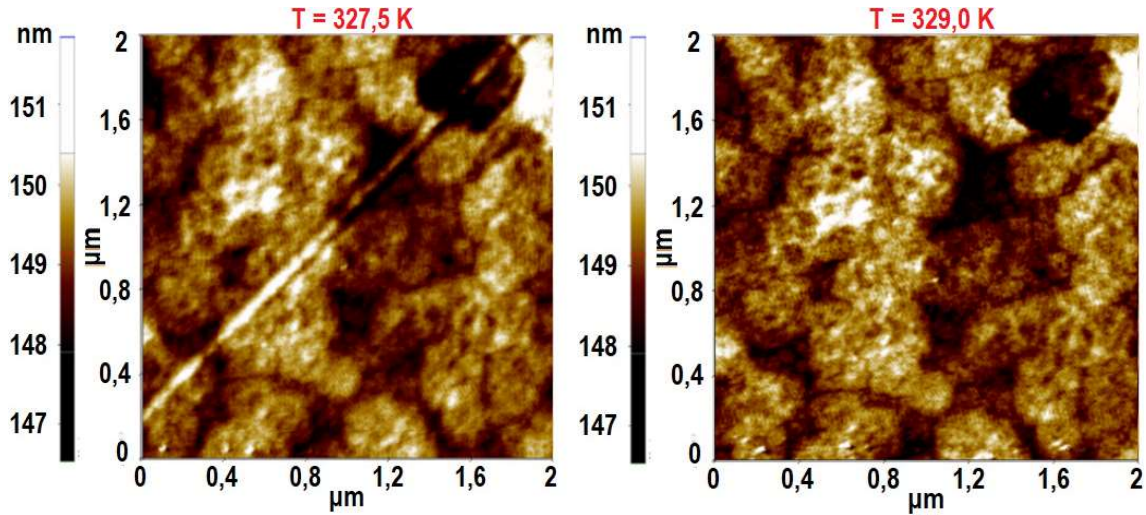
Fig. 5.23 - Topography scans of a 2µmx2µm area of the NMG1537 sample at different temperatures.

Fig. 5.24 shows the location of selected horizontal and vertical lines in the topography of the scanned area, whose profiles' characteristics will be shown in Figs. 5.25 to 5.30. Fig. 5.25 shows topography line profiles for all temperatures at which the area of the film was scanned, providing information on the behavior of wave width and height with temperature. It should be noted that in Figs. 5.25, 5.26 and 5.28, where horizontal line profiles (1H and 2H) are contemplated, in the horizontal axis "Line length", the values 0.0 µm and 2.0 µm correspond, respectively, to the left and right extremities of the red horizontal lines represented on the AFM scan image (Fig. 5.24). Also, in Figs. 5.29 and 5.30, where vertical line profiles (1V and 2V) are contemplated, in the horizontal axis "Line length", the values 0.0 µm and 2.0 µm correspond, respectively, to the bottom and top extremities of the red vertical lines represented on the AFM scan image (Fig. 5.24).

In the angle at which the lines cross the martensitic twinning pattern, the wave seems to be, in average, 100 nm wide and 1,5 nm high. Transformation causes the wave height to decrease. Transformations occurring between 327,0K and 327,5K suggest that such decrease is quite abrupt, since intermediate wave heights are not particularly noticeable.

Fig. 5.26 shows the topography of NMG1537 film in line 1H for several temperatures after subtraction of the height of the background (in the absence of

martensitic twinning, at 329 K). It is clear from Figs. 5.23 to 5.26 that line 1H crosses areas of the sample which transform at different temperatures. Through the observation of the line profile in both Figs. 5.25 and 5.26, we can say that when "line length" values are around 0.25 µm, and within the range 1.00 µm to 1.75 µm, the material shows lower T_Ms. For the other "line length" values, higher T_Ms are observed. From Fig. 5.26 we have estimated the average wave height separately for each of these sets for the studied temperatures and plotted it against these temperatures (Fig. 5.27).
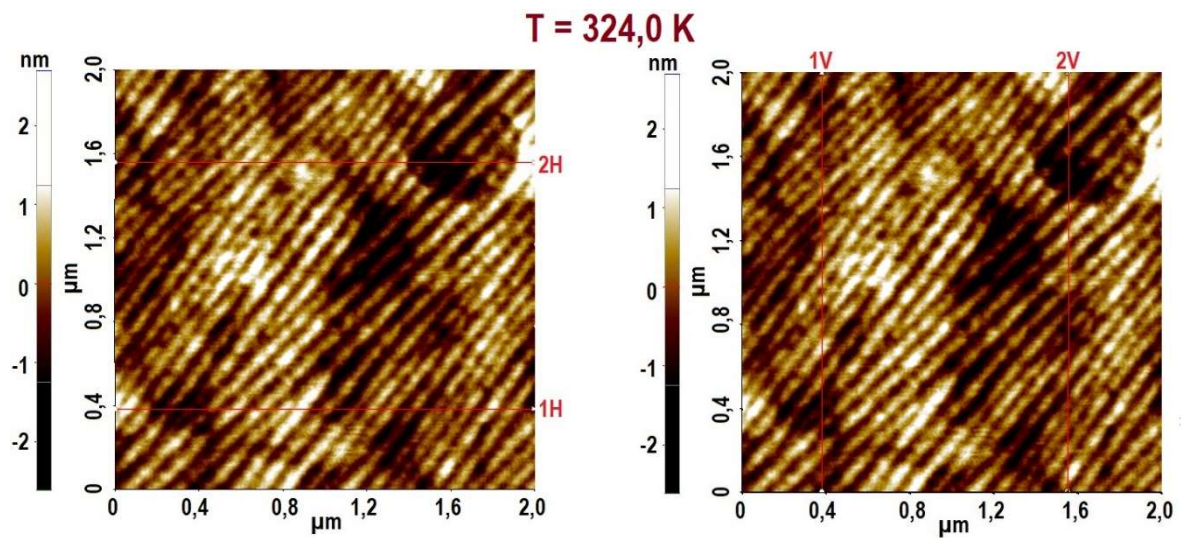
Fig. 5.24 - Location of the horizontal and vertical lines whose profiles at different temperatures will be shown in Figs. 5.25 to 5.30.
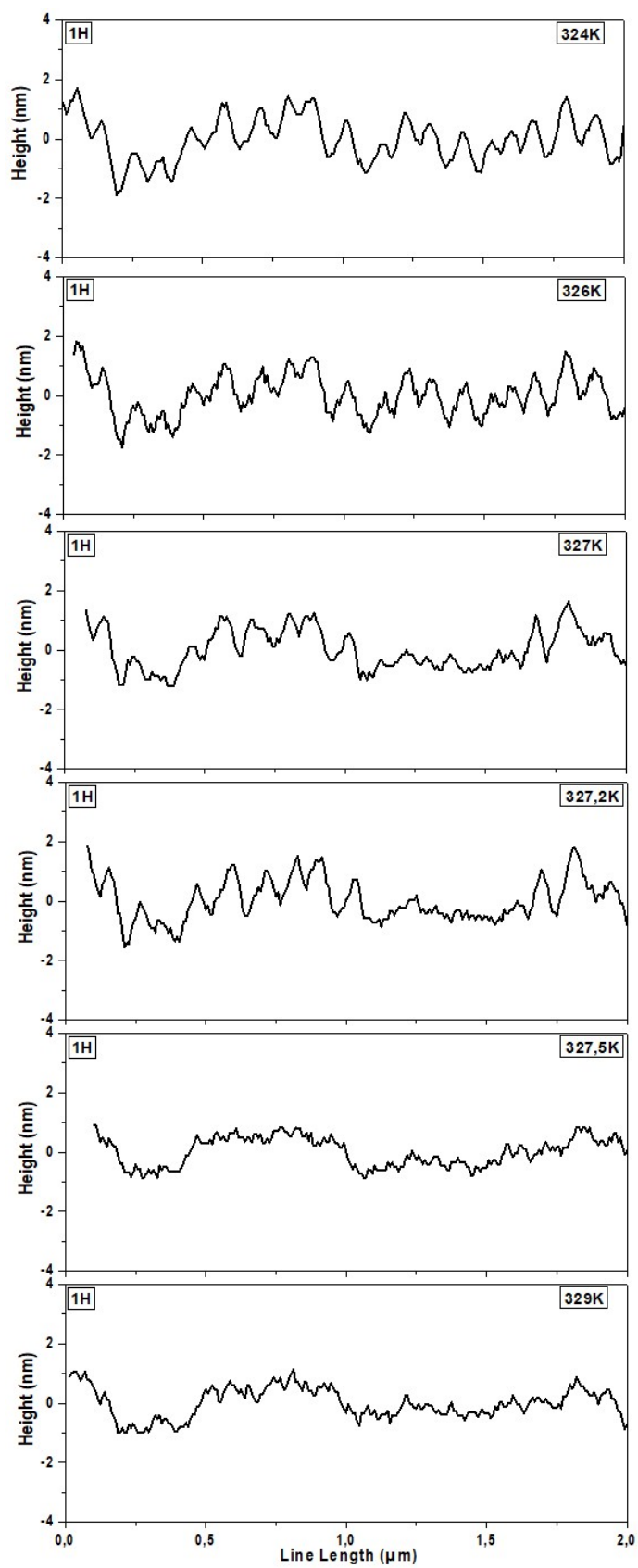
Fig. 5.25 - Topography of NMG1537 film in line 1H for several temperatures.
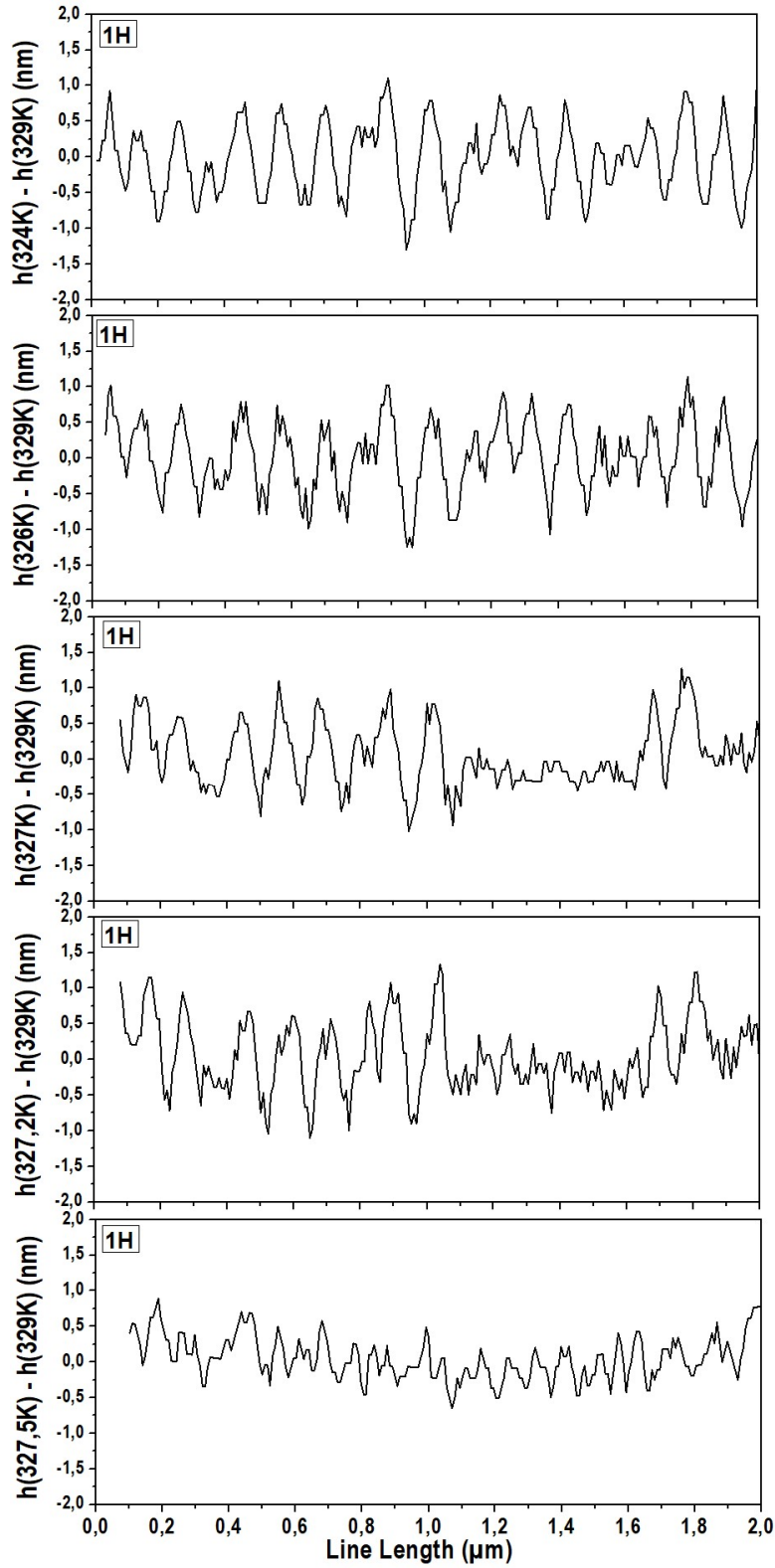
Fig. 5.26 - Topography of NMG1537 film in line 1H for several temperatures after subtraction of the height of the background (in the absence of martensitic twinning, at 329 K).
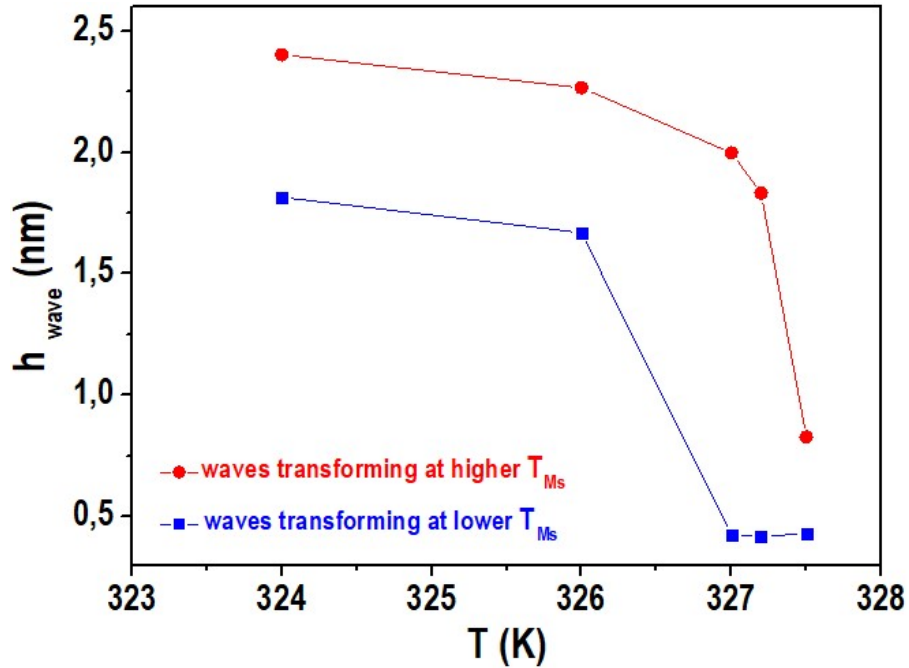
Fig. 5.27 - Average wave height (estimated from Fig.5.26) for the two different areas crossed by line 1H.

Similar results were found for lines 2H (Fig. 5.28), 1V (Fig. 5.29) and 2V (Fig. 5.30), which are not presented to avoid redundancy.

We have also estimated the decrease in the percentage of the remaining martensitic area for each topography scan taken at different temperatures during the structural transformation. This estimation was performed by observation of the topography scans of the studied area at the different temperatures, by approximating the remaining martensitic areas to geometrical figures, whose areas were calculated by measuring their dimensions with an ordinary ruler.

The percentage of martensitic area drops from 100% at 326.0 K to ~4.3% at 327.5 K. It is worth noticing the sudden decrease in martensitic area percentage with temperature, which mirrors the abruptness characteristic of the locally induced structural transformations previously observed.
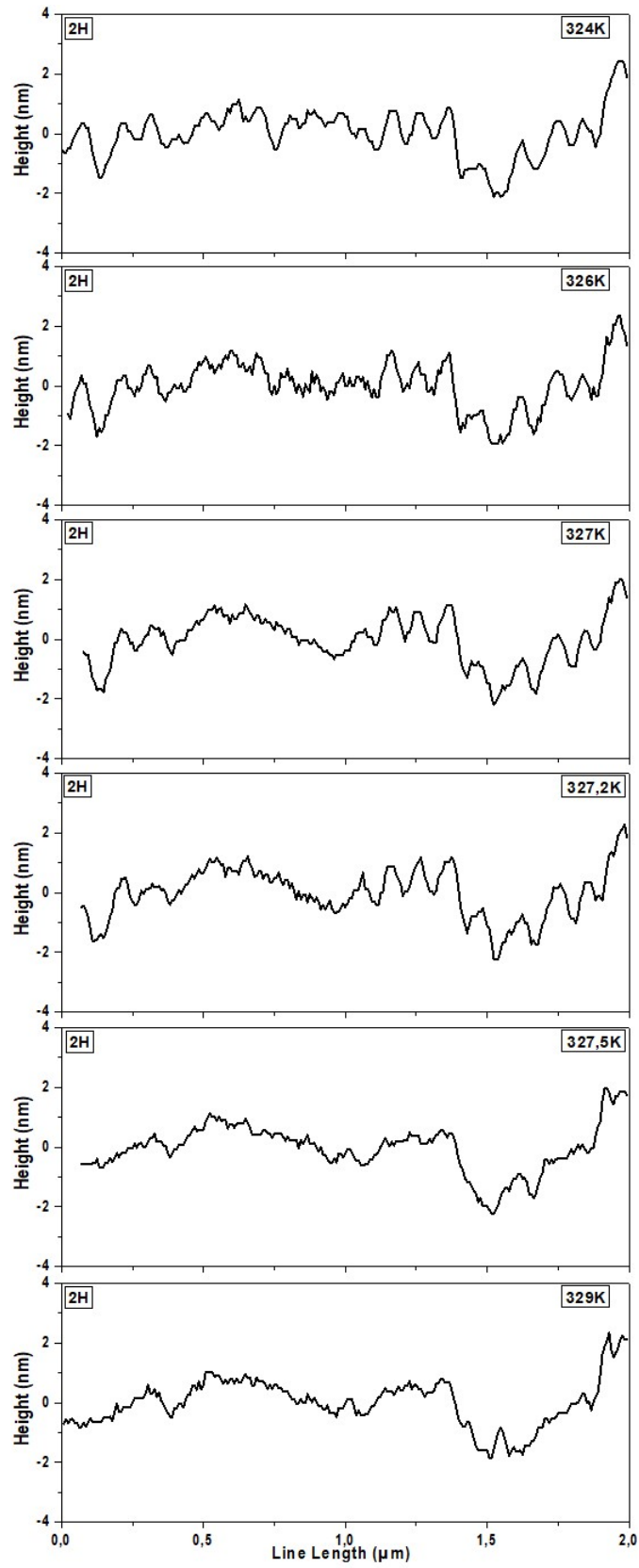
Fig. 5.28 - Topography of NMG1537 film in line 2H for several temperatures.
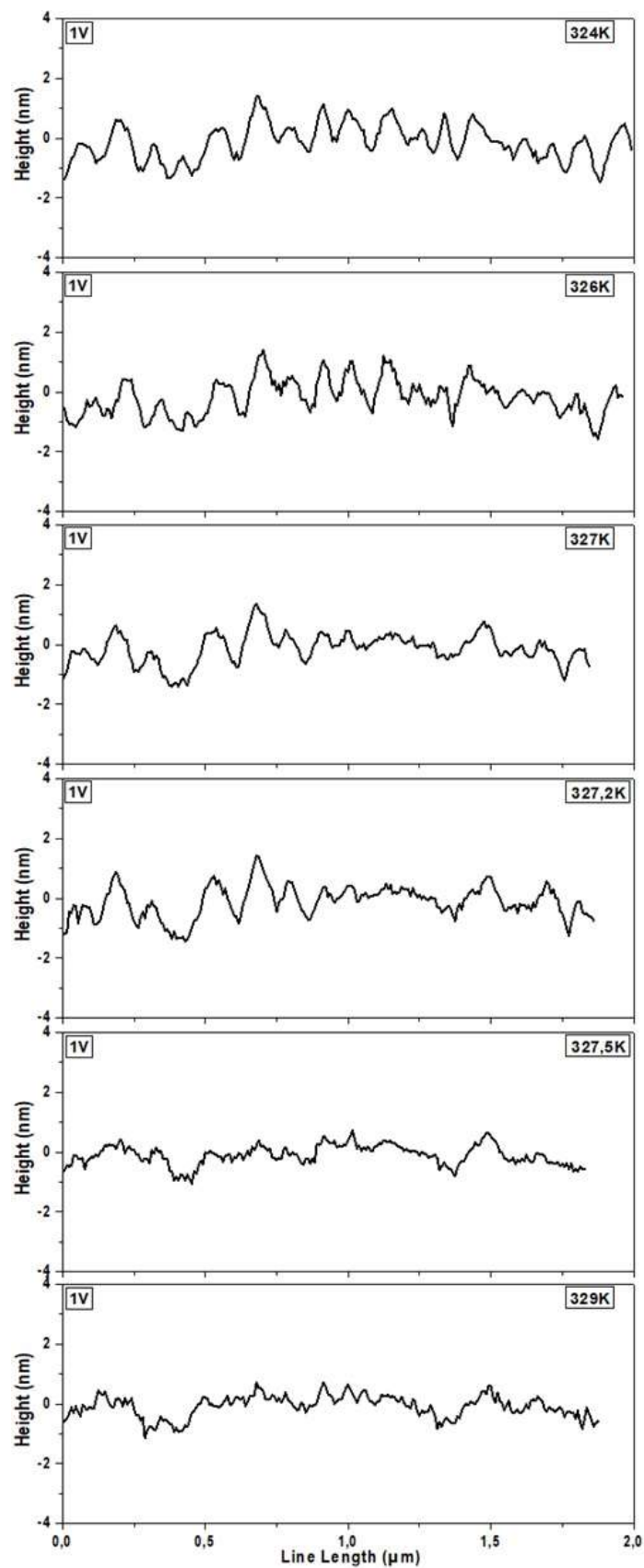
Fig. 5.29 - Topography of NMG1537 film in line 1V for several temperatures.
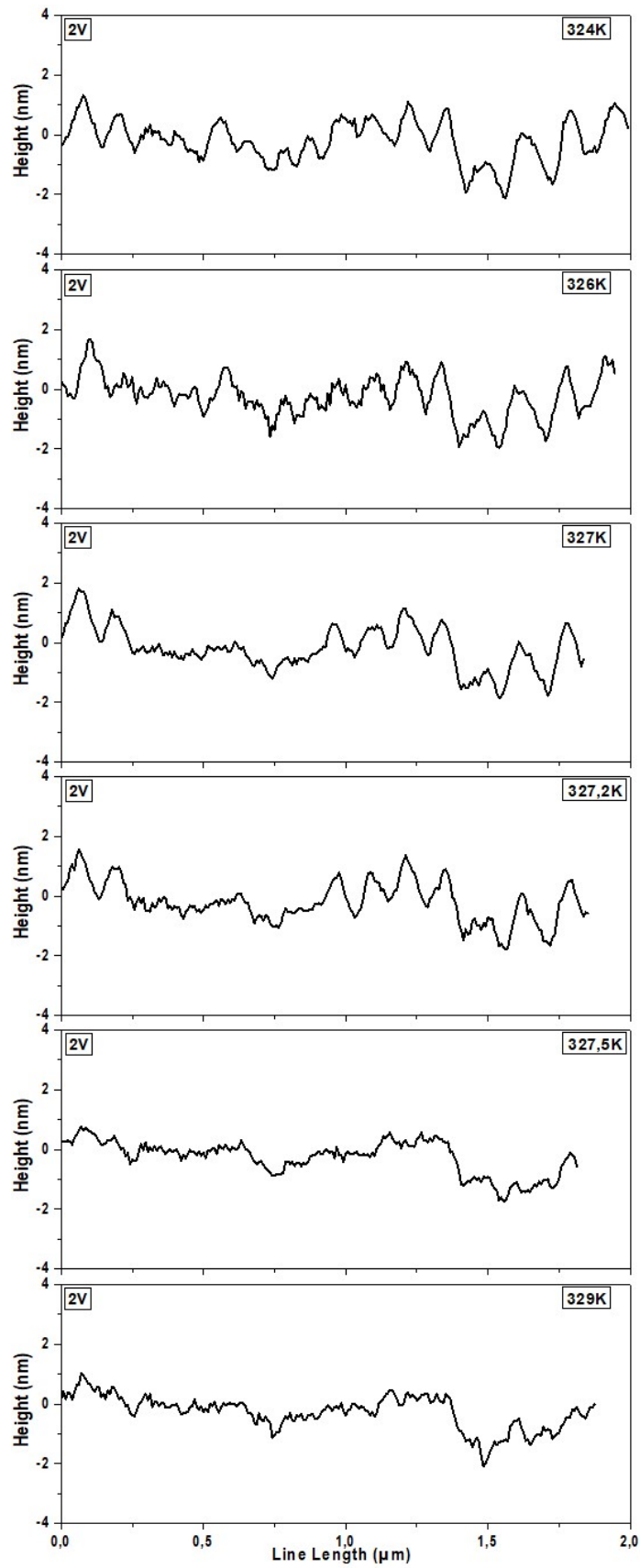
Fig. 5.30 - Topography of NMG1537 film in line 2V for several temperatures.
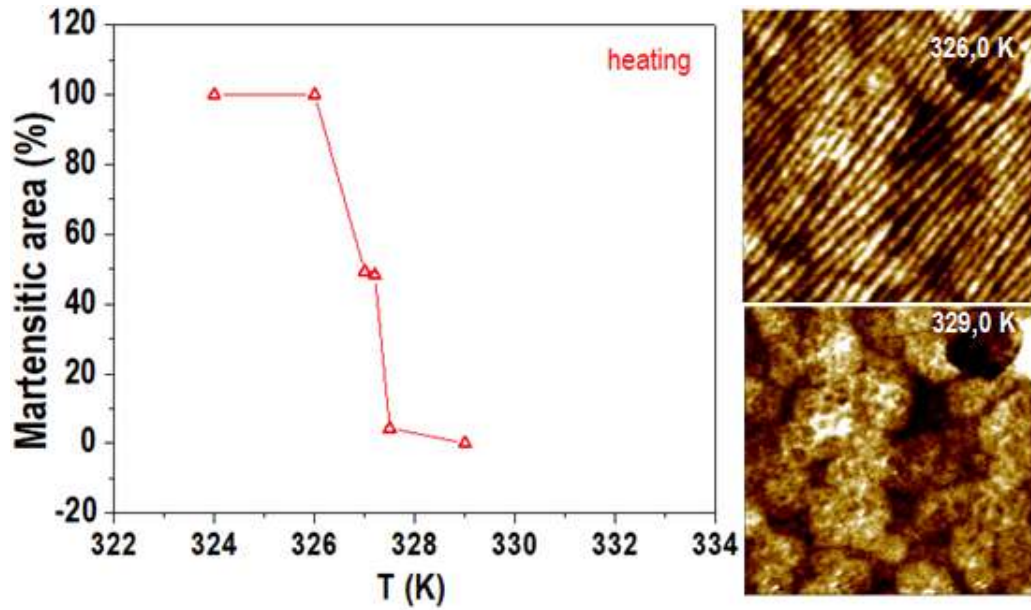
Fig. 5.31 - Martensitic area percentage as a function of temperature in heating of the 2x2 μm² area
of the NMG1537 film shown in Fig. 5.23.

Within the same area shown in Fig. 5.23, and with the film kept at the base
temperature of 313 K, the structural transformation was locally induced in 100
different points. The order in which the transformation was induced on the 100
points was carefully chosen to assure that when a given point was being
transformed, no heat remaining from a recently transformed neighbor would affect
the local measurement.

Transformation temperatures were found to fall within an interval of about
15K. The transformation temperatures obtained are mapped in Fig. 5.32. The results
translate into the distribution of transformation temperatures shown in fig. 5.33. In
Fig. 5.32 we can see that the higher transformation temperatures (above 353 K)
seem to be concentrated mostly on the top right area of the analyzed portion of film,
whereas lower transformation temperatures (below 350 K) appear more frequently
on the bottom left.

The combination of the results presented in Figs. 5.21, 5.22 and 5.33 shows
that, when subjected to different local environmental conditions, the same 2x2 μm²

area presents significant differences in terms of transformation temperatures. This points to differences in transformation progress within any area depending on the conditions and behavior of the surrounding structures.
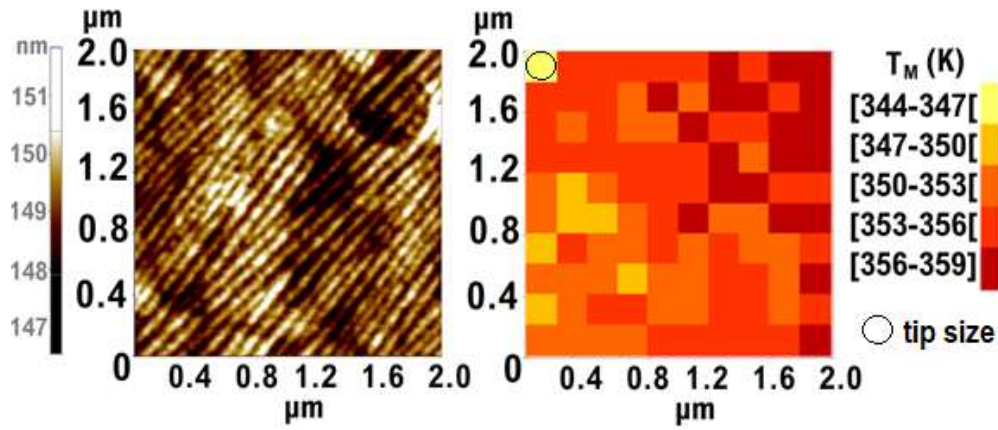
Fig. 5.32 - Mapping of local transformation temperatures in a 2 μm x 2 μm area of the NMG1537 film.
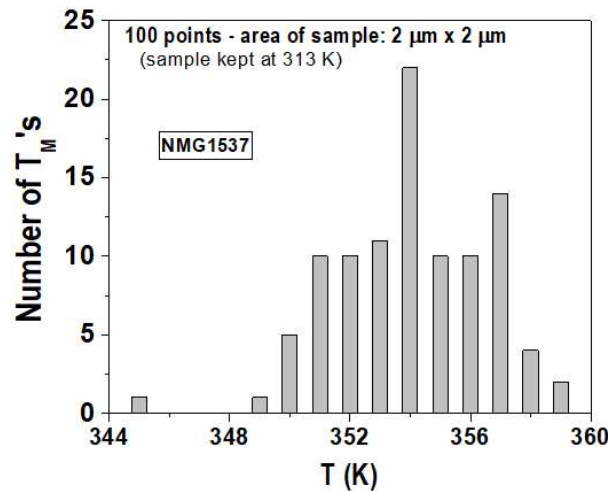
Fig. 5.33 - Transformation temperature distribution for 100 points in the 2 μm x 2 μm area of the NMG1537 sample, when the whole film is kept at 313 K.

There is a difference in the width of the interval of T_Ms obtained when the whole sample is being heated (3 K) and when the transformations are being locally induced (14 K) within an observation area of ~ 2x2 μm^2. M(T) results (Fig. 5.2) for this sample showed a transformation occurring within an interval of 10 K, between 336 K and 346 K. Thus, aside from the differences in interval width for the

occurrence of the transformation, we observe a shift of about 12 K and 25 K from the Peltier performed measurements to the SQUID and SThM (locally induced transformations) performed measurements, respectively.

The whole area of the film under study is about 3000x3000 μm^2. The already analyzed 2x2 μm^2 constitute mere 0.00004% of that area. Inducing the transformation and probing the corresponding temperature in different locations within the whole available area allows us to evaluate the impact on the transformation temperature of wider variations in local environmental conditions.

Thus, we extended the local inducement of the structural transformation to different points over the whole area of the film.

A schematic representation of the points analyzed and the order in which the measurements were performed can be seen in Fig. 5.34. As in previous studies, the sample was kept at the constant temperature of 313 K by the same Peltier element (RS 490-1339, 21.2W, 3.9A, 8.8V, 20x20mm^2).
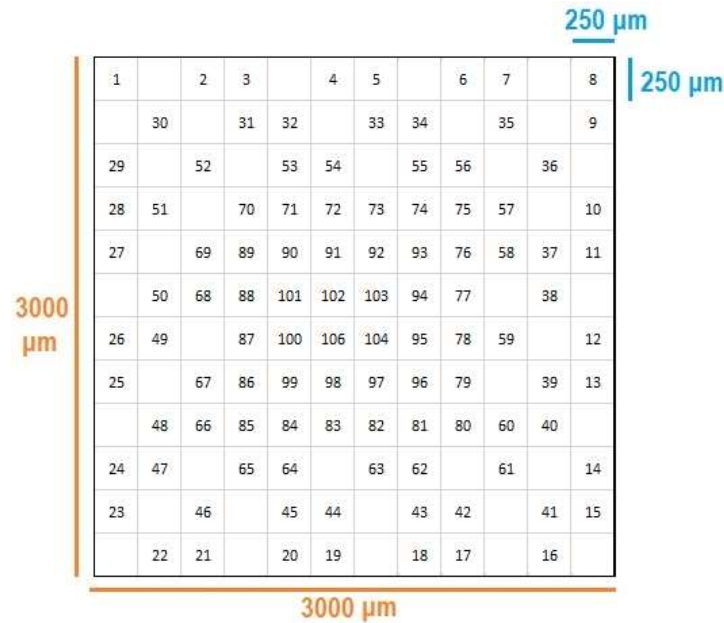
Fig. 5.34 - Schematic representation of the points analyzed in the 3000 μm x 3000 μm area of the NMG1537 film.

It is very important to note that, in the 2x2 μm^2 study, we had the probed points distributed within a grid containing 100 squares, with an area of 40000 nm^2 each. The probe, possessing a radius of about 100 nm, has an area of about

3.14×10^4 nm², meaning that it was in contact with roughly 80% of the area of each square of the grid. When we extend the study to the whole area of the film, we establish a grid with 144 squares, with an area of 6.25×10^{10} nm² each. The probe is now placed at an approximately central position in each numbered square seen in Fig. 5.34 and is in contact with an area of the sample which is roughly a 100 nm circumference (0.00005% of the total area of each grid square). Thus, it is not possible to represent probe-sample contact area on scale in Fig. 5.34.

The results show transformation temperatures registered within an even much larger interval of ~ 70 K, from ~ 323 K to 393 K (Fig. 5.35), with a distribution that can be seen in Fig. 5.36. A significant dip in the number of transformation temperatures was observed between 340 K and 345 K.
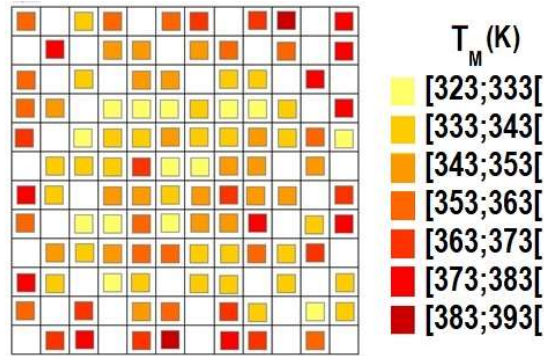
Fig. 5.35 - Mapping of the transformation temperatures measured for 105 points within the 3000 µm x 3000 µm area of the NMG1537 film.
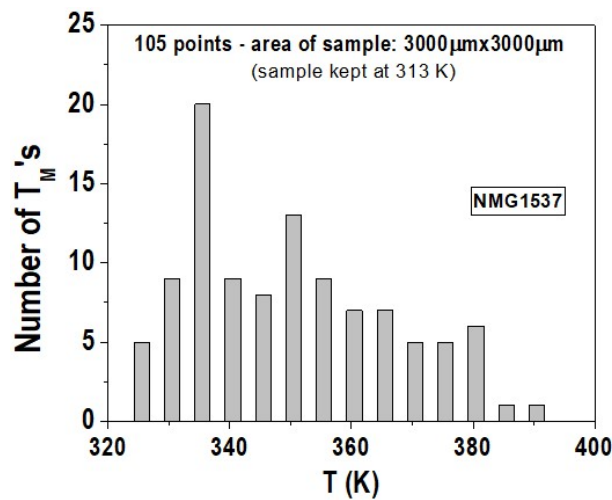
Fig. 5.36 - Distribution of transformation temperatures for 105 points in the 3000 µm x 3000 µm area of the NMG1537 film.

A second analysis in the same 3000 µm x 3000 µm total area of the NMG1537 film was performed, contemplating 125 points (not necessarily coinciding with points analyzed in the first analysis). The results are presented in Figs. 5.37 and 5.38. In this analysis, transformation temperatures are found within a 65 K interval.

Table 5.2 shows the summary of the results for local T_M inducing/probing in the studied areas. The T_Ms with highest frequency distribution for the 2x2(a) (Fig. 5.22), 2x2(b) (Fig. 5.23), 3000x3000(a) and 3000x3000(b) μm^2 studies are, respectively, 354K, 335K and 345K. When we locally induce the transformation and probe the corresponding T_M values to in over a hundred different points over the whole are of the film, the most frequent T_Ms observed correspond to lower temperature values, when compared to the 2x2(b) μm^2 study. When comparing the results for the studies performed in the whole area of the film (a and b), the 20% increase in the number of probed points in study b) increases the temperature value for the most frequently observed T_M, bringing the results closer to the most frequent T_M value observed for the smaller 2x2 μm^2 area. The range of T_M values is similar in both cases (323 to 393 K).
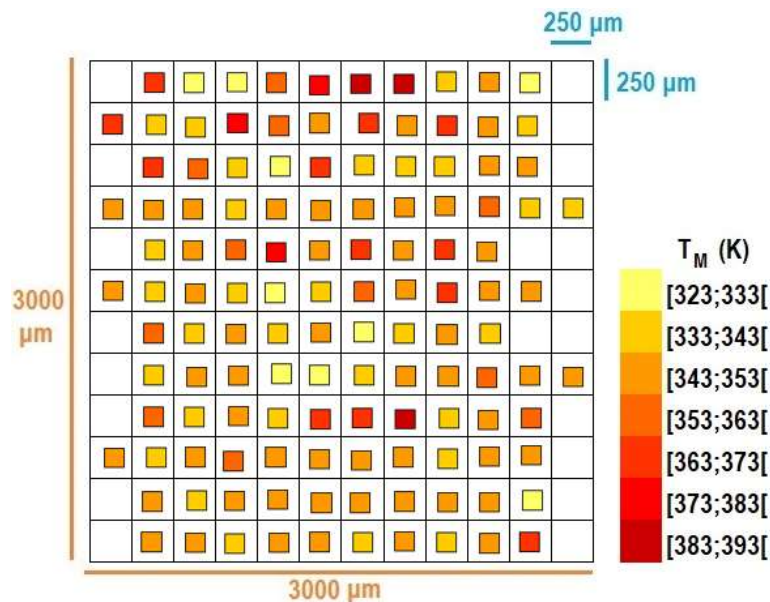
Fig. 5.37 - Mapping of the transformation temperatures measured for 125 points within the 3000x3000 µm2 area of the NMG1537 film.
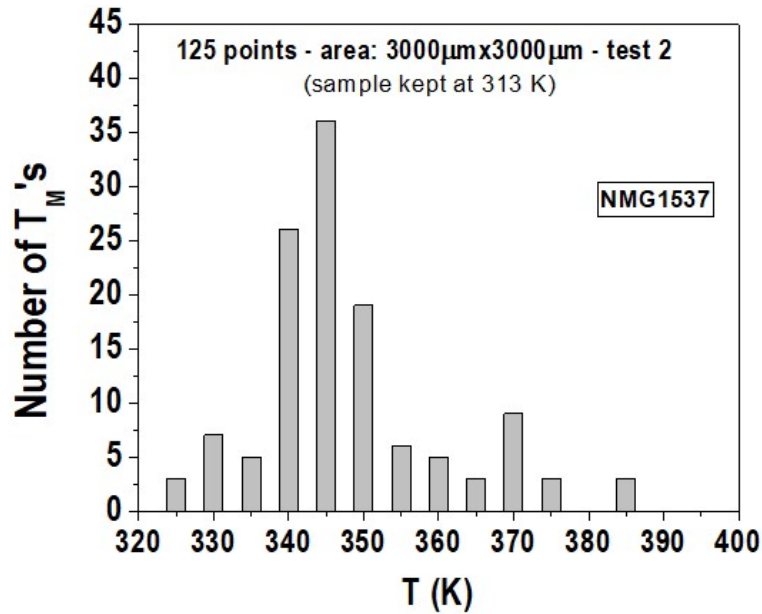
Fig. 5.38 - Distribution of transformation temperatures for 125 points in the 3000x3000 µm² area of the NMG1537 film.

Table 5.2 - Summary of results for local T_M inducing/probing in studied areas

Area (µm²)	Number of probed points	Range of T_Ms observeded (K)	T_M with highest frequency distribution (K)
2x2(a)	26	329 to 363	340 ; 350
2x2(b)	100	345 to 359	354
3000x3000(a)	105	325 to 390	335
3000x3000(b)	125	325 to 390	345

Finally, we present the topography scans performed at different temperatures on a 2,4x2,4 µm² area of the NMG1537 film in heating and cooling of the sample by the Peltier. The scans were performed in the same way as those presented in Fig. 5.23, which was previously described. Fig. 5.39 and Fig. 5.40 show the sequence of topography scans taken during heating and cooling, respectively.

In heating, the sample transforms from martensite to austenite between 330 K and 333 K, approximately. In cooling, the martensitic transformation takes place between 330 K and 323 K. The results show thermal hysteresis of about 7 K for the transformation in this area of the sample. The interval of transformation temperatures is wider in cooling than in heating. This is consistent with the magnetization vs temperature curves for the NMG1537 film (see Fig. 5.1).

Here also, we have estimated the variation in percentage of the remaining martensitic area for each topography scan, taken at different temperatures, during the structural transformation, both in heating and cooling. Fig. 5.41 displays the thermal hysteresis of the percentage of remaining martensite during the martensitic transformation.
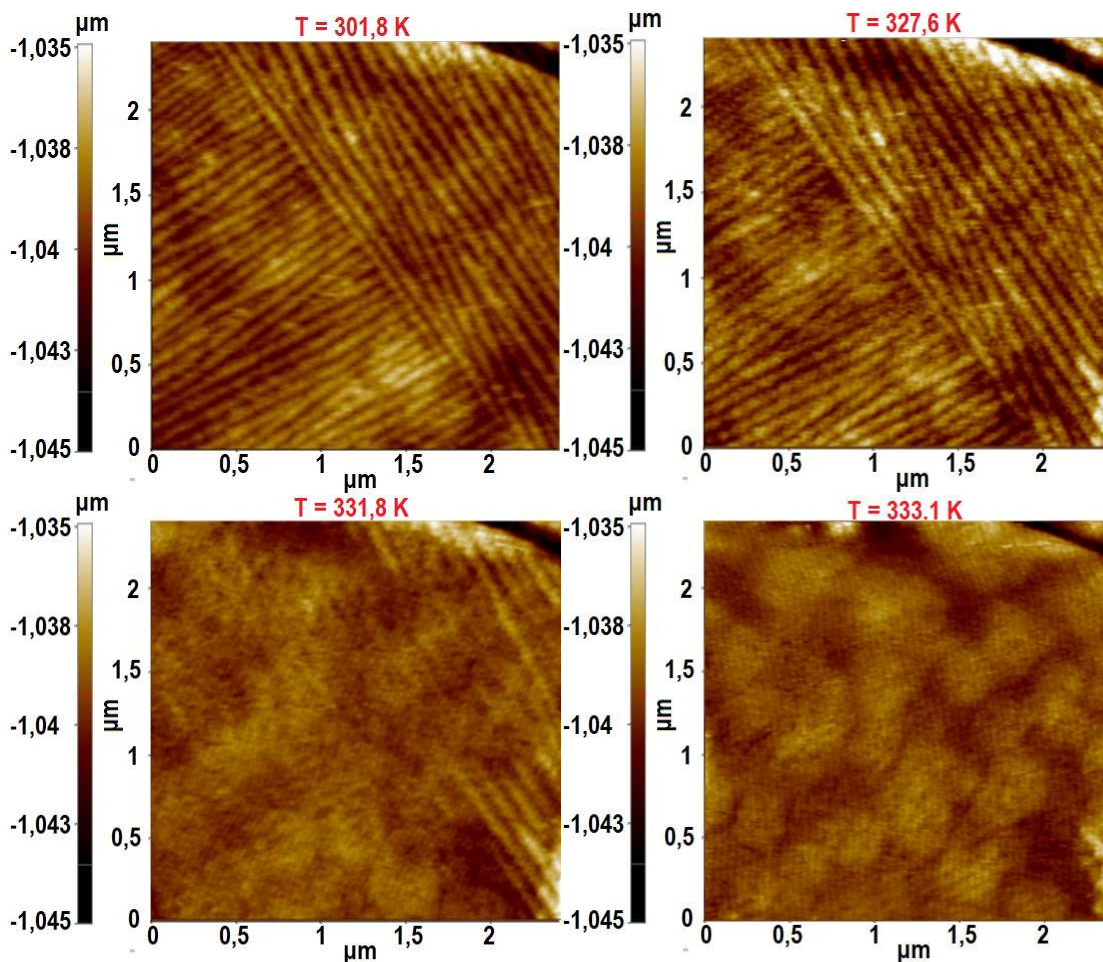
Fig. 5.39 - Sequence of topography scans performed on 2,4 μm x 2,4 μm area of the NMG1537 film during heating.
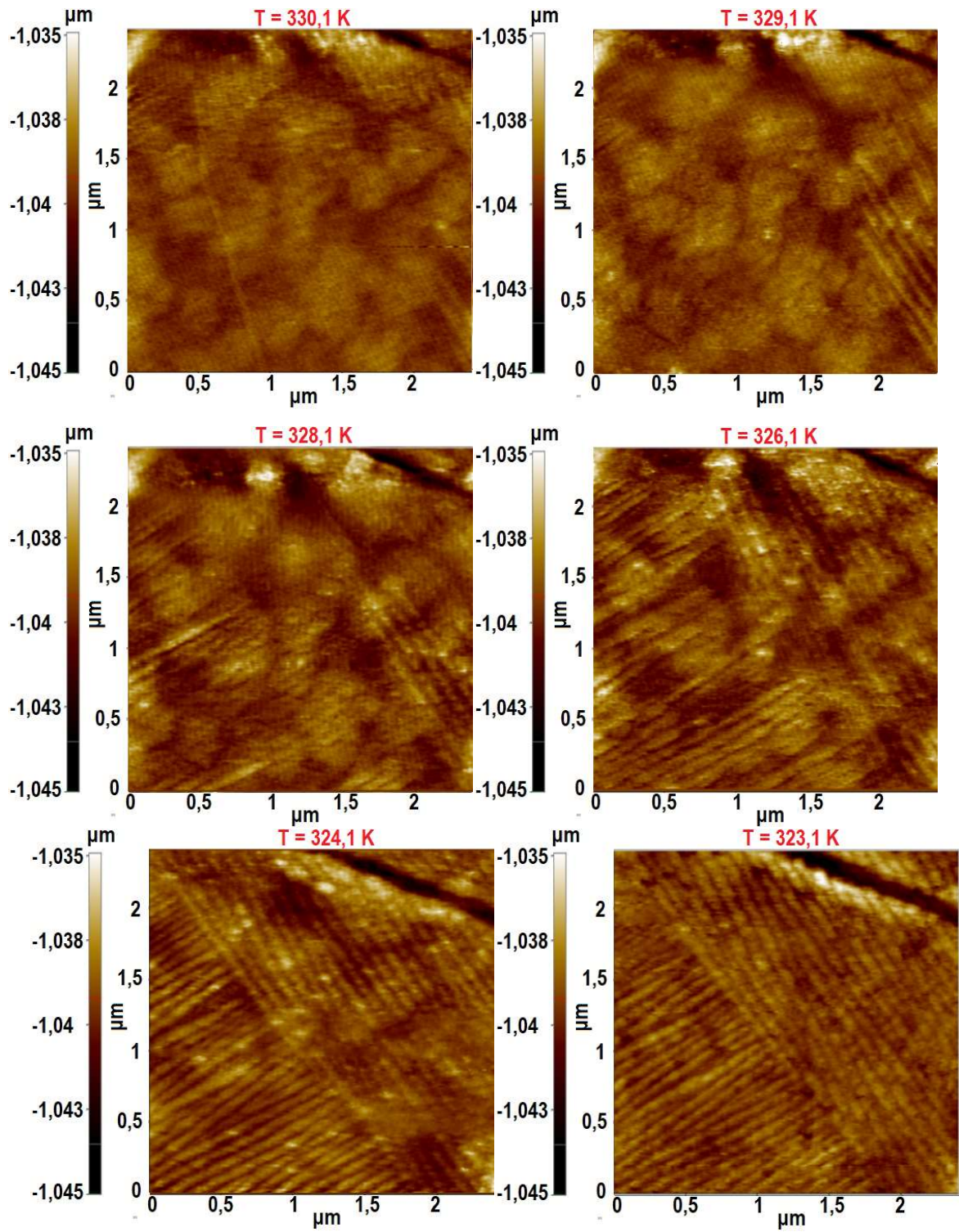
Fig. 5.40 - Sequence of topography scans performed on 2,4 µm x 2,4 µm area of the NMG1537 film during cooling.
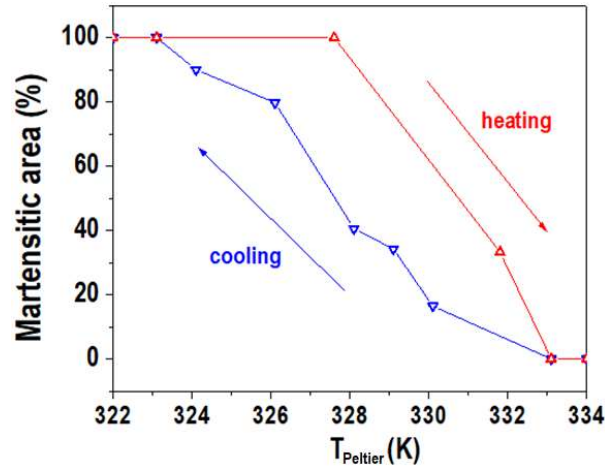
Fig. 5.41 - Martensitic area percentage as a function of temperature of the sample (set by the Peltier element and measured by the thermocouple attached to it) in heating and cooling of a 2x2 μm^2 area of the NMG1537 film, showing thermal hysteresis.

Fig. 5.42 shows the location of topography line profiles taken for all temperatures at which the area of the film was scanned. While in Figs. 5.25 to 5.30, we were certain to observe the same 1H, 1V, 2H and 2V lines for each temperature value, in this situation, due to minor displacements in scanned area and lack of good reference features, we are not able to guarantee that we are always observing the same 1H or 2H lines, only that we are observing lines that are in close proximity. For this reason, we will call them 1H and 2H areas and we will not develop much more than what was already asserted in the study performed on the first considered area.
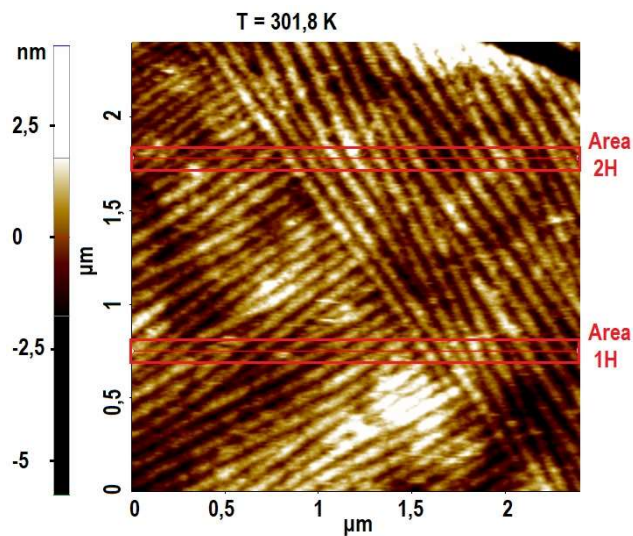
Fig. 5.42 - Location of the horizontal areas where line profiles shown in Figs. 5.25 to 5.30 were collected at several temperatures.

Figs. 5.43 to 5.44 and 5.45 to 5.46 show the data concerning both areas in heating and cooling, respectively.

The results consistently show a martensitic twinning pattern with an average wave width and height of, respectively, 100 nm and 1,5 nm. Decrease of wave height with the transformation in heating is confirmed, and as expected, an increase of wave height in cooling is shown. The available data do not contradict the abrupt nature of wave height variation during the transformation.
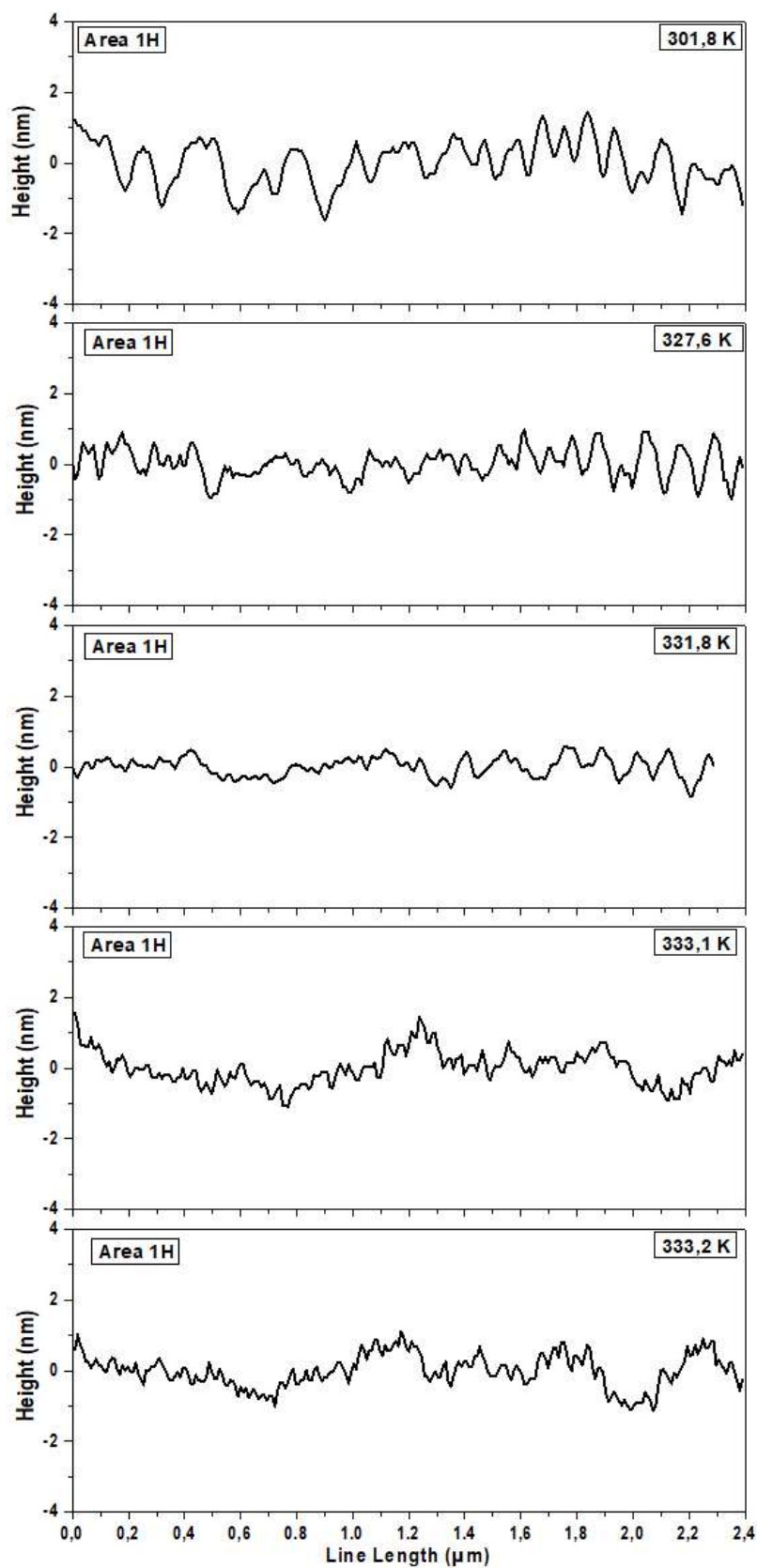
Fig. 5.43 - Line profiles in area 1H of the topography scans of the 2.4µmx2.4µm area in Fig. 5.39 (in heating).
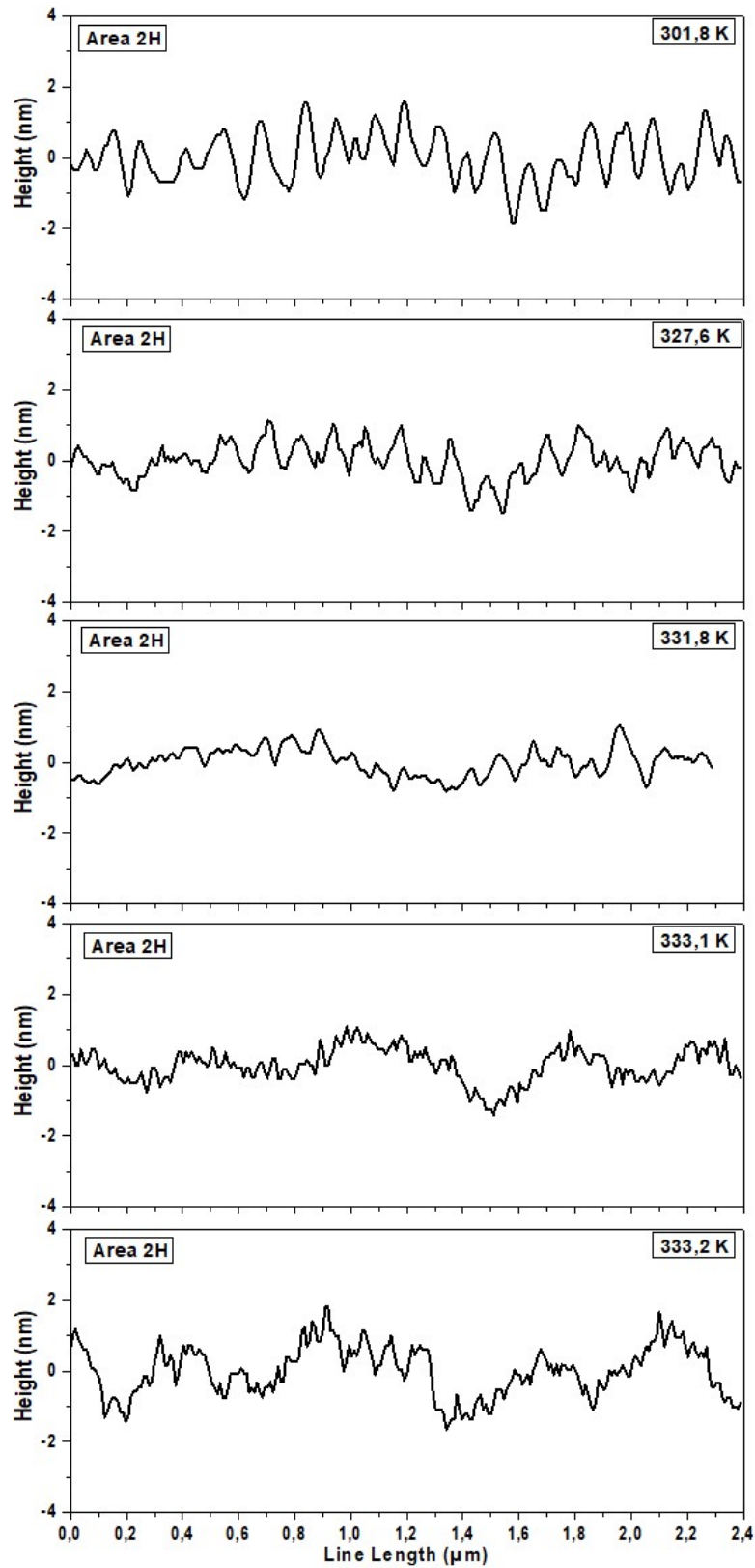
Fig. 5.44 - Line profiles in area 2H of the topography scans of the 2.4μmx2.4μm area in Fig. 5.39 (in heating).
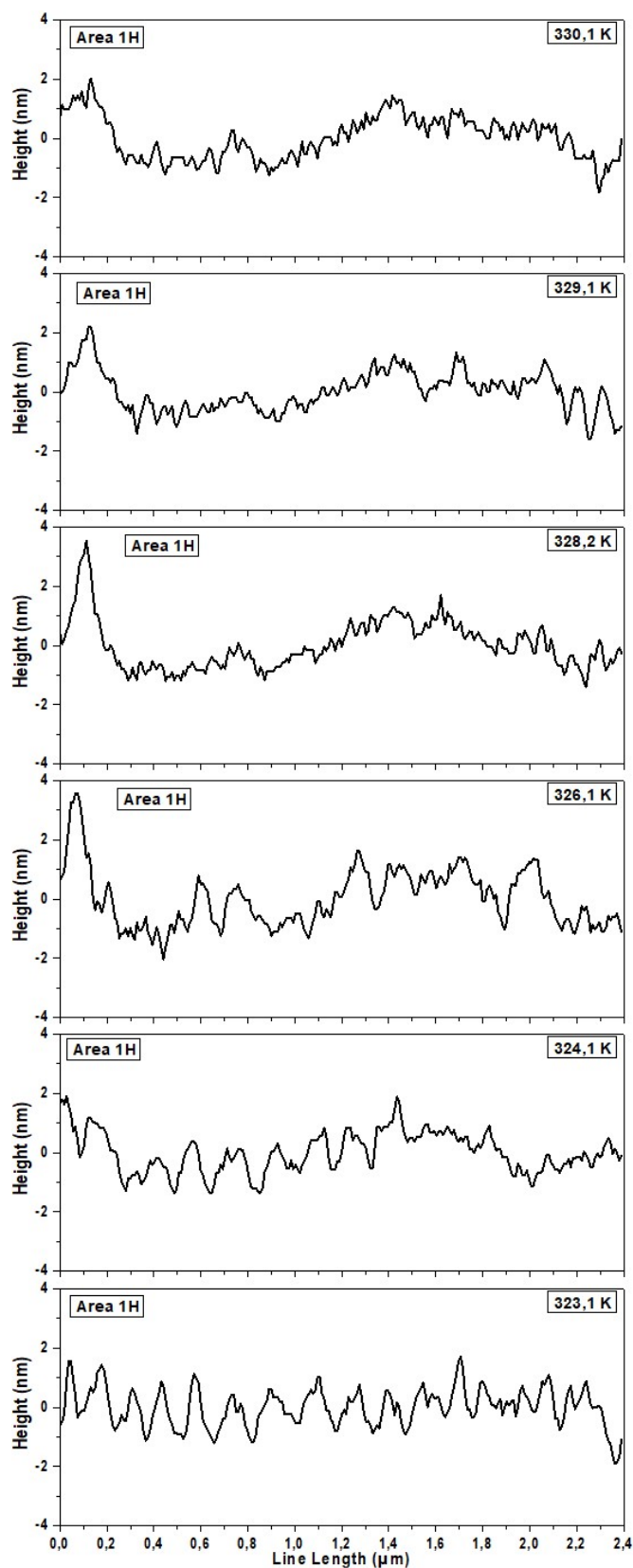
Fig. 5.45 - Line profiles in area 1H of the topography scans of the 2.4x2.4μm² area in Fig. 5.40 (in cooling).
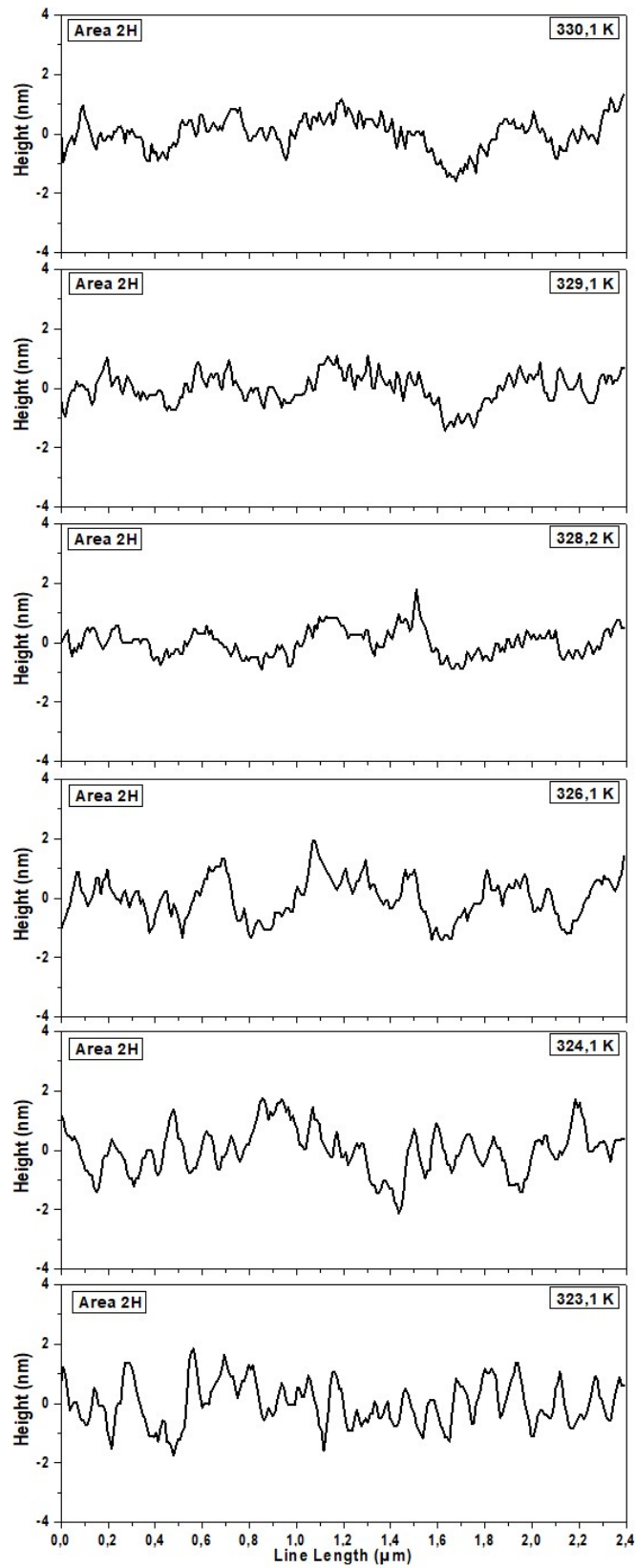
Fig. 5.46 - Line profiles in area 2H of the topography scans of the 2.4x2.4µm^2 area in Fig. 5.40 (in cooling).

b) NMG1535 (100 nm thin film)

In the 100 nm thin film (NMG1535), the observed protuberances on the surface create an elevated number of distortions and artifacts in topography scans (Fig. 5.47), severely compromising the image quality and disallowing the proper visibility of the "wavy-like" topographic pattern characteristic of the martensitic phase. The topography scan and line profile in Fig. 5.48 allow us to discern, on the bottom right of the scan, and to very limited extent, a portion of martensitic features of the 100 nm NMG1535 film.
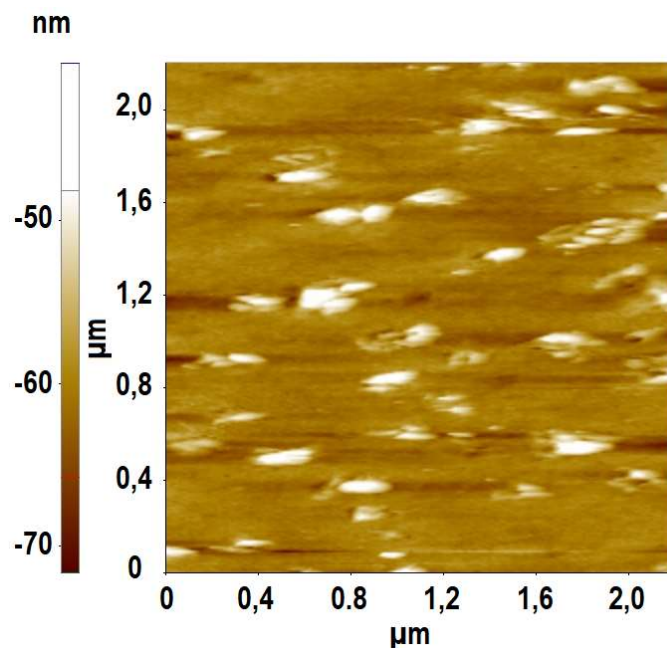
Fig. 5.47 - Topography scan of 2,2x2,2 μm area of Nano-TA analysis performed at room temperature with SThM tip: martensitic phase very subtly visible.

The line profile, showing the outline of a roughly perpendicular section of the "wavy-like" pattern of the film's surface, appears to suggest a "wave" about 40 nm wide and 1 nm high. These features are considerably smaller than the ones in the 400 nm NMG1537 film and very hard to distinguish in a topography scan with acceptable resolution. Moreover, scan quality tends to decrease as the temperature of the sample rises. Due to the aforementioned reasons, topography scans at different temperatures were not performed on this sample.
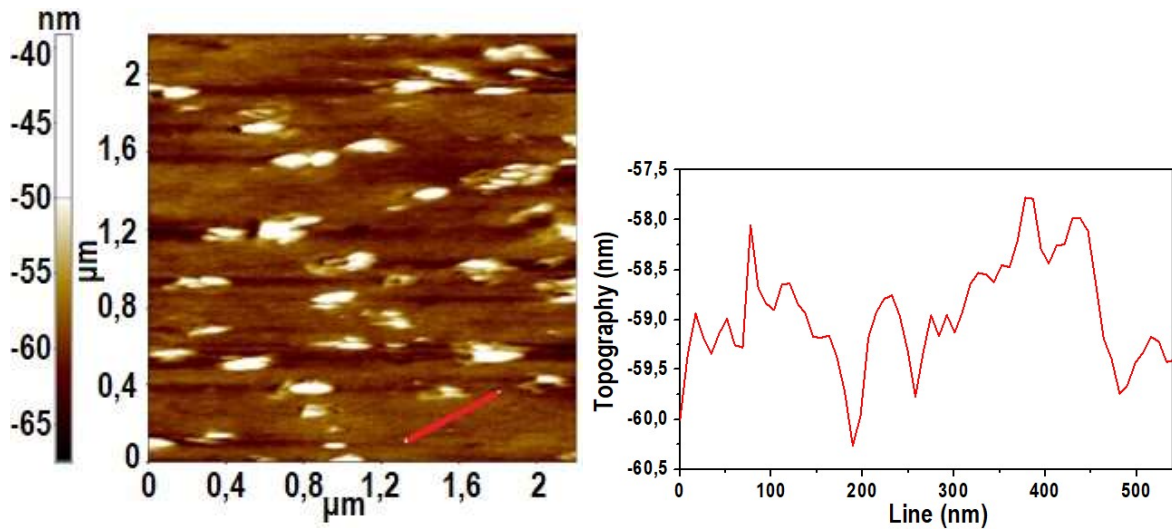
Fig. 5.48 - Line profile taken in an area of the sample where the martensitic phase is subtly visible.

The process of locally inducing temperature dependent structural transformations by SThM thermal nanoprobe described for the 400 nm NMG1537 sample was also performed in this film. In this case, the film was kept at the constant temperature of 310 K by the Peltier element (RS 490-1339, 21.2W, 3.9A, 8.8V, 20x20mm^2).

The 2,2 μm x 2,2 μm area whose topography was shown in Fig. 5.47 was divided into 121 squares of 200nmx200nm (Fig. 5.49). In each of these areas, the structural transformation was locally induced, one at a time. The same concern regarding the order in which the different points were transformed applied to the 400 nm NMG1537 film was also applied here.

With the film kept at 310 K, the results show transformation temperatures registered within an interval of ~ 65 K, from ~ 327 K to 392 K (Fig. 5.50), with a distribution that can be seen in Fig. 5.51. A dip in the distribution of transformation temperatures was observed between 353 K and 363 K.

The T_M value with highest frequency in the distribution is 348 K for the 2.2 μm^2 studied area. There is another value of T_M which has the second highest incidence rate (~ 76% of the highest one) in the analyzed area, 370 K.
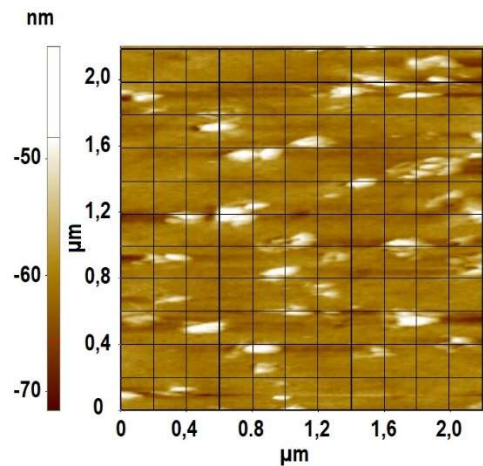
Fig. 5.49 - Grid of areas where the structural transformation was locally induced in a 2,2 μm x 2,2 μm area of the 100 nm NMG1535 film.
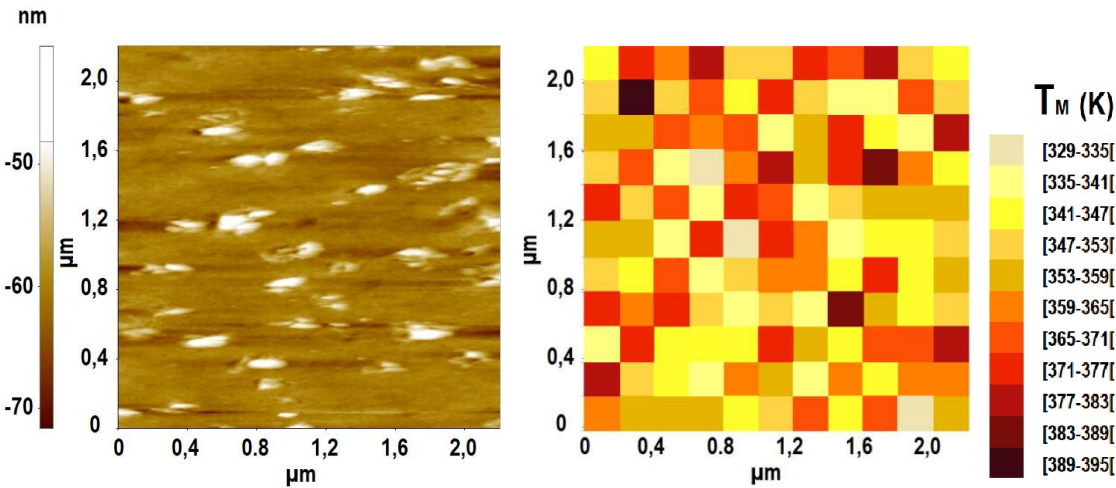
Fig. 5.50 - Mapping of local transformation temperatures in a 2,2 μm x 2,2 μm area of the 100 nm NMG1535 film.
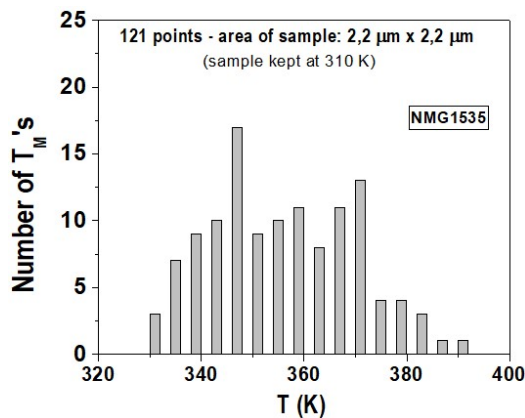
Fig. 5.51 - Transformation temperature distribution for 121 points in the 2,2 μm x 2,2 μm area of the 100 nm NMG1535 film.

5.1.3 – Final remarks

Magnetic measurements performed for the 400 nm NMG1537 film revealed a T_C of 346 K (in cooling and heating), with the austenitic transformation occurring within an interval of ~15K (335K to 350K), with a considered T_A ~ 336 K. The martensitic transformation takes place in a temperature interval of ~ 20K, from 350K to 330K, and T_M is considered to be ~ 330K. The thermal hysteresis of the transformation is thus approximately 6 K.

These measurements were obtained when the whole sample is being heated or cooled. That is also the case when we take topography scans of a micrometric area of the film at different temperatures. For two different micrometric areas of the film, we observed that, for area 1 of 400 nm film NMG1537 (Fig. 5.23), the austenitic transformation takes place within an interval of 3K (326K to 329K). For area 2 of 400 nm film NMG1537 (Figs. 5.39 and 5.40), the austenitic and martensitic transformations take place within temperature intervals of 5K (328K to 333K) and 10K (333K to 323K), respectively. This confirms the thermal hysteresis of the structural transformation and shows that different areas of the film transform at slightly different temperature intervals when the whole film is being heated. We see that the austenitic transformation occurs within narrower temperature intervals than the martensitic transformation. This is coherent with what is observed in the magnetization vs temperature plot shown in Fig. 5.1.

When inducing the structural transformation locally for roughly a hundred different points, whether these points are selected within a micrometric portion of the sample or spread all over the sample, we obtain distributions of transformation temperatures, accordingly. An analysis of the micrometric area 1 of the 400 nm NMG1537 film (Fig. 5.32) shows a distribution of T_Ms from 345 K to 359 K (14K interval), while extending the probing to the whole area of the film in two different tests delivers a T_M distribution from 325 K to 390 K in both cases. Each one of these three studies show a specific transformation temperature which appears more frequently, and it is different for each of these studies (2x2, 354 K; 3000x300(a), 335 K; 3000x300(b), 345 K. Knowing beforehand that the sample doesn't transform in all

areas at the same temperature, the existence of temperature distributions in local transformation inducing/probing is hardly surprising. The main breakthrough in this chapter is finding that locally transforming the sample translates into much wider T_M intervals. This is very clear when we contrast the results given by topography scans taken at different temperatures (Fig. 5.23) and the local T_Ms map made in the very same area, shown in Fig. 5.32. It is relevant to notice that most of the higher T_Ms seen in the map coincide with the portion of the $2x2\mu m^2$ area that transforms at higher temperatures when the whole film is being heated simultaneously (see Fig. 5.23). What we find is that, when a nanometric volume of Ni-Mn-Ga is transforming to the austenitic phase while the surrounding volume of the material remains in the martensitic phase, the transformation temperatures are modified. So, different local environmental conditions translate into differences in transformation temperature, which points in the direction of differences in local transformation progress. It will be relevant to assert if it makes sense to include local differences in the material's composition within the differences in local environmental conditions. The material's phase diagram indicates that transformation temperature is strongly dependent on composition, and it would be pertinent to dwell deeper into this aspect to ascertain whether it is relevant for the present discussion.

In the previous sections, SThM was successfully shown to be a consistent and relevant tool to locally study and act on shape memory alloys at a nanometric scale. When used in local nano-thermal analysis mode, the technique takes an active stand, leaving the realm of passive measurement and assuming the role of actuator as a structural transition thermal inducer. The obstacle raised in thermally inducing such transformations by fast local heat dissipation in materials with high thermal conductivity was overcome by external heating of the sample just below the material's transformation temperature. Local acting and probing with SThM will benefit from gaining further insight on the behavior of cantilever deflection when an electrical current is being fed to the tip while there is a solid-solid contact between probe and different materials, with and without structural transformation in the temperature range allowed by the equipment, and different thermal conductivities.

5.2 Study of avalanche effects in martensitic transformation in Ni-Mn-Ga thin films

The martensitic transformation in the Ni-Mn-Ga system is an event that has been exposed in previous works but benefits from further study. For instance, basic electrical properties of this alloy system in the region of the martensitic transition haven't been systematically studied, and otherwise well characterized bulk $Ni_{2+x}Mn_{1-x}Ga$ alloys should be substantiated in literature concerning the study of their magnetoresistance (MR). Jin et al. [153] detected a jump-like behaviour in the resistivity of Ni-Mn-Ga marking the transformation from the austenitic to the martensitic structure and displaying an increase of 12% in the resistivity and Vasil'ev et al. [154] have shown that measurements of the resistivity dependence on temperature can be used, for some compositions of the $Ni_{2+x}Mn_{1-x}Ga$ alloy system, as a simple and effective tool to detect both structural and magnetic transitions. Anomalous behaviours of the electrical resistivity as a function of temperature during the martensitic transition in the Ni-Mn-Ga compounds have been reported in a few works [155] [156]. Some studies have suggested that anomalies observed between T_M and T_C indicate the occurrence of a pre-martensitic transition, while others state that no sign of such transition can be determined by several measurements [157] [154][158].

The fundamental mechanisms leading to the resistivity behaviour caused by a variation of temperature in the range of the martensitic transition are thus not fully understood, which is why intense investigations need to be taking place in order to clarify such complex features.

To rigorously study anomalies in the resistivity measured as temperature varies, many different aspects should be taken in consideration, such as, among others, the influence of composition and the result of cycling and ageing. Also, in general, in the martensitic phase of Ni-Mn-Ga, any measurement results depend on the initial variant microstructure, which means that if the initial microstructure varies due to, for instance, applied fields, stresses, or repeated warming/cooling cycles, measurements for a given specimen may not be reproducible [159]. We report

experimental results from an investigation of the resistivity dependence in temperature, in the vicinity of the martensitic transition, of a $Ni_{2,20}Mn_{1,08}Ga_{0,72}$ thin film deposited onto a Si/SiO_2 substrate, where we find avalanche and return point memory phenomena. The study of the return-point memory effect in films is particularly relevant, since it has a significant applicability in magnetic recording technologies through tailoring of their structure and surface morphology, in order to obtain desired memory effects. We also discuss the influence of the electrical current and applied magnetic field in the observed phenomena.

5.2.1 – Experimental details

A Ni-Mn-Ga thin film (NMG28c) was deposited onto a $Si(100)/SiO_2$ substrate by radio-frequency (RF) magnetron sputtering at the magnetic properties lab, at UA, by Armando Lourenço. The deposition was performed with two sputtering targets, $Ni_{50}Ga_{50}$ and $Ni_{50}Mn_{50}$, with magnetron powers of 12W and 14W, respectively. During deposition, the substrate temperature was 413 ºC and the argon pressure was $5x10^{-3}$ mbar. The chemical composition of the NMG28c sample was determined to be $Ni_{2,20}Mn_{1,08}Ga_{0,72}$ by EDS (Energy-dispersive X-ray Spectroscopy). Magnetic measurements were performed with a SQUID magnetometer. The crystallographic structures of the film was analyzed using a PANalytical X'Pert PRO MRD X-ray diffraction (XRD) instrument with a Cu-Kα radiation source. Resistivity measurements were performed with a system developed by the group, using the four-probe technique (described in section 2.5).

5.2.2 – Sample Characterization

5.2.2.1 – XRD

Fig. 5.52 shows the diffractogram which resulted from an XRD scan in Bragg-Brentano geometry of the NMG28c film, recorded in the range 20º < 2θ < 75º. The result shows that they possess some degree of crystallinity, exhibiting only two split

peaks in 2θ between approximately 42º and 45º. A grazing incidence measurement was performed in the film (Fig. 5.53), to obtain a better representation of the split peak. This is a common feature in films that contain simultaneously austenitic and martensitic phases in their compositions [160]. The lattice parameter of the cubic phase calculated from the 2θ value of the $(220)_C$ peak is 5,81 Å, which agrees with the value obtained for bulk Ni_2MnGa [161]. There seems to be a preponderance of the cubic phase over the tetragonal phase, which might be due to a contribution of the amorphous SiO_2 layer of the substrate, on top of which the film is deposited, to the growth of the cubic phase [162]. The relevant background of the scan may be possibly hindering the exhibition of other diffraction peaks, which might suggest strong texturing and/or partially disordered state of film. Fig. 5.54 shows the X-ray reflectivity measurement performed on the NMG28c film. Although there are not enough Kiessig fringes on the range of the measurement to calculate with confidence the thickness of the film, we can see that they present a large period, which means that the film is quite thin. This is confirmed by TEM images, shown in the next section. The very sudden drop in intensity right after the critical angle suggests high surface rugosity, also confirmed by TEM measurements.
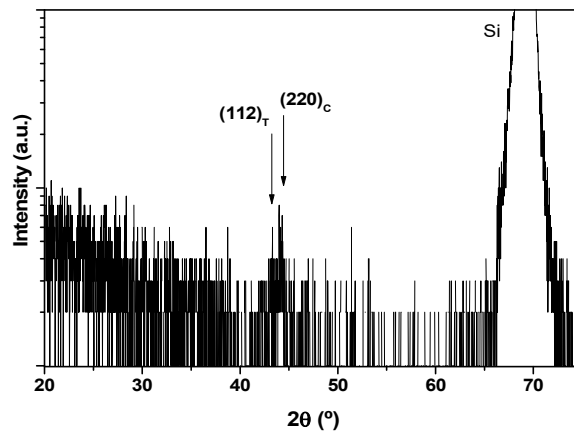
Fig. 5.52 - XRD scan in Bragg-Brentano geometry of the NMG28c film.
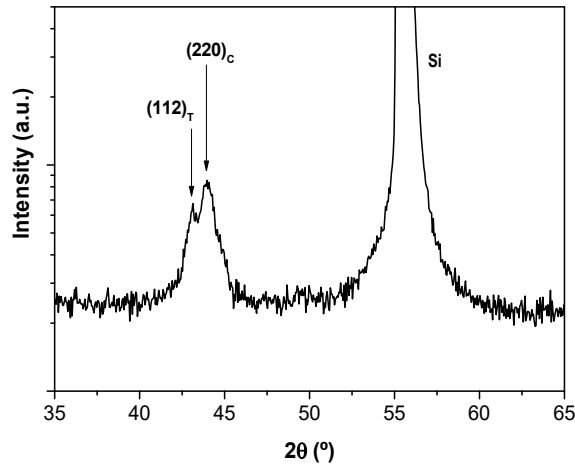
Fig. 5.53 - Grazing incidence measurement ($\omega = 2°$) for the NMG28c film.
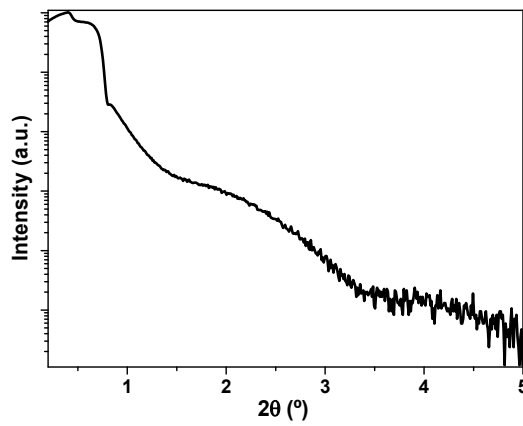
Fig. 5.54 - X-ray reflectivity measurement performed on the NMG28c film.

5.2.2.2 – TEM

Figs. 5.55 and 5.56 show the TEM image of the NMG28c sample, the SiO_2 intermediate layer and the Si (100) substrate at a 100 and 10 nm scales, respectively. Fig. 5.55 clearly shows the topography of the film, providing information concerning the surface roughness of the film. It also shows that the film has a thickness around 60 nm, confirming the result from the x-ray reflectivity measurement (Fig. 5.54).

Fig. 5.57a shows, at a 2 nm scale, several areas of the sample: the Ni-Mn-Ga film, the SiO_2 intermediate layer and the Si (100) substrate. Fig. 5.57b to 5.57e shows

the Fourier transform of the selected area labelled as A to D, respectively. A TEM image of the cross section of the NMG28c sample is represented in Fig. 5.58 where the different orientations of the film are quite evident, showing its policrystallinity. This policrystallinity is also visible in Fig. 5.57a.
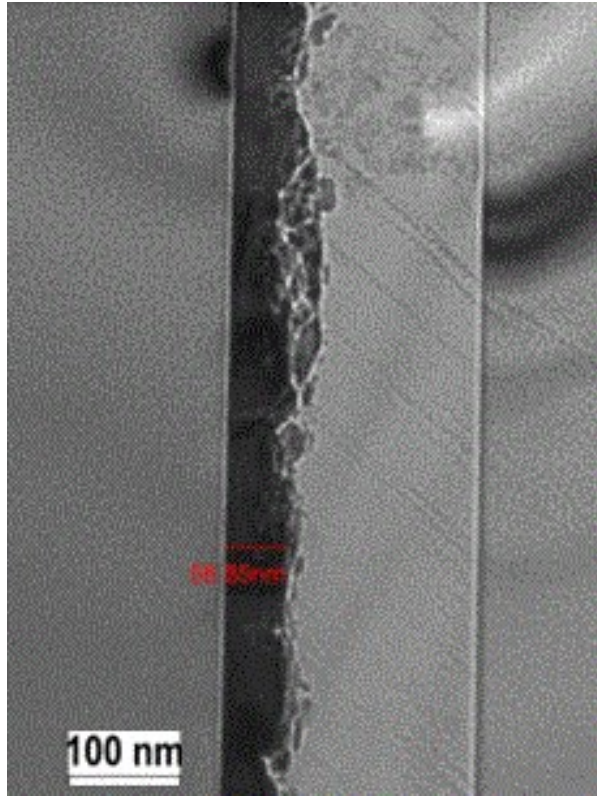
Fig. 5.55 - TEM image of the NMG28c sample; the image provides a measurement of 58,85 nm for the film thickness at the location marked on the image.
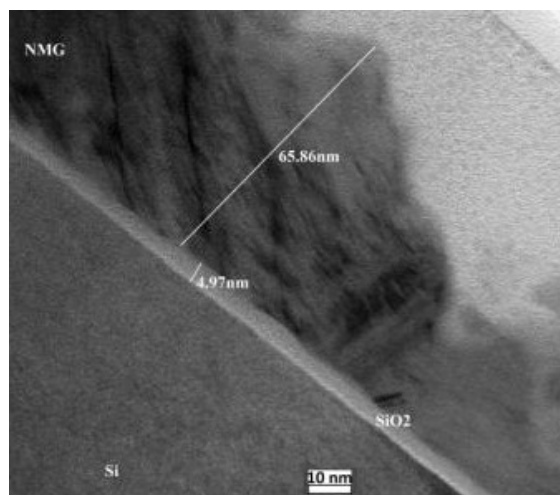
Fig. 5.56 - TEM image of the NMG28c sample: $Ni_{2,20}Mn_{1,08}Ga_{0,72}$ film, the SiO_2 intermediate layer and the Si (100) substrate at a 10 nm scale.
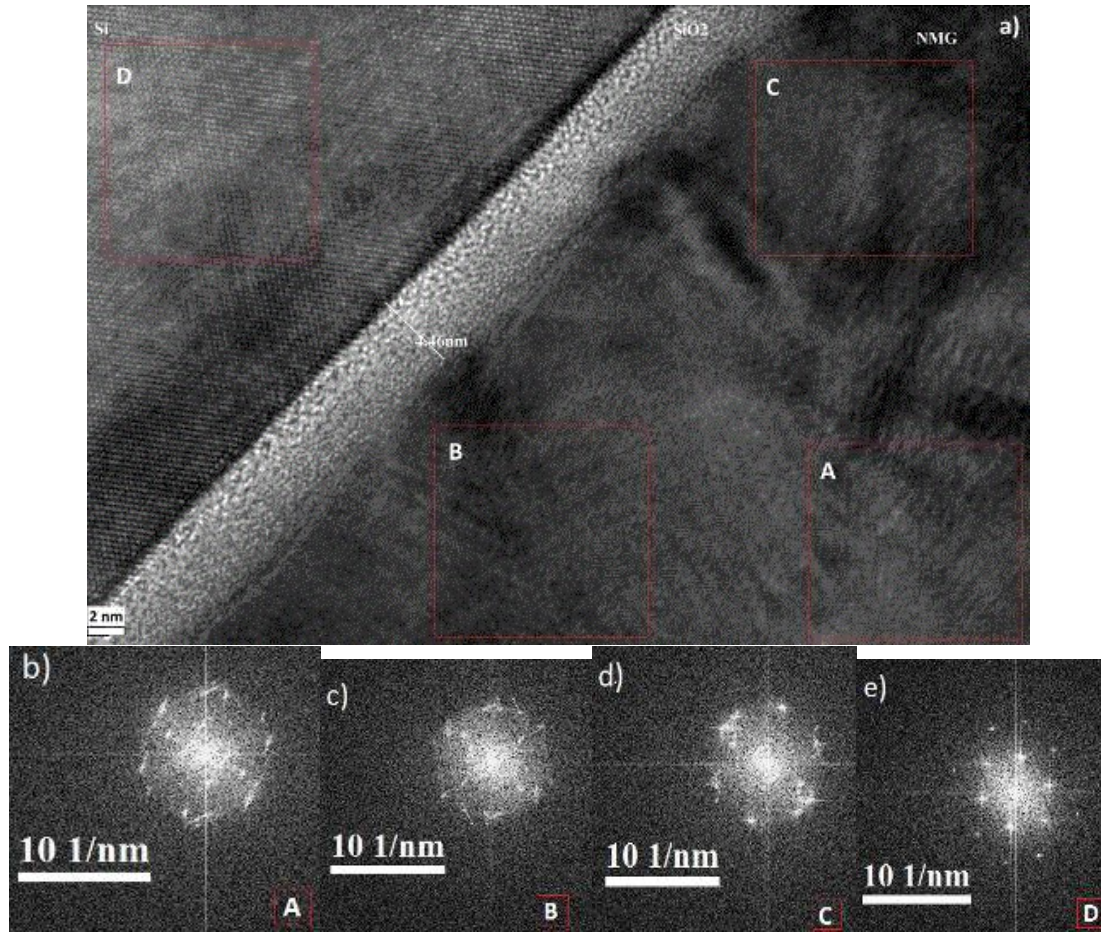
Fig. 5.57 - a) TEM image of the NMG28c sample: $Ni_{2,20}Mn_{1,08}Ga_{0,72}$ film, the SiO_2 intermediate layer and the Si (100) substrate at a 2 nm scale; b) Fourier transform of the A selected area; c) Fourier transform of the B selected area; d) Fourier transform of the C selected area; e) Fourier transform of the D selected area.
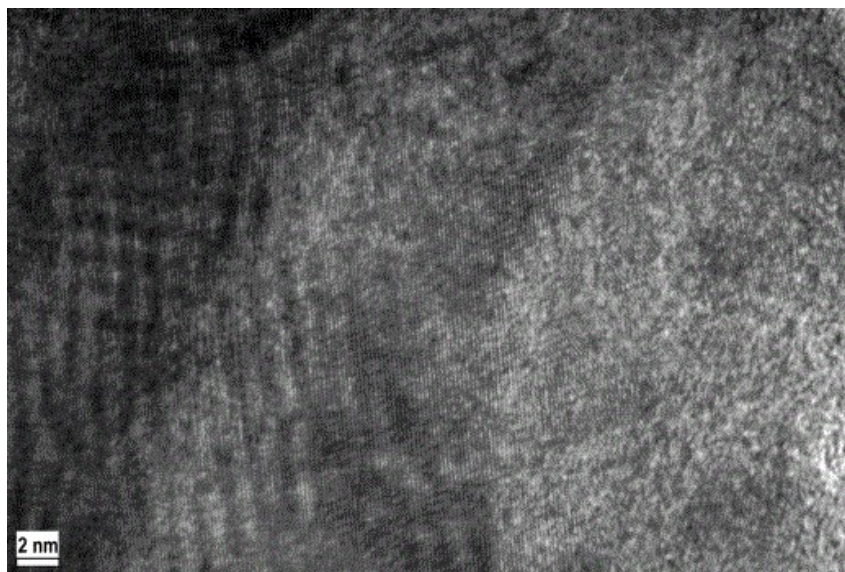
Fig. 5.58 - TEM image of a cross section of the NMG28c sample.

5.2.2.3 – Magnetic properties

Fig. 5.59 presents the magnetization as a function of the applied magnetic field for sample NMG28c at two different temperatures: 5 K and 300 K. The measurements were performed within the magnetic field range of -2 T and 2 T. The M(H) curves taken at 5K and 300K suggest the existence of the diamagnetic contribution from the Si substrate. The saturation magnetization, obtained by extrapolating the high field behavior to zero field give M_{sat} = 4 x 10^5 A/m (400 emu/cm^3) and M_{sat} = 2.5 x 10^5 A/m (250 emu/cm^3) at 5 K and 300 K, respectively. The M_{sat} value for 5 K is comparable to the M_{sat} value of the bulk Ni-Mn-Ga with the same composition [50]. For M_{sat} at 300 K, comparable to the 200 emu/cm^3 at room temperature (~300 K) [148].

Fig. 5.60 presents a zoom for smaller fields of the magnetization as a function of the applied magnetic field for the two considered temperatures shown in Fig. 5.59. At 5 K, the film presents a coercive field (H_C) of about 500 Oe and becomes saturated for fields higher than 2500 Oe. At 300 K, the film presents a H_C of about 70 Oe and becomes saturated for fields higher than 5000 Oe.

Fig. 5.61 presents the temperature dependence of the magnetization of the film under the applied magnetic field of 2000 Oe. The T_C of the film appears to be 336 K. The structural martensitic transition, usually characterized in thermo-magnetic curves by a sudden rise in magnetization, is not observed The absence of the martensitic transformation feature at the considered temperature range may be due to the use the 2000 Oe magnetic field, since it is typical for Ni_2MnGa to show a pronounced martensitic transition signature only when low fields are used [49].

The films studied in the previous section (NMG1537 and NMG1535) can be compared with film NMG28c in therms of their magnetic properties. Films NMG1537 and NMG1535 presented M_{sat} (5 K) = 5x10^5 A/m, M_{sat} (300 K) = 3x10^5 A/m and T_C = 346 K, and M_{sat} (5 K) = 9.2x10^5 A/m, M_{sat} (300 K) = 3.8x10^5 A/m and T_C = 340 K, respectively, while NMG28c presents M_{sat} (5 K) = 4x10^5 A/m, M_{sat} (300 K) = 2.5x10^5 A/m and T_C = 336 K. Although for film NMG1537 T_M is very clearly identified in all

presented M(T) curves, for NMG1535, T_M cannot be identified in the FC M(T) curve,
it's only perceivable in the ZFC M(T) curve.
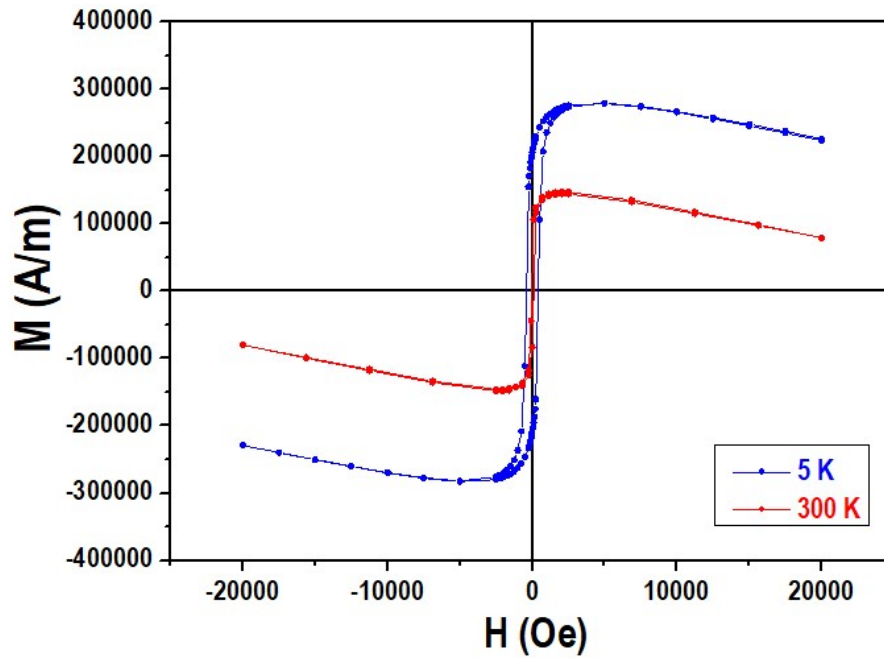
Fig. 5.59 - Magnetization versus magnetic field hysteresis curves for sample NMG28c.
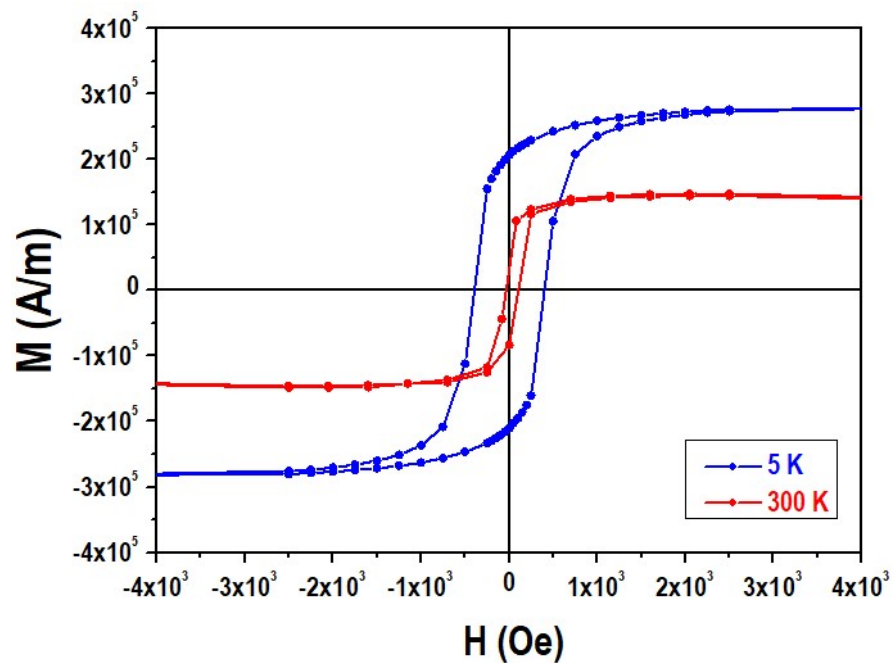
Fig. 5.60 - Magnetization versus magnetic field hysteresis curves for sample NMG28c – zoom of Fig.
5.59.
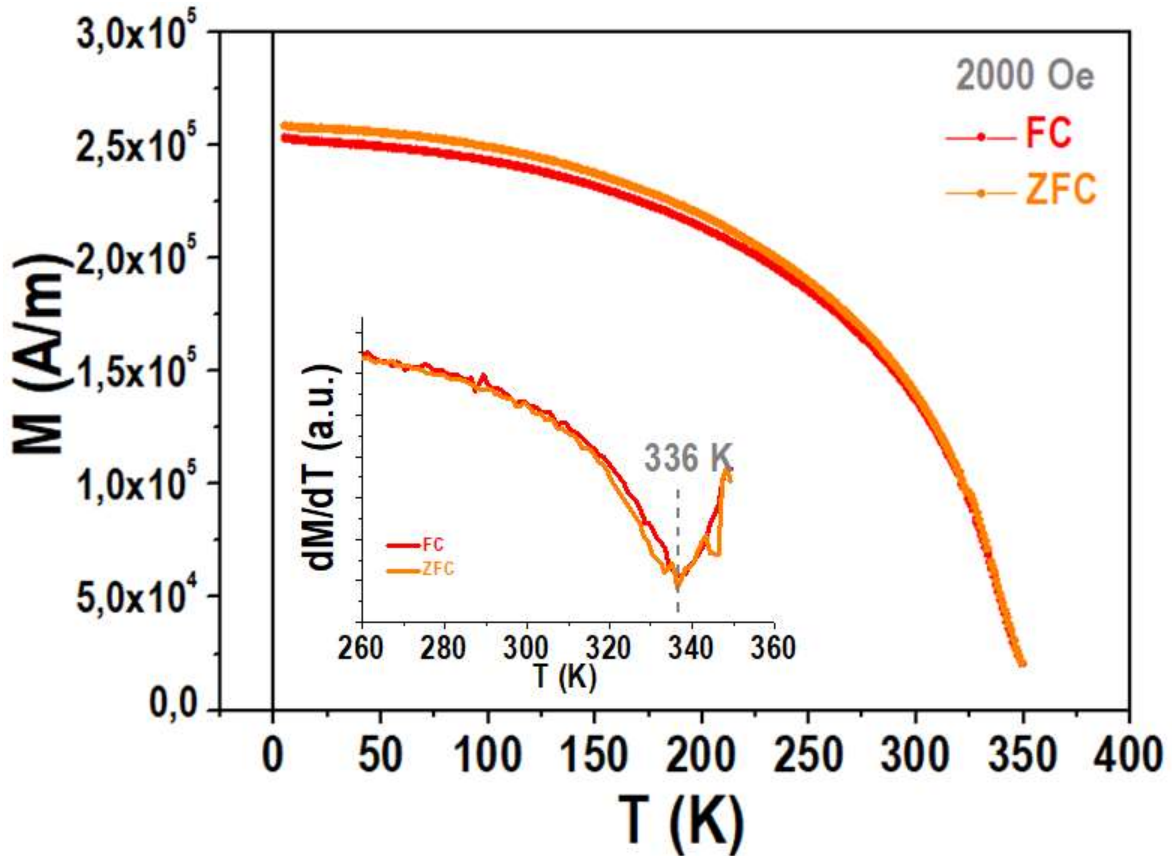
Fig. 5.61 - Magnetization versus temperature curves for sample NMG28c: ZFC and 2000 Oe FC.

5.2.3 – Electrical resistivity measurements and discussion of avalanche effects

In this section we present the study of electrical resistivity as a function of temperature by performing two heating and cooling cycles in the absence and presence of a magnetic field (1 T) on sample NMG28c.

We have also measured both voltage and electrical resistance as a function of the electrical current at two different temperatures (293 K and 350 K) in the absence and presence of a magnetic field (1 T).

Finally, we measured electrical resistivity as a function of temperature by performing heating and cooling cycles in the presence of a magnetic field (1 T) for three different values of electrical current applied: 0.1 mA, 0.5 mA and 1 mA.

Fig. 5.62 shows that the electrical resistivity as a function of temperature presents hysteresis on heating and cooling (which is the typical behavior of films of shape memory alloys [163]), in the temperature range of 9 K on the first cycle and

122

21 K on the second cycle. The presence of depressions and jumps in the heating and cooling curves, respectively, is observed when temperature cycles from 300 K to 370 K are performed. In the heating curve of the first cycle, the resistivity of the film shows a sharp decrease at T ≈ 340 K. In the heating curve of the second cycle, the resistivity of the film also shows a sharp decrease which occurs at about 360 K. These depressions have approximately the same magnitude in both previously mentioned curves. In the cooling curve of the first cycle, there is a jump in resistivity occurring at T ≈ 330K. In the cooling curve of the second cycle, the resistivity of the film also shows a jump which occurs at about 340 K.

Once again, the variation of resistivity displayed in these jumps is of the same magnitude in both cooling curves. In general, electrical resistivity is very sensitive to defects and inhomogeneities of the structure. Therefore, it is expected that the resistance depends on the magnetic/structural domain distribution, the domain wall structure and the energy barriers involved in the motion of the domain boundaries.
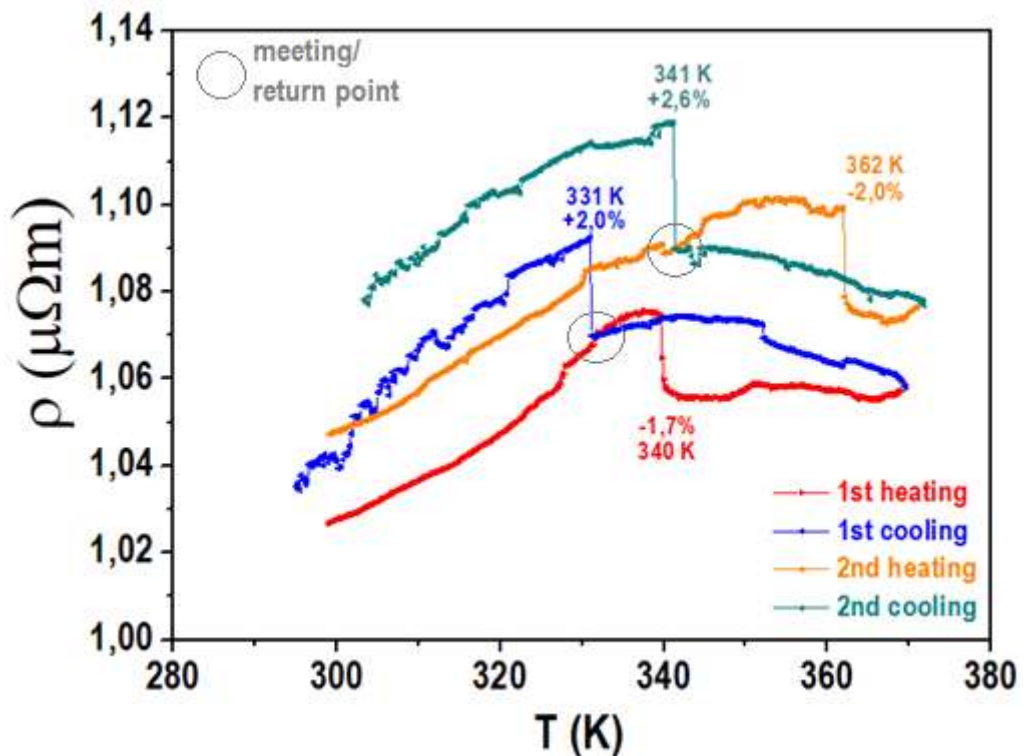
Fig. 5.62 - Consecutive cycles of resistivity as a function of temperature for sample NMG28c.

For this material, a shape memory alloy, all this can establish quite a complex web of interactions, resulting in very particular behaviors in resistivity. The jumps and depressions observed in resistivity during a continuous process of temperature variation might be the manifestation of sudden changes in the size and orientation of domains. They are probably the result of changing domain boundaries, or, more precisely, changing avalanches of domains. Some domains are modified by the temperature changes or by the influence of other domains in its vicinity. The transformation of one domain may trigger some of its neighbors, who in turn will trigger some of their neighbors and so on, resulting in such effects that can be named as avalanches. Avalanches in ferromagnetic materials and in shape memory alloys, which go through martensitic transitions, have been observed through other types of measurements, but they were not yet observed in resistivity as a function of the temperature measurements for these materials.

The cooling curves, although exhibiting the similar features of the corresponding heating curves that we have just mentioned, do not follow the exact same path as the aforementioned curves. Additionally, in both cycles, the jump in the cooling curve happens when it meets its corresponding heating curve at a temperature below the depression experienced by this curve. This return to a state previously observed at a given temperature seems to trigger a jump-like behaviour in resistivity. It should also be noted that, for the same temperature (T≈299K) in cooling of the first cycle and in heating in the second cycle, there is a difference in resistance of about 0,1 Ω (0.72%). It is important to state that the conditions of the second cycle measurement are exactly the same as before, except that between the first and the second cycles, about thirteen hours had elapsed. This variation in resistivity with time which was previously mentioned, leads us to consider for future reference that elapsed time is a relevant variable in the study these phenomena.

Figs. 5.63 and 5.64 show consecutive cycles of resistivity as a function of temperature, in the absence and presence, respectively, of a magnetic field applied to the NMG28c sample. Analyzing the second heating and cooling curves in Fig. 5.63, it is noticeable that the resistivity seems to pursue earlier paths at given points, returning to previously experienced states. These pursued states do not exclusively

belong to the immediately preceding measurement, but also to those which were performed beforehand. The sample seems thus to show a behavior that could be understood as some kind of thermal return point memory behavior.

The return point memory (RPM) behavior is an interesting property of hysteresis in SMA, and it is very well established in polycrystals. After a cyclic variation, the system follows the same trajectory that it would have followed if the cyclic variation had not occurred, which leads to the formation of a hierarchy of loops within loops, each internal loop being characterized by the point at which the variation was introduced [164].
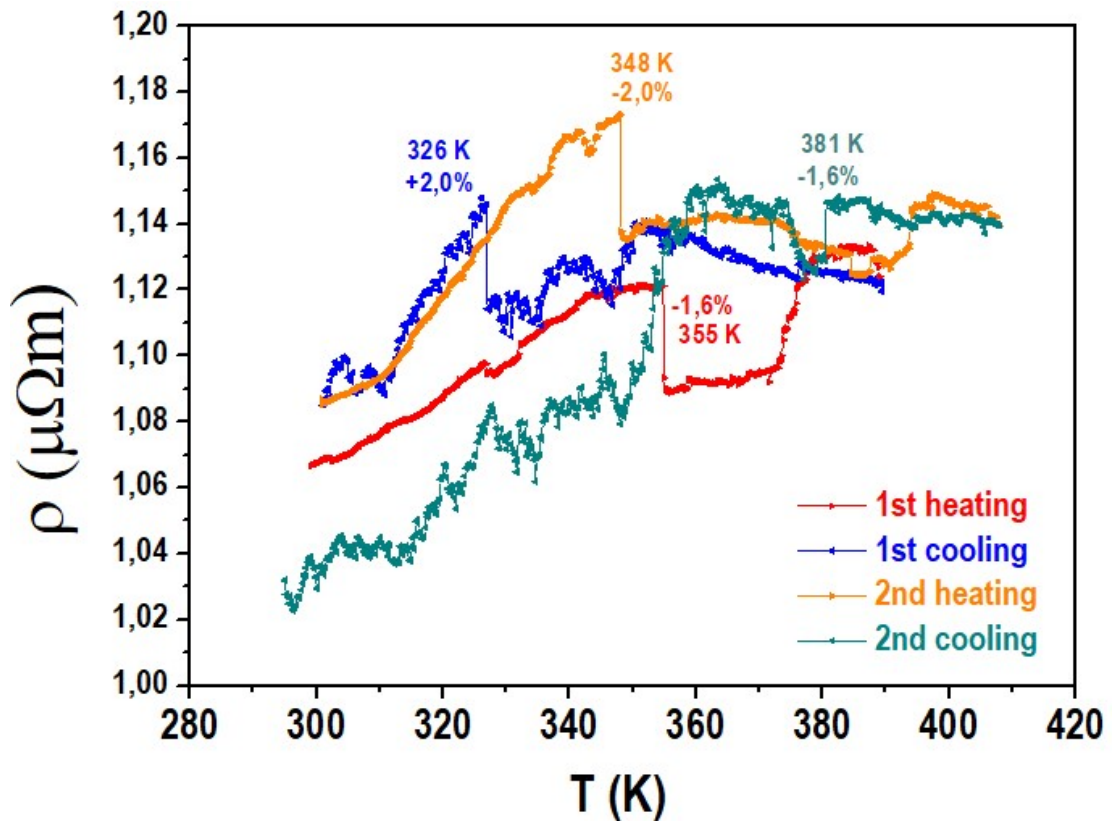
Fig. 5.63 - Consecutive cycles of resistivity as a function of temperature for sample NMG28c with temperature ranging from 300K to 400K.
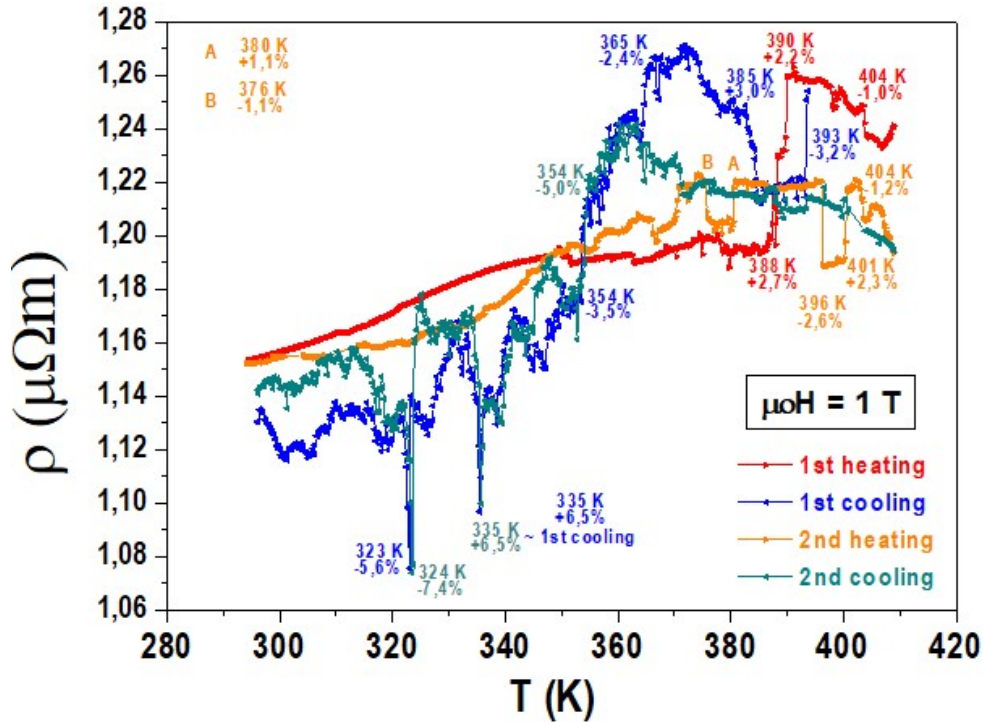
Fig. 5.64 -Consecutive cycles of resistivity as a function of temperature for sample NMG28c under an applied magnetic field of 1T, with temperature ranging from 300K to 400K.

We investigated a possible dependency of the avalanche phenomena in the electrical current, as well as the influence of the magnetic field on the electrical resistance measurements. Figs. 5.65 and 5.66 show the results for the voltage and resistance, respectively, as a function of the electrical current at two different temperatures (293 K and 350 K) in the absence and presence of a magnetic field (1 T).

In Fig. 5.67 the avalanches still occur under an applied magnetic field with enough magnitude to saturate the sample. This means that the motions of magnetic domain walls are not responsible for the observed avalanches in resistivity as the temperature varies. These avalanches must originate exclusively from structural domain walls transformations.

Contrarily to what happens when we maintain the temperature at a constant value and vary the current (Fig. 5.66) where the applied magnetic field decreases the resistance, the presence of the magnetic field does not lower the resistivity values measured during the temperature cycle compared to when we perform such a cycle without an applied magnetic field. In the plot presented in Fig. 5.68 it seems

even clearer that, with an applied magnetic field, the avalanches seem to increase in number and magnitude when compared to those occurred when no magnetic field is applied. These observations reinforce the hypothesis that states that the resistance's behavior is being strongly determined by structural features. Once again it is important to note that the curves measured with a 1 T applied field (Figs. 5.67 and 5.68) were collected a few days after the ones without an applied magnetic field. Fig. 5.69 shows three heating curves from different temperature cycles, performed with different values of current and the same applied magnetic field of 10 kOe. Once more, no connection between the current value and the occurrence of the avalanches can be established. Tables 5.3 to 5.8 quantify the $\Delta\rho/\rho$ in percentage for each sudden significant variation in resistivity, associating it with the temperatures at which they occur (in fact, the variation occurs within an interval ΔT, whose width is also included on the table) for the plots in Figs. 5.62 to 5.64 and 5.67 to 5.69, respectively. Results presented on the tables are colored matching the color of its corresponding set on the plot of the figure in question.
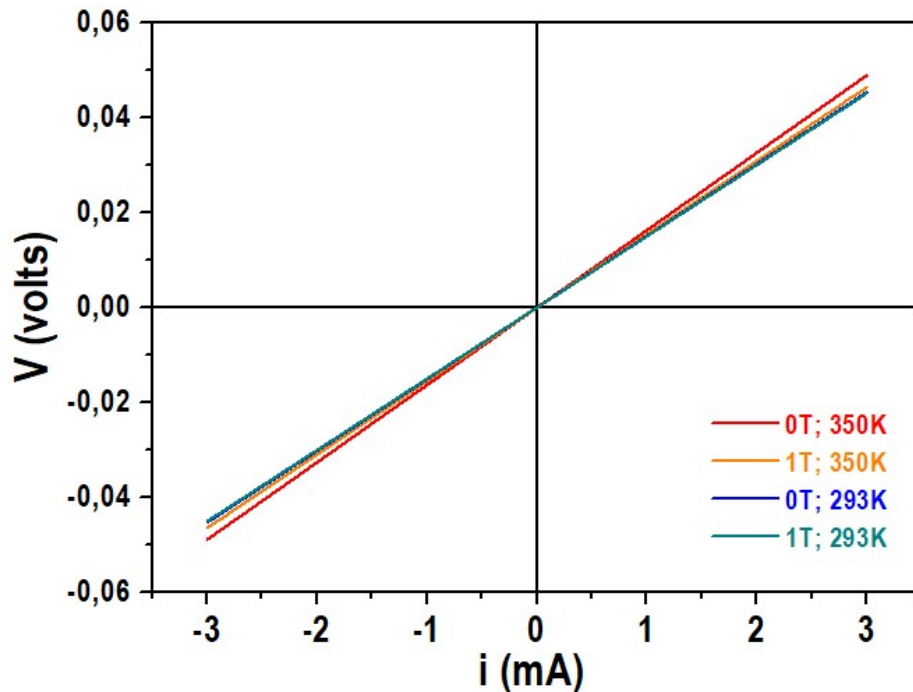
Fig. 5.65 - Voltage as a function of electrical current for sample NMG28c at room temperature and at 350K, with and without a 1T applied magnetic field for both temperatures.
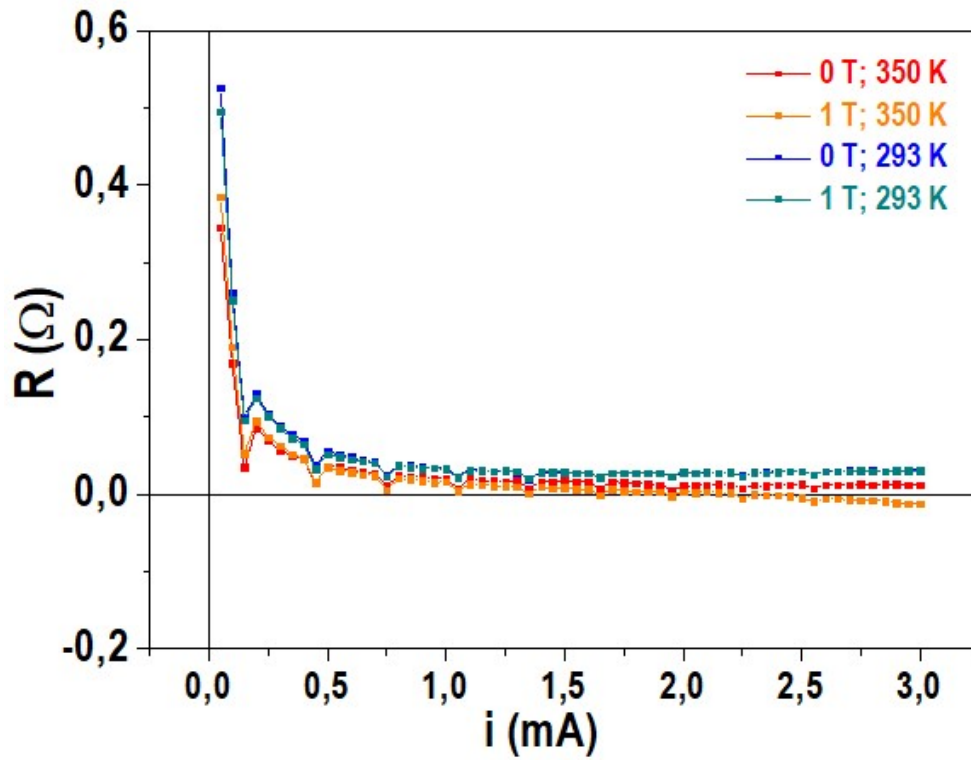
Fig. 5.66 - Resistance as a function of current for sample NMG28c at room temperature and at 350K, with and without a 1T applied magnetic field for both temperatures.
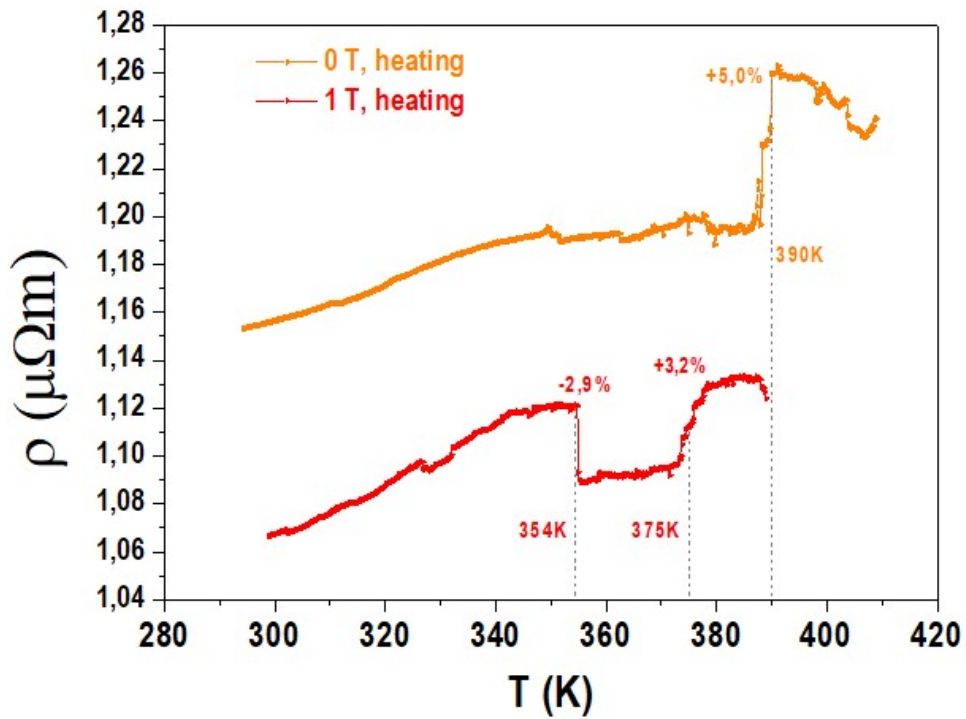
Fig. 5.67 - Heating curves for sample NMG28c belonging to two different temperature cycles, with and without applied magnetic field.
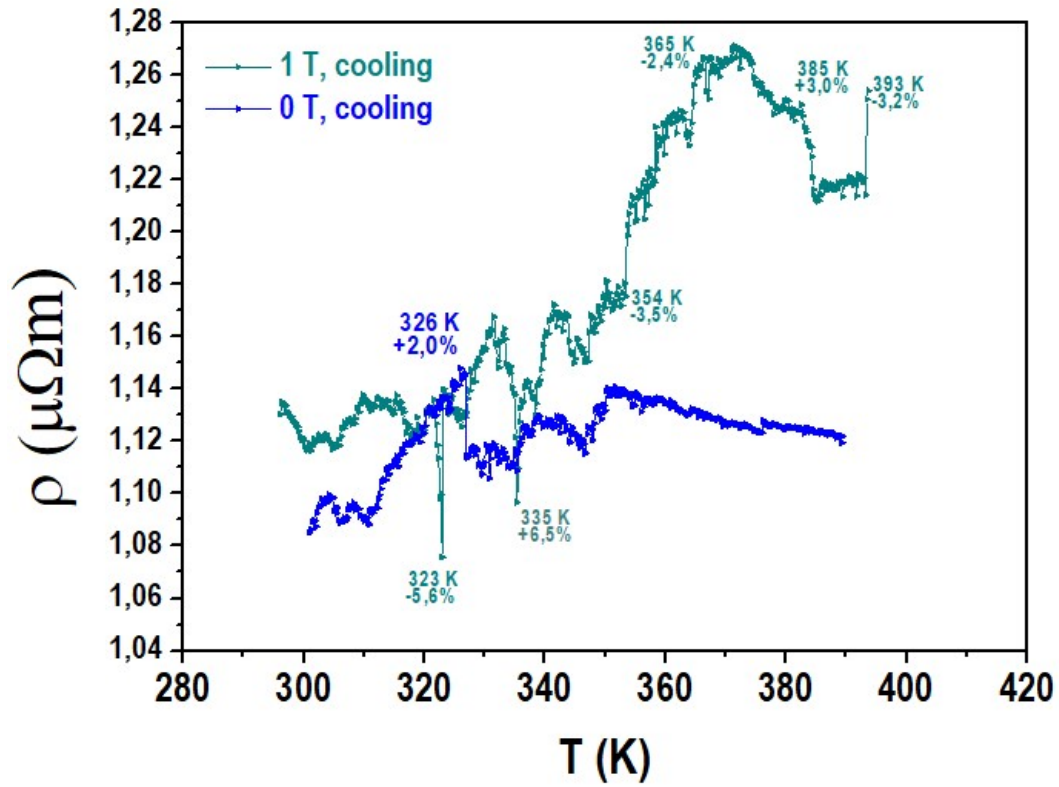
Fig. 5.68 - Cooling curves for sample NMG28c belonging to two different temperature cycles, with and without applied magnetic field.
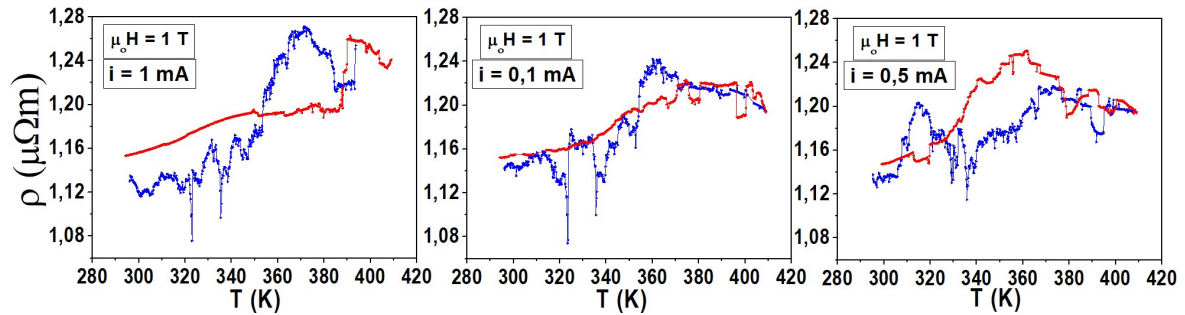
Fig. 5.69 - Heating and cooling curves for sample NMG28c belonging to three different temperature cycles, with a 1 T applied magnetic field, for several electrical current values.

Table 5.3 – T, Δρ/ρ (%) and ΔT for the plots in Fig. 5.62

i (mA)	Field (T)		T (K)	Δρ/ρ (%)	ΔT (K)
1	**0**	1st heating	340	-1.7	1.0
		1st cooling	331	+2.0	0.2
		2nd heating	362	-2.0	0.8
		2nd cooling	341	+2.6	0.2

Table 5.4 - T, Δρ/ρ (%) and ΔT for the plots in Fig. 5.63

i (mA)	Field (T)		T (K)	Δρ/ρ (%)	ΔT (K)
1	0	1st heating	355	-1.6	0.6
		1st cooling	326	+2.0	0.2
		2nd heating	348	-2.0	0.6
		2nd cooling	381	-1.6	0.2

Table 5.5 - T, Δρ/ρ (%) and ΔT for the plots in Fig. 5.64

i (mA)	Field (T)		T (K)	Δρ/ρ (%)	ΔT (K)
1	1	1st heating	388	+2.7	0.4
			390	+2.2	0.4
			404	-1.0	0.6
		1st cooling	393	-3.2	0.5
			385	3.0	1.2
			365	-2.4	1.2
			354	-3.5	0.2
			335	+6.5	0.6
			323	-5.6	0.2
		2nd heating	376	-1.1	1.6
			380	+1.1	0.8
			396	-2.6	0.2
			401	+2.3	0.6
			404	-1.2	0.8
		2nd cooling	354	-5.0	1.8
			335	+6.5	1.6
			324	-7.4	1.6

Table 5.6 - T, Δρ/ρ (%) and ΔT for the plots in Fig. 5.67

i (mA)	Field (T)		T (K)	Δρ/ρ (%)	ΔT (K)
1	0	heating	390	+5.0	2.0
	1		354	-2.9	0.6
			375	+3.2	5.6

Table 5.7 - T, Δρ/ρ (%) and ΔT for the plots in Fig. 5.68

i (mA)	Field (T)		T (K)	Δρ/ρ (%)	ΔT (K)
1	0	cooling	326	+2.0	0.2
			393	-3.2	0.5
			385	+3.0	-2.7
			365	-2.4	1.2
	1		354	-3.5	1.0
			335	+6.5	2.2
			323	-5.6	0.2

Table 5.8 - T, Δρ/ρ (%) and ΔT for the plots in Fig. 5.69; DIP equates to a sudden drop and recovery for the measured value of ρ

i (mA)	T (K)	Δρ/ρ (%)	ΔT (K)
1	388	+2.8	0.4
	390	+2.2	0.6
	394	-3.2	0.5
	365	-2.3	1.2
	335	3.7 (DIP)	1.2
	323	5.6 (DIP)	1.6
0.1	376	-1.1	0.6
	380	+1.1	0.8
	396	+2.6	0.2
	401	+2.3	0.4
	404	-1.2	1.4
	354	+5.0	1.8
	335	-6.5	1.6
	324	+7.4	1
0.5	313	-0.68	0.8
	319	-0.43	0.5
	320	+1.5	0.5
	356	1.4 DIP	0.8
	375	-0.8	0.1
	378$_A$	-1.4	0.4
	378$_B$	-1.4	0.4
	388	+0.4	0.2
	392	-1.1	0.8
	400	+0.6	0.6
	399	-1.0	0.4
	398	+1.3	0.6
	395	-2.0	0.2
	390	+2.0	1.2
	385	+1.6	0.6
	383	-0.9	0.6
	367	-1.6	1.2
	365	+1.5	1.8
	336	-2.7	1.8
	335	+4.5	2.4
	311	-1.7	1.0
	310	+1.0	0.4
	308	-2.0	0.6

Figs. 5.70 to 5.73 show plots of the data presented on Tables 5.3 to 5.8. We observe that sudden changes in electrical resistivity with wider Δρ/ρ (%) values occur especially for temperatures around 325 K and 335 K.
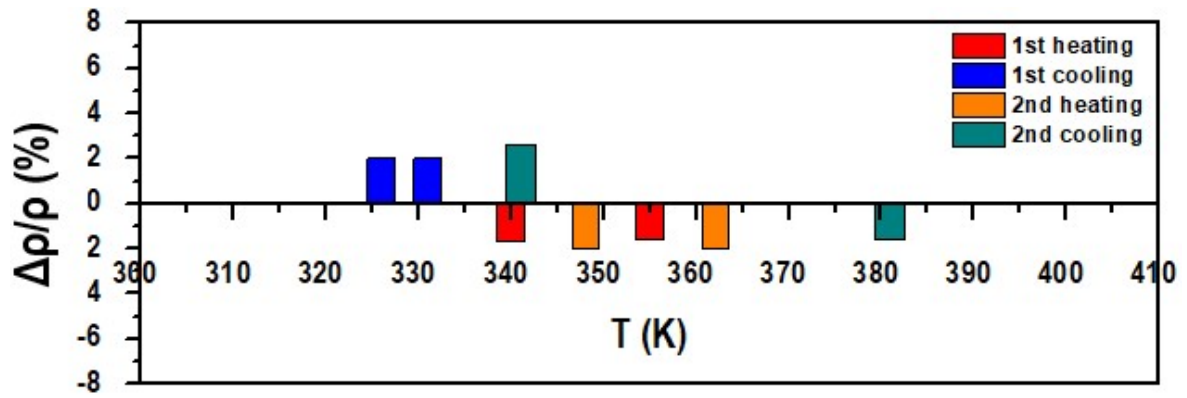
Fig. 5.70 - Plot of Δρ/ρ (%) vs T data presented on Tables 5.3 and 5.4.
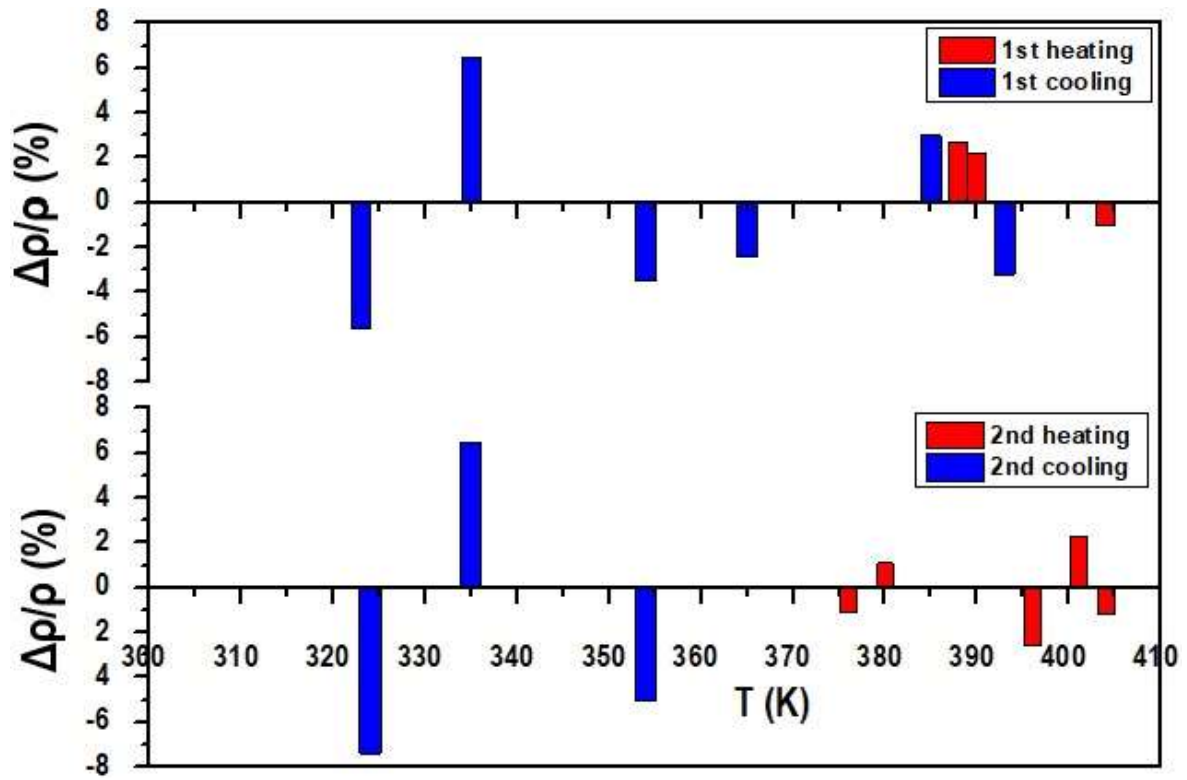
Fig. 5.71 - Plot of Δρ/ρ (%) vs T data presented on Table 5.5.
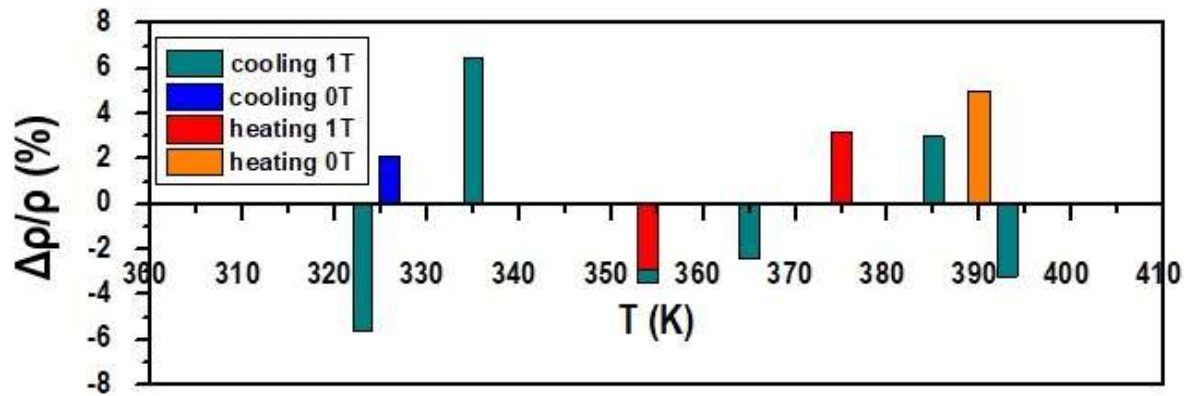
Fig. 5.72 - Plot of Δρ/ρ (%) vs T data presented on Tables 5.6 and 5.7.
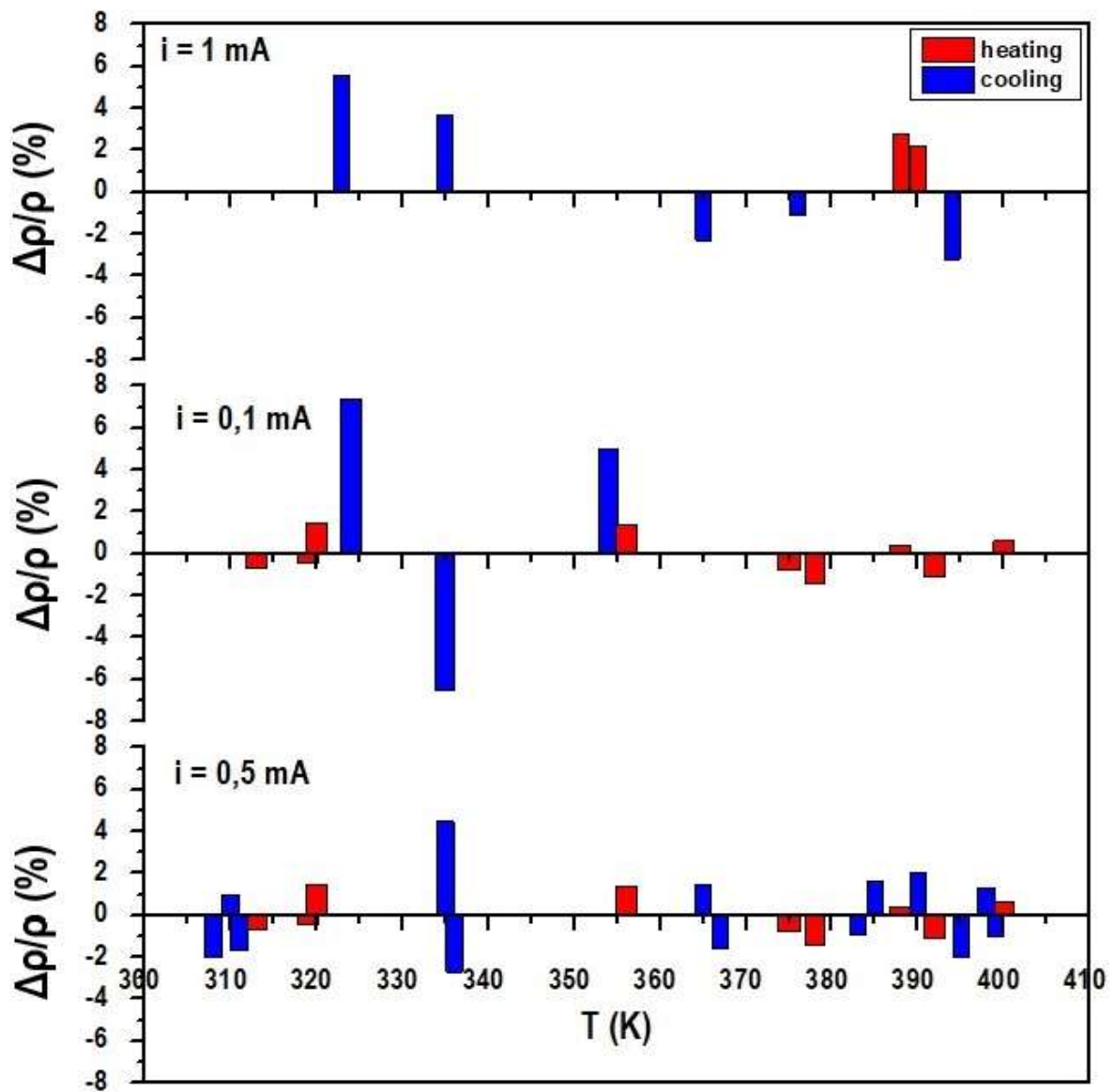
Fig. 5.73 - Plot of Δρ/ρ (%) vs T data presented on Table 5.8.

5.2.4 – Final remarks

Sample NMG28c is a thin film deposited onto Si/SiO_2 substrates, with the composition of $Ni_{2,20}Mn_{1,08}Ga_{0,72}$. At room temperature the sample is ferromagnetic and shows a coexistence of both tetragonal and cubic phase, with a slight predominance of the last one, which is known to be promoted by the substrate in question.

The sample shows previously unobserved jumps and depressions in the electrical resistivity dependence on temperature, which we attribute to changes in avalanches of domain walls. These phenomena were not susceptible of being eliminated by an applied magnetic field strong enough to saturate the sample. They were also demonstrated to be independent of the electrical current magnitude. The studied films also exhibit thermal return-point memory behavior, which is a reported characteristic of magnetic shape memory (MSM) systems.

5.3 – Martensitic transformation in NiTi

5.3.1 – Sample description

From the same NiTi wire acquired from the company Smartwires (https://smartwires.eu/), two samples with different shapes were produced, for different studies. The manufacturer provides the information of a structural transformation temperature of 35+/-5 ºC.

The first sample, NiTi_1 (Fig. 5.74), consists of an approximately 0,15 m long piece of wire as acquired.

For the second sample, several pieces of wire with similar lengths were glued together, aligned in the same direction, and placed inside an aluminum foil mold, where they were embedded in a resin with a hardener. Both top and bottom cross sections of the wires were polished. The result can be seen in Fig. 5.75 and in the SEM image in Fig. 5.76.

Fig. 5.74 - Sample NiTi_1.
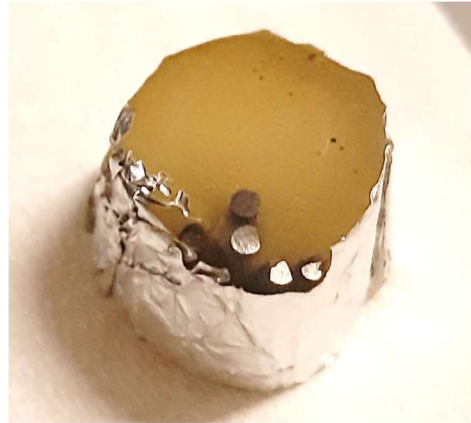
Fig. 5.75 - Sample NiTi_2.

5.3.2 – Sample characterization

5.3.2.1 – SEM

SEM images were taken from sample NiTi_2. The results are shown in Figs. 5.76 and 5.77, where we can observe the sections of two wires and the resin, and images of the surface of the wires at different scales, respectively. These images show a gap between the lateral part of the wires and the resin, which is important for heating of the whole sample purposes. Scratches can be seen at all scales (about 2 µm width of most scratches). No different structural phases are identified, and domains are not observed.
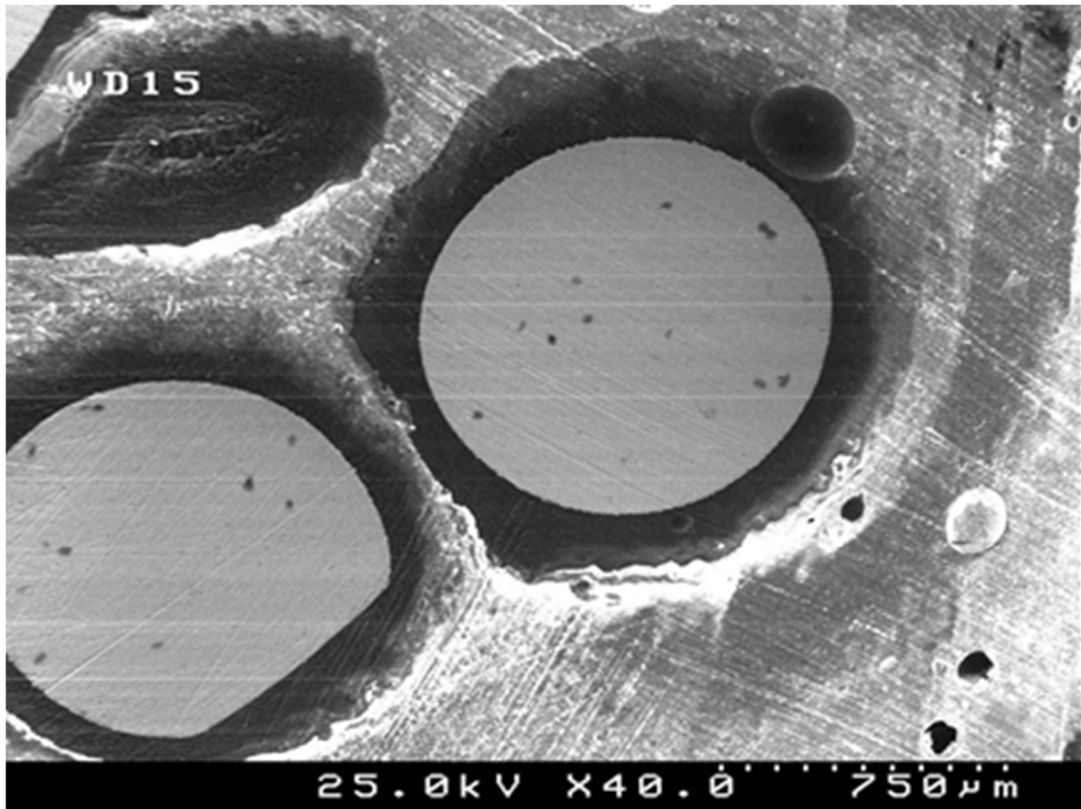
Fig. 5.76 - SEM images of the NiTi_2 sample at where the sections of two wires and the resin can be seen.
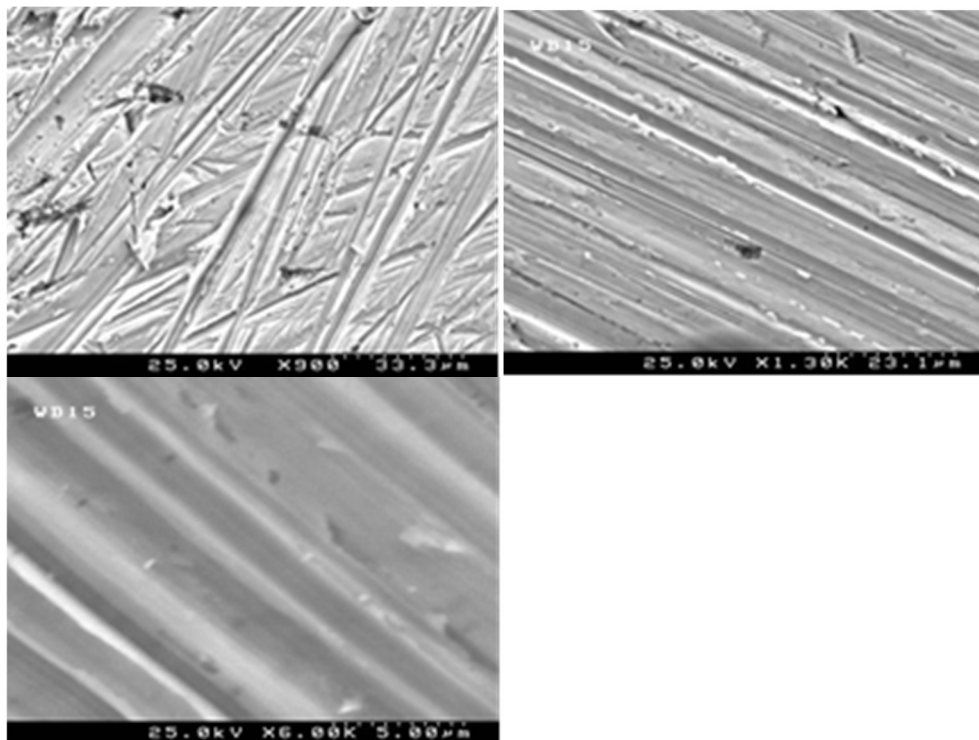
Fig. 5.77 - SEM images of the surface of the wires on sample NiTi_2 at different scales.

5.3.2.2 – AFM

Topography scans were performed on sample NiTi_2. The measurements were performed with a PARK XE7 atomic force microscope, in contact mode, with CONTR probes [149]. Figs. 5.78 and 5.80 show scans of 8x8 μm^2 and 4x4 μm^2 areas of the sections of the NiTi wires, respectively. The roughness average (r_a, determined by the XEI software) of the 8x8 μm^2 area is 281 nm and that of the 4x4 μm^2 area is 66 nm.

Fig. 5.79 shows a scratch from polishing with 1.6 μm width and 0.4 μm depth and a line profile of a section. Fig. 5.80 also shows a line profile of a section of a scratch. The results are consistent with what was observed on the SEM images.
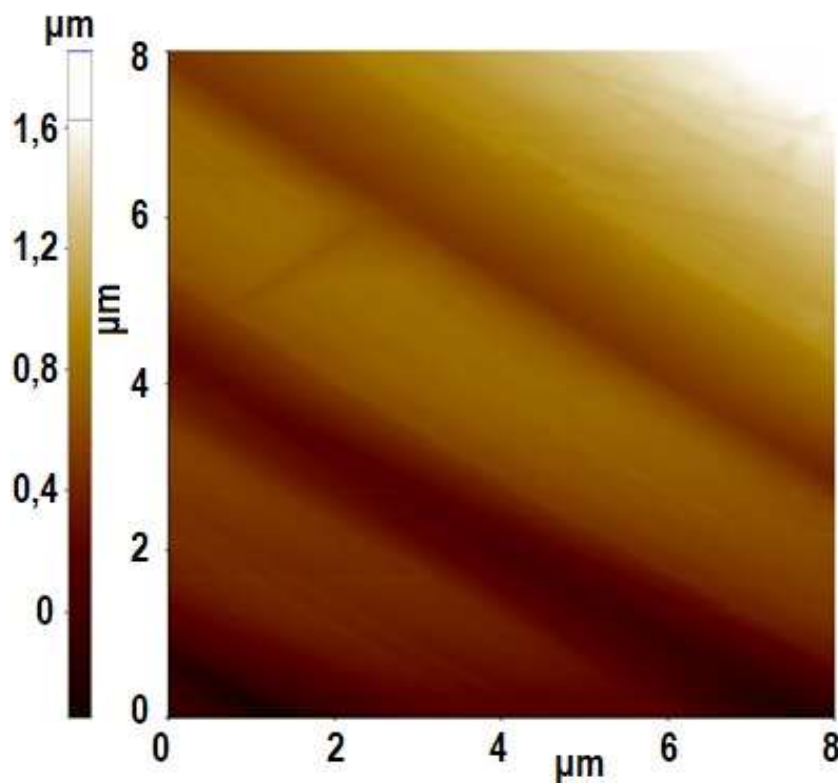
Fig. 5.78 - Topography scan of an 8x8 μm^2 area of one of the wires of the NiTi_2 sample surface.
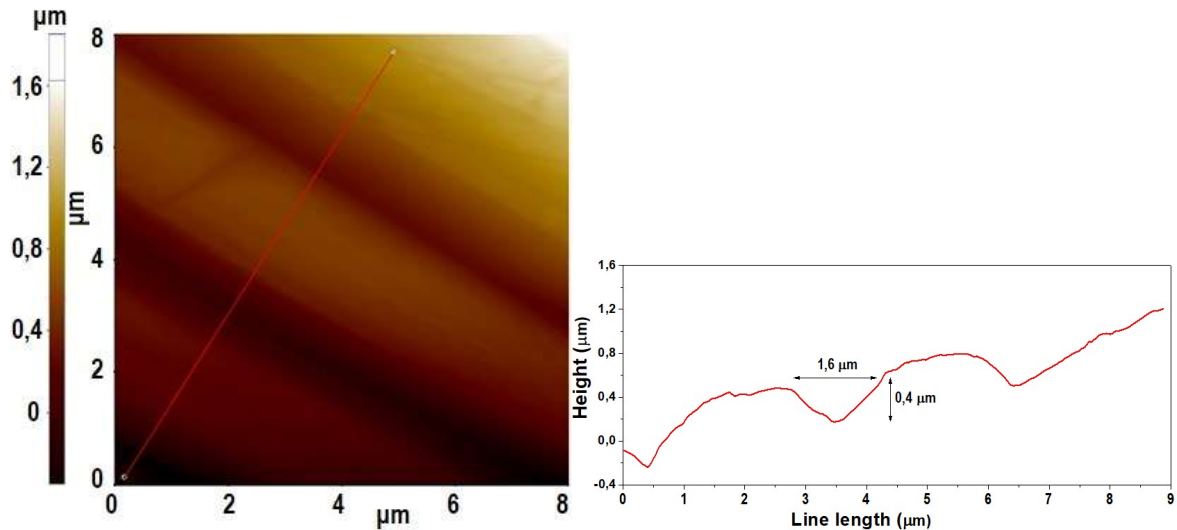
Fig. 5.79 - Line profile of a topography scan of an 8x8 μm^2 area of one of the wires of the NiTi_2 sample surface.
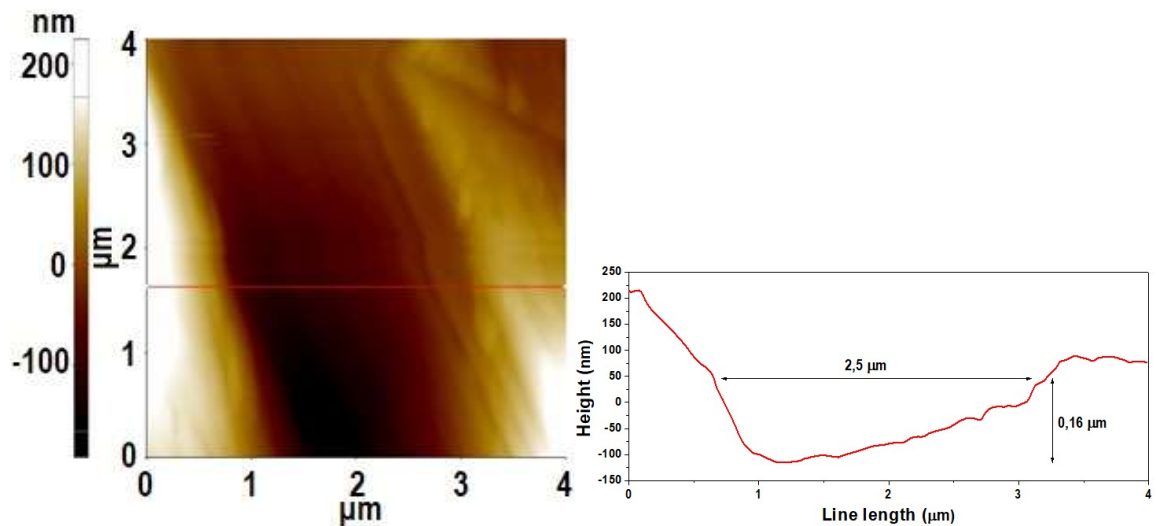
Fig. 5.80 - Line profile of a topography scan of an 4x4 μm^2 area of one of the wires of the NiTi_2 sample surface.

5.3.2.3 – EDS

These measurements were performed at the Materials Department at the University of Aveiro with the Hitachi SU-70 SEM equipment (described in chapter 2). Four different areas of a NiTi wire as acquired were analyzed and a representative result is shown in Fig. 5.81. Table 5.9 shows the atomic percentages for Ni and Ti

for the four different areas, which agree within errors. The average value of these results gives us a composition of $Ni_{50.32}Ti_{49.68}$ with an uncertainty of 0.58.

Table 5.9 - Composition for four different areas analyzed on sample NiTi_1

Area 1	$Ni_{50,61}Ti_{49,39}$
Area 2	$Ni_{50,05}Ti_{49,95}$
Area 2	$Ni_{50,86}Ti_{49,14}$
Area 3	$Ni_{49,74}Ti_{50,26}$


```
1.spx Date:22-11-2019 15:23:49     HV:15.0kV    Puls th.:3.01kcps

Spectrum: 1.spx

Element   Series  unn. C norm. C Atom. C Error (3 Sigma)
                  [wt.%]  [wt.%]  [at.%]         [wt.%]
-------------------------------------------------------
Nickel    K-series 49.33  55.68   50.61          4.82
Titanium  K-series 39.27  44.32   49.39          3.55
-------------------------------------------------------
          Total:   88.60 100.00  100.00
```
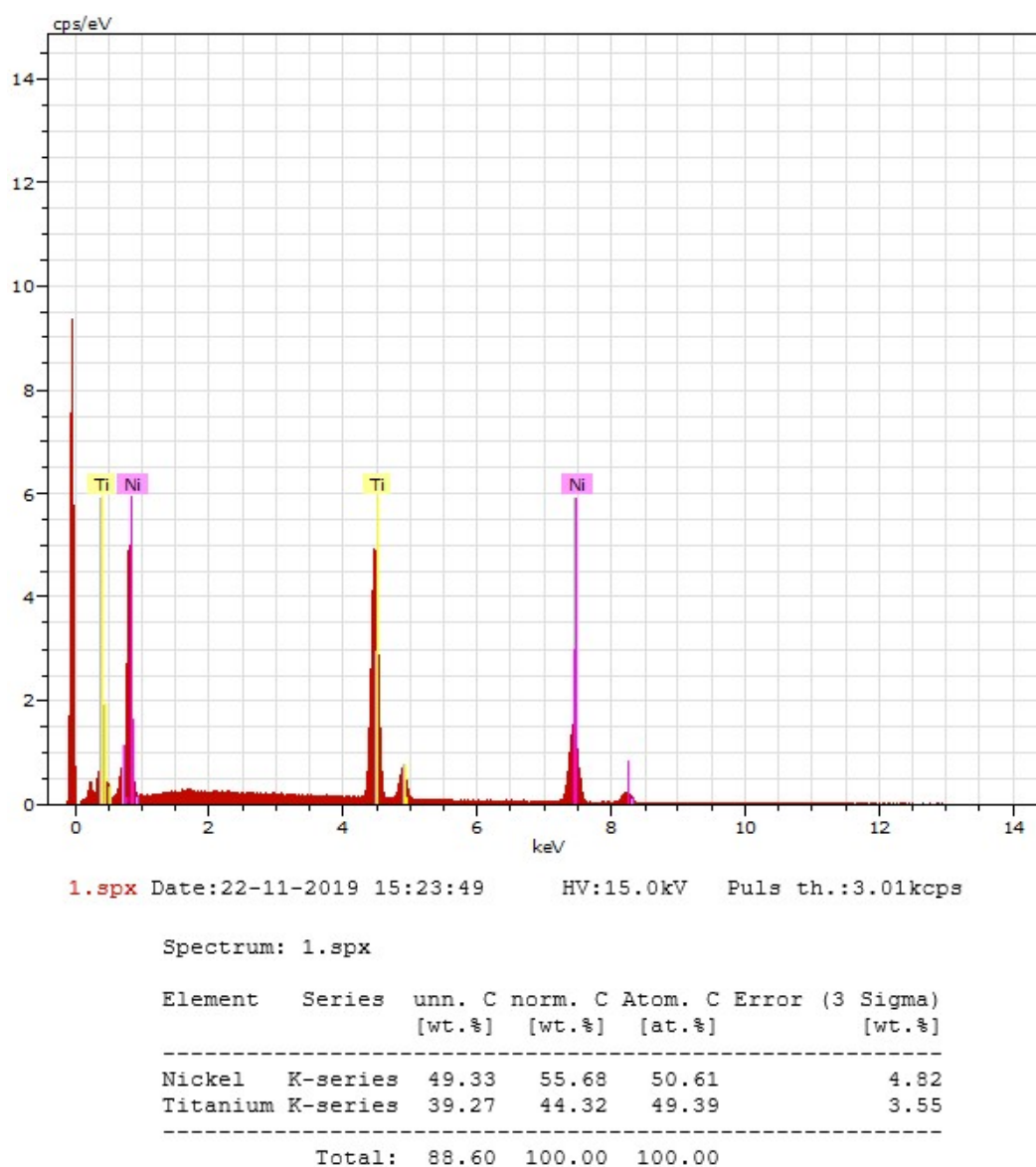
Fig. 5.81 - Representative EDS Spectrum of one area of sample NiTi_1.

5.3.2.4 – Thermally induced structural transformation in NiTi

Sample NiTi_1 was placed on the surface of a Peltier element using high thermal conductivity silicon paste for good thermal contact. The Peltier element was connected to a power source so that its temperature could be varied. A K type thermocouple, connected to a Lakeshore 325 temperature controller (acting merely as a reader for the thermocouple), was placed on the Peltier's surface. While the sample was being heated (by manually operating the power source feeding the Peltier), the structural transformation could be directly observed, and the temperatures for which any change in the shape of the material occurred were read by the temperature controller. Fig. 5. 82 shows an image of the setup described above. Fig. 5. 83 shows images of the state of the sample before and after the transformation. Images of the sample while the transformation is occurring, and the corresponding temperatures, are presented on Table 5.10. These images are snapshots from the video in which the experiment is recorded.

Fig. 5.82 - Setup designed to thermally induced the structural transformation in sample NiTi_1.
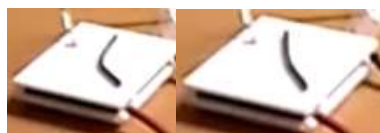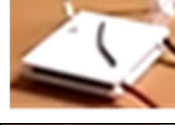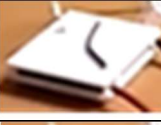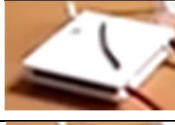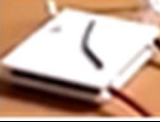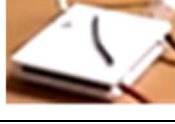
Fig. 5.83 - NiTi_1 sample before the structural transformation (left) and after the structural transformation (right).

Table 5.10 - Evolution of sample NiTi_1 shape with increasing temperature

$T_{Peltier}$ (ºC)	Sample NiTi_1	$T_{Peltier}$ (ºC)	Sample NiTi_1
35.87		40.09	
37.53		40.41	
38.16		40.71	
39.09		40.87	
39.72		40.94	

It is clear from the images on Table 5.10 that, for lower temperatures of the Peltier element (and hence the sample), the wire is bent in two different directions. One of the directions, as temperature rises, varies considerably. We have established a method to quantify that variation with temperature, by measuring the value X, marked in Fig. 5.84. We have established a straight line in the direction of the "fixated" direction (black dotted line) and then used an L shape (forming a 90º angle) which allows us to place one of its sides along the dotted arrow and the perpendicular side reaching the extremity of the portion of wire which changes direction with temperature. The perpendicular distance between this point and the dotted line is the value X, which we used to quantify the change in direction with temperature. The blue L shape was adjusted along the black dotted line and to reach the extremity of the wire by the user. The dimensions of the L shape were provided in the section "shape properties", subsection "size-width" by the software Powerpoint from Microsoft, where this operation was performed. To make sure that the scale of the image was the same for all temperatures, a blue line (Fig.5.84, right) with constant length was made sure to fit the same edge of the Peltier element. The

results for these measurements of X vs $T_{Peltier}$ can be seen in Fig. 5.85. The plot shows that a dramatic change in the shape of the material occurs for a quite narrow interval of temperature, starting at 39.1 ºC and ending at 40.9 ºC. The derivative dX/dT signals the transformation occurring at 40.1 ºC.
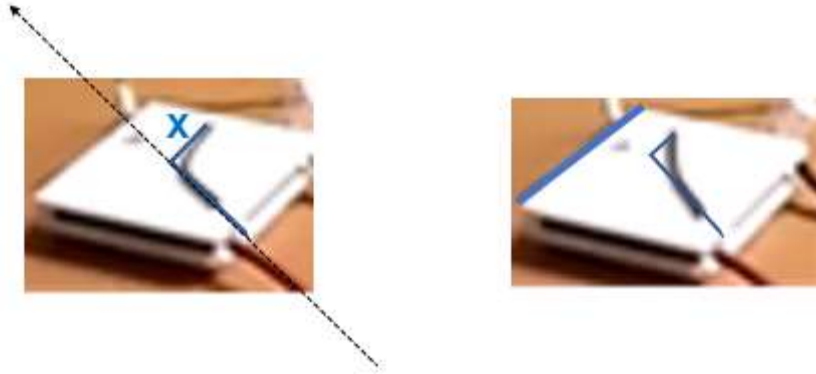
Fig. 5.84 - Schematics of the method used to measure the value X, in this case using the images when the Peltier element is at 35.87 ºC (left) and 40.94 ºC (right).
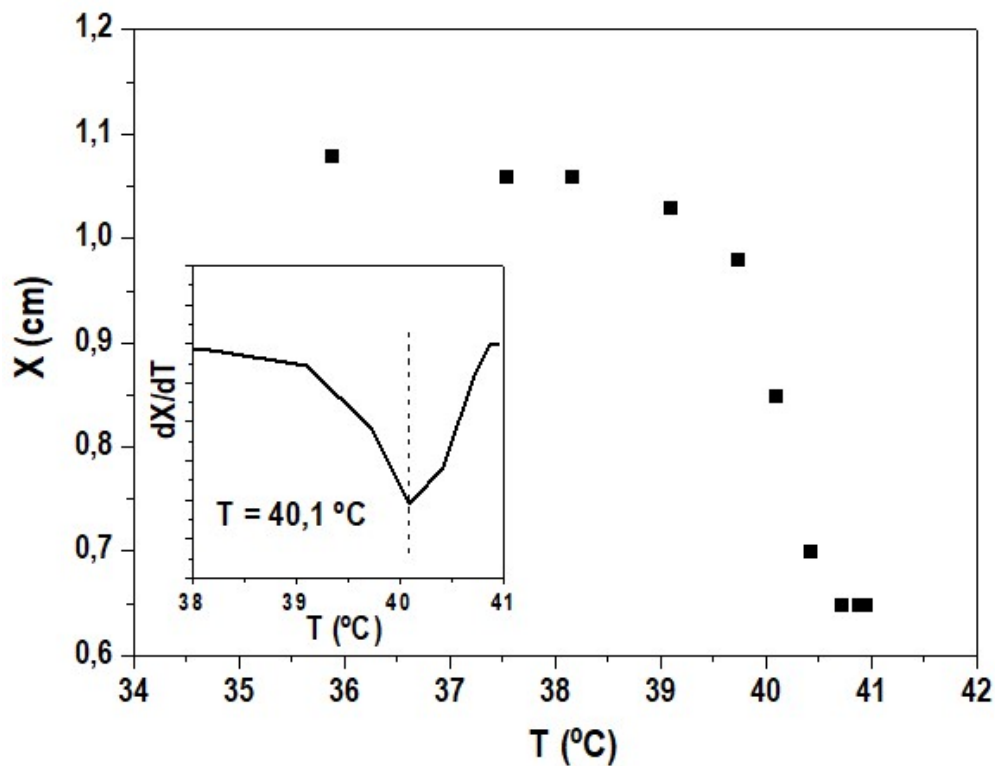
Fig. 5.85 - Plot showing the dependence of X on temperature of the Peltier element.

5.3.2.5 – Electrical Resistivity

Sample NiTi_1 was fixed to the copper sample holder of the closed cycle cryostat with GE varnish (Fig. 5.86). The GE varnish was also used to attach a thermocouple to the sample. In this way, the sample is partially constrained by the GE varnish and is not completely free to move. All measurements took place in an atmosphere of $7x10^{-3}$ mbar and with a temperature variation rate of 5 K/min.

The electrical resistivity was measured for two thermal cycles performed on sample NiTi_1 on the setup and with the method described on chapter 2. The results are presented in Fig. 5.87.

Fig. 5.86 - Sample holder with sample NiTi_1 mounted for resistivity measurements.

These cycles were performed starting from 300 K up to 330 K, then down to 200 K and up to 300 K again. There is a considerably large thermal hysteresis. The first cooling sequence shows some noise due to instability in the system, which ceases to exist in subsequent measurements. The structural transformation happens from 290 K to 300 K, and from 253 K to 240 K, in heating and cooling, respectively.

In literature we find that subsequent thermal cycles tend to induce defects (mainly dislocations) in NiTi, promoting an intermediate rhombohedral phase (R-phase) between the martensitic and austenitic phases [165] which is usually absent

in the first few cycles. The presence of the R-phase can be detected in resistivity vs temperature curves by identifying a cap on the resistivity peaks observed during the transformation [166]. The fraction of R-phase is indicated by the height of the resistivity transformation peak, which increases with the number of cycles until a stable value, when a limit for the formation of defects is reached.
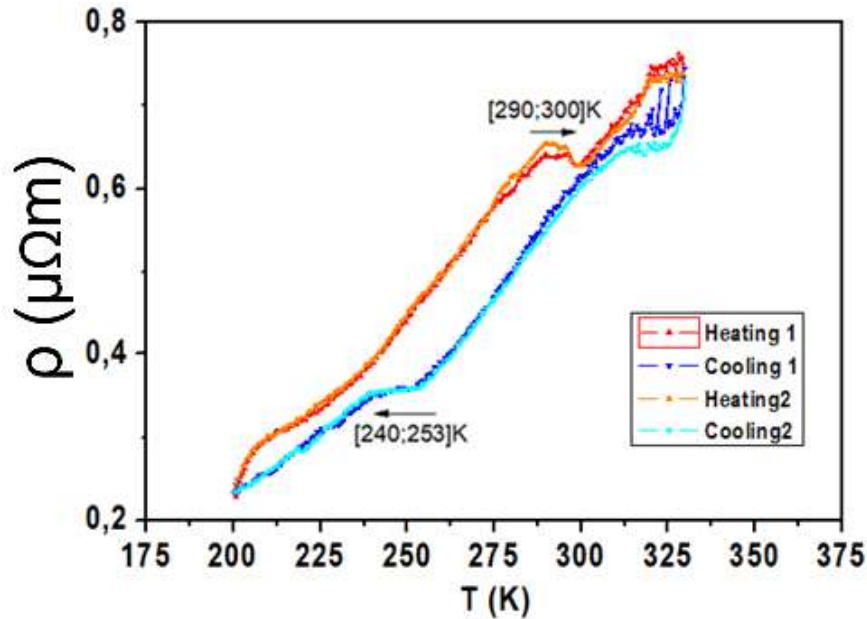
Fig. 5.87 - Resistivity vs temperature for sample NiTi_1 measured for two thermal cycles from 300 K to 330 K, then to 200 K and back to 300 K.

The effect of thermal cycling on the electrical resistivity (ρ) of the sample was studied for different temperature intervals (T_{max}- T_{min}).

Figs. 5.88 to 5.94 show different resistivity vs temperature cycles performed on the sample, with different T_{max} and T_{min} limits, and in the order in which they were performed. The measurements can be separated in distinct groups according to specific parameters varied and this is organized in Table 5.11.

The different cycle sequences were programmed mainly to assess the effect that successively increasing and decreasing T_{max} - T_{min} had on the resistivity of the sample. Another parameter tested was the direction in which the cycle started: heating taking place first vs cooling taking place first.

All electrical resistivity measurements show thermal hysteresis, which is expected for shape memory alloys, as previously discussed in section 5.2.3.

In Group I, Fig. 5.88 shows the minor cycles, I-A and I-B. In this group of measurements, we observe that only for cycle I-C we begin to observe an increase and a very subtle decrease in ρ as temperature increases and decreases, respectively. Such events are characteristic of the occurrence of a phase transformation in the material. As T_{max} - T_{min} increases (cycles I-D and I-E), the number of such events increases. Cycle I-F shows improvement in the reproducibility of the events when the cycle is repeated.

Measurements gathered in Group II do not indicate that starting the cycles by cooling the sample (instead of heating it, as in Group I) has any particular effect on the behavior of the sample's resistivity. The events already observed in Group I begin to show for cycle II-C. Here, as T_{max} - T_{min} increases (cycles II-D and II-E), the number of events increases and its reproducibility improves (as well as the overall reproducibility of ρ), as observed in Group I.

Group III (Fig. 5. 90) consists solely of a repetition of the last cycle (same T_{max} - T_{min} and measurement conditions) performed in Group II (Fig. 5.89, cycle II-E). Such repetition reinforces the reproducibility of the behavior of the electrical resistivity.

In Group IV (Fig. 5.91), no different observations form the ones already mentioned for the previous groups were made, except that from cycle IV-G to cycle IV-H, the number of events remained constant, with increased overall reproducibility of ρ.

In Groups V and VI (Figs. 5.92 and 5.93, respectively), all measurements exhibit the expected behavior given all measurements and corresponding considerations made for the preceding groups. Reproducibility arises from repeated cycling with large T_{max} - T_{min} intervals, after which changing T_{max} - T_{min} of the cycle seems to have no significant impact on the behavior of ρ.

In Group VII (Fig. 5. 115), five cycles with T_{max} - T_{min} = 450 K – 300 K are shown. Apart from the fact that, after the second cycle, an event occurring just before T ~ 350 K in heating ceases to be observed, ρ's behavior is fairly reproducible.

As a final note, some of the events observed occur in such a sudden way that seem somewhat relatable to those referred to in section 5.2.3, where avalanche effects were discussed. A few examples of such events are as follows: cycle I-D (cooling 1, T ~ 300 K; cooling 2, T ~ 312 K), cycle I-E (cooling 1, T ~ 250 K and 270 K; cooling 2, T ~ 275 K), cycle I-F (cooling 1, T ~ 250 K; cooling 2, T ~ 260 K), and Group VII (heating, T ~ 360 K).

Table 5.11 - Sets of electrical resistivity measurements performed on sample NiTi_1

Group			Cycle	Temperature path of the cycle (K)	Fig.
I	Heating 1st, cooling 2nd	Successively increasing T_{max} and decreasing T_{min} of cycles	I-A	300 – 310 – 300 – 310 - 300	5.88
			I-B	300 - 310 - 290 - 310 - 290 - 300	
			I-C	300 – 325 – 275 – 325 – 275 - 300	
			I-D	300 – 350 – 250 – 350 – 250 - 300	
			I-E	300 – 375 -225 – 375 – 225 - 300	
			I-F	300 - 400 - 200 - 400 – 200 - 300	
II	Cooling 1st, heating 2nd (except minor cycles)	Successively decreasing T_{min} and increasing T_{max} of cycles	II-A	300 – 310 – 300 – 310 - 300	5.89
			II-B	300 - 310 - 290 - 310 - 290 - 300	
			II-C	300 – 250 – 350 – 250 – 350 - 300	
			II-D	300 - 200 - 400 - 200 - 400 - 300	
			II-E	300 - 450 - 150 - 450 - 150 - 300	
III	Heating 1st, cooling 2nd	N/A	III	300 - 450 - 150 - 450 - 150 - 300	5.90
IV	Heating 1st, cooling 2nd	Successively increasing T_{max} and decreasing T_{min} of cycles	IV-A	300 – 310 – 300 – 310 - 300	5.91
			IV-B	300 - 310 - 290 - 310 - 290 - 300	
			IV-C	300 – 325 – 275 – 325 – 275 - 300	
			IV-D	300-350-250-350-250-350-250-350	
			IV-E	300 – 375 -225 – 375 – 225 - 300	
			IV-F	300 - 400 - 200 - 400 - 200- 300	
			IV-G	300 – 425 -175 – 425 – 175 - 300	
			IV-H	300 - 450 - 150 - 450 - 150 - 300	
V	Cooling 1st, heating 2nd	Successively increasing T_{min} and decreasing T_{max} of cycles	V-A	300 – 150 - 450 - 150 - 450 - 300	5.92
			V-B	300 – 175 – 425 – 175 – 425 - 300	
			V-C	300 - 200 - 400 - 200 - 400 - 300	
			V-D	300 – 250 - 350 – 250 – 350 - 300	
VI	Cooling 1st, heating 2nd	Successively increasing T_{max} and decreasing T_{min} of cycles	VI-A	300 - 200 - 400 - 200 - 400 - 300	5.93
			VI-B	300 – 175 – 425 – 175 – 425 - 300	
			VI-C	300 – 150 - 450 - 150 - 450 - 300	
VII	Heating 1st, cooling 2nd	N/A	1st to 5th	300 - 450 - 350	5.94

GROUP I
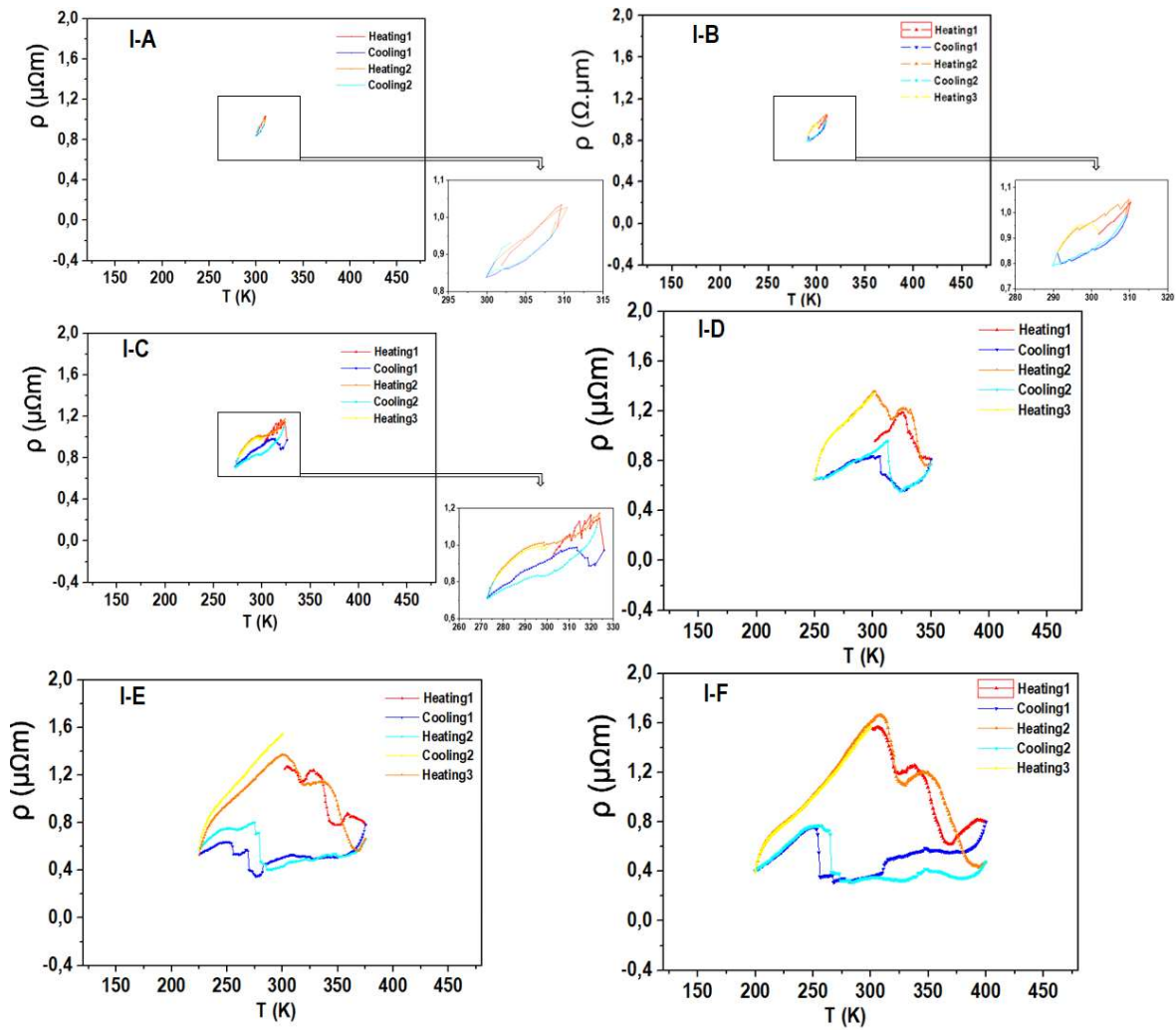
Fig. 5.88 – Cycles performed in Group I: starting cycle by heating the sample; successively increasing cycle temperature range (details on Table 5.11).
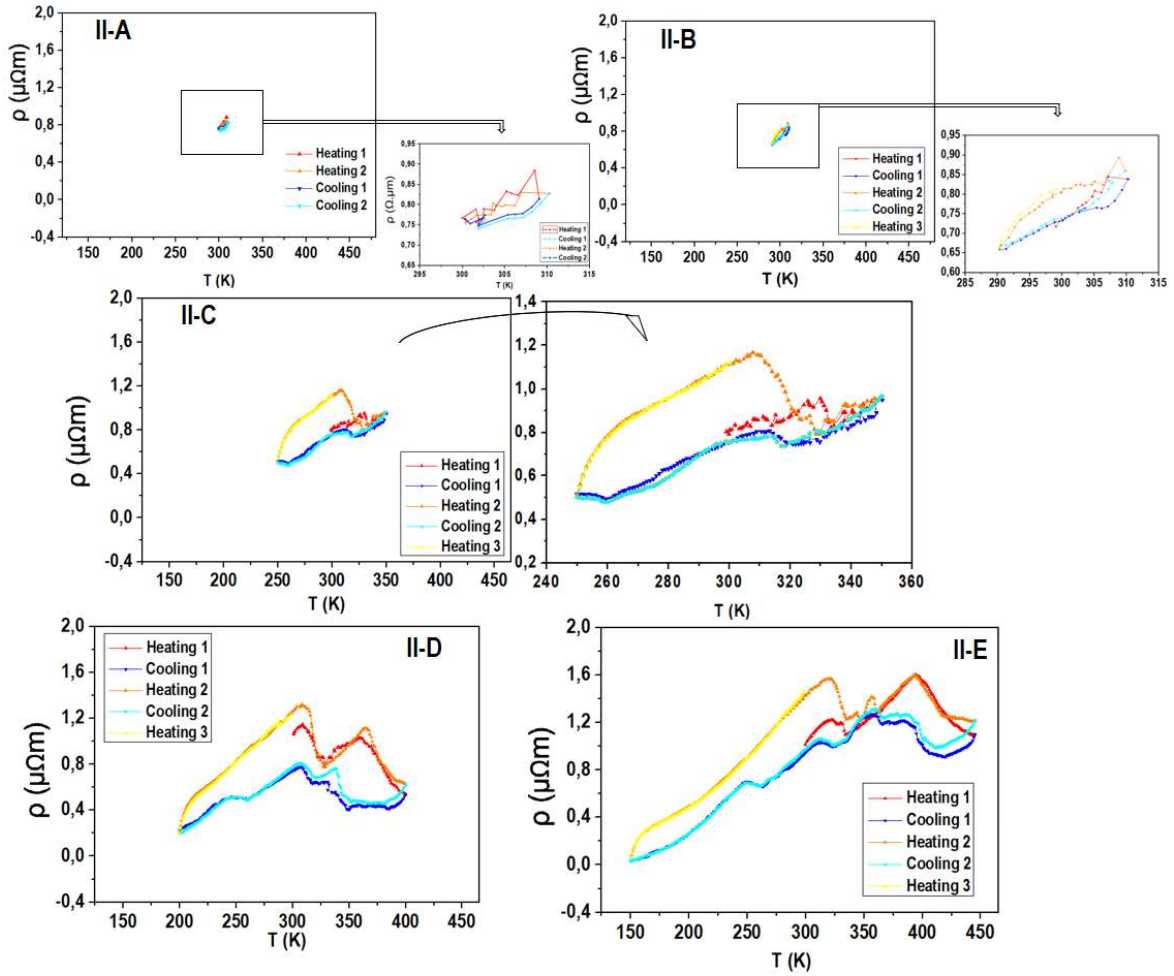
GROUP II

Fig. 5.89 – Cycles performed in Group II: starting cycle by cooling the sample; successively decreasing cycle temperature range (details on Table 5.11).

GROUP III
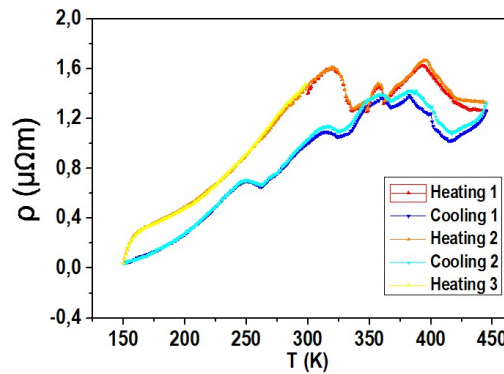
Fig. 5.90 – Cycle performed in Group III: starting from 300 K to 450 K, then to 150 K and back to 300 K. Cycle repeated.

GROUP IV
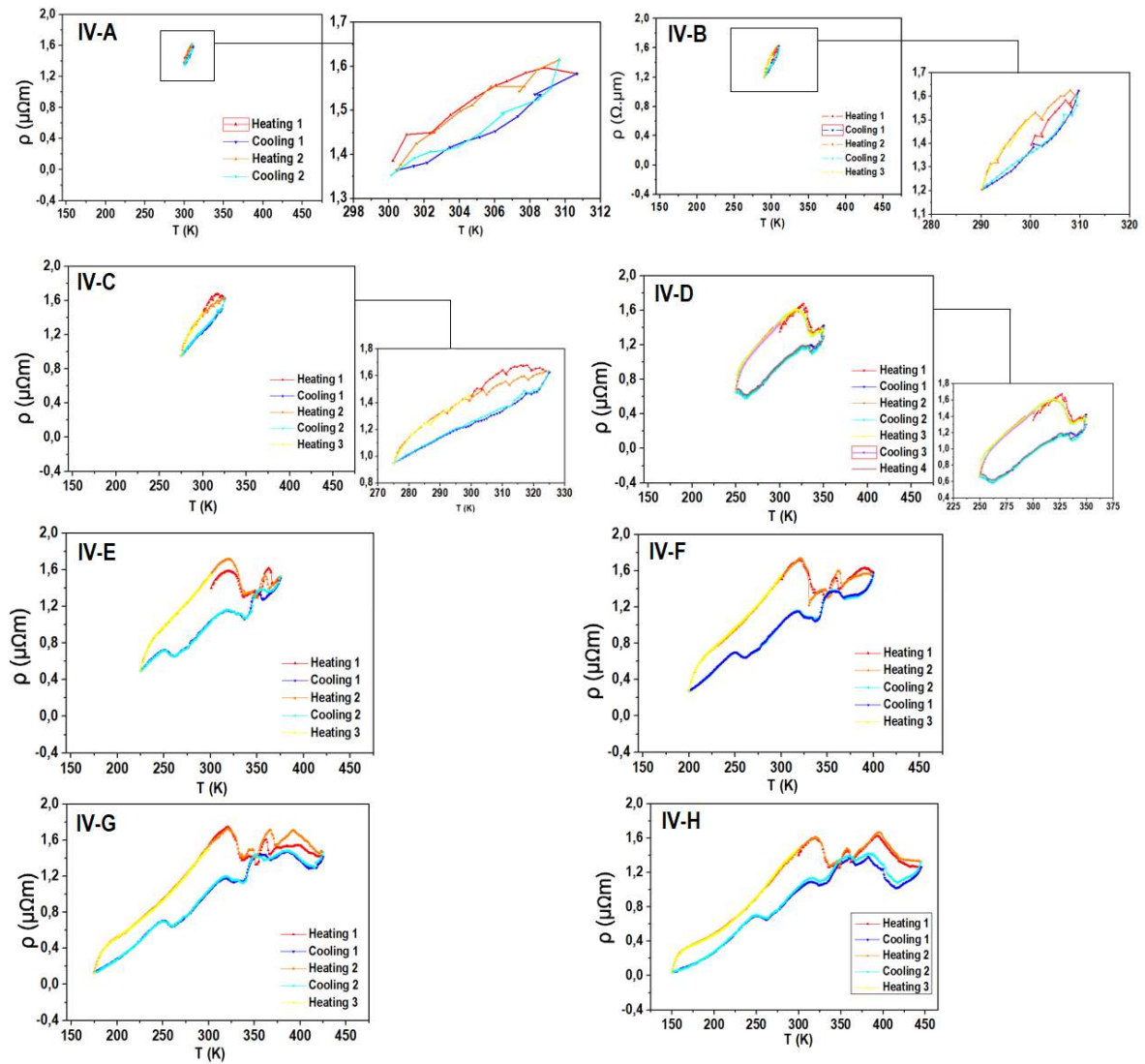
Fig. 5.91 - Cycles performed in Group I: starting cycle by heating the sample; successively increasing cycle temperature range (details on Table 5.11).
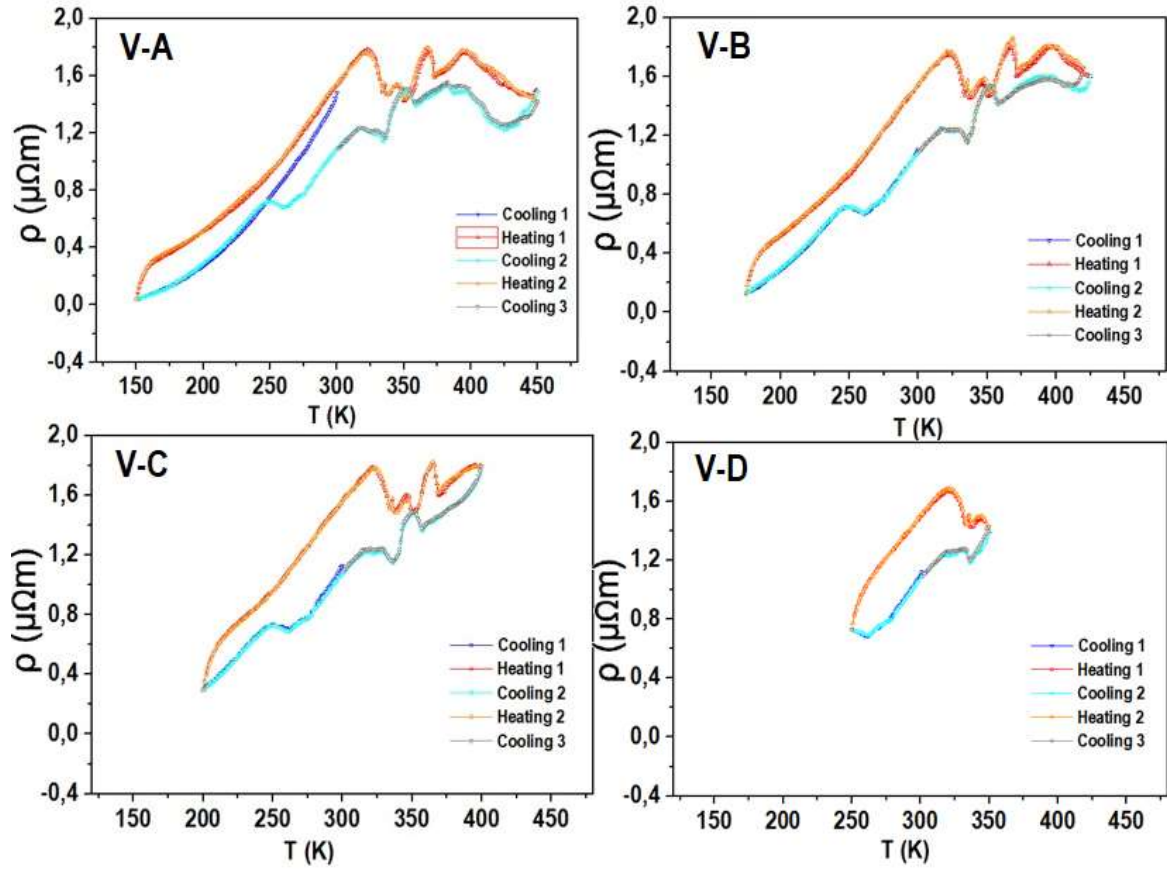
GROUP V

Fig. 5.92 - Cycles performed in Group V: starting cycle by cooling the sample; successively increasing and decreasing cycle temperature range (details on Table 5.11).
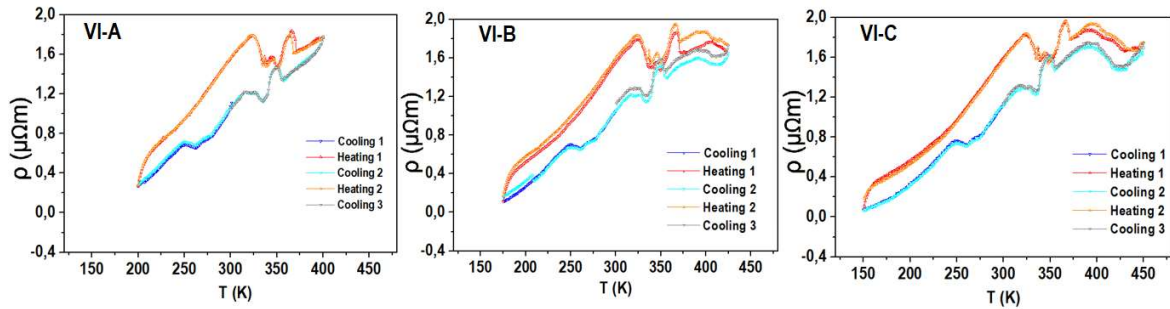
GROUP VI

Fig. 5.93 - Cycles performed in Group VI: starting cycle by cooling the sample; successively increasing and decreasing cycle temperature range (details on Table 5.11).

GROUP VII
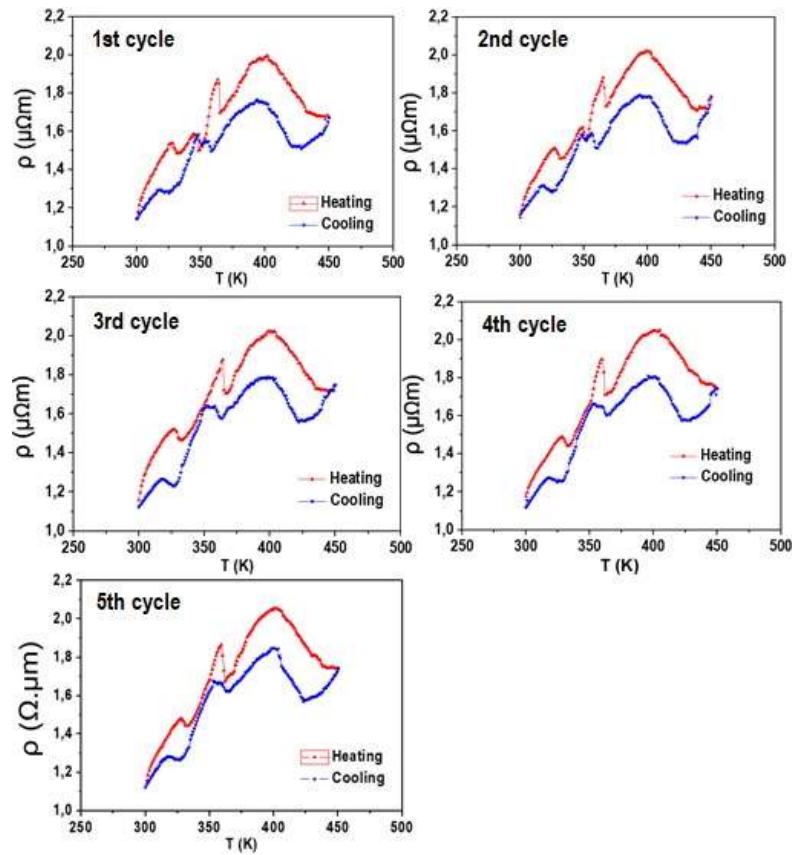
Fig. 5.94 - Cycles performed in Group VII: five consecutive cycles from 300 K to 450 K and back to 300 K.

5.3.2.6 – XRD

Two samples were analyzed by XRD at the Materials Department at University of Aveiro (equipment described on chapter 2): a piece of as acquired wire with the coating removed, sample NiTi_XRD, and the previously mentioned sample NiTi_1, used in the resistivity measurements, thus already thermally cycled. Both samples are 0,15 m long.

NiTi_XRD and NiTi_1 were scanned at room temperature (Figs. 5.95 and 5.96, respectively) over a 2theta range of 10° and 15º, respectively, to 80°. Sample NiTi_XRD was only measured at room temperature. Diffractograms were taken at different temperatures (from room temperature to 147 ºC) for the thermally cycled wire (NiTi_1) (Fig. 5.97).

For NiTi_XRD, measurement parameters were as follows: divergence slit fixed 1/8, no monochromator was used, scan step size was 0.026° and scan step time was 96,39 s. For NiTi_1, measurement parameters were as follows: divergence lit fixed 1/4, a monochromator was used, scan step size was 0.026° and scan step time was 1197 s.

The diffractogram taken at room temperature for NiTi_XRD (Fig. 5.95) shows a predominance of the martensitic phase, with the presence of the austenitic phase manifesting in the peaks 42,4° (1 1 0) , 61,5° (2 0 0) and 77,6° (2 1 1) [167]. The diffractogram taken at room temperature for NiTi_1 (Fig. 5.96) also shows a predominance of the martensitic phase, with the presence of the austenitic phase manifesting the same three peaks previously mentioned. In NiTi_1, at room temperature, some of the martensitic peaks observed in NiTi_XRD are present ((0 1 1), (0 2 0) and (-1 2 0)), but others do not appear ((0 2 1), (0 1 2) and (-1 1 2)) [168]. Three new martensitic peaks appear in this diffractogram: (1 0 0), (1 0 1) and (0 0 2). For 2θ between 30° and 40° there are a set of small peaks which do not belong either to the austenitic or the martensitic phase of NiTi.

From before thermal cycling (sample NiTi_XRD) to after thermal cycling (sample NiTi_1), the difference consists in a better definition on the latter diffractogram due to higher exposure time and the use of a monochromator, so the only peak we would venture to say that isn't in the uncycled wire is the one around 67,4°, which however we haven't been able to identify as belonging to either austenitic or martensitic phase.

With increasing temperature, austenite does not become dominant over the martensitic phase in the thermally cycled wire.

The plots for NiTi_1 at different temperatures (Fig. 5.97) suggest no observable structural alterations as temperature increases, at least with the parameters used in these measurements.
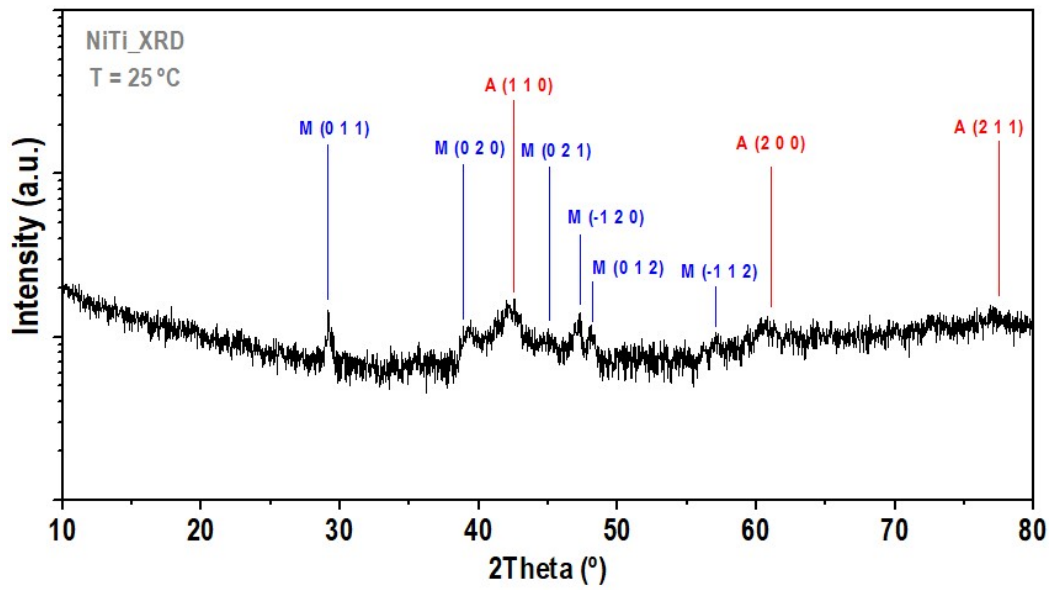
Fig. 5.95 - XRD diffractogram taken at 25 °C for NiTi_XRD (wire as acquired, without thermal cycling) with peaks corresponding to both phases identified.
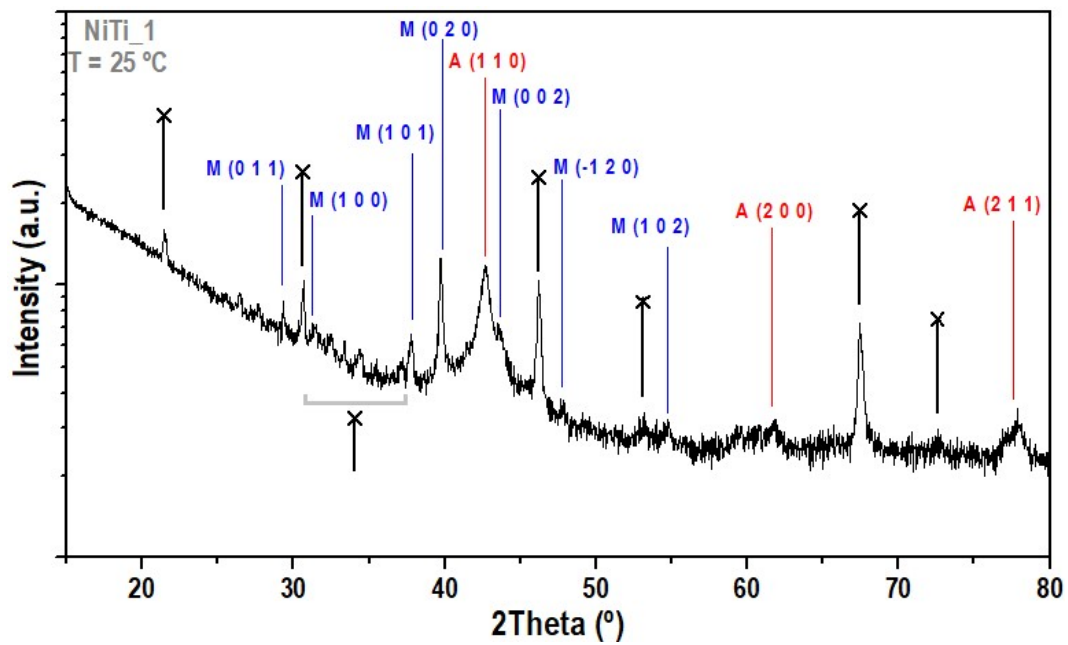
Fig. 5.96 - XRD diffractogram taken at 25 °C for sample NiTi_1 (after thermal cycling) with peaks corresponding to both phases identified.
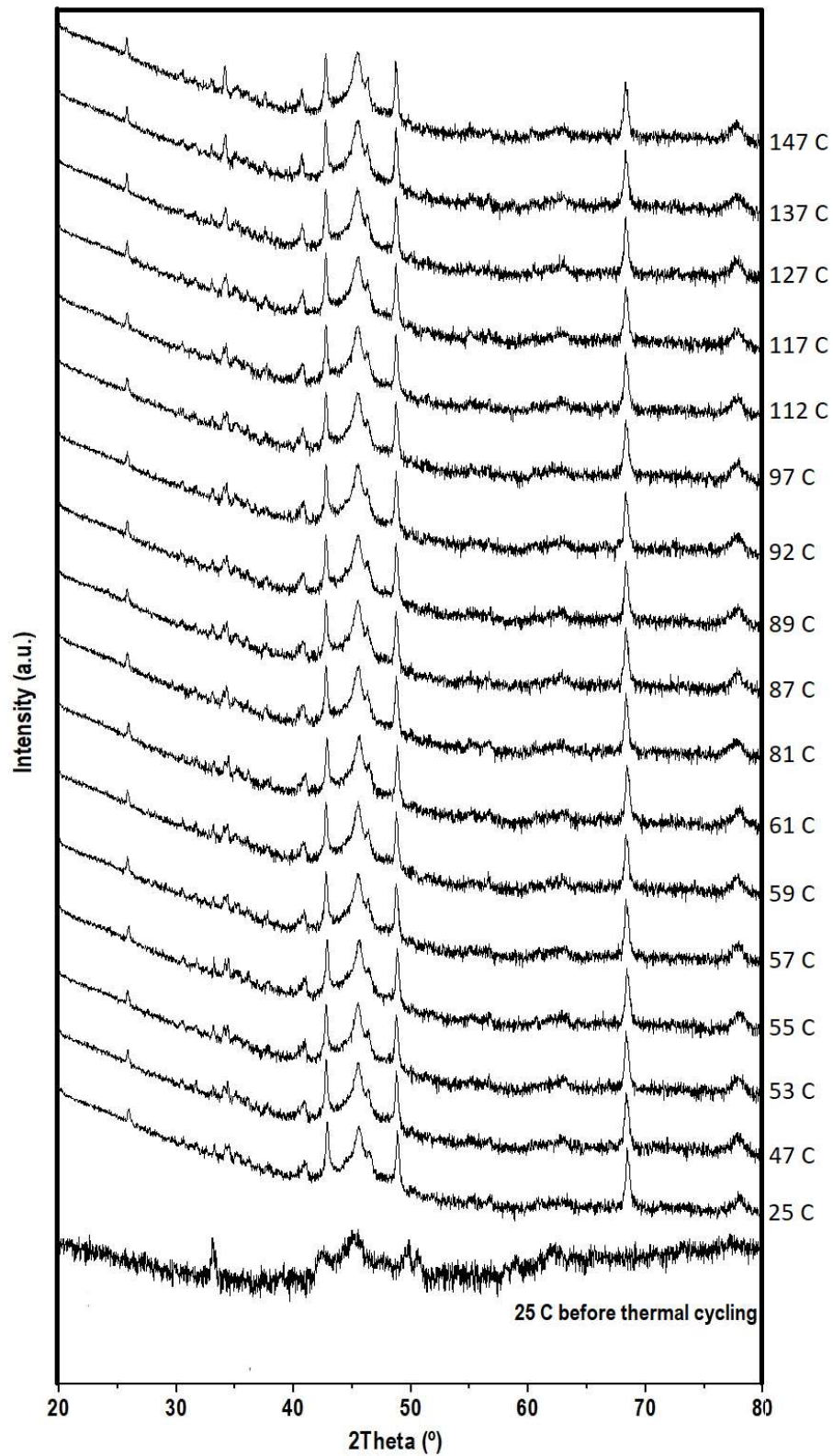
Fig. 5.97 - XRD diffractograms for different temperatures for NiTi_XRD (wire as acquired, without thermal cycling) at 25 ºC and sample NiTi_1 (after thermal cycling) at different temperatures.

Fig. 5.98 shows a comparison between the diffractograms for sample NiTi_1 at 25 °C and 47 °C, temperatures between which the structural transformation was expected to occur from the reported experiments. The phase transformation would likely bring a change in the peaks observed, with a predominance of austenite over martensite, which does not appear.
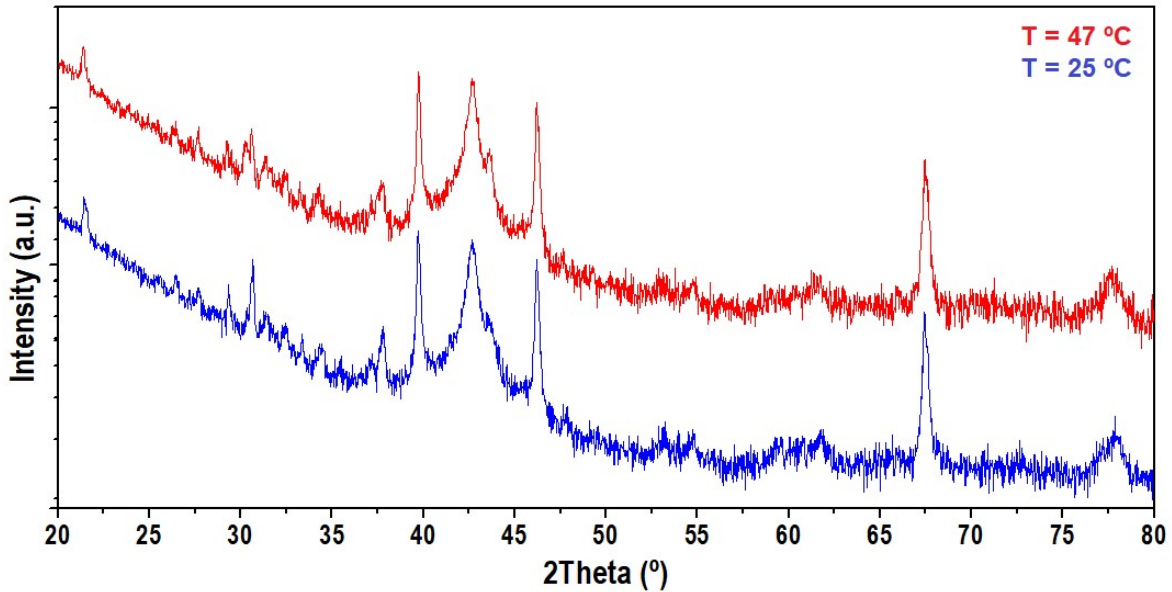
Fig. 5.98 - XRD diffractograms for sample NiTi_1 at 25 °C and 47 °C, temperatures between which the structural transformation was expected to occur.

In literature, XRD analysis on orthodontic wires have shown, at 25 °C, peaks corresponding to the rhombohedral phase ($(1\ 1\ 2)_R$ and $(3\ 0\ 0)_R$ for $2\theta \sim 40°$, near the $(1\ 1\ 0)_A$ peak. Two rhombohedral phase peaks ($(4\ 1\ 2)_R$ $(3\ 3\ 0)_R$) also appear $2\theta \sim 77°$ (where we find the $(2\ 1\ 1)_A$ peak) [169].

The effect of bending of those wires is also reported, with, at 25 °C, the not bending wire showing the $2\theta \sim 40°$ $(1\ 1\ 0)_A$ peak and for higher values of 2θ showing the reflections from austenitic atomic planes: $(2\ 0\ 0)_A$, $(2\ 1\ 1)_A$, $(2\ 2\ 0)_A$ and $(3\ 1\ 0)_A$. A bending of 135° on the wire removes the presence of the reflections of the austenitic atomic planes for higher values of 2θ and, while maintaining the presence of the $2\theta \sim 40°$ $(1\ 1\ 0)_A$ peak, adds three martensitic phase peaks in its vicinity: $((1\ -1\ 1)_M$, $(0\ 0\ 2)_M$ and $(1\ 1\ 1)_M)$ [169]. A discussion on the stable structure of the

155

austenitic phase in NiTi takes place on an article from 2014 [170], comparing the diffraction patterns of the calculated spectrum of the ideal B2 phase and a proposed stable austenitic phase for NiTi (Fig. 5.99). The authors claim that there is experimental evidence that NiTi austenitic structure deviates from the ideal B2, so accurately determining the structure of austenite is a priority to understand NiTi phase stability and its transformations.
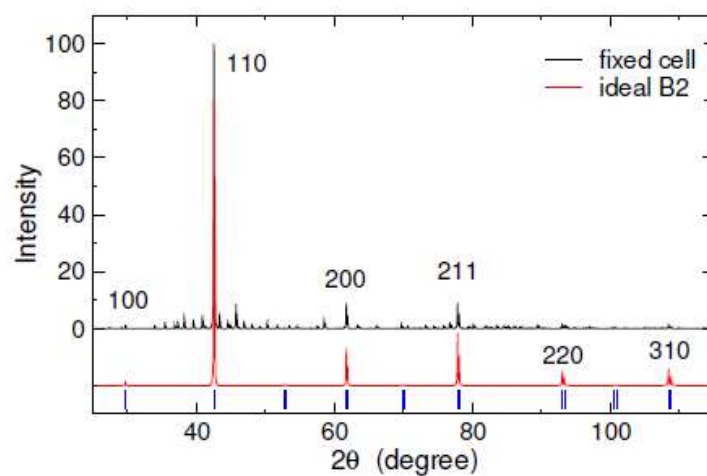
Fig. 5.99 - Simulated XRD spectrum of the proposed austenite structure (black) compared to ideal B2 (red). [170].

5.3.2.7 – MAGNETIC MEASUREMENTS

The magnetic measurements presented in this section were performed on a NiTi_35 sample with the same characteristics of sample NiTi_1 before it was subjected to the thermal cycling performed during the electrical resistivity measurements. All magnetic measurements were performed with the SQUID magnetometer described in chapter 2. Paramagnetic behavior is observed for all temperatures. The M(H) measurements were performed after the M(T) cycles which will subsequently be presented.
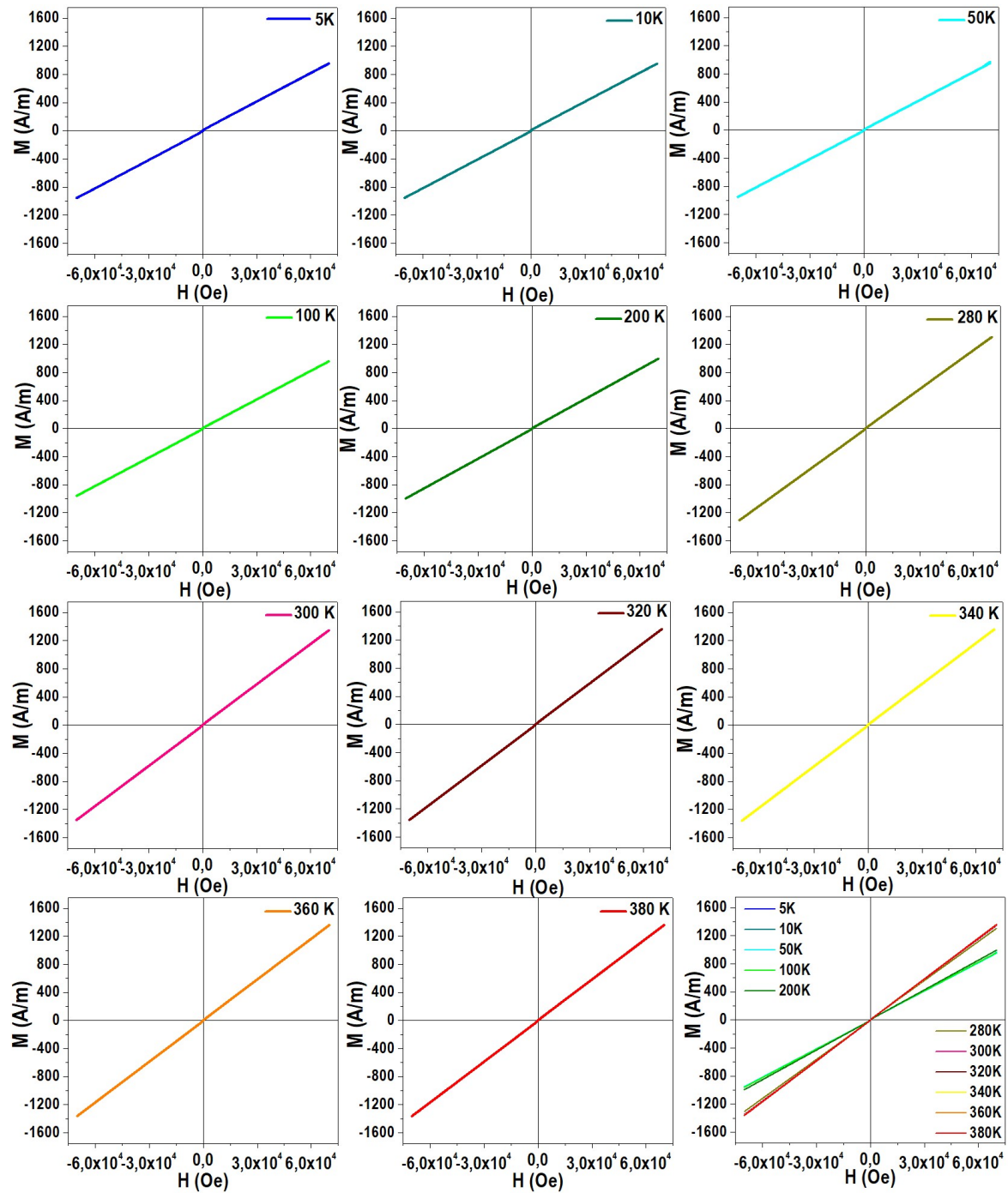
Fig. 5.100 - M vs H hysteresis loops for different temperatures for the NiTi_35 sample, with H ranging from -70000 Oe to 70000 Oe.

Fig. 5.101 shows several magnetization vs temperature curves presenting different temperature cycles performed on the NiTi_35 sample, in the order in which they were performed, at a 1.5 K/min rate. On heating, the reverse martensitic transformation occurs at 295 K, and on cooling, we observe two transformations occurring at 287 K and 246 K.
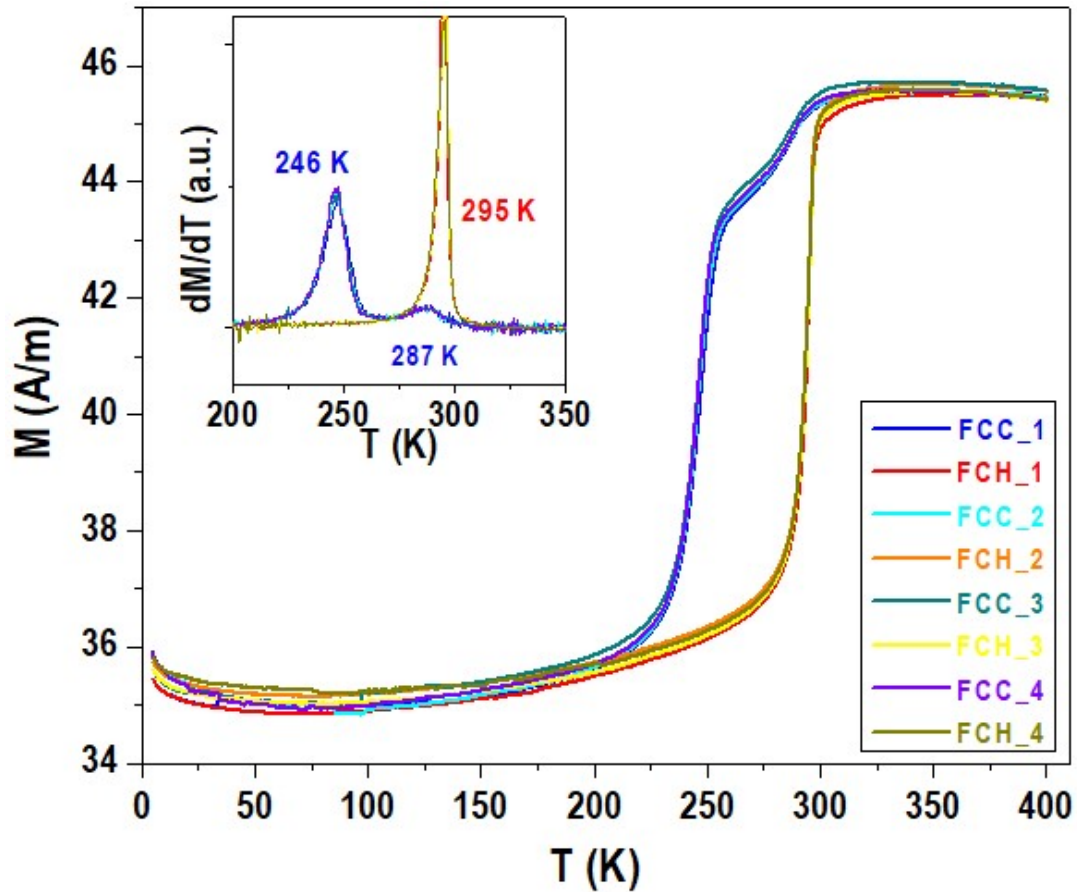
Fig. 5.101 - Magnetization vs Temperature curves for the NiTi_35 sample: set of four thermal cycles (400 K - 5 K – 400 K, H = 2000 Oe).

Fig. 5.102 shows the magnetization vs temperature results for different cycles for sample NiTi_35, with different temperature intervals, and in different directions (either cooling or heating first), under a 2000 Oe magnetic field. All measurements were performed at 1.5 K/min. Table 5.12 summarizes that information regarding these cycles.
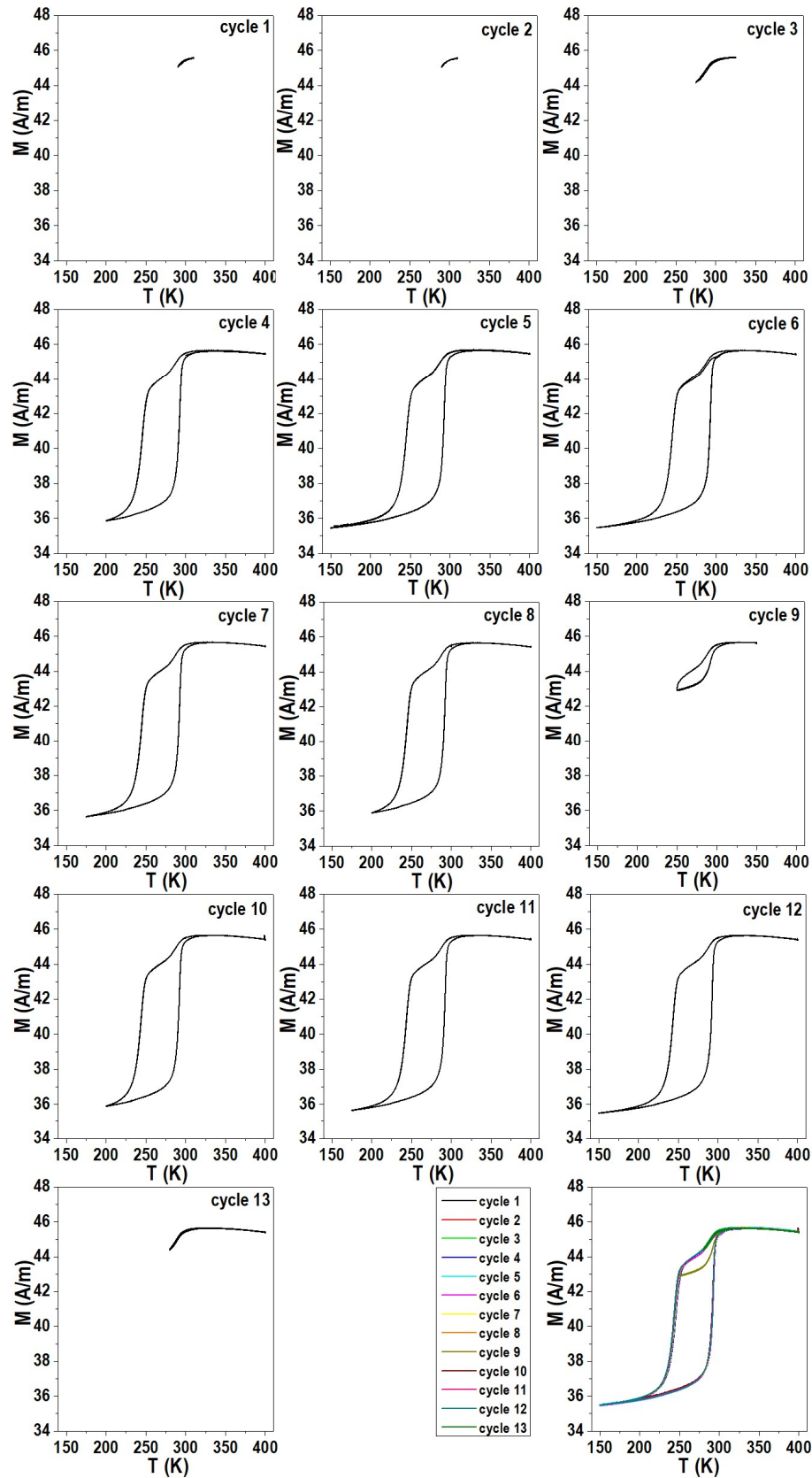
Fig. 5.102 - Magnetization vs Temperature curves for sample NiTi_35: set of 13 thermal cycles, with different temperature limits (bottom right image represents all cycles plotted together).

Table 5.12 - Summary of the information of the measurements M(T) cycles performed on the NiTi_M3 shown in Fig. 5.127

Cycle	Temperature paths of the cycle
1	300 K – 310 K – 290 K; 300 K – 310 K – 300 K
2	300 K – 310 K – 290 K – 310 K – 290 K – 300 K
3	300 K – 325 K – 275 K – 325 K – 275 K – 300 K
4	300 K – 400 K – 200 K – 400 K – 200 K – 300 K
5	300 K – 400 K – 150 K – 400 K – 150 K – 300 K
6	300 K – 150 K – 400 K – 150 K – 400 K – 300 K
7	300 K – 175 K – 400 K – 175 K – 400 K – 300 K
8	300 K – 200 K – 400 K – 200 K – 400 K – 300 K
9	300 K – 250 K – 350 K – 250 K – 350 K – 300 K
10	300 K – 200 K – 400 K – 200 K – 400 K – 300 K
11	300 K – 175 K – 400 K – 175 K – 400 K – 300 K
12	300 K – 150 K – 400 K – 150 K – 400 K – 300 K
13	300 K – 280 K – 400 K – 280 K – 400 K – 280 K – 400 K – 280 K – 400 K – 280 K – 400 K – 280 K – 400 K – 280 K – 400 K – 300 K

Beginning the cycle by heating or cooling the sample has no relevance in the results obtained. The feature highlight is that cycles with lower temperature limit below or equal to 250 K, the cycle exhibits thermal hysteresis. For cycles with lower temperature limit above 250 K (cycles 1 to 3, and 13), the thermal cycle is reversible. This behavior contrasts with that of the electrical resistivity, which is much more sensitive to local effects (for instance, domain boundaries).

Given the popularity of NiTi as a material for applications, it is puzzling how little information on the magnetic properties of this material is available in literature. In 1967 [171] we witness a first approach to the concept that NiTi's magnetic susceptibility (χ) is affected by the martensitic transformation. A publication from the following year [172] advances a martensitic transformation model where austenite and martensite would be prevalently covalent and conduction states, respectively. Between phases, the s-band would shift, the d-band width would be altered, and the

density of states (DOS) would remain constant. Also, χ of both phases is claimed to be independent of temperature, leaving room for linking its origin to Pauli paramagnetism [173]. More recent results [174] clarified that DOS suffers alterations in the NiTi transformation. The structure of the high-energy part of DOS (mainly formed by Ti states) changes from the B2 to the B19' phase, although the low-energy part (mainly formed by Ni states) is not relevantly modified, and d-contributions play the most significant part in the establishment of the DOS structure. In 1999 [175] it was found that the total DOS at the Fermi energy, $D(\varepsilon_\mathrm{F})$, of NiTi is decreased with the occurrence of the B2 – R – B19' sequence of transformations.

More recently, in 2019, a dissertation [176] was published on the magnetic and magnetoelastic properties of NiTi films, forming a more comprehensible source on this subject. Some of the conclusions drawn are that χ in NiTi is strongly affected by tensile deformation and that it was experimentally correlated to DOS at Fermi energy, reinforcing the prior suggestion about it originating from Pauli paramagnetism.

5.3.3 – Structural transformation with SThM

NiTi, being a shape memory alloy, endures the same structural transformation as the Ni-Mn-Ga system. As for Ni-Mn-Ga, it is of interest to observe if the SThM probe can locally induce and determine the transformation temperature for bulk NiTi, which, to the best our knowledge, has not yet been performed.

The procedure described in section 5.1.2 to locally induce the structural transformation was also applied here on sample NiTi_2. The sample was mounted on a Peltier element which was provided with enough power so that the calibrated SThM probe, placed in contact with the surface of the cross section of one of the NiTi wires, measured a temperature of 302 K. Then, probe current sweeps were performed on four different locations of the sample and the probe's cantilever response was observed. The results are presented in Fig. 5.103.
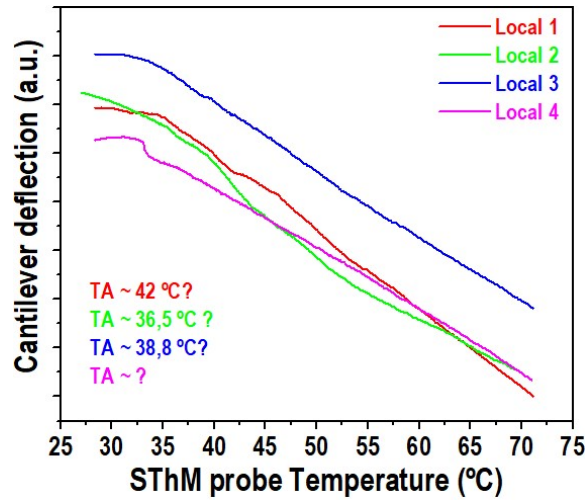
Fig. 5.103 - Cantilever deflection vs SThM temperature for local 1, heated and analyzed by the SThM probe.

Reproducibility tests for the cantilever deflection curve, presented in Fig. 5.104, were performed on two different locations, A and B, respectively. Three probe current sweeps were performed in each location. The results for location A have a clear deviation in cantilever deflection behavior for run number three. For location B, run number two behaves differently from the other two runs for lower temperatures, up to about 45 ºC. From what we have previously observed, the estimation of T_A in our cantilever deflection curves relied on somewhat subtle changes in cantilever deflection, whose reproducibility is seriously questioned by the tests performed on locations A and B. The method does not provide clear enough results for the purpose of this study, which is the determination of the local structural transformation temperature through observation of changes in cantilever deflection. This may be due to changes in the material's structure during the transformation not occurring in the direction in which the cantilever can properly sense them.

In 2004, Botterill et al. applied this method for the characterization of the transition temperatures of thin film NiTi shape memory alloys, obtaining only significant cantilever changes (sensor height) for heat treated films [177]. No changes were observed in as-deposited films. Also, they used a probe which had a diameter of several micrometers, in contrast with the 100 nm radius probe used in this study.
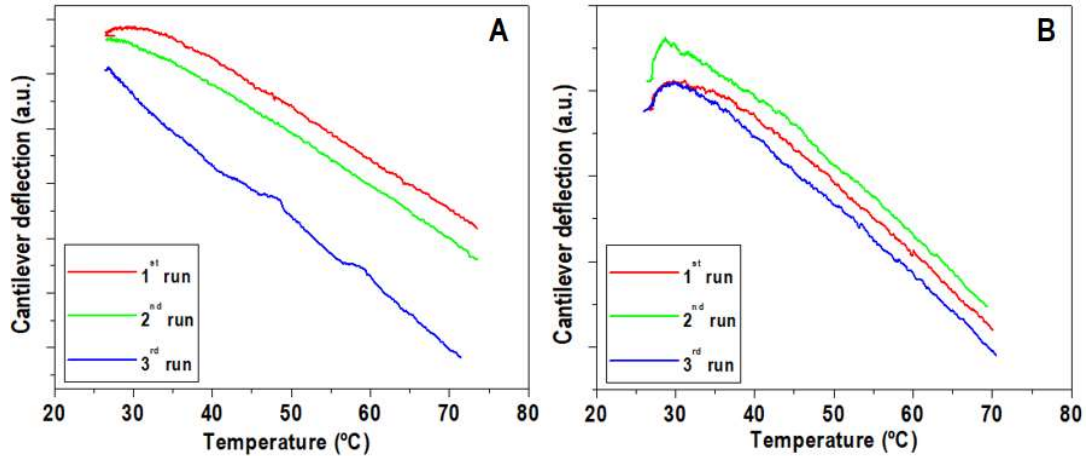
Fig. 5.104 - Reproducibility tests for the cantilever deflection curve on locations A (left) and B (right).

5.3.4 – Temperature dependent AFM

A 30 µm x 30 µm area of one of the NiTi wire sections which compose the NiTi_2 sample was selected, and topography scans were taken at different temperatures. For each scan, the whole sample was kept at one specific temperature by the Peltier element, and the probe used was a standard contact mode probe, manufactured by NANOSENSORS [149]. The scans were performed at temperatures ranging from 26.9 ºC and 48.1 ºC, from lower to higher temperatures. The structural transformation is expected to occur within this temperature interval. The collected scans (Fig. 5.105) show no significant differences in the topography registered, reinforcing the suggestion given by the previous section that the transformation does not affect the surface of the sample in a way which can be sensed by the probe . From all the performed scans, only a few representative examples are shown. The absence of topography changes in scans performed for increasing temperatures deemed unnecessary the execution of such scans for decreasing temperatures.
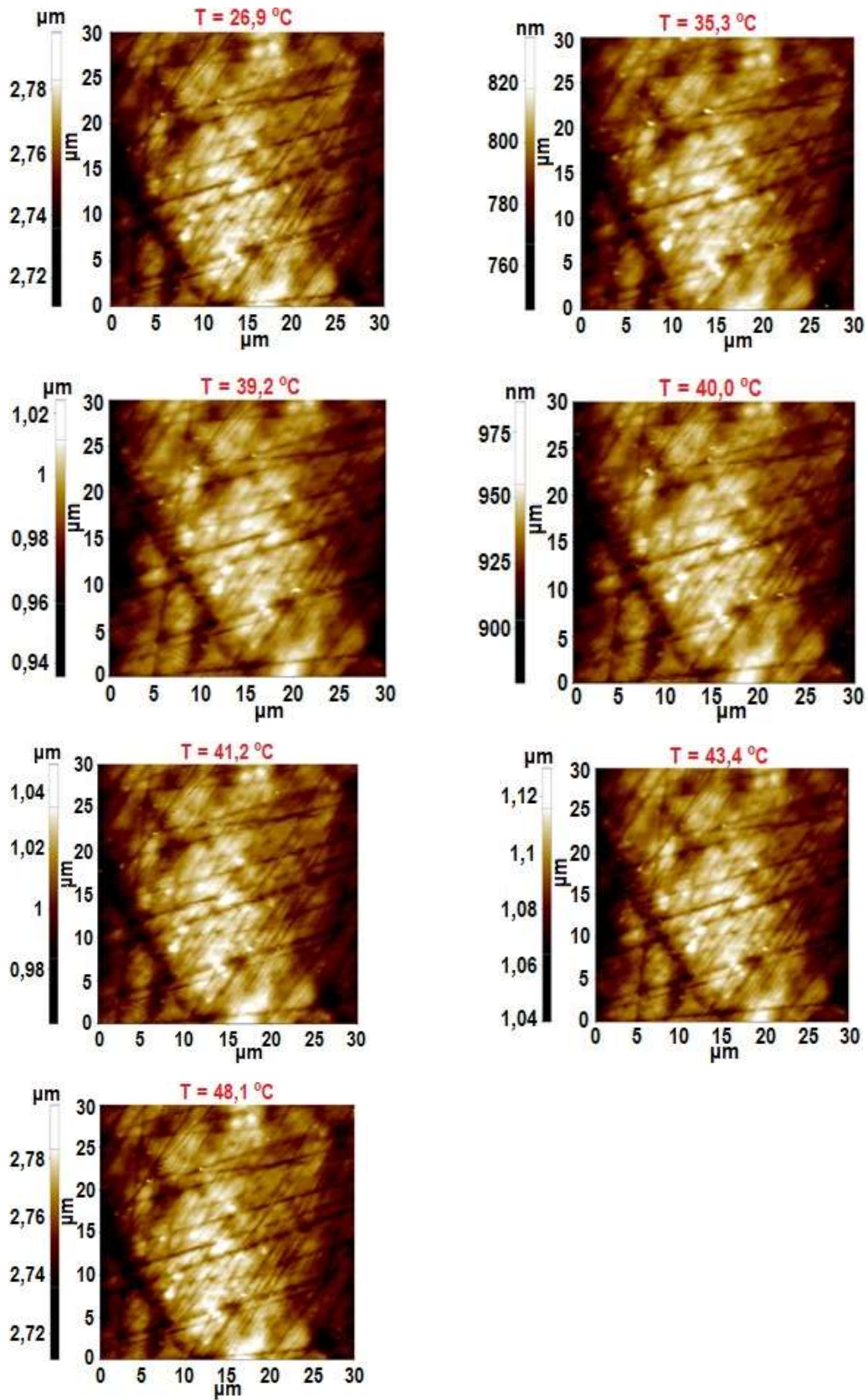
Fig. 5.105 - Topography scans of a 2x2 μm^2 area of the NMG1537 sample at different temperatures.

5.3.5 – Final remarks

Two samples different in shape were produced from commercial NiTi wire: NiTi_1 (Fig. 5.74, piece of wire as acquired, length ~ 0,15 m) and NiTi_2 (Fig. 5.75, pieces of wire, similar lengths, embedded in resin in the same direction, top and bottom cross sections of the wires polished).

SEM images were taken for sample NiTi_2. No different structural phases are identified, and domains are not observed. AFM scans are consistent with these results. EDS measurements provided a material average value composition of $Ni_{50.32}Ti_{49.68}$ with an uncertainty of 0.58.

NiTi_1's structural transformation was thermally induced in NiTi with a Peltier element. By observation of sample NiTi_1's shape transformation while its temperature was being measured, we have established that the structural transformation occurs at 40.1 ºC.

Two samples were analyzed by XRD: a piece of as acquired wire and sample NiTi_1, already thermally cycled, both samples 0,15 m long. NiTi_XRD was only measured at room temperature. Diffractograms were taken at different temperatures (from room temperature to 147 ºC) for NiTi_1 (Fig. 5.97).

At room temperature for NiTi_XRD and NiTi_1 show predominance of the martensitic phase. The diffractograms for NiTi_1 at different temperatures (Fig. 5.97) do not show structural alterations as temperature increases: austenite does not become dominant over the martensitic phase in the thermally cycled wire.

The magnetic measurements presented in this section were performed on a sample with the same characteristics of sample NiTi_1 before it was subjected to the thermal cycling. The magnetic properties of the samples were studied and a paramagnetic behavior was found. Transformations take place on heating at 295 K, and in cooling at 287 K and 246 K. Several M(T) cycles were performed on these samples, with the same spirit as the electrical resistivity measurements. We highlight that cycles with minimum temperature limit below or equal to 250 K exhibit thermal hysteresis, while for minimum temperature limits above 250 K, reversibility is observed.

The procedure described in section 5.1.2 to locally induce the structural transformation on the Ni-Mn-Ga films was applied on sample NiTi_2. The method did not provide satisfactory results for the purpose of this study, which is the determination of the local structural transformation temperature through observation of changes in cantilever deflection. The changes observed, when existing, were too subtle and could not offer a reliable degree of reproducibility. This may be due to changes in the material's structure during the transformation not occurring in the direction in which the cantilever can properly sense them.

6 – ELECTROCALORIC EFFECT

At the nano/microscale, a primary challenge in terms of the electrocaloric (EC) effect research was addressing the direct measurement of this caloric effect in thin films. When a substrate is attached to the thin film, the difference in their masses makes it rather difficult to directly measure the EC effect displayed by the film. On the other hand, removing the substrate and performing direct EC effect measurements on stand-alone thin films is not as straightforward as desirable.

In 2010 and 2013, Kar-Naryan et al [91] [98] addressed this issue in two articles, where they studied $BaTiO_3$-based multi-layered capacitors (MLCs), which exhibited the EC effect, with a two-fold goal: suggesting that these components could play a significant role in the cooling industry and that they could assist in determining the best technique to be used in order to circumvent the obstacles hindering the direct measurement of the EC effect in thin films. SThM was pointed by the authors as being the more suitable technique for the purpose when studying thin films coupled with their substrates. The follow up in literature concerning EC direct measurements with SThM is sparse, being mainly composed of the Crossley *et al.* 2016 article on the direct electrocaloric measurement of 0.9Pb(Mg1/3Nb2/3)O3-0.1PbTiO3 films using SThM [178], and, much more recently, in 2020, the work of Shan *et al.* [179], presenting a high fidelity local measurement of ECE response by experimentally probing MLCs made of doped barium titanate with SThM and applying finite element model based quantitative analysis. Concerning the direct measurement of the EC effect on multilayer capacitors, it is also worth mentioning the 2019 Nair *et al* article on large electrocaloric effects in oxide multilayer capacitors over a wide temperature range [180].

This scarceness motivated our retracing the steps taken by Kar-Narayan *et al.* in their studies, using the appointed technique, in an effort to find justification for the scarcity of studies in this context, while simultaneously attempting to contribute

with additional information on the difficulties remaining in this path and potential strategies to overcome them.

6.1 – Sample specification and setup requirements

To study the electrocaloric effect at the micro/nanoscale we used a $BaTiO_3$ multilayer capacitor (MLC), Y5V Dielectric, with 22 µF capacitance, manufactured by AVX, which is the exact same model as the one used by Kar-Naryan et al in their studies. As the authors mentioned in 2010 [91], these capacitors are a very good starting point for these studies due to a myriad of reasons. They are extremely inexpensive and easily obtained in the electronic components market. Also, while presenting the EC effect, they possess an extremely agreeable configuration that allows easy thermal access for the SThM tip (acting as a temperature measuring device). The electrical contacts needed for the application of an electrical field with enough strength to produce a discernible EC effect are also of effortless execution.

The MLC has the following dimensions: length 3.20±0.20 mm; width 2.50±0.20 mm; height 2,29±0.20 mm. The terminals are made of plated Ni and Sn.

It can perform within the temperature range of 85ºC and -30ºC. Fig. 6.1 shows an amplified representative image of the MLC and a subtitled longitudinal cut of the MLC.

It is known that there are about 200 Ni electrodes in total (100 connected to each terminal). Each electrode is 2 µm thick and the layers of material between two electrodes have a thickness of about 6.5 µm. [89]

The several electrodes with a small thickness of dielectric material in between require a relatively small voltage applied to the terminals to promote the necessary electrical field. This field should be high enough so that it produces a change in temperature on the $BaTiO_3$-based MLC that can be measured by the SThM probe: 200 V applied to each electrode of each terminal promotes an electrical field of about 300kVcm^{-1}.
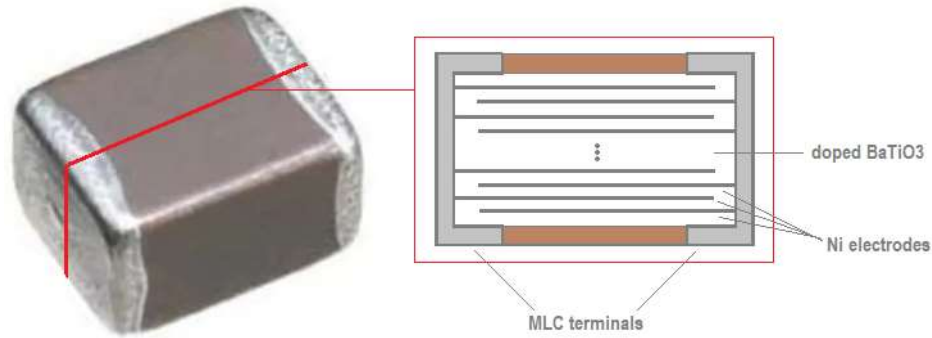
Fig. 6.1 - Amplified image of the BaTiO$_3$ multilayer capacitor (MLC), 22 µF, manufactured by AVX [181], with a subtitled schematic longitudinal cut.

To apply the voltage to the MLC, a Keithley 2290-5 5kV power source was used, which can supply voltage values from ~ 35 V to 5000 V.

Voltage value measured in the wires that would connect to the terminals of the MLC vs voltage provided by the source.
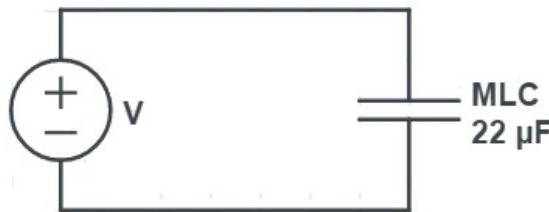
Fig. 6.2 - Schematics of the first circuit used on the EC effect studies.

The measurement of the EC effect was here performed by approaching the SThM probe close to the surface of the MLC electrodes, applying (and removing) different voltage values to the MLC terminals (thus applying an electrical field to the BaTiO$_3$ material) and measuring the SThM probe's response in terms of variations in temperature.

Preliminary procedures took place to ensure the best possible conditions for the experiment to take place. We evaluated fluctuations in the SThM's probe temperature (T$_{probe}$) while the probe was merely in contact with air, not measuring any response from the sample, to ascertain the resolution of our temperature measurements. The impact over time derived by aspects concerning the probe's

calibration method (described in section 4.1.1) were discussed in this context also. We followed to experimentally analyze the discharge time of the capacitor in the circuit considered in Fig. 6.2 and described the changes introduced for obtaining a faster discharge and thus voltage drop in the MLC terminals.

6.2 – Impact of ambient conditions on measurements performed by the thermal probe

We evaluated the changes in T_{probe} when a given voltage was applied to the MLC terminals for different probe-terminal distances. While probe-terminal distance was kept constant, we measured ΔT_{probe} for different voltage values applied to the MLC terminals. The same procedure was then executed for other probe-terminal distances, and the reproducibility of these results tested.

Before such experiments took place, however, it was essential to assess the impact of ambient conditions on the temperature measured by the probe. For the measurement of the EC effect, the SThM probe was calibrated according to the method already described in section 4.1.1. This calibration method is characteristically valid only when an electrical current of at least 0.1 mA is flowing through the SThM probe. Two different probes, A and B, were calibrated and, while in contact with air and with a current of 0.1 mA flowing through them, the values of their temperatures were collected over a period of 30 s. The results provide us with information on the behavior of the SThM probe temperature over time under ambient conditions and in the absence of an electrical field applied to the electrocaloric sample. This leads to the possibility of estimating the uncertainty due to environmental conditions present during the measurements of the EC effect. We tested probe A twice (results presented in Figs. 6.3a to 6.4b) and probe B once (Fig. 6.5a).

Consecutive temperature values on the plots shown in Figs 6.3a, 6.4a and 6.5a were taken with a 0.5 s difference.

Histograms taken for the three tests performed are presented in Figs. 6.3b, 6.4b and 6.5b. The temperature distribution for the SThM probe A (in contact with

air and with a current of 0.1 mA flowing through it) taken for an interval of 30 s shows values between 26.8 ºC and 27.4 ºC, with the highest incidence for the temperature value of 27.0 ºC for the 1st test (Fig. 6.3b) and values between 27.0 ºC and 27.6 ºC, with the highest incidence for the temperature value of 27.4 ºC for the 2nd test (Fig. 5.4 b)). The temperature distribution for the SThM probe B (in contact with air and with a current of 0.1 mA flowing through it) taken for an interval of 30 s shows values between 27.8 ºC and 28.6 ºC, with the highest incidence for the temperature values of 28.1 ºC and 28.2 ºC (Fig. 6.5b).
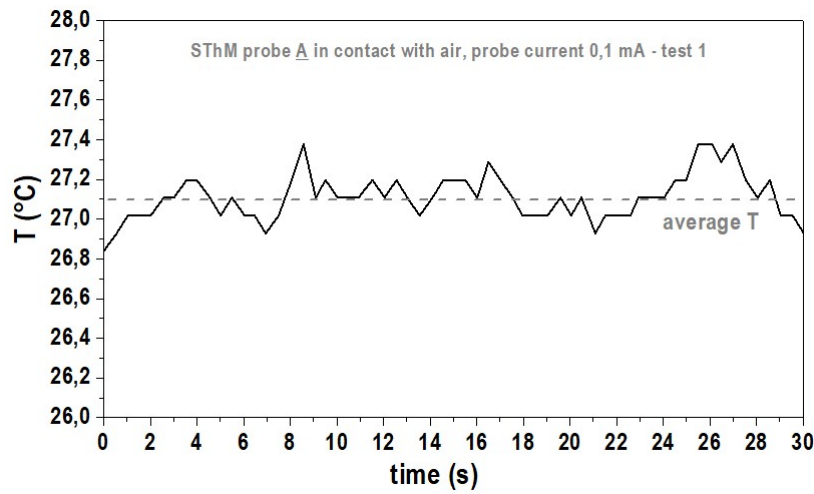
Fig. 6.3a - Time dependence of the temperature of SThM probe A (in contact with air and with a current of 0.1 mA flowing through it) as a function of time - 1st test.
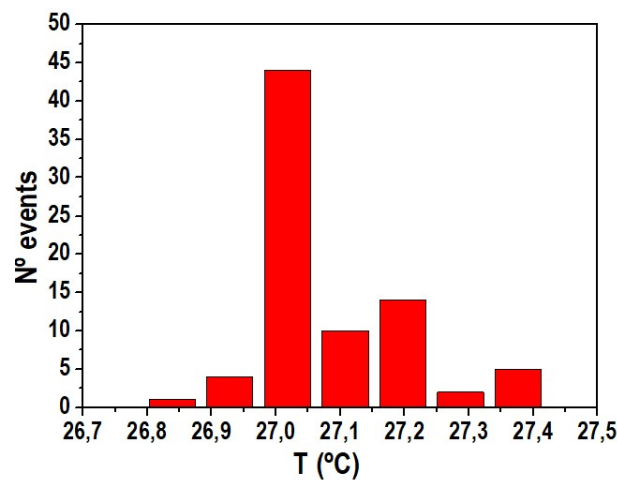
Fig. 6.3b - Temperature distribution for the SThM probe A (in contact with air and with a current of 0.1 mA flowing through it) taken for an interval of 30 s - 1st test.
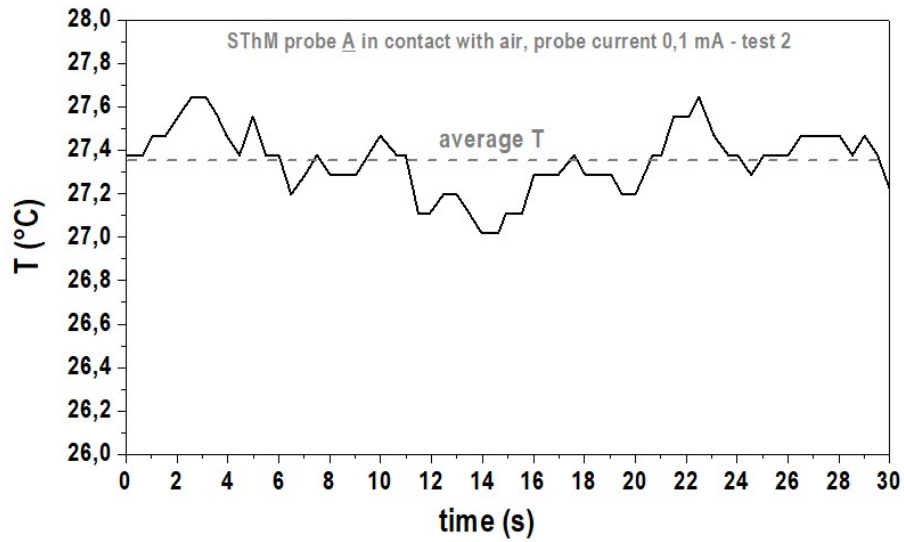
Fig. 6.4a - Time dependence of the temperature of SThM probe A (in contact with air and with a current of 0.1 mA flowing through it) as a function of time – 2nd test.
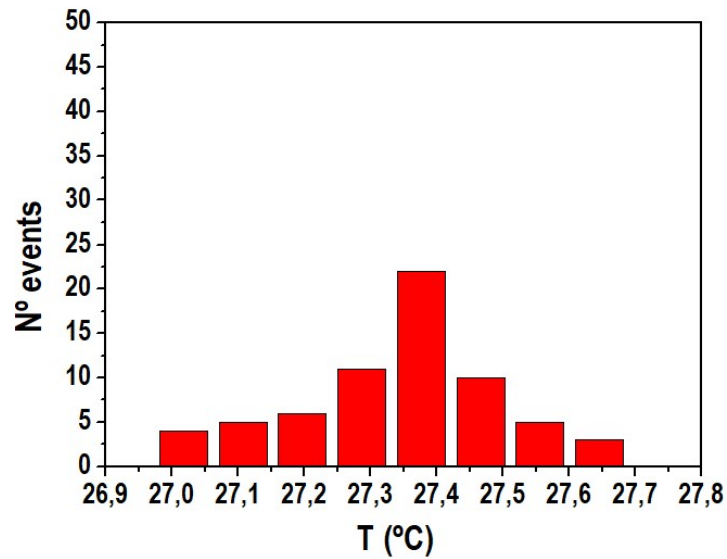
Fig. 6.4b - Temperature distribution for the SThM probe A (in contact with air and with a current of 0.1 mA flowing through it) taken for an interval of 30 s - 2nd test.

The second test performed with probe A took place about an hour after the first test took place. During this time, the probe current remained at 0.1 mA. This resulted in an increase of 0,24ºC in the average temperature from the first (27,11ºC) to the second test (27,35ºC). This translates into less than 0.01% increase in

temperature per second due to the 0.1 mA probe current, which is irrelevant for the
time frame that will be considered in our EC studies.
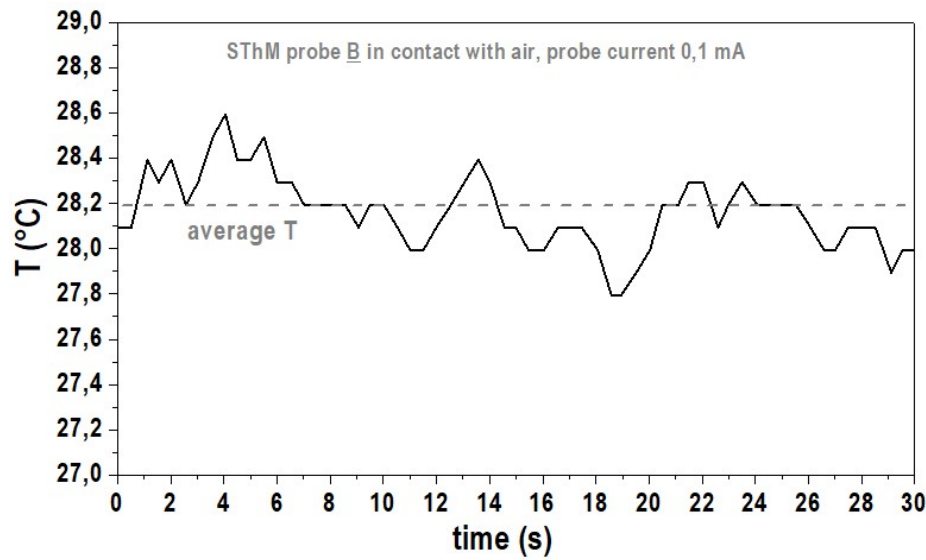
Fig. 6.5a - Time dependence of the temperature of SThM probe B (in contact with air and with a
current of 0.1 mA flowing through it) as a function of time.
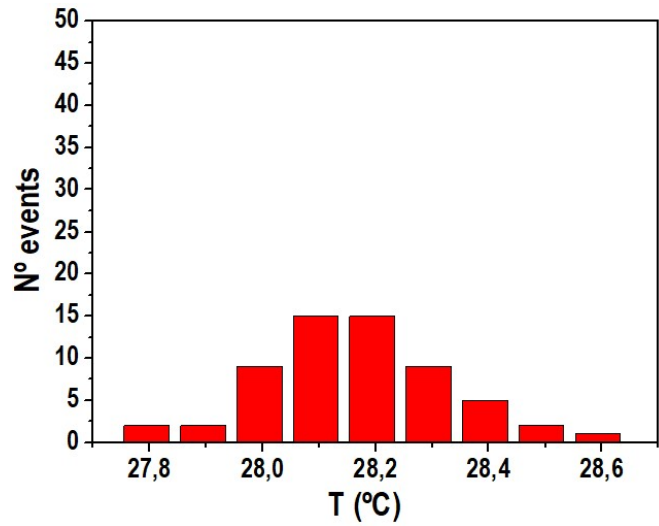
Fig. 6.5b - Temperature distribution for the SThM probe B (in contact with air and with a current of
0.1 mA flowing through it) taken for an interval of 30 s.

In addition to this information, right before the measurements of the EC effect
took place, with both probes, similar tests were performed in order to assess the

temperature oscillations due to environmental conditions experienced by the SThM probe specifically at the ambient conditions at which the EC effect measurements took place.

6.3 – Experimental setup development

The circuit employed for the first EC effect direct measurement tests is composed by the capacitor and the power source, as shown in Fig. 6.2.

Fig. 6.6 shows images of the MLC on the SThM stage. The MLC is placed on the sample holder on top of several layers of red insulating tape. A white piece of Teflon tape was used to aid the positioning of the MLC in order to make the access of the probe to the terminal easier and safer for the probe. Contact between probe and the terminal should be avoided to prevent damage to the probe and its electrical circuit shown in section 4.1.1. Each MLC terminal surface accessible to the probe in the montage has an area of 0.50±0.25 mm by 2.50±0.20 mm.

The connections between the MLC terminals and the source were made by soldering wires with 0.5 mm diameter to the terminals of the MLC.
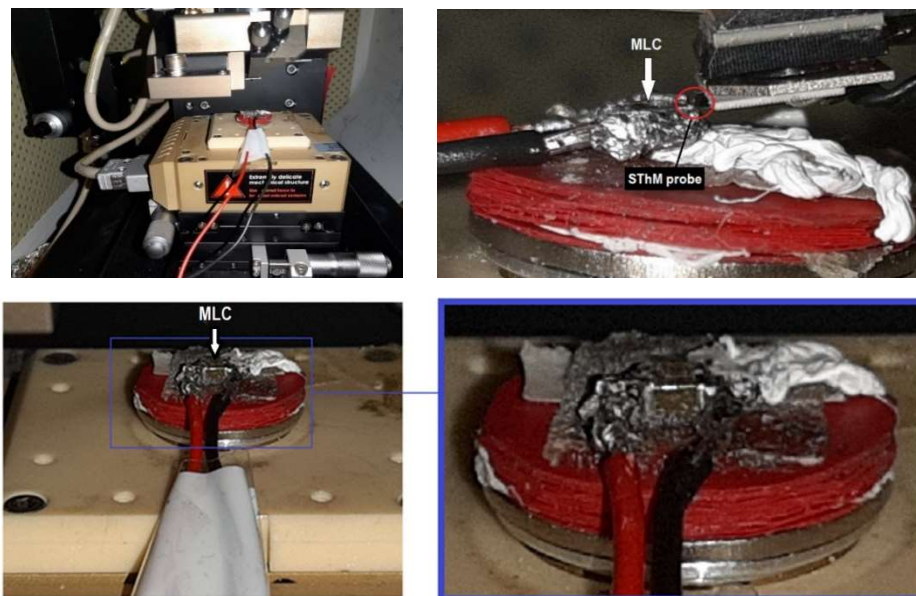
Fig. 6.6 - MLC mounted on the SThM stage. The sample holder has several layers of red insulating tape on top of it and where the MLC is placed.

The first analysis of the EC effect on the MLC was performed as follows: calibrated SThM probe A was placed at ~ 12 μm above the surface of one of the MLC terminals. The temperature measured by the probe was registered over time while 200 V were applied to the MLC terminals and later removed. The circuit involving the MLC and the voltage source in these tests was shown on Fig. 6.2. Two tests, A.1 and B.1, using probe A, were performed. The results are shown on Figs. 6.7 and 6.8, respectively.

Both in Fig. 6.7 and 6.8, application of 200 V causes an increase of T_{probe} applied to the MLC terminals, but the expected sudden decrease in T_{probe} when voltage is turned off is not observed. Fig. 6.9 and 6.10 show the plots of the voltage displayed by the source vs time throughout the whole tests in Figs. 6.7 and 6.8, respectively. The observed behavior explains the absence of sudden temperature drop after the source stops applying 200 V to the MLC terminals. The configuration of the circuit used in this test (Fig. 6.2) allows, at that point, the MLC discharge through the resistance of the source, which is considerably high. This implies a longer than desired discharge time, no sudden removal of electrical field, hence no sudden drop in T_{probe}. In Fig. 6.7, there is a ~ -0.80 ºC variation in temperature before voltage is turned off and the plot in Fig. 6.8 shows an abnormal fluctuation in temperature well after the field was removed. These behaviors are non-EC effect related and have no clear interpretation.
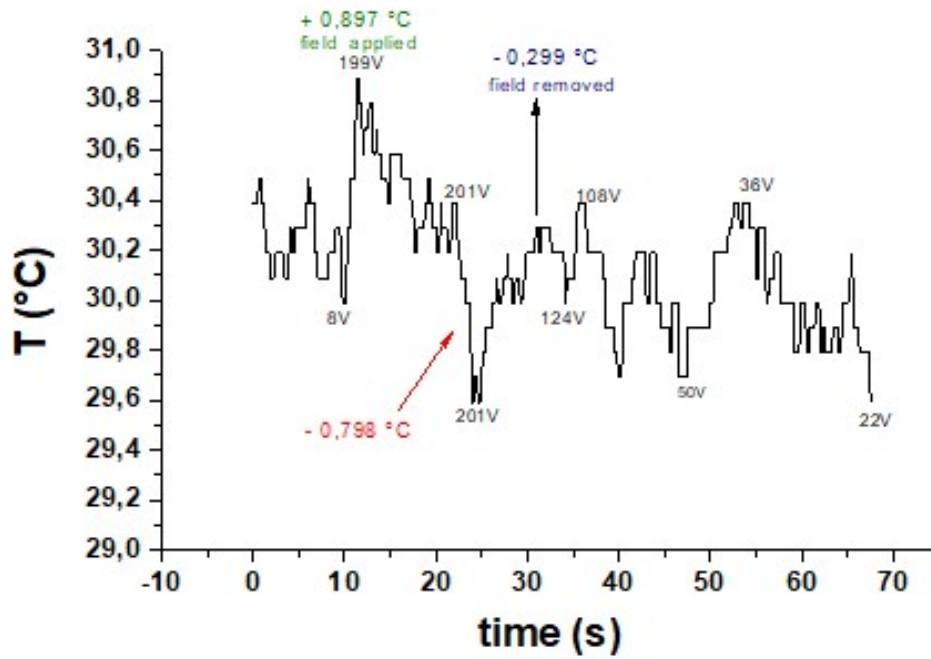
Fig. 6.7 - Plot of probe temperature vs time while 200V are applied and removed from MLC terminals: Test A.1.
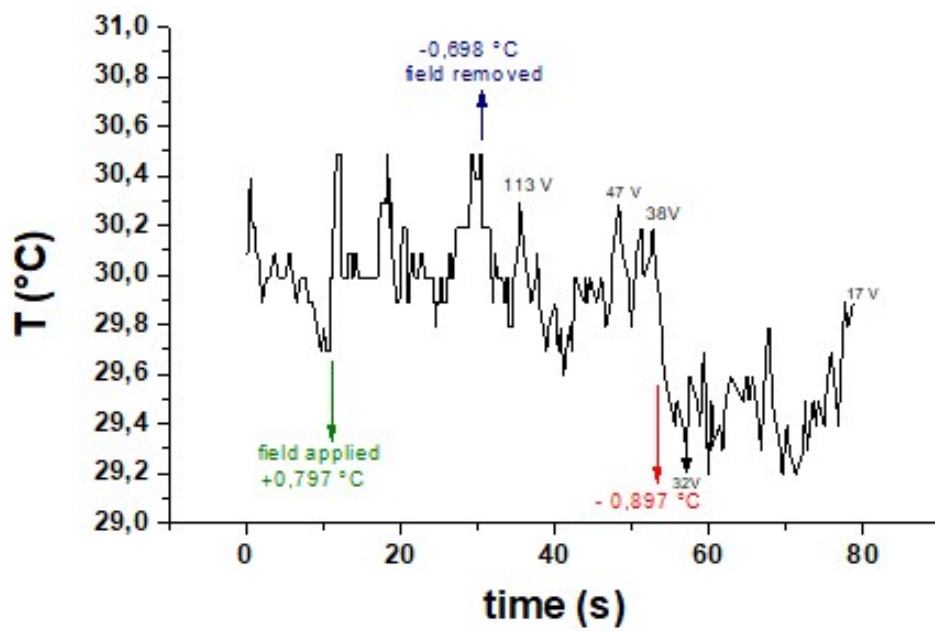
Fig. 6.8 - Plot of probe temperature vs time while 200V are applied and removed from MLC terminals: Test B.1.
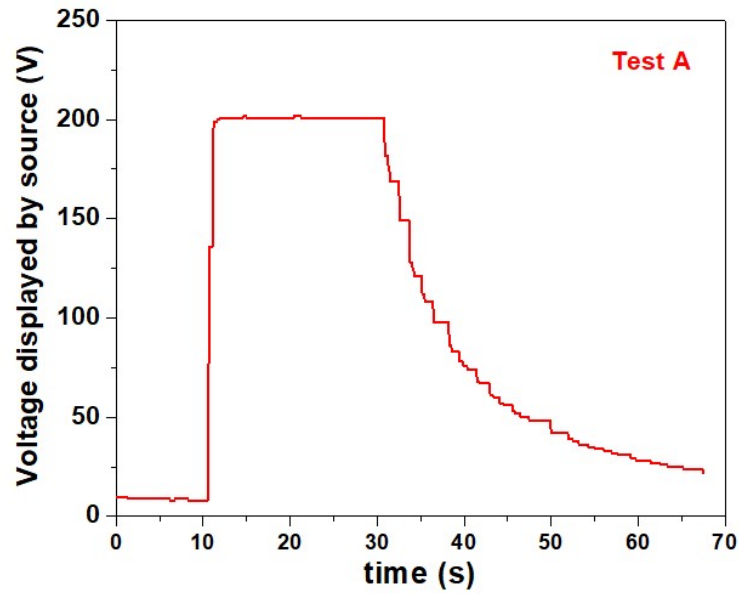
Fig. 6.9 - Plot of $V_{applied}$ vs time: Test A.1.
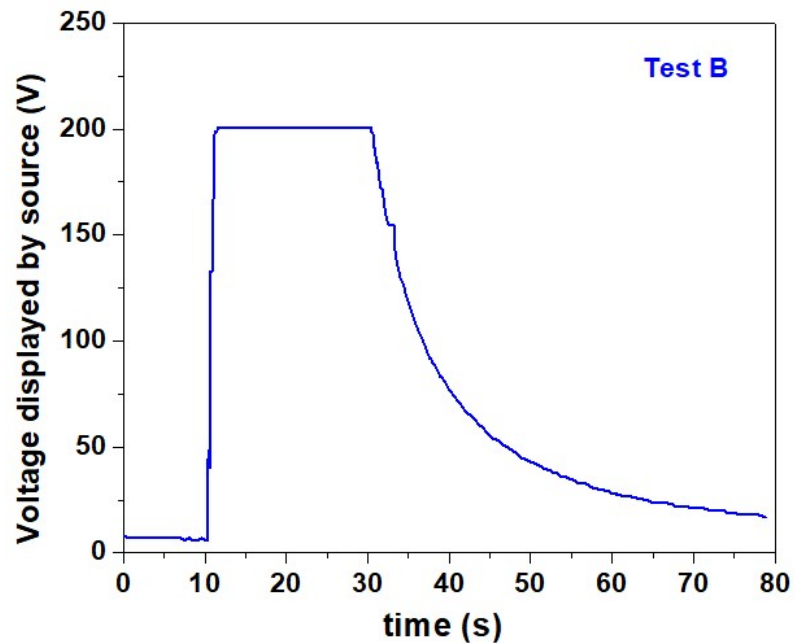
Fig. 6.10 - Plot of $V_{applied}$ vs time: Test B.1.

The inadequacy of the discharge time for the purpose of the present study demanded that adjustments were made to the circuit of the capacitor.

Fig. 6.11 shows the improved circuit, both in MLC charge and discharge modes (or applying and removing the 200 V voltage, respectively). A desired ~ under 1 s discharge time for the capacitor was achieved by introducing two switches

177

and a resistor with a value about three orders of magnitude below the one on the voltage source. This allowed the observation of the sudden fall in temperature caused by the EC effect.

Charging of the capacitor

Capacitor discharge
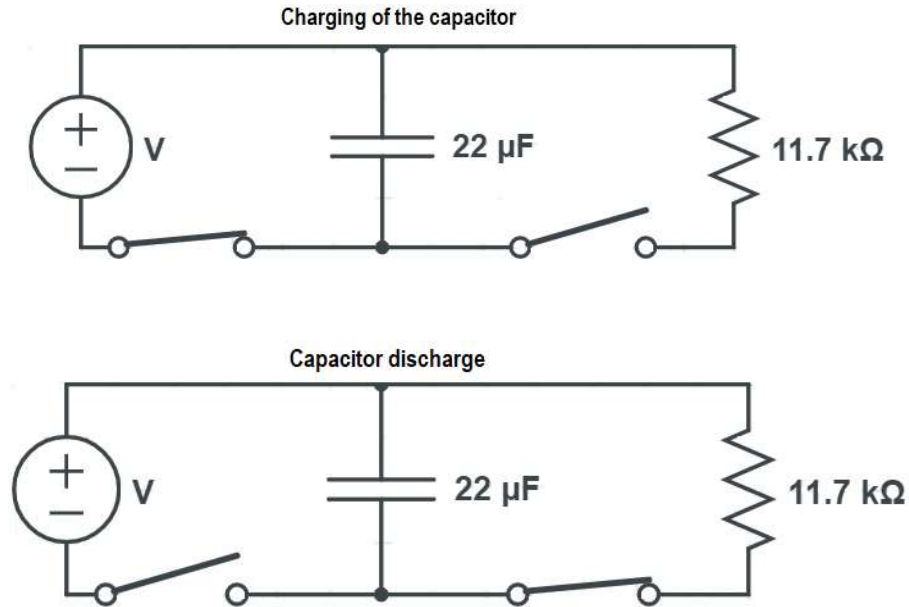
Fig. 6.11 - Schematics of the circuits of charge (top) and discharge (bottom) of the MLC.

The probe used in the studies conducted with the MLC integrated in the reconfigured circuit (Fig. 6.11) was SThM probe B.

6.4 – Probe temperature vs terminal-probe distance studies

Figs. 6.12a to 6.12c show three different tests for the dependence of probe temperature with time while 200V are applied and removed from the MLC terminals when the probe is initially placed at ~110 µm of the MLC terminal surface.

Figs. 6.13a to 6.13c show three different tests for the dependence of probe temperature with time while 200V are applied and removed from the MLC terminals when the probe is initially placed at ~80 µm of the MLC terminal surface.

Similar tests were conducted for when the probe is initially placed at ~90 µm of the MLC terminal surface, which are not shown here for brevity. These are

included in Fig. 6.14, which exhibits the plot for the magnitude of the EC effect ($|\Delta T|$)
vs initial distance from tip to sample.
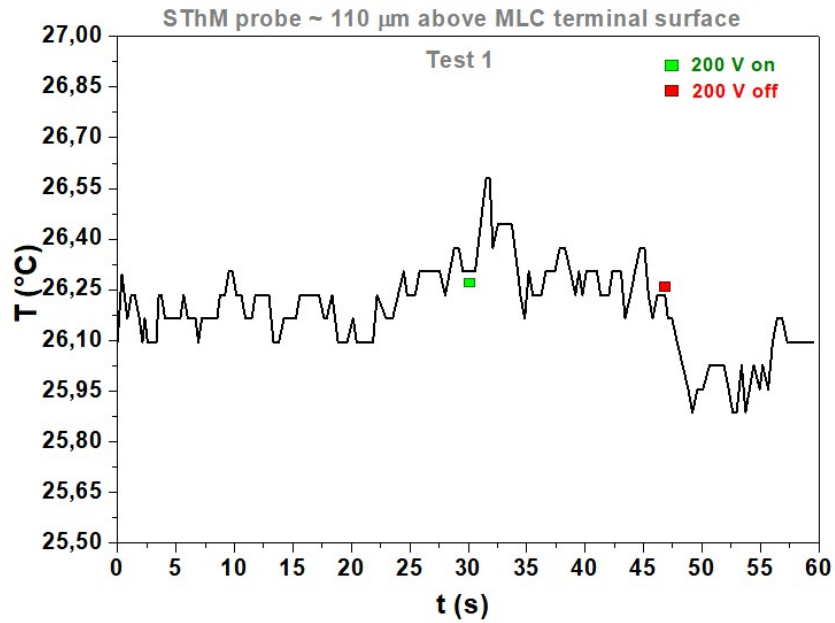
Fig. 6.12a - Plot of probe temperature vs time while 200V are applied and removed from MLC
terminals – SThM probe initially placed at ~110 μm of MLC terminal surface, Test 1.
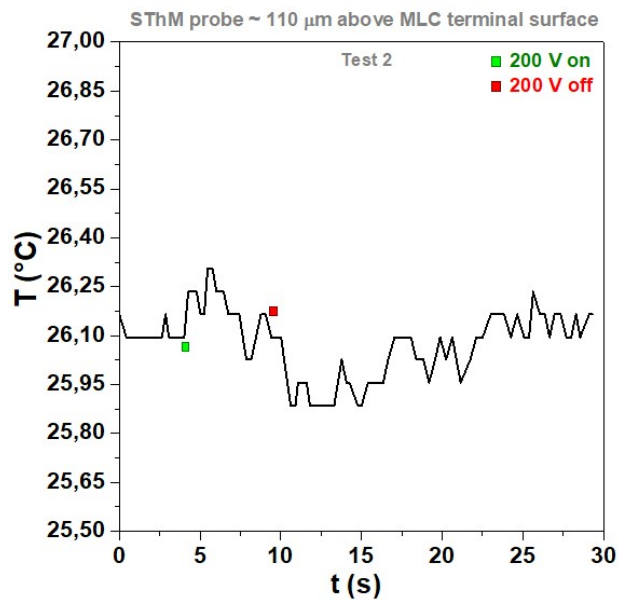
Fig. 6.12b - Plot of probe temperature vs time while 200V are applied and removed from MLC
terminals – SThM probe initially placed at ~110 μm of MLC terminal surface, Test 2.
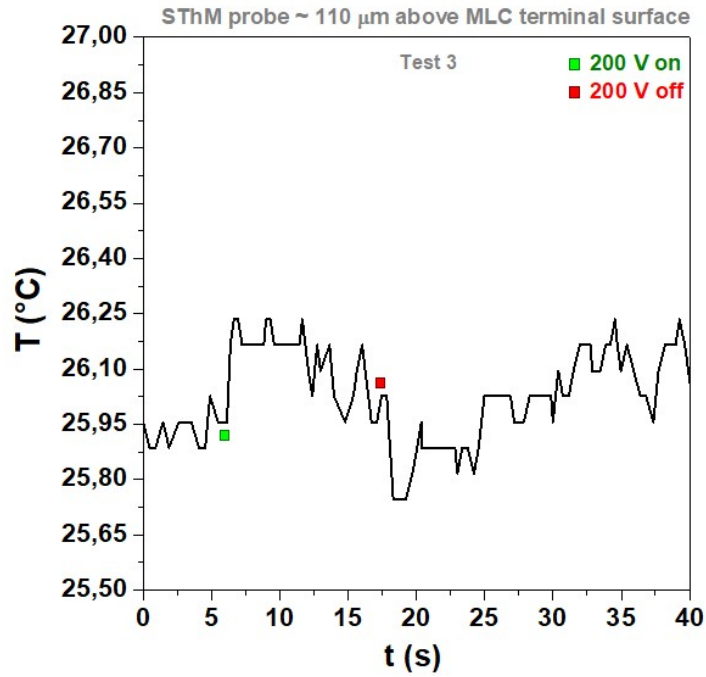
Fig. 6.12c - Plot of probe temperature vs time while 200V are applied and removed from MLC terminals – SThM probe initially placed at ~110 µm of MLC terminal surface, Test 3.
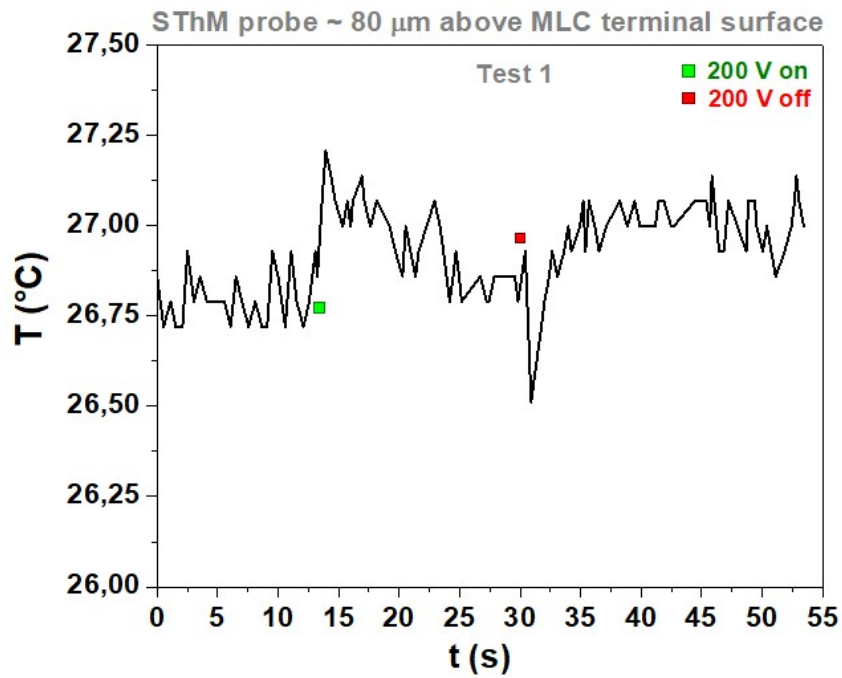
Fig. 6.13a - Plot of probe temperature vs time while 200V are applied and removed from MLC terminals – SThM probe initially placed at ~80 µm of MLC terminal surface, Test 1.
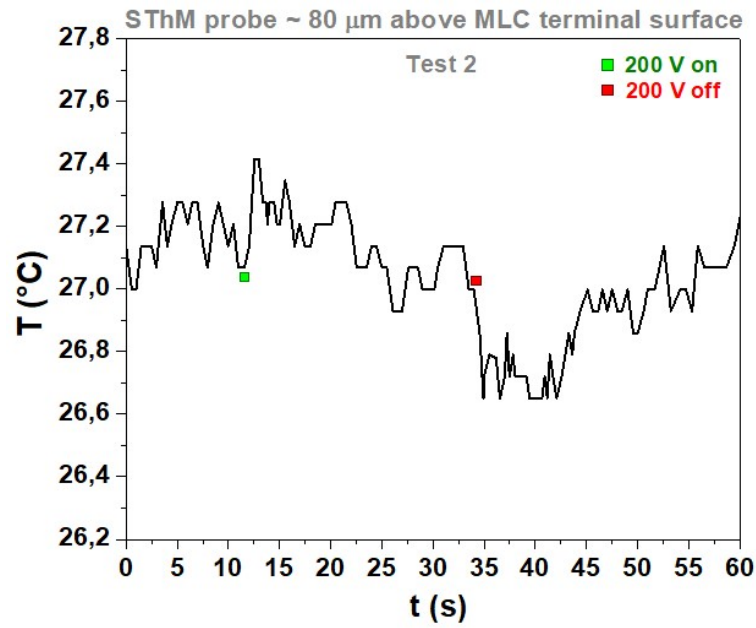
Fig. 6.13b - Plot of probe temperature vs time while 200V are applied and removed from MLC terminals – SThM probe initially placed at ~80 µm of MLC terminal surface, Test 2
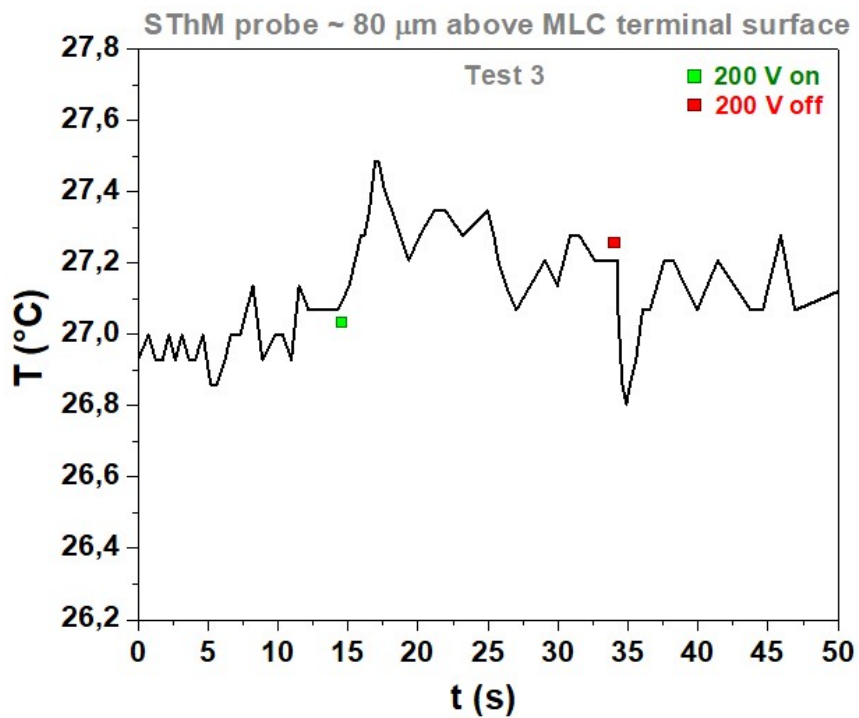
Fig. 6.13c - Plot of probe temperature vs time while 200V are applied and removed from MLC terminals – SThM probe initially placed at ~80 µm of MLC terminal surface, Test 3.
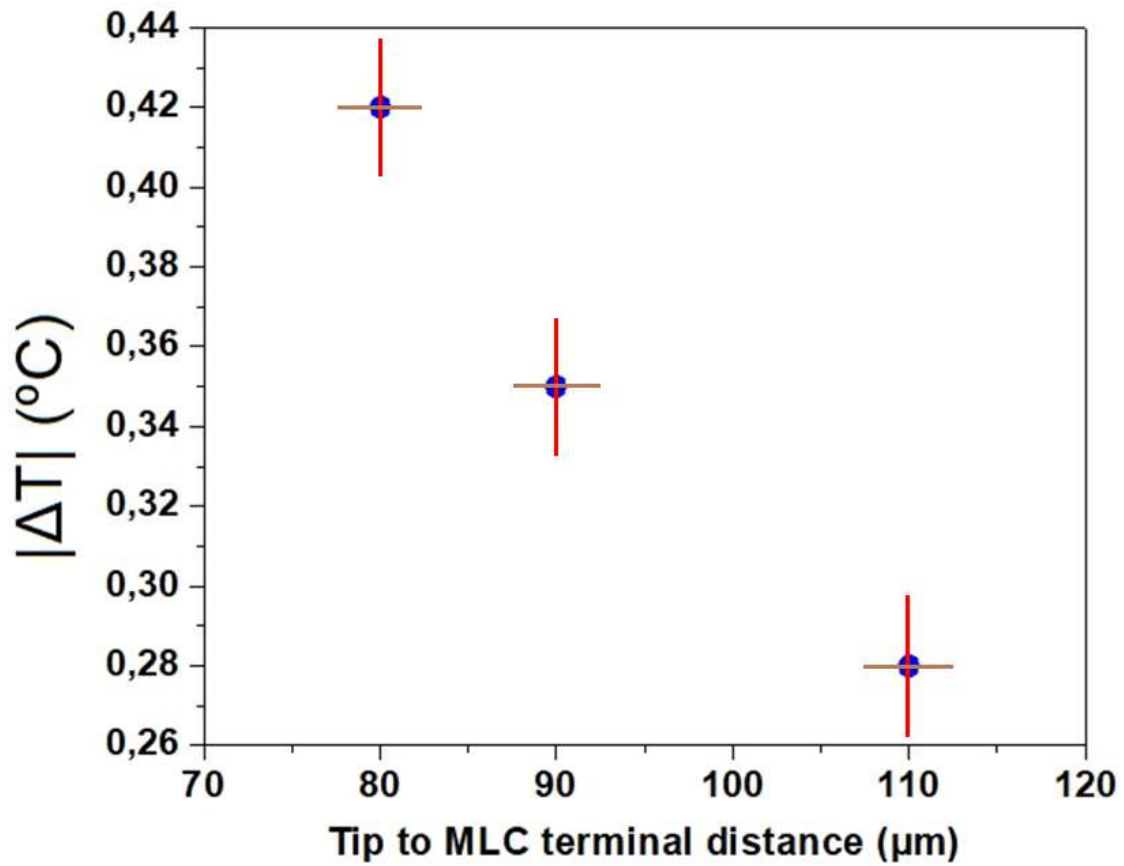
Fig. 6.14 - Plot of magnitude of the EC effect ($|\Delta T|$) vs initial distance from SThM tip to MLC terminal.

The plot on Fig. 6.14 includes, in red vertical lines, the order of magnitude of the uncertainty in the measurement of the probe's temperature in ambient conditions, obtained just prior to the execution of the tests. The horizontal lines represent the unknown uncertainty of the value indicated for the distance between tip and MLC terminal in each case studied. As expected, the magnitude of the EC effect decreases with increasing initial distance from SThM tip to MLC terminal.

Joule effect is considered not to have a discernible impact on the EC effect measurements, due to its estimated value of the order of 1 mK/s contribution for the temperature change in the MLC terminal [91].

An approach with an initial SThM tip to MLC terminal distance of ~ 20 µm was attempted. When the 200 V were applied to the MLC in this situation, the cantilever was very powerfully pulled towards the MLC in a way that eventually detached it

from the probe's support. A possible explanation for probe A being able to measure the EC effect at ~12 μm distance from the MLC terminal and probe B being damaged at ~ 20 μm might reside in the fact that the probes were placed above different spots of the MLC terminal, and, probe B, as the 200 V were being applied, might have had some part of its circuit (other than the tip) in contact with the MLC. This hypothesis is strengthened by the fact that after this experiment, the SThM module presented signs of damage in its circuit, preventing us thus far from making any further experiments on this topic. The module was sent for reparation in January 2020 and, due to unforeseeable circumstances, could only be retrieved for testing in our premises around June in the same year. By then, after mounting of the module, a different malfunction was detected, so it had to be returned for further reparation. It arrived in proper condition only by the end of July 2020, outside the appropriate timeframe for the development of further experimental work for this dissertation.

6.5 – Effect of the electrical field on cantilever deflection

Before closing this chapter, a critical note must be made. In the very first tests it was perceptible that the cantilever to which the tip is attached was pulled towards the surface of the sample whenever an electrical field was applied to the sample. This could be observed through the images shown by the camera attached to the optical microscope that composes the PARK XE7 system. This effect is not discussed in the Kar Narayan article that approaches these studies with SThM [89]. This is surprising, since the characteristics of the SThM probe described by the authors match those of the SThM probes used in the present study, both in terms of composition and design. The fact that there is a 0.1 mA current flowing through the probe was dismissed as the cause for this effect.

This effect of the electric field on the SThM probe cantilever is bound to have a significant impact on the direct EC effect measurement results, especially those involving the dependency of the amplitude of the effect on the distance between probe and MLC terminal surface.

We have studied this effect on probe B and will proceed to explain how this can jeopardize the accurate assertion of the distance between tip and MLC terminal.

Fig. 6.15 shows the effect of the voltage applied to the MLC terminals on cantilever deflection as a function of time when SThM probe is initially placed ~ 250 μm above the MLC terminal surface. When the voltage is applied, there is a sudden change in cantilever deflection caused by the effect of the electric field on the cantilever. The magnitude of this sudden change in cantilever deflection is accentuated with increasing values of voltage applied/strengths of electric field created. The magnitude of the cantilever deflection change does not seem to have a linear relationship with the increasing voltage. Between 60 V and 100 V the drop in cantilever deflection is more accentuated. Also, after the sudden change in deflection caused by the switch in voltage from zero to non-zero value, and while the non-zero voltage value is maintained (electric field present), there is still a decrease (albeit less accentuated) in cantilever deflection over time. This is particularly visible for $V_{applied}$ = 100 V, since for 30 V and 60 V the effect of the voltage is lessened so this smaller decrease is not as clearly noticeable, and for $V_{applied} \geq$ 150V, the change in deflection rapidly reaches the detection limits of the equipment, so we can't actually measure what happens to cantilever deflection beyond that point. The complete removal of the electrical field allows the cantilever to return to its initial shape, which we can see through the return of the cantilever deflection to its initial value. A more detailed plot in applied voltage values is presented in Fig. 6.16. It is between 80 V and 90 V that the effect of the electrical field in cantilever deflection begins to manifest slightly differently. At 90 V, there is an even more accentuated initial drop in cantilever deflection. The drop in cantilever deflection over time while V is applied seems to follow a tendency with very similar slope values for the lower voltages until V = 80 V. For 90 V $\leq V_{applied} \leq$ 100 V this slope increases to a higher value and even higher for $V_{applied}$ = 105 V. For voltages above 105 V, the equipment's detection limit is reached, and no further information can be collected on this topic. Fig. 6.17 allowed to collect a little more information for $V_{applied}$ = 110 V, by initially placing the cantilever deflection signal as close as possible to the upper

detection limit. The results suggest that the slope value is roughly the same for $V_{applied}$ = 105 V and 110 V.
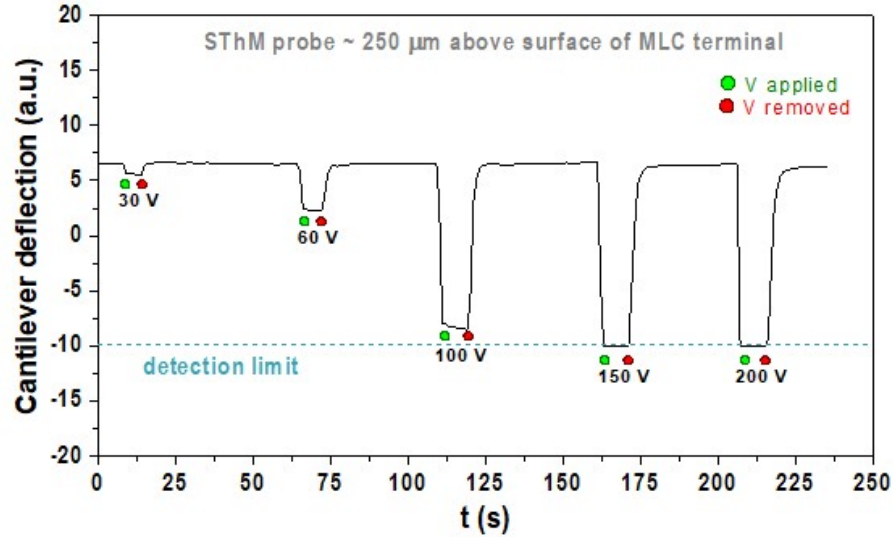
Fig. 6.15 - Cantilever deflection as a function of time for different values of V applied to MLC terminals when SThM probe is initially placed ~ 250 μm above the MLC terminal surface.
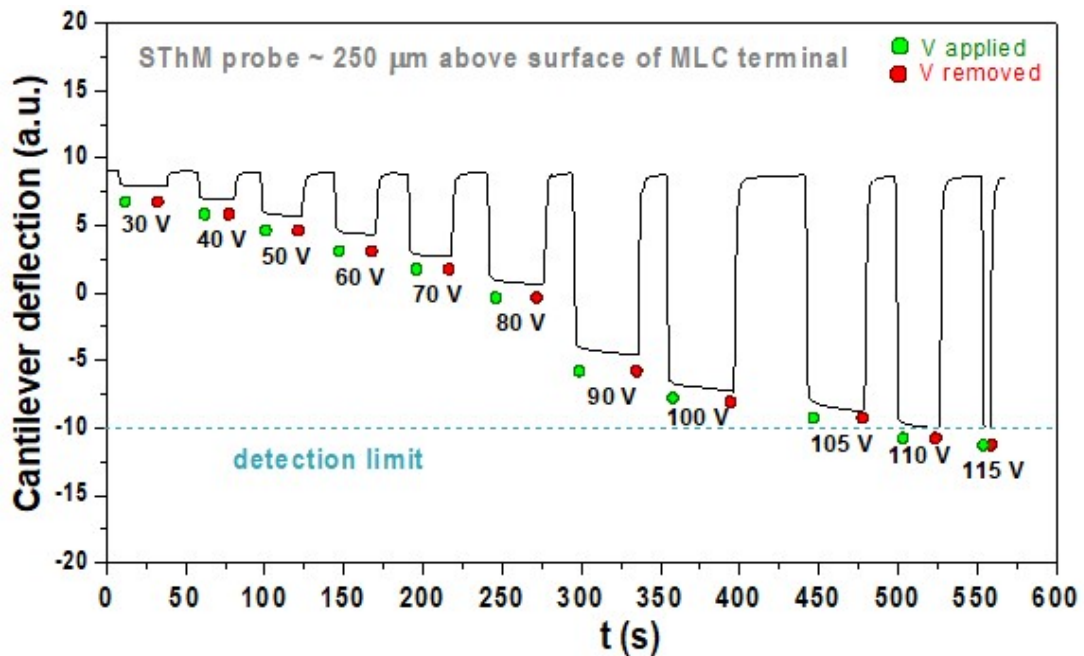
Fig. 6.16 - Cantilever deflection as a function of time for different values of $V_{applied}$ when the SThM probe is initially placed ~ 250 μm above the MLC terminal surface – more $V_{applied}$ values featured than in the plot in Fig. 6.15.
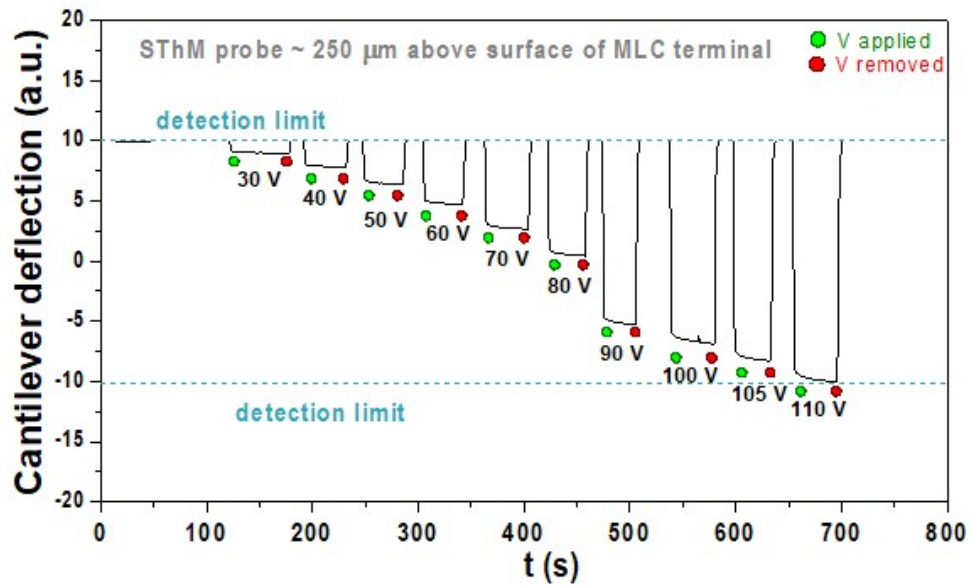
Fig. 6.17 - Cantilever deflection as a function of time for different values of $V_{applied}$ when SThM probe is initially placed ~ 250 μm above the MLC terminal surface and cantilever deflection signal initially placed near the maximum detection limit of the photodetector.

Fig. 6.18 shows the effect of the voltage applied to the MLC terminals on cantilever deflection as a function of time when the SThM probe is initially placed ~ 230 μm above the MLC terminal surface. The results shown are consistent with the ones observed for the initial tip position of ~ 250 μm above the MLC terminal surface, in Fig. 6.15.
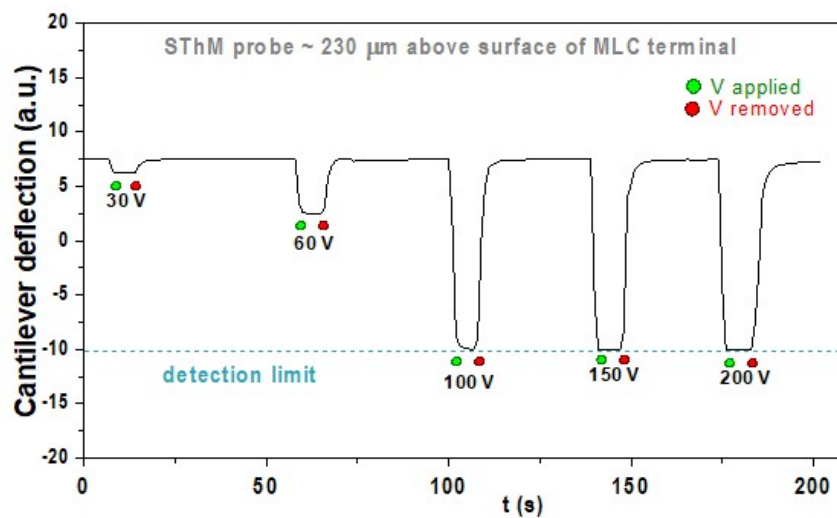
Fig. 6.18 - Cantilever deflection as a function of time for different values of applied V when SThM probe is initially placed ~ 230 μm above the MLC terminal surface.

Figs. 6.19 and 6.20 show the effect of the voltage applied to the MLC terminals on cantilever deflection as a function of time when SThM probe is initially placed ~ 210 μm above the MLC terminal surface. The sudden change in cantilever deflection due to initial V applied unsurprisingly reaches the detection limit for a lower value of V applied, since the cantilever is now closer to the sample that is sustaning the electrical field. Applying V higher than 100 V provides useless information for this study.

When the SThM probe is initially placed ~ 210 μm above the MLC terminal surface (Fig. 6.20) it is now between 70 V and 80 V that the effect of the electrical field in cantilever deflection starts to manifest

starts to show in a distinct way. At 80 V we find the more accentuated initial drop in cantilever deflection. The drop in cantilever deflection over time while V is applied presents similar slopes for the different lower voltages until V = 70 V. For $V_{applied}$ = 80 V and 90 V the slope value seems to increase.
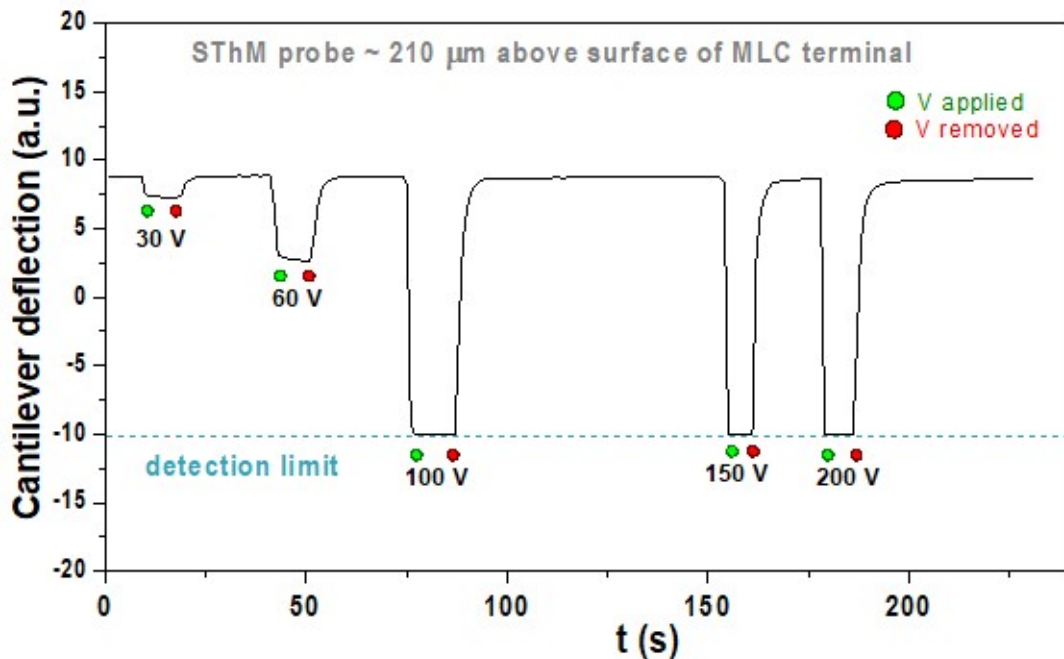
Fig. 6.19 - Cantilever deflection as a function of time for different values of applied V when SThM probe is initially placed ~ 210 μm above the MLC terminal surface.
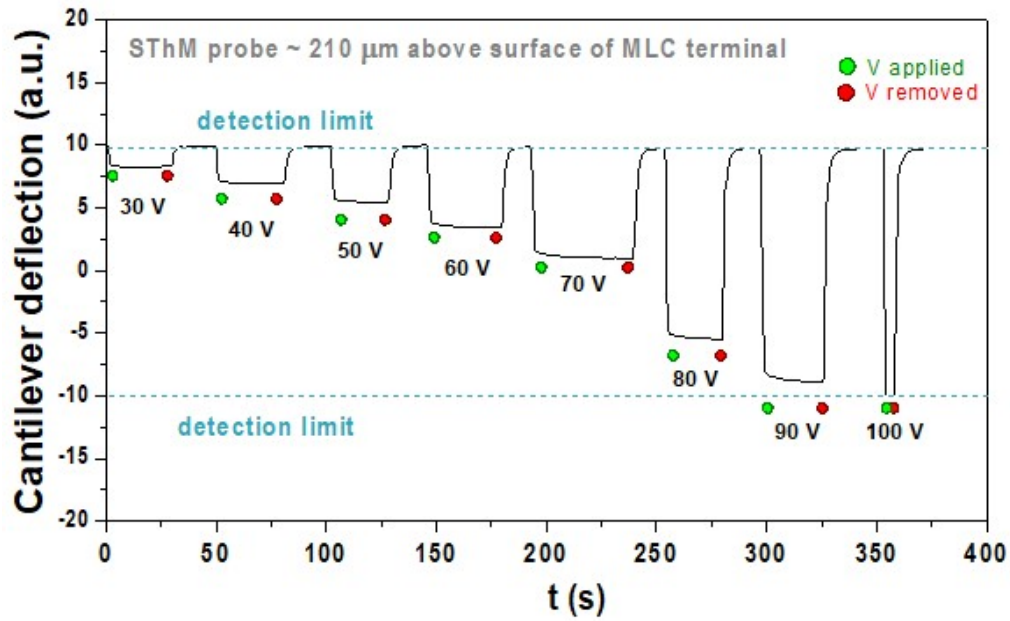
Fig. 6.20 - Cantilever deflection as a function of time for different values of $V_{applied}$ when the SThM probe is initially placed ~ 210 μm above the MLC terminal surface – more $V_{applied}$ values featured than in the plot in Fig. 5.20.

Figs. 6.21 and 6.22 show the plots for the variation in cantilever deflection (difference between cantilever deflections when V is on and off) vs V applied to the MLC terminals when the SThM probe is initially placed ~ 250 μm and ~210 μm, respectively, above the MLC terminal surface using the results from the three different tests previously shown in Figs. 6.15 to 6.17 and Figs. 6.19 to 6.20, respectively.

These plots show that the results obtained from different tests performed for the same initial tip to sample distance are consistent. Also, the observations already made concerning the effect of the electrical field on the behavior of the cantilever were accurate.

A direct comparison of the results obtained from tests performed at different initial tip to sample distances is shown in Fig. 6.23, which displays the variation in cantilever deflection vs applied V for the three distances of SThM probe from MLC terminal surface studied.
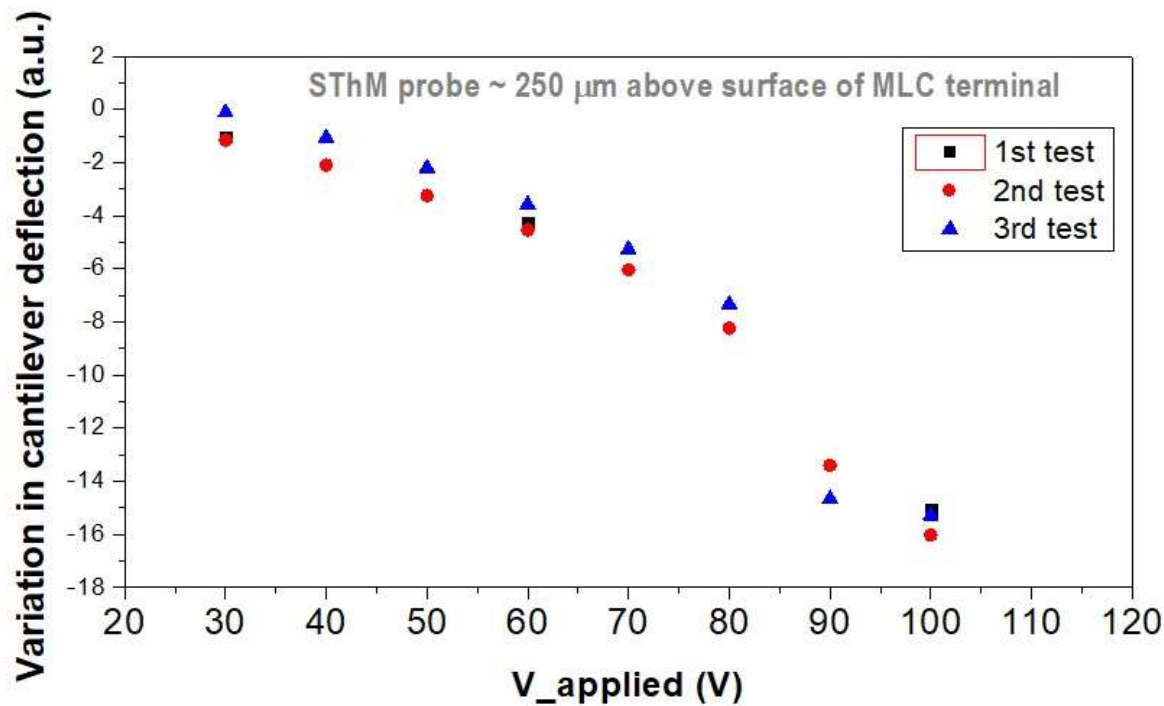
Fig. 6.21 - Plot of variation in cantilever deflection (difference between cantilever deflections when V is on and V is off) vs V applied to the MLC terminals – results for three different tests when the SThM probe is initially placed ~ 250 μm above the MLC terminal surface.
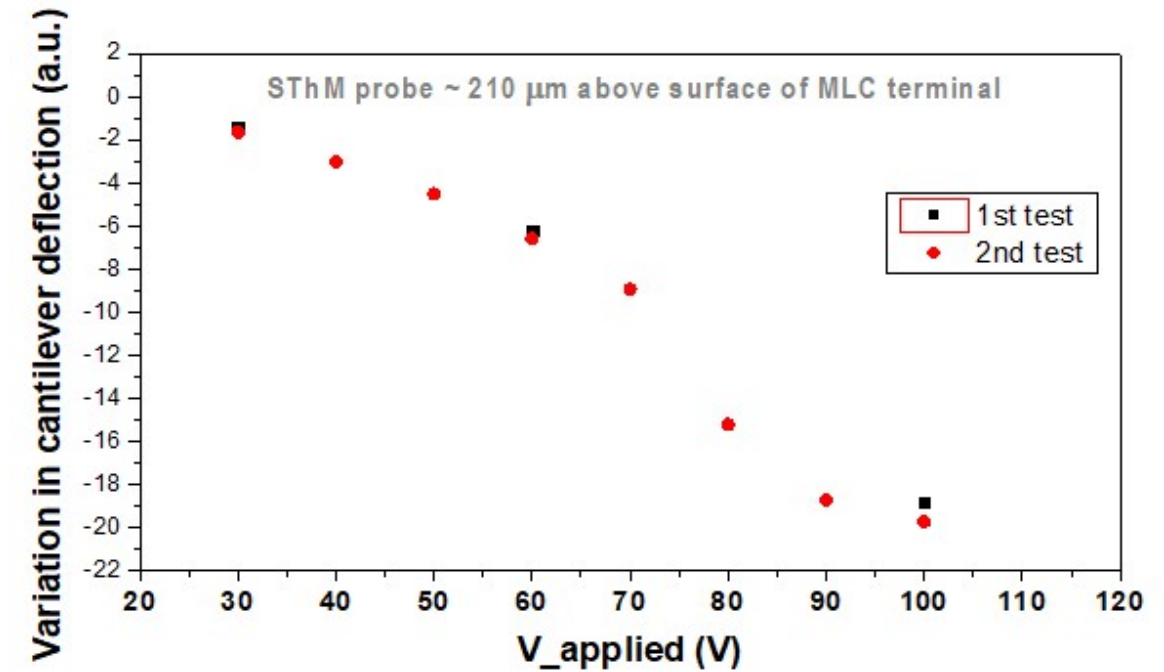
Fig. 6.22 - Plot of variation in cantilever deflection (difference between cantilever deflections when V is on and V is off) vs V applied to the MLC terminals – results for two different tests when the SThM probe is initially placed ~ 210 μm above the MLC terminal surface.
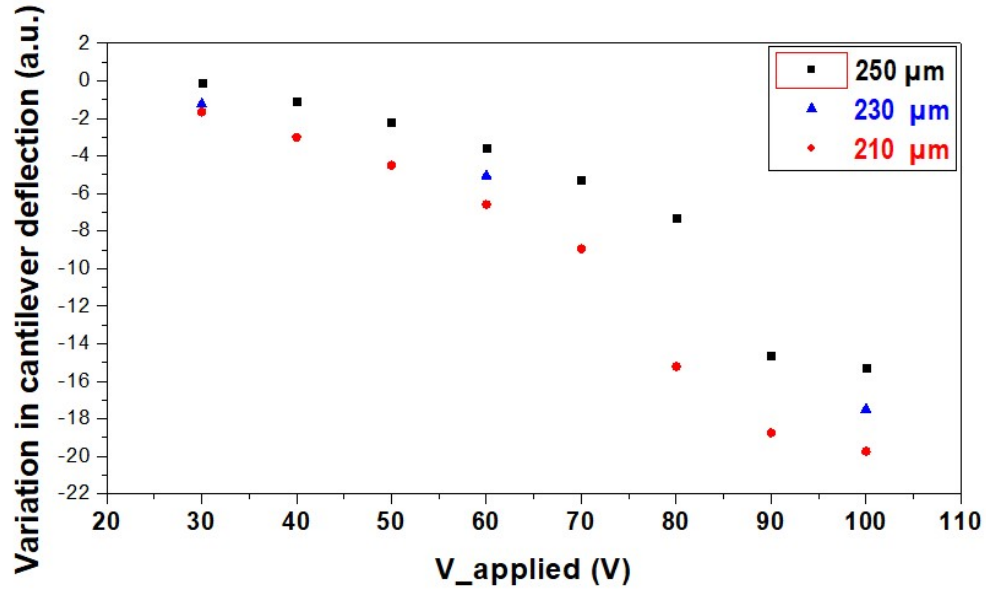
Fig. 6.23 - Variation in cantilever deflection vs applied V for the three distances of SThM probe from MLC terminal surface studied.

The changes in cantilever deflection can be accentuated or lessened, depending on which area of the cantilever is receiving the laser beam. The changes can be lessened by positioning the laser nearer the edge where it is attached to the support of the probe (as far away from the tip as possible). Placing the laser in this position will limit the information on the cantilever changes occurring where we are interested the most, which is as near to the tip as possible.

It would have been interesting to perform the exact same tests of cantilever deflection behavior with applied voltage while reversing the polarization of the voltage applied. However, the breakdown in the SThM module prevented us from applying a 0.1 mA current to any SThM probe available. Although, as already mentioned, the 0.1 mA current flowing was dismissed as having any relevance to this effect, the same conditions of the here presented study could not be reproduced for the reverse polarization study. For that reason, the study was not conducted.

From the plots above presented we see that the z position of the probe is changed from its initial location while the electrical field is on. So, at the voltage needed for obtaining a measurable temperature variation due to the EC effect, 200 V, the electrical field bends the cantilever, changing its position beyond our

knowledge, outside the limits of detectability (-10 $\leq$ cantilever deflection signal $\leq$ 10, a range that typically corresponds to several hundreds of nanometers [182]). This indicates that the position of the tip in relation to the surface of the MLC terminal can be dramatically changed during the EC effect measurement and we must take this into consideration while interpreting the EC effect study results. A deeper addressing of this issue was not deemed suitable as part of the role ultimately defined for this chapter within the scope of this dissertation.

6.6 – Final remarks

SThM has shown to be a technique that enables the direct measurement at the nanoscale of a ΔT in electrocaloric materials by subjecting them to an electrical field. In this sense, we can say that SThM can successfully directly measure the EC effect at the nanoscale. However, the main conclusion drawn from our study in conjugation with those performed by Kar Narayan and Shan is that, how close the measured ΔT is to the actual ΔT resulting from the EC effect, taking into consideration the impact of collateral effects, is not straightforward.

While Kar-Naryan *et al.* [98] consider that Joule effect has no relevant impact on the measured value of ΔT, Shan *et al.* [179] demonstrate that heating by Joule effect is significant, thus interfering with the EC effect measurement. They suggest a correction for the Joule heating effect.

7 – MAGNETOCALORIC EFFECT

Like for other caloric effects major trends, current research in magnetocalorics may be faced from the materials engineering perspective, where the mechanisms of the effect at the macroscopic scale are considerably well understood and the main goal is to find the materials that maximize its magnitude. Another challenge presents itself in a more fundamental light, since currently the more promising and achievable applications reside in the context of the micro and nano scales [32], where the quirks of the effect are not yet entirely unveiled, preventing proper control and full use. Localized nano and micro-thermal characterization plays a huge role in this endeavor [32][41], and techniques such as scanning thermal microscopy and infrared thermography are assets to be used as vigorously as possible in these explorations.

Ni-Mn-Ga's martensitic transformation has been extensively explored in the work already described in this dissertation. As further proof of its richness (if any was still needed), we will once again resort to it, this time to study the magnetocaloric effect at the microscale with infrared thermography. Near the martensitic transformation, the magnetocaloric effect is enhanced due to sharp differences in the magnetizations of the phases involved. In this chapter, though, instead of using a ternary Ni-Mn-Ga parent alloy, we will use a Co doped Ni-Mn-Ga quaternary compound. While the parent alloy usually has a martensitic phase with higher magnetization than the austenitic phase, the presence of Co in the alloy reverses this characteristic and, while still introducing a massive difference between the magnetizations of the two phases, it is now the austenite which possesses the upper hand when it comes to magnetization values [64].

7.1 – Sample characterization

To study the magnetocaloric effect (MCE) at the microscale, we have used a bulk NMG sample doped with Co (Sample NCMG279), with the nominal composition $Ni_{44}Co_6Mn_{30}Ga_{20}$. The sample was prepared by Simone Fabbrici at IMEM-CNR, Parma, in a section of the Magnetic and Multiferroic Materials group led by Franca Albertini. More detailed information on sample composition is presented in this chapter.

The sample can be seen in Fig. 7.1. The sample is about 8 mm long, 4 mm large and 1 mm thick.
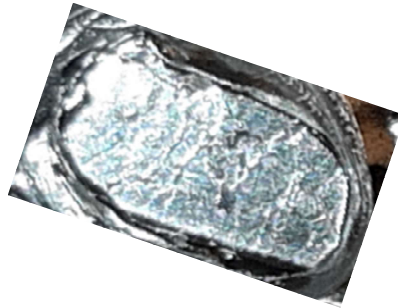
Fig. 7.1 - Image of sample NCMG279, a $Ni_{44}Co_6Mn_{30}Ga_{20}$ bulk alloy.

7.1.1 – Magnetic properties of sample NCMG279

The sample's magnetization (Figs. 7.2 and 7.3) and magnetic susceptibility (Fig. 7.4) dependence on temperature were measured. Fig. 7.5 shows magnetization vs magnetic field at different temperatures.

All magnetic measurements were performed with the SQUID magnetometer described on chapter 2.

The sample's magnetization (Figs. 7.2 and 7.3) and magnetic susceptibility (Fig. 7.4) dependence on temperature show that the structural transformation conveniently occurs approximately at room temperature for this quaternary compound with a "ferro-ferro" transition. In Fig. 7.2, the behavior presented by the sample on the ZFC results below 75 K seems to suggest spin-glass behavior, previously mentioned in other works [183] [184]. Fig. 7.2 shows, through the

derivative of the magnetization, that the reverse martensitic transformation (in heating) occurs at about 297 K and the direct martensitic transformation (in cooling) occurs at approximately 288 K. Fig. 7.3, showing a close-up of the M(T), allow a clear observation of the magnetization behavior through the transformations. Fig. 7.4 provides information on the Curie temperature, which is approximately 430 K.

Table 7.1 shows the values for the saturation magnetization and coercive field for each temperature. It is worth noting that the saturation magnetization does not show a monotonic behavior as a function of temperature due to the occurrence of the transformation between two phase that have different magnetic moments (the moment/F.U. of austenite is higher than that of martensite). On the other hand, the drastic decrease of coercivity by crossing the transformation on heating reflects the lower magnetocrystalline anisotropy of austenite with respect to martensite. Values for the specific saturation magnetization are also shown for purposes of comparison with values available in literature. Although there are no reference values for the specific composition of this sample, we find that these values are compatible with those measured for samples with the composition $Ni_{43}Co_7Mn_{30}Ga_{20}$ [182].
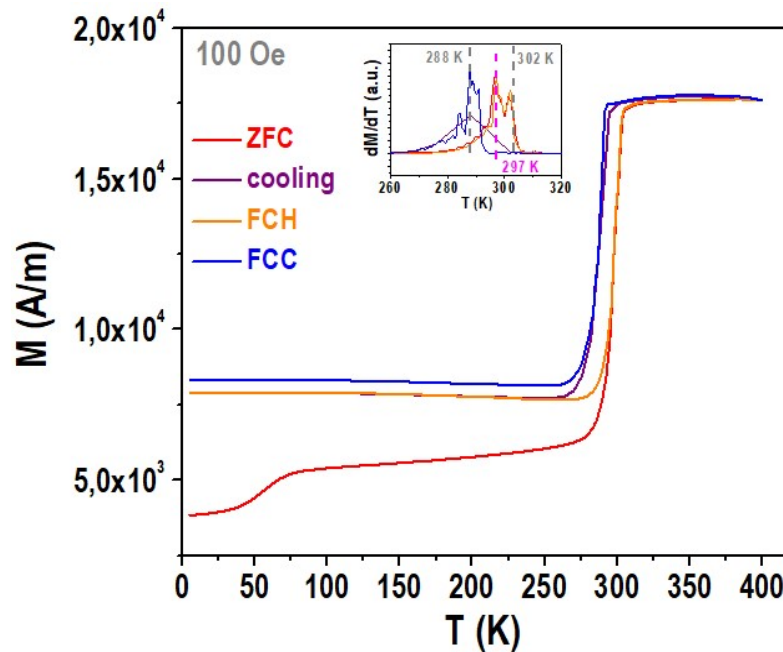
Fig. 7.2 - Magnetization vs temperature for sample NCMG279. ZFC: zero field cooled magnetization; cooling: magnetization of the sample during cooling after ZFC; FCH: Field cooled magnetization on heating after cooling; FCC: Field cooled magnetization on cooling after FCH.
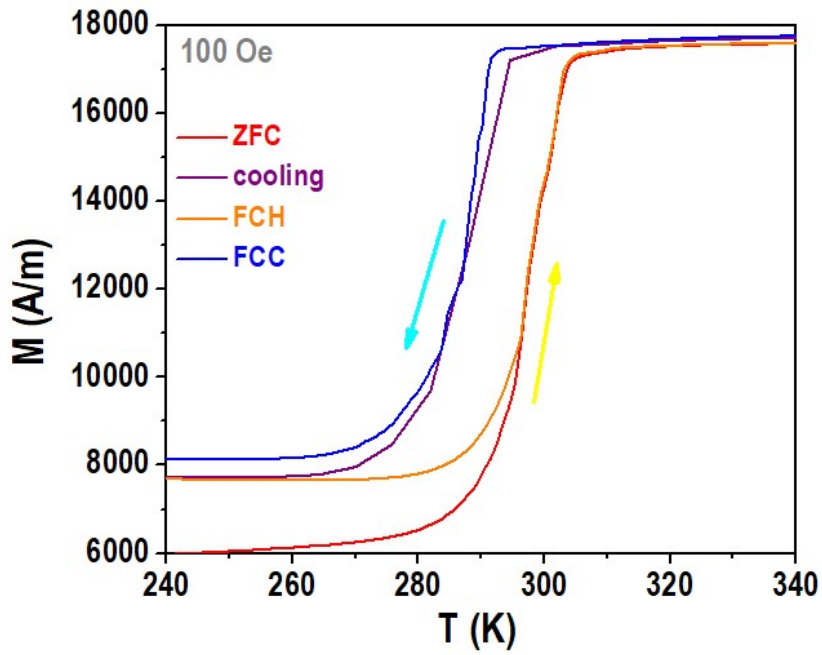
Fig. 7.3 - Magnetization as a function of temperature for sample NCMG279: close-up.
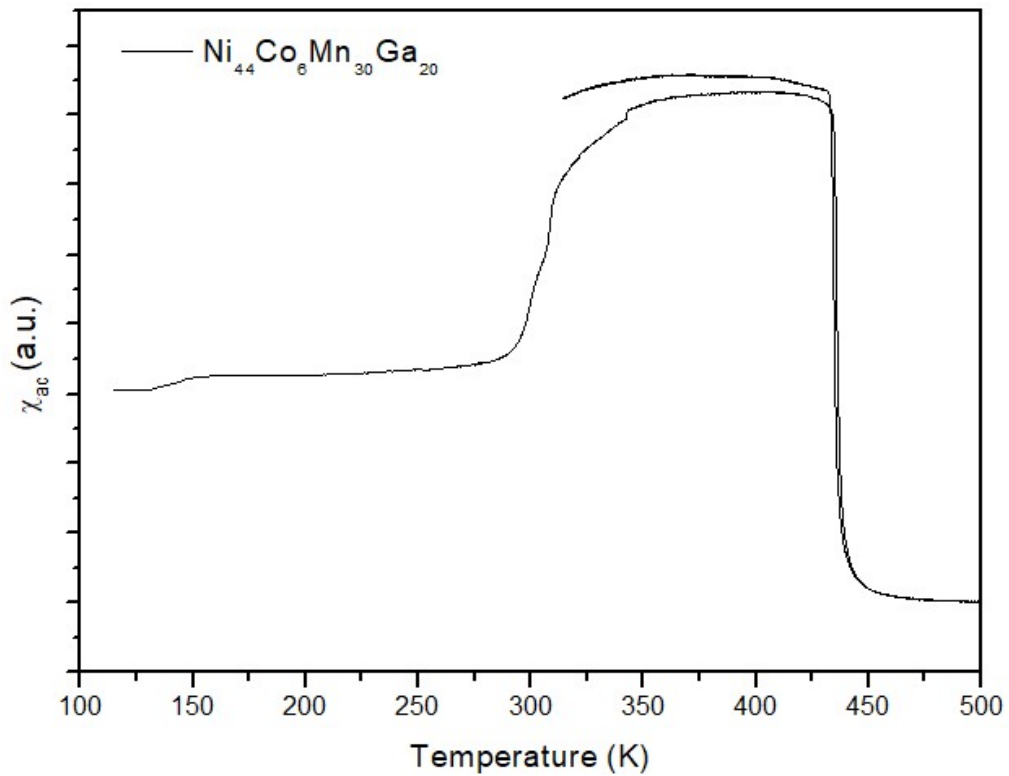
Fig. 7.4 - Magnetic susceptibility χ_ac as a function of temperature for sample NCMG279 (measurement performed at IMEM-Parma).
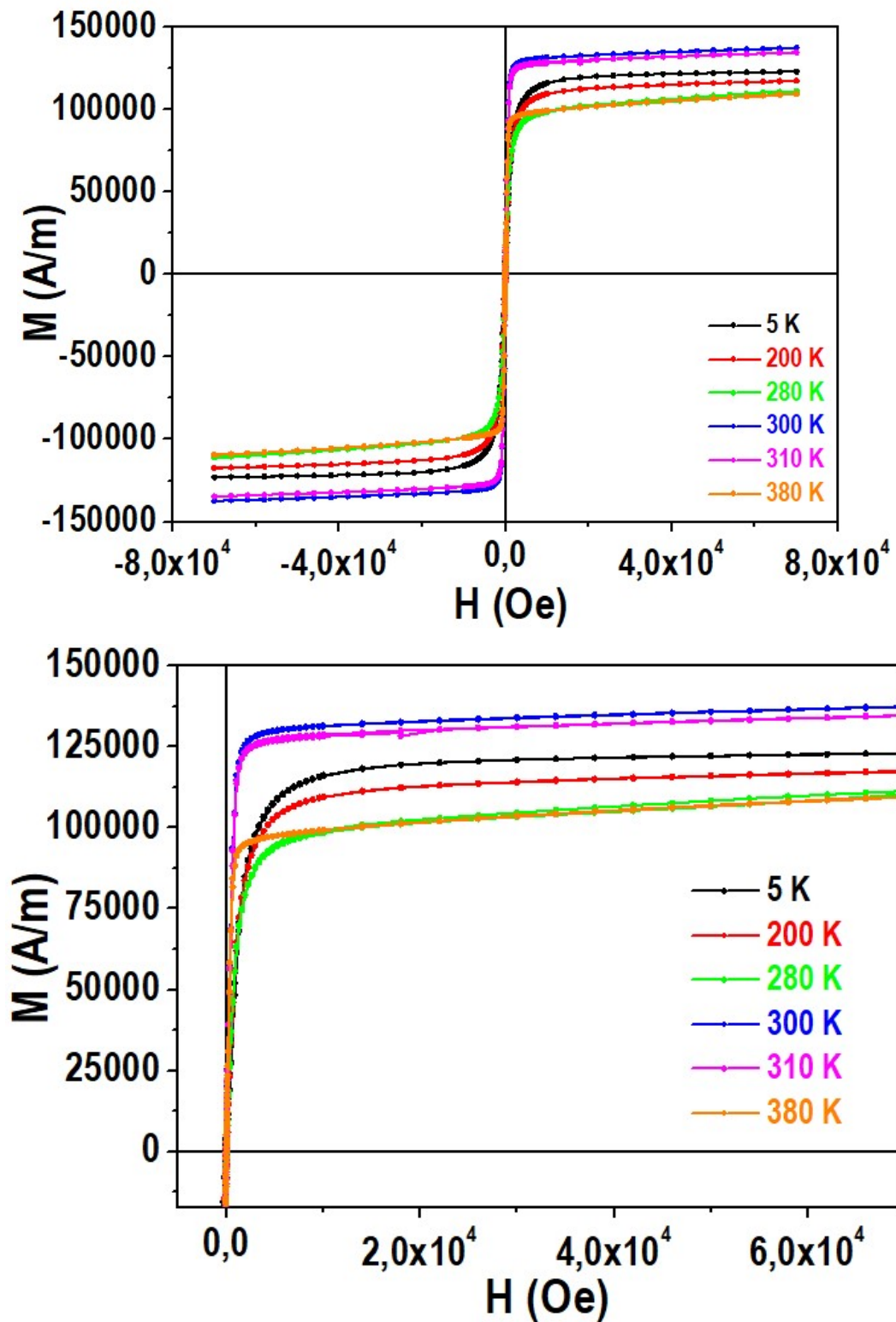
Fig. 7.5 - Magnetization vs magnetic field at different temperatures for sample NCMG279.
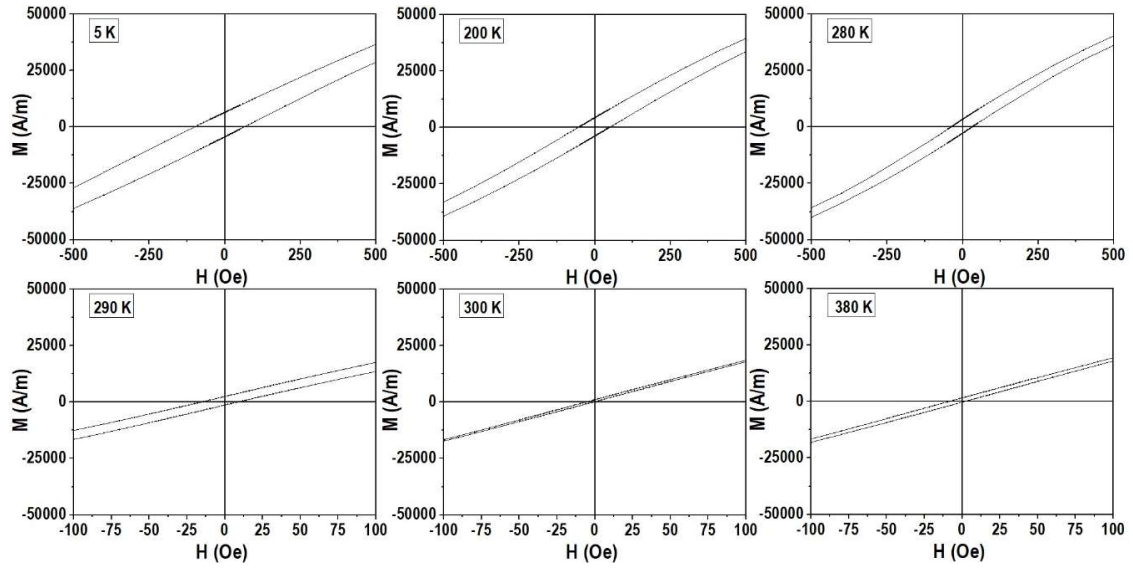
Fig. 7.6 - Coercive field (H_C) for different temperatures for sample NCMG279.

Table 7.1 - Saturation magnetization and coercive field values for several temperatures of the NCMG279 sample

Temperature (K)	Saturation magnetization (10^5 A/m)	Specific saturation magnetization (Am^2/Kg)	Coercive field (Hc)
5	1,2300	71,90	82,8
200	1,1750	68,68	51,4
280	1,1100	64,88	34,8
290	-	-	12,1
300	1,373	80,26	2,5
310	1,3500	78,91	-
380	1,1000	64,30	5,2

7.1.2 – EDS analysis of sample NCMG279

Fig. 7.7 shows an image of sample NCMG279 which was divided in six different areas which were analyzed by EDS. SEM images of one of these areas is shown in Fig. 7.8. SEM images for the five remaining areas can be found in Appendix II. In each of these six areas, the composition of three different points (spot area: radius ~ 0,4 μm) was analyzed. The quantified results are compiled on Table 7.2 and the respective spectra are shown in Appendix II.

The average of the EDS results for each of the six analyzed areas lead us to a composition $Ni_{44\pm4}Co_{6\pm1}Mn_{27\pm2}Ga_{23\pm2}$ (the uncertainty was considered as the major

of individual uncertainties rounded to unit), which is compatible with the initial information obtained on the composition of the sample after preparation at IMEM-Parma, stating that we are in the presence of a $Ni_{44}Co_6Mn_{30}Ga_{20}$ alloy.
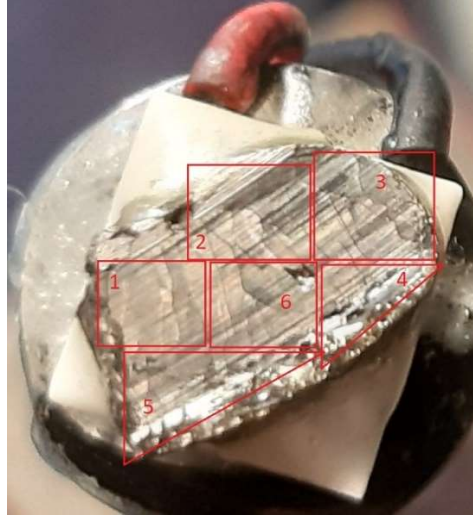
Fig. 7.7 - Image of sample NCMG279 with different areas analyzed by EDS signaled.
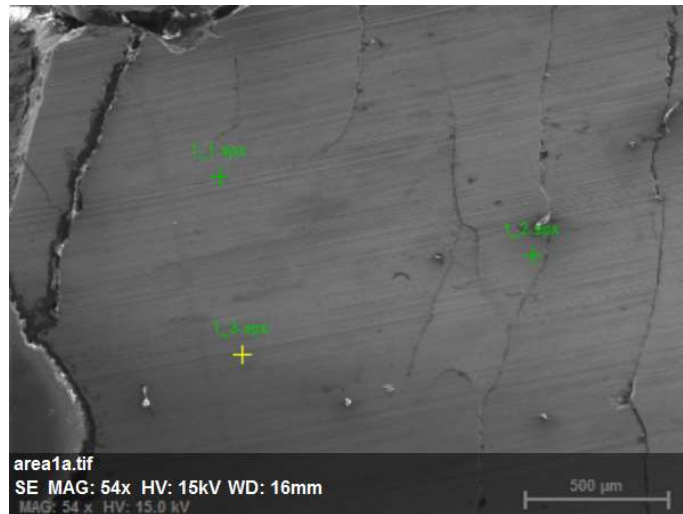
Fig. 7.8 - SEM image of area corresponding approximately to area 1 signaled in Fig. 6.7.

The plots in Figs. 7.9 and 7.10 show plots comparing the EDS results obtained for the 6 areas and for the points within these areas, respectively, of the NCMG279 sample. Of all the elements present on sample NCMG279, Co is the most consistent in its percentage, in all areas and in the points analyzed within each area. The percentage of Ni is similar in areas 1, 2 and 3, which are poorer in this element than

areas 4, 5 and 6 (all three similar in Ni percentage). Mn is present in identical percentages in areas 1 and 4, where it is more abundant than in areas 2, 3, 5 and 6. Areas 1, 2 and 3 are similarly richer in Ga than areas 4, 5 and 6.

Table 7.2 - EDS results for the areas of the NCMG279 sample differentiated in Fig. 7.7 and points signaled within said areas in their corresponding SEM images (result for each area corresponds to beam incidence in the whole area)

AREA	POINT	Mn [wt%]	Co [wt%]	Ni [wt%]	Ga [wt%]
1	-	**27.5 ± 2.4**	**5.5 ± 0.7**	**43.7 ± 4.0**	**23.3 ± 2.8**
	1.1	26.5 ± 2.4	6.5 ± 0.8	46.6 ± 4.45	20.43 ± 2.60
	1.2	26.8 ± 2.4	6.1 ± 0.8	42.7 ± 4.00	24.42 ± 3.10
	1.3	28.2 ± 2.4	5.3 ± 0.6	41.7 ± 3.68	24.74 ± 2.90
2	-	**26.2 ± 2.3**	**5.7 ± 0.7**	**43.6 ± 4.1**	**24.5 ± 3.0**
	2.1	26.2 ± 2.3	6.0 ± 0.7	43.7 ± 4.1	24.1 ± 3.0
	2.2	28.3 ± 2.5	6.4 ± 0.8	44.3 ± 4.1	21.0 ± 2.6
	2.3	25.9 ± 2.3	6.1 ± 0.8	46.0 ± 4.4	22.0 ± 2.8
3	-	**26.6 ± 2.4**	**5.9 ± 0.8**	**43.1 ± 4.0**	**24.4 ± 3.0**
	3.1	26.8 ± 2.3	5.7 ± 0.7	42.2 ± 3.9	25.3 ± 3.0
	3.2	26.0 ± 2.3	6.1 ± 0.8	43.8 ± 4.1	24.1 ± 3.1
	3.3	26.3 ± 2.4	5.7 ± 0.7	43.3 ± 4.1	24.7 ± 3.1
4	-	**28.4 ± 2.4**	**6.0 ± 0.7**	**44.5 ± 3.9**	**21.1 ± 2.5**
	4.1	26.4 ± 2.4	5.6 ± 0.7	43.1 ± 4.1	24.9 ± 3.1
	4.2	27.7 ± 2.4	5.6 ± 0.8	44.0 ± 4.0	22.7 ± 3.0
	4.3	26.5 ± 2.4	5.7 ± 0.8	43.4 ± 4.1	24.4 ± 3.2
5	-	**26.7 ± 2.4**	**6.2 ± 0.78**	**45.4 ± 4.2**	**21.7 ± 2.7**
	5.1	26.6 ± 2.3	6.1 ± 0.74	45.2 ± 4.1	22.1 ± 2.7
	5.2	26.4 ± 2.2	6.3 ± 0.74	44.2 ± 4.0	23.1 ± 2.8
	5.3	28.7 ± 2.4	6.2 ± 0.76	43.9 ± 3.9	21.2 ± 2.6
6	-	**26.7 ± 2.4**	**6.0 ± 0.7**	**45.6 ± 4.2**	**21.7 ± 2.7**
	6.1	27.6 ± 2.4	6.5 ± 0.8	44.1 ± 4.0	21.8 ± 2.6
	6.2	26.4 ± 2.4	6.2 ± 0.8	45.0 ± 4.2	22.4 ± 3.0
	6.3	25.1 ± 2.8	5.7 ± 1.2	43.2 ± 5.3	26.0 ± 5.1

A closer look at the plot in Fig. 7.10 informs us that, from the observation of the composition of three points per area, the least and most compositionally homogeneous are areas number 1 and 6, and areas 3 and 4, respectively. The elements whose percentage most varies are Ni and Mn, while Co presents quite stable percentage values all over.
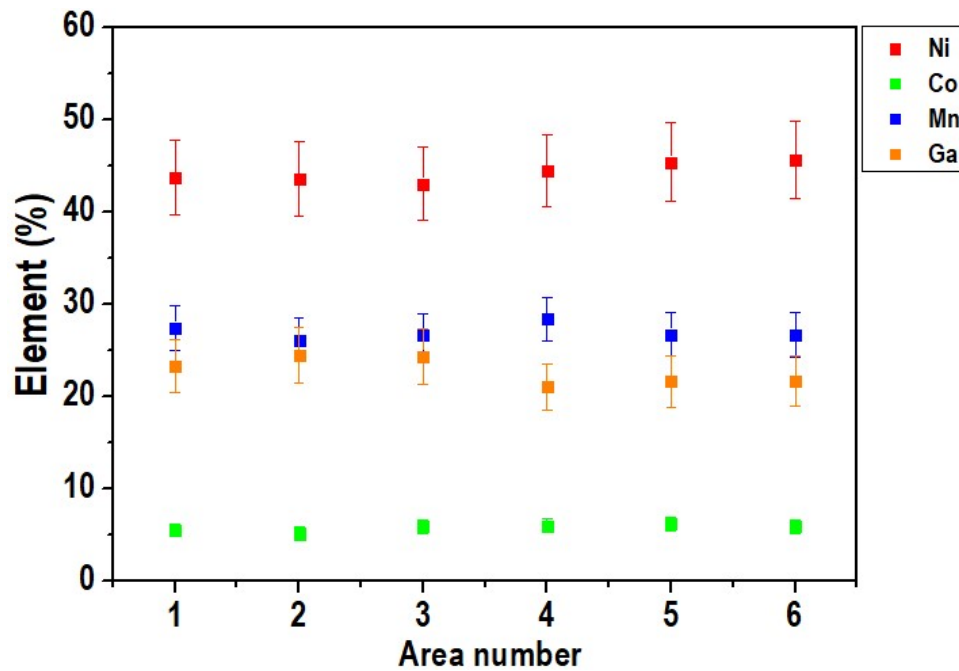
Fig. 7.9 - Plot comparing the EDS results obtained for the 6 areas of the NCMG279 sample.
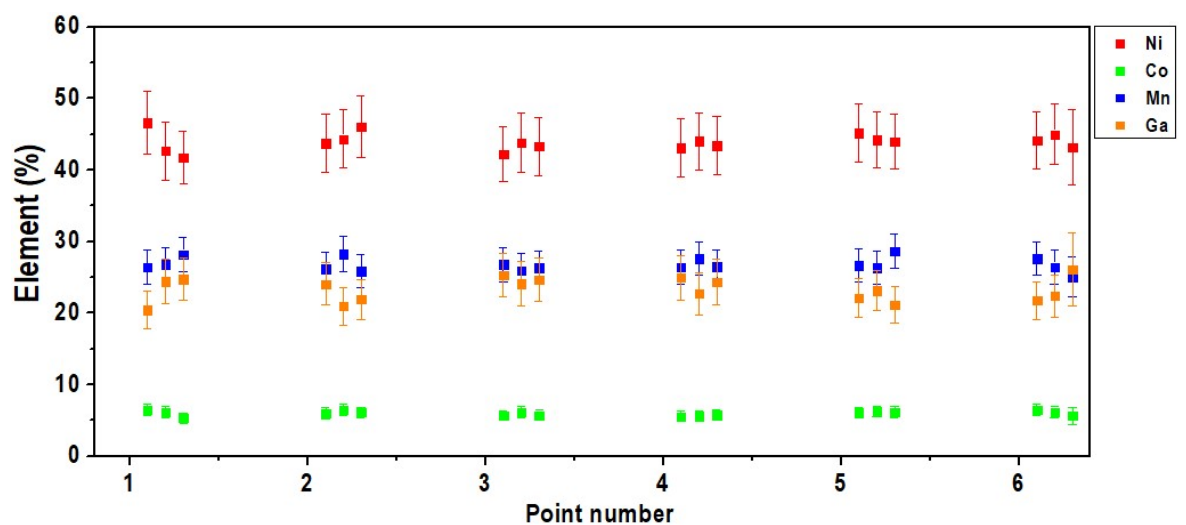
Fig. 7.10 - Plot comparing the EDS results obtained for the points within the 6 areas of the NCMG279 sample.

7.2 – Direct measurement of the magnetocaloric effect (MCE)

7.2.1 – Experimental setup

In the study of the magnetocaloric effect, we measure the (quasi-)adiabatic variation in temperature of a material when it is subject to a magnetic field.

In this study, the Ni-Co-Mn-Ga bulk sample (NCMG279) was mounted on a Peltier element, (which allowed to change the sample's temperature) and a thermocouple was attached to the sample. This assemblage was fixated on a setting where NdFeB permanent magnets in a Halbach geometry could be moved back and forth in order to be applied to and removed from the sample several times. Details on this setting will be provided in the next paragraphs and the complete setup is illustrated in Fig. 7.14. We have studied de MCE on the Ni-Co-Mn-Ga bulk sample for different sample temperatures (first by heating and later by cooling the sample to certain temperature "values") by applying and removing the magnetic field several consecutive times while the sample is kept at the same temperature.

For the study of the magnetocaloric effect on sample NCMG279, we use a support made of a ~1 m long aluminum rod (1,5 cm diameter) with a Peltier thermoelectric element (RS 490-1193, 6x6 mm^2, maximum current 2.2 mA, maximum voltage 0.9V) glued to one of its extremities. The aluminum rod is used as a heat sink for the Peltier element. The sample was then placed in contact with the free surface of the Peltier with thermal contact being established by a thermal paste placed between the bottom of the sample and the surface of the Peltier. The sample was then glued to the Peltier surface. A thermocouple type K was attached to the lateral of the sample, placed in contact with the sample's surface. The thermocouple was firmly fixated and pressed against the sample with Teflon tape. During this process, some parts of the sample's surface near the edges were partially covered with glue and Teflon tape, which can be seen in the setup photos and the IR camera measurements (Figs. 7.18 and 7.37). The setup was coated with a thin layer of black acrylic spray paint black in order to have a surface with the emissivity close to 1 and thus improve the accuracy of the IR camera measurements. The thermocouple and Peltier wires were firmly held in place around the aluminum rod. The aluminum rod

with the sample was then inserted in a PVC beige tube wider in diameter (aluminum rod with sample inside the PVC beige tube). A black tube made of cardboard was inserted on the end side of the PVC tube where the sample is located, to protect the sample area from external sources of radiation. Images depicting these steps are shown in Figs. 7.16 to 7.18. The set was then incorporated in the setup shown in Fig. 7.14.
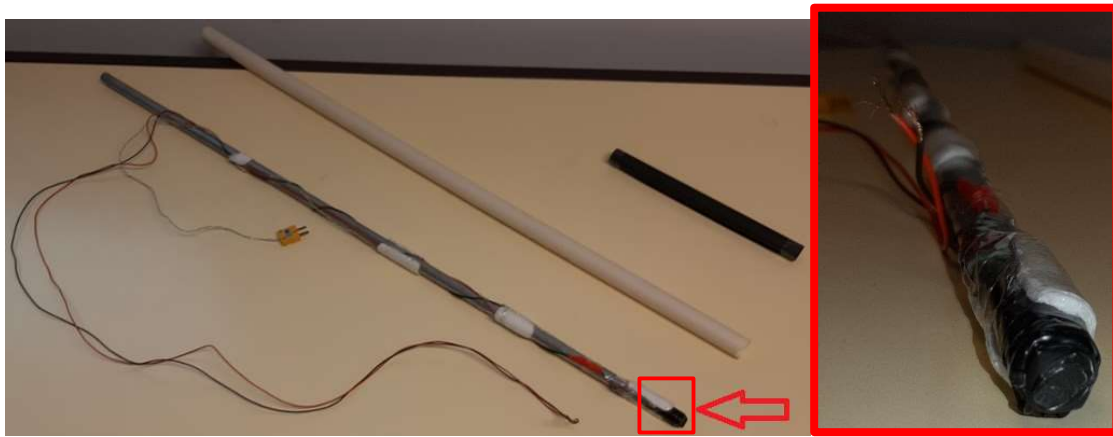
Fig. 7.11 - Left: Aluminum rod with Peltier and thermocouple wires attached, and sample mounted on Peltier in one extremity, PVC tube and black cardboard tube; Right: extremity of the aluminum rod where the sample is mounted.
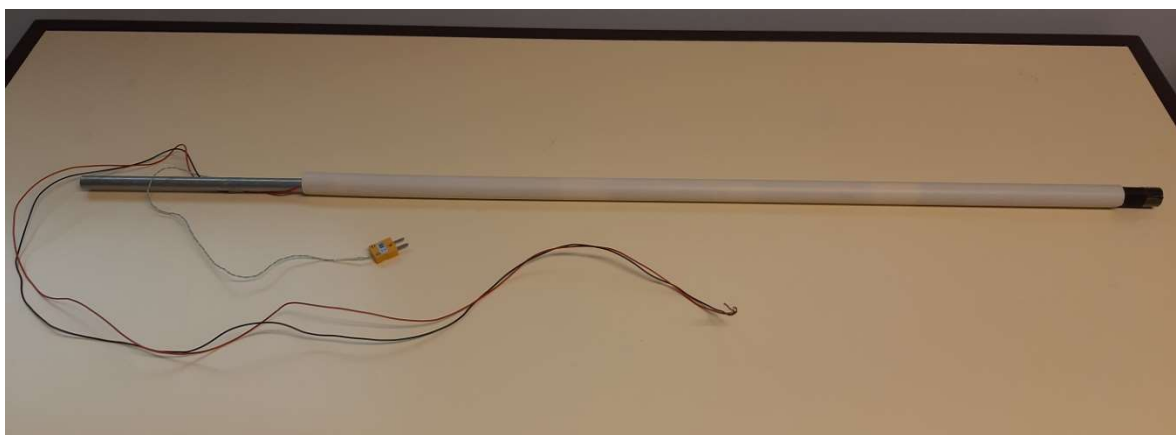
Fig. 7.12 - Aluminum rod with sample inside the PVC beige tube with black paper to protect sample area from external sources of radiation.

The magnetic field was produced by an assembly of NdFeB permanent magnets of grade N45 in a Halbach geometry. The Halbach magnet has inner and outer diameters of 30 and 100 mm, respectively, and a thickness of 100 mm. With a 10 mm wall thin aluminum housing, it possesses a mass of 6.95 kg (Fig. 7.15). The permanent magnets were positioned in the K2 configuration magnetization pattern (Fig. 7.16), which provides the most homogeneous and intense magnetic field inside the Halbach.

Fig. 7.13 - Photos of the sample after being sprayed with black paint.

The setup used to apply and remove the magnetic field while the IR camera measured the magnetocaloric effect is shown in detail in Fig. 7.14.
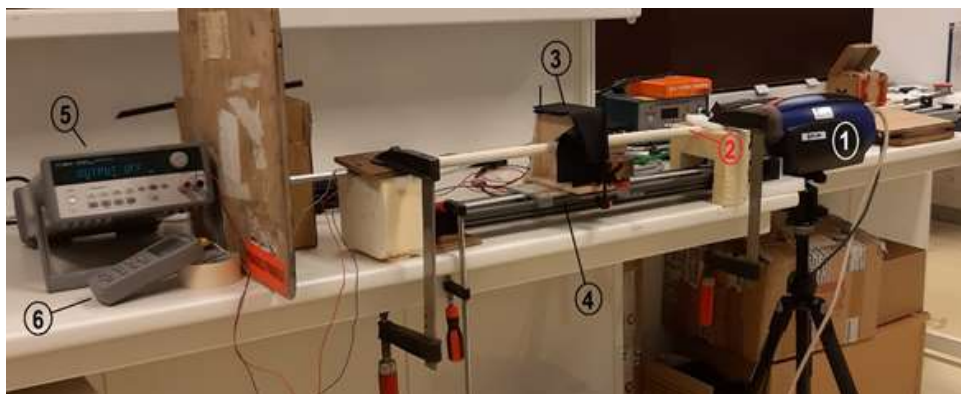
Fig. 7.14 - Setup used to apply and remove the magnetic field to the sample: 1) IR camera; 2) Area where sample is located inside the PVC tube; 3) Magnet (Halbach); 4) Actuator (moves the magnet towards and away from the sample); 5) Voltage source that feeds the peltier; 6) Temperature monitor.

The homogeneity of the magnetic field was investigated, both axial and in plane. Using COMSOL Multiphysics Software v 4.3 and resorting to the magnetic field module, a simulation was performed for the magnetic field along the z-axis, which is along the aluminum rod (holding the sample) cylinder axis. The sample's surface is positioned at z = 0 when the Halbach's movement ceases and the magnetic field remains applied to the sample until it is removed. According to the simulation (Fig. 7.17), a maximum magnetic field of 1.37 T would be expected, while experimental data point to a maximum of about 1.2 T. The experimental data were obtained by placing a Hall probe on the setup depicted in Fig. 7.14. The Hall probe took the place which was later occupied by the sample to be used in the study of the magnetocaloric effect.

Fig. 7.15 - Image of the magnet used in the setup.
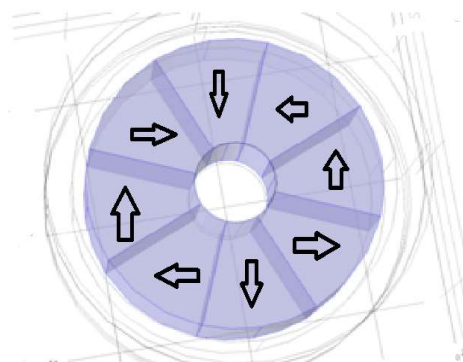
Fig. 7.16 - K2 magnetization pattern of the Halbach.
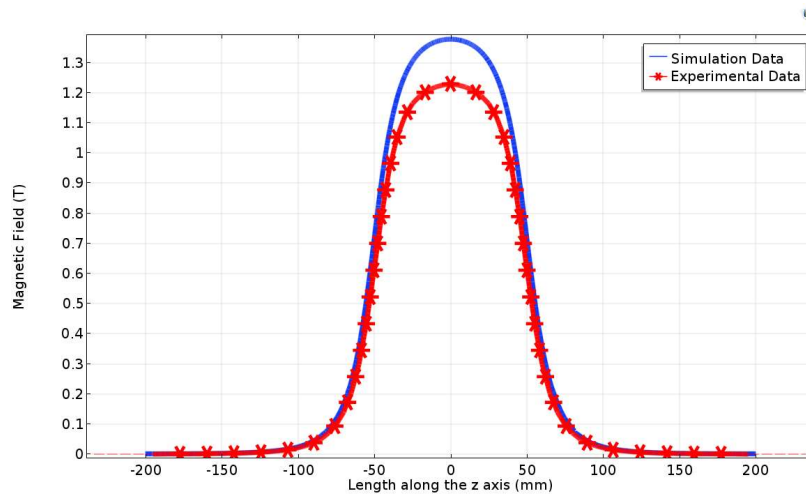
Fig. 7.17 - Magnetic field along the z-axis (through the center) of a Halbach with an external diameter of 100 mm, thickness of 100 mm and inner diameter of 30 mm: simulation and experimental data.

The actuator accelerates the Halbach to a constant speed of about 0.5 m/s within about 5 milliseconds. When the Halbach approaches the sample, the actuator decelerates it to zero, also within about 5 milliseconds. The following link will take you to a video showing the Halbach in motion: https://youtu.be/fZwC3F6ZtMw. Figs. 7.18 and 7.19 show simulations for the magnetic field inside the Halbach in the xy and yz planes, respectively.

Details about the setup of the actuator that moves the Halbach are depicted in Fig. 7.20: the setup is composed by a drylin® ZLW series Standard toothed belt axes [185], along which the actuator slides, energized by a motor. This motor is powered by the transformer which connects to a regular socket and is controlled by an IGUS motor controller [186]. This controller connects to the motor and to a computer, through which the motor (and thus the actuator motion) can be controlled. This control by computer is performed through online software provided by IGUS [186].

The IR camera is the FLIR SC5600-M, described in section 4.2.
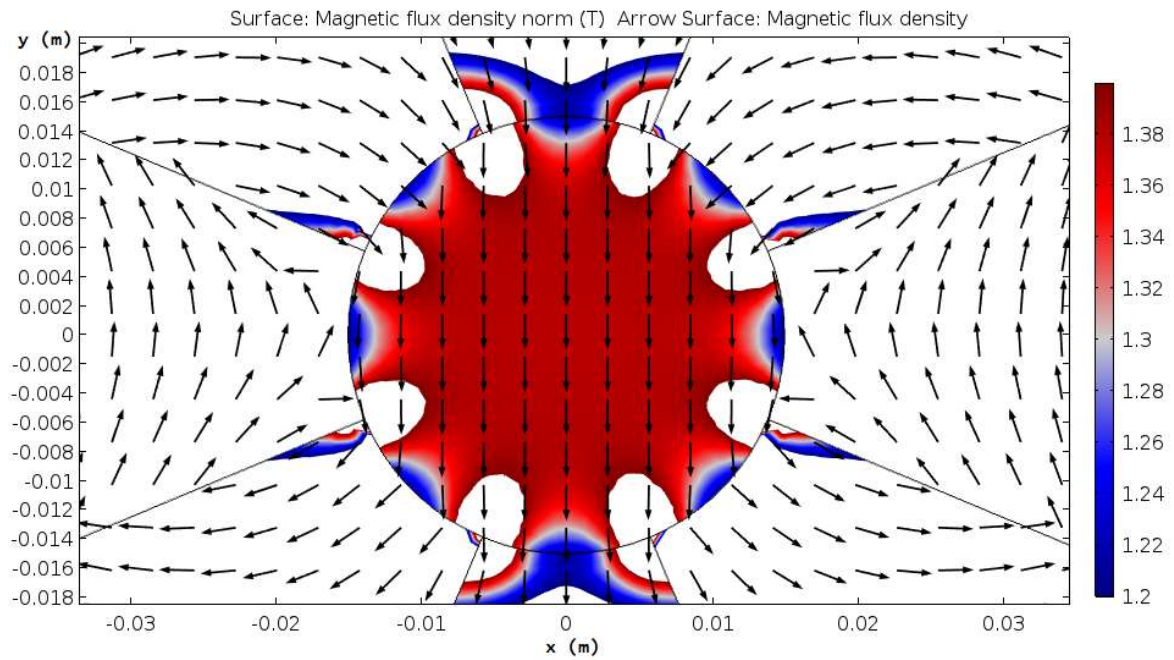
Fig. 7.18 - Magnetic field inside of the Halbach in the xy plane: simulation.
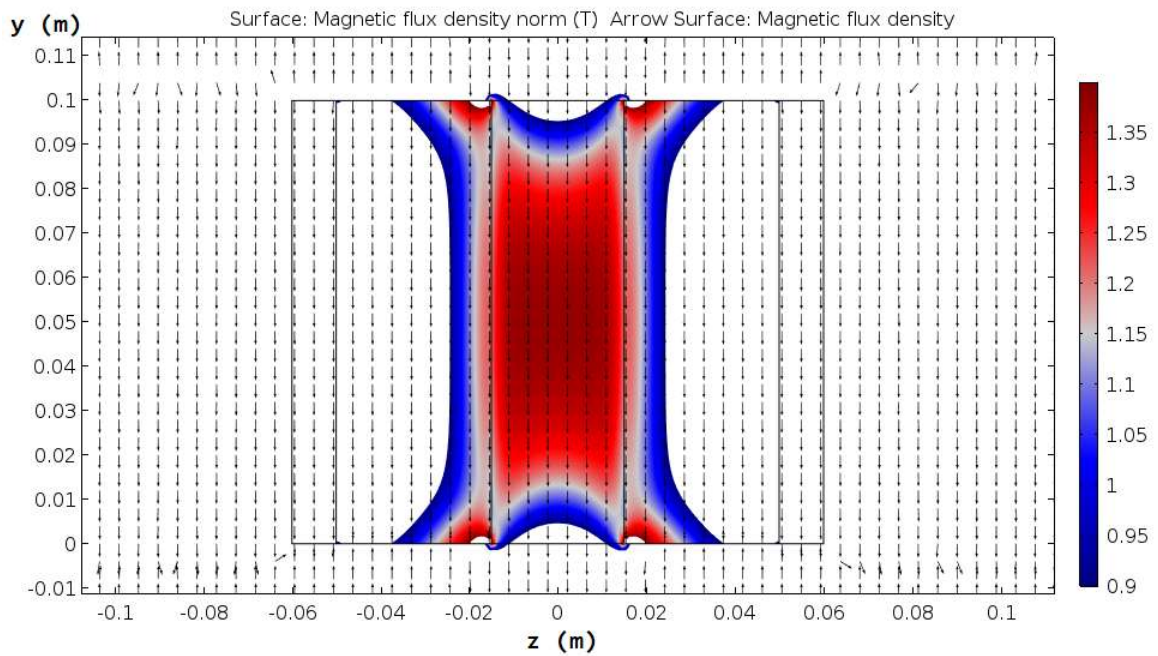
Fig. 7.19 - Magnetic field inside of the Halbach in the yz plane: simulation.
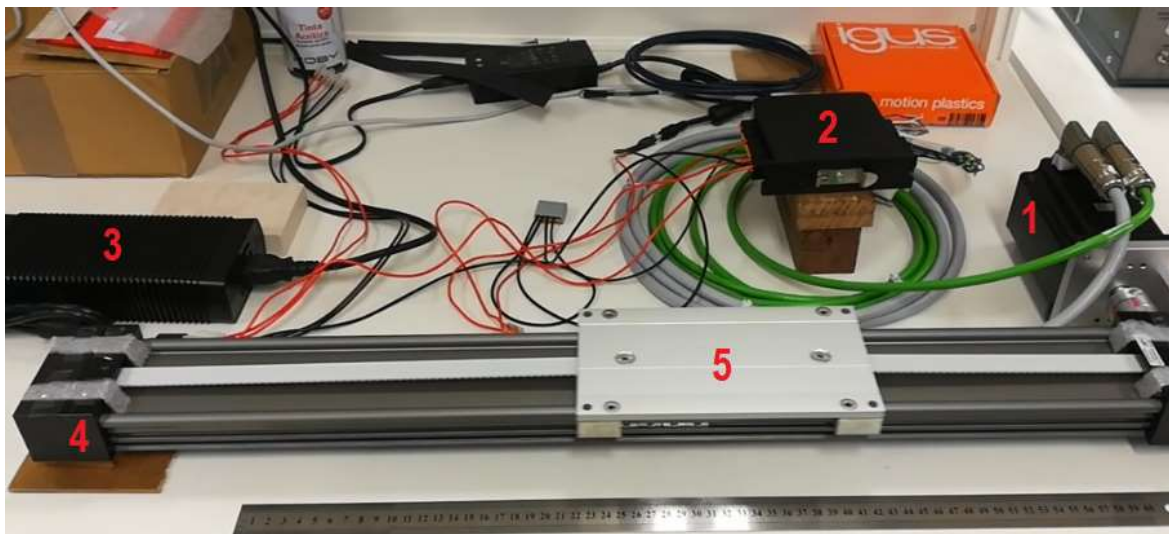
Fig. 7.20 - Details on the setup of the actuator that moves the Halbach: (1) motor; (2) igus motor controller; (3) transformer; (4) drylin® ZLW toothed belt axes, (5) actuator.

Fig. 7.21 shows a comparison between a photograph of the sample when mounted on the Peltier exactly as it is when introduced in the setup to be measured by the IR camera (top) and the image collected by the IR camera (bottom) when the sample was at 316.4 K and no magnetic field applied. The temperature scale of the image provided by the IR camera is on the right. The image provided by IR camera shows two areas bounded by a blue (outer) line and a yellow (inner) line. Further explanation will be given on these lines when discussing Fig. 7.22a, but it is important to notice in this comparison, that the blue line is touching the limits of the sample where it is covered with Teflon tape, and that the yellow line is safely defined within the exposed area of the sample.

7.2.2 – Experimental procedures

The IR camera measurements of the MCE on sample NCMG279 were performed by following two different protocols: protocol A, for setting temperature, and protocol B, for measurement under field.

Protocol B is performed within protocol A.

Let us begin with protocol A.
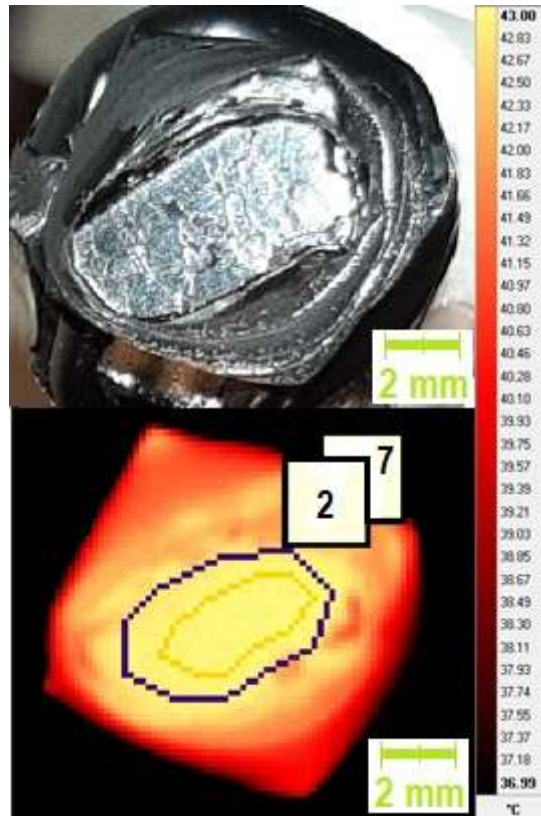
Fig. 7.21 - Photograph of the sample when mounted on the Peltier (top) and image provided by the IR camera when the sample was at 316.4 K and no magnetic field applied (bottom).

Protocol A consists in first cooling the sample to 272.8 K (well below the sample's T_M suggested by M(T) measurements) with the Peltier element at zero field. Since the temperature was varied by manually controlling the power applied to a Peltier element, the temperature variation rate in time (dT/dt) is not precisely defined nor easy to estimate. With the IR camera measuring the sample's surface temperature (as can be seen in Fig. 7.21) and the Peltier element maintaining the sample at 272.8 K, protocol B (described below) is performed. After protocol B is applied, the Peltier element increases the sample's temperature (T_{sample}) to 273.8 K (zero field). Protocol B is performed. At zero field, T_{sample} is lowered to 272.8 K with the Peltier element, and then increased to 277.0 K. Protocol B is performed. Again, T_{sample} is lowered to 272.8 K (zero field). T_{sample} is then increased at zero field to higher values, with protocol B being performed for each of these values and the sample being cooled to 272.8 K (at 0 field) before being heated to a different T_{sample} value.

This process takes place for successively higher T_{sample} values until we reach T_{sample} ~ 340 K, where no measurement is performed due to inability to maintain that temperature stable. The sample is then cooled to 323.3 K (at zero field). Protocol B is performed. The sample is heated at zero field to ~ 340 K and then cooled to 321.6 K. Protocol B is performed. This process takes place for successively lower T_{sample} values until we reach T_{sample} = 266.8 K, where protocol B was performed.

Protocol B consists in the following procedure: while the Peltier element keeps the sample's temperature at a given T_{sample} value, in the absence of magnetic field, the temperature of the sample starts to be measured by the IR camera. Then, the Halbach is accelerated towards the sample (and the IR camera), reaching the speed of 0.5 m/s within about 5 milliseconds, decelerating within a similar timeframe, and finally stopping while placing the sample's surface at the position z = 0. The Halbach remains in this position for about 5 seconds, after which it pulls away from the sample, in the opposite direction. This retreating motion of the Halbach has the same characteristics as the approaching motion. This approach and retreat process is done several times, with about 5 seconds between each performance. In between performances, the sample's temperature measured by the IR camera is the result of the combination of the power supplied by the Peltier element and the occurring of the MCE. Fig. 7.22 shows a schematics of protocols A and B.
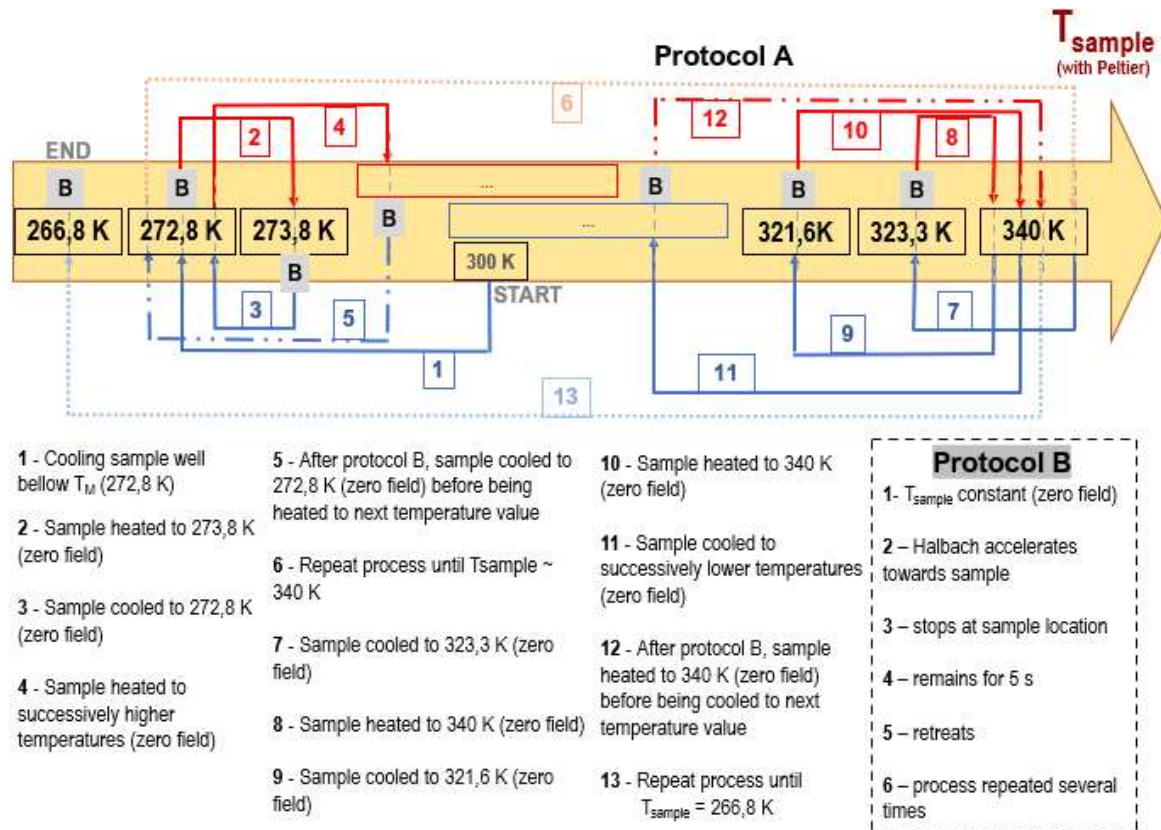
Fig. 7.22 - Schematics of protocols A and B.

7.2.3 – Direct measurement of (quasi-)adiabatic variation in temperature when NCMG279 is subject to a magnetic field at different temperatures

The IR camera provides the temperature data for each pixel and allows the study of selected areas. A smaller and a larger area of the sample were analyzed. These areas and the information collected are represented in Figs. 7.23a and 7.23b. These were taken at the temperature stage of 297.9 K, during the heating process. In Fig. 7.23a, the area signaled with number 7, encircled, by the blue line, is the larger area, while the area signaled with the number 2, encircled by the yellow line, is the smaller area. These areas were already shown in Fig. 7.21, which allows us to identify which areas of the sample we are now considering. In Fig. 7.23b, the plot shows us the minimum, maximum and average temperature values registered in areas number 7 and 2, within 50 seconds of measuring with the IR camera, while the magnetic field was consecutively applied and removed from the sample. Area 7,

being wider, would provide better statistics for an average result, but being placed so near the border between the covered and uncovered parts of the sample could introduce undesired uncertainties. Smaller area 2 was surely providing results concerning only the uncovered surface of the sample. Results showed no significant difference between the average values observed for the magnitude of the MCE in the studied temperatures. It is important to notice that the maximum and minimum temperature values collected for each instant may correspond to different pixels.
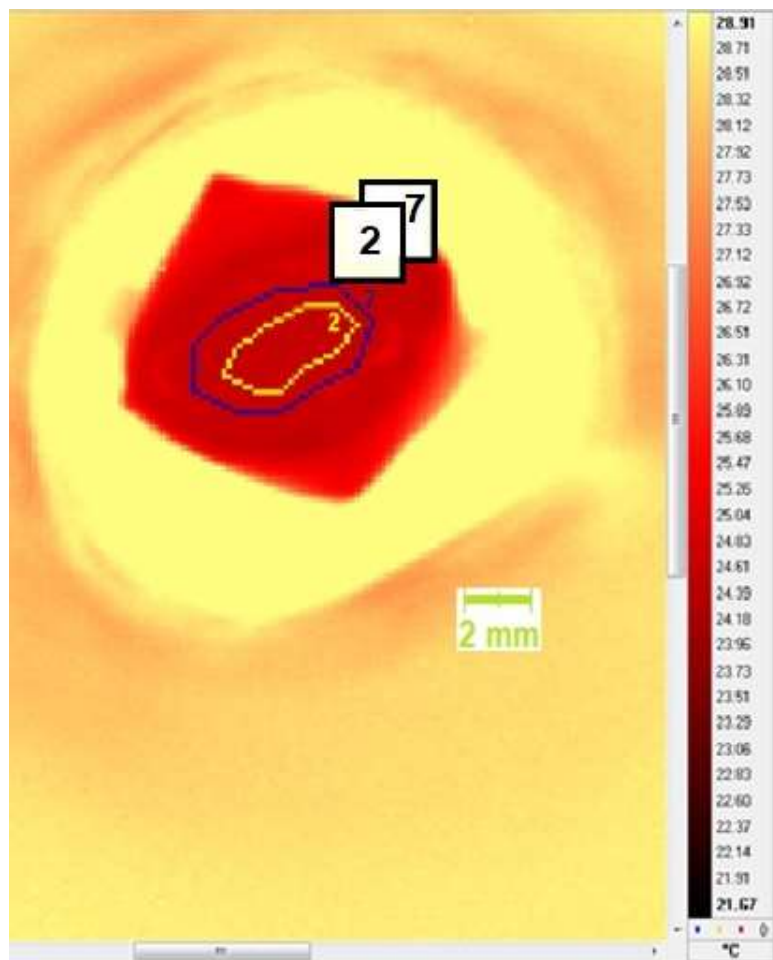
Fig. 7.23a - Infrared image of the sample provided by the IR camera when T_{sample} = 297.9 K.
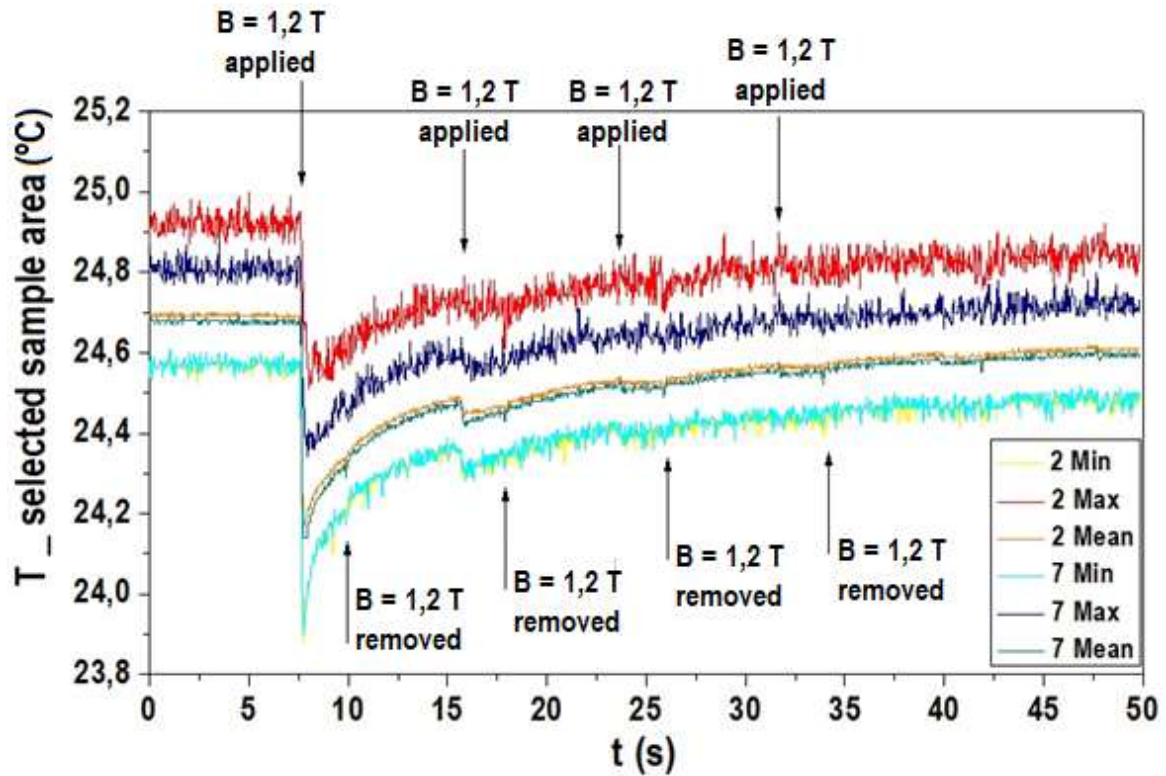
Fig. 7.23b - Plotted data provided by the IR camera when T_{sample} = 297.9 K.

The plot in Fig. 7.23b allows us to observe that the first removal of the magnetic field and subsequent field applications and removals of field possess specific characteristics which are relevant for this study, one of them being the dramatic reduction of the magnitude of the MCE observed mainly due to the hysteretic nature of the martensitic transformation. At this point in the chapter, we will focus solely on the results obtained for the first application of the magnetic field, and we will postpone the analysis of the response of the sample to the ensuing actions of the magnetic field for later in this chapter.

We calculated the variations in the mean value of T for the different sample temperatures and plotted them as a function of sample temperature (Fig. 7.24).
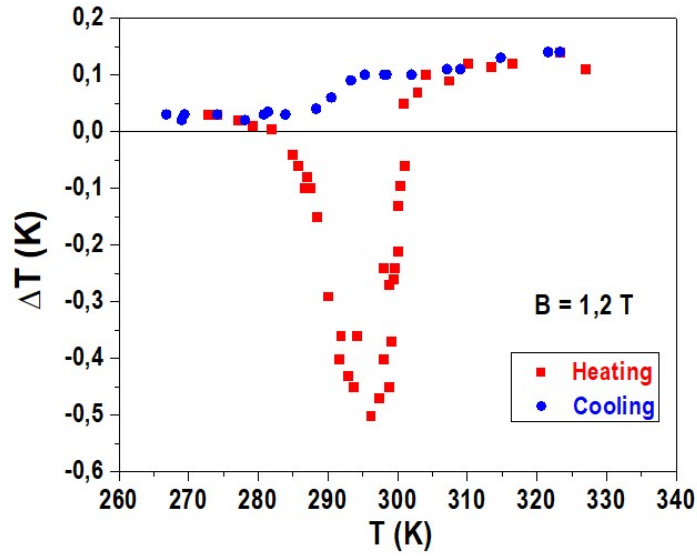
Fig. 7.24 - Variation in the average temperature measured for the smallest selected area (2) when B = 1.2 T is applied (in heating and cooling).

Figs. 7.25 and 7.26 show two representative examples of how ΔT values were calculated. Through observation of the plot of the mean average value of T of area (smaller area) over time, we have identified the occurrence of the MCE due to the first application of the magnetic field to the sample with the dramatic change in the temperature measured by the camera. We then took the highest/lowest T value observed "immediately" after the manifestation of the effect and the lowest/highest T value observed "immediately" before the manifestation of the effect, depending on whether we were in the presence of the direct/reverse MCE. Sample temperature was measured by the type K thermocouple in contact with the NCMG279 sample's surface. Differences in calibration between the IR camera and the thermocouple attached to the sample can be responsible for shifts (in absolute terms) in temperature readings performed by both. The relationship between the measured values by both devices was evaluated (Fig. 7.27).

ΔT values were obtained with a 0.04 ºC uncertainty, which is the maximum oscillation of the average temperature of area 7 (used to calculate T) in the instants before and after field application and removal for each considered sample temperature. This can be appreciated in Figs. 7.25 and 7.26, shown here as representative examples.
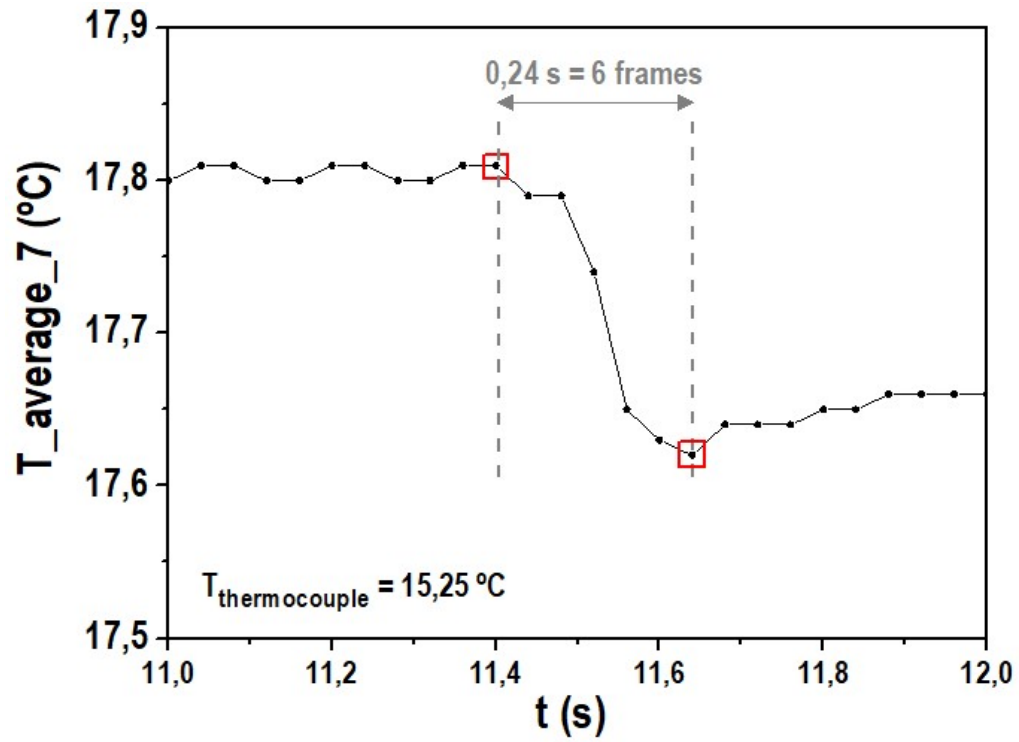
Fig. 7.25 - Average temperature of smaller area (7) for T_{sample} = 288.4 K in the heating part of protocol A.
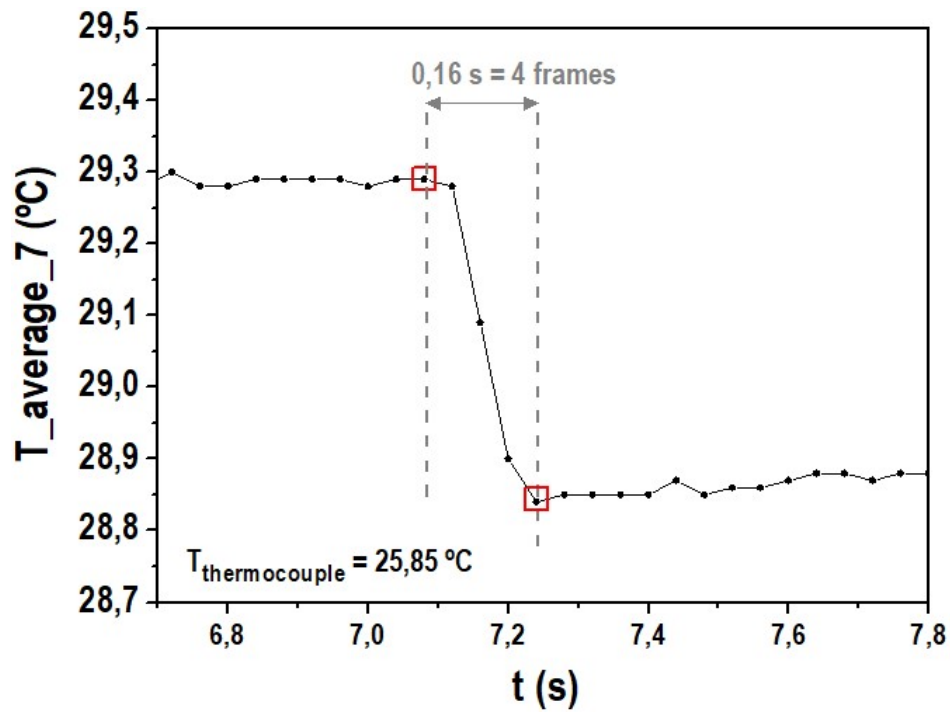
Fig. 7.26 - Average temperature of smaller area (7) for T_{sample} = 299.0 K in the heating part of protocol A.
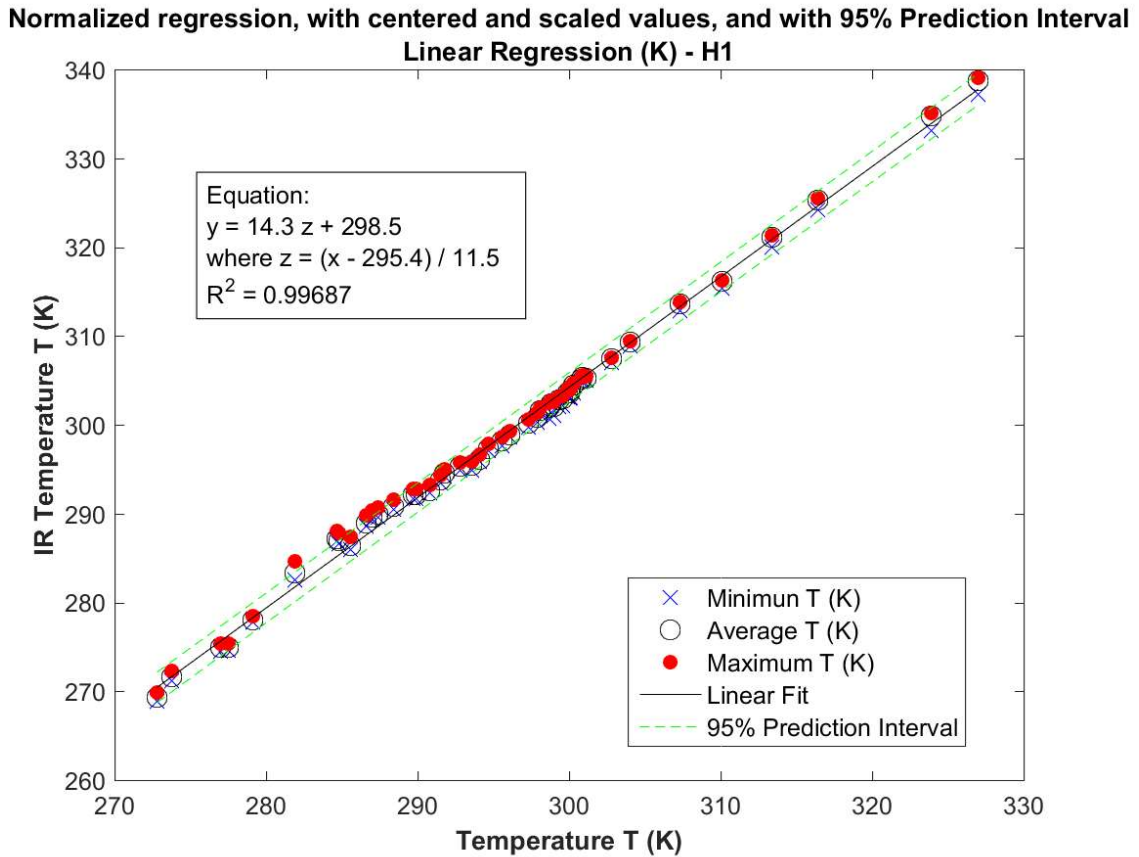
Fig. 7.27 - The relationship between the measured values by the IR camera (vertical axis) and the temperature measured by the thermocouple (horizontal axis).

In heating (red squares), the very slightly positive ΔT values observed for T< 285 K, correspond to a ferromagnetic martensitic phase, so a weak direct magnetocaloric effect (MCE) is to be expected. It is known that the presence of Co in these compounds mainly promotes the ferromagnetic interactions in austenite [182]. The negative ΔT values correspond to the inverse MCE, which is known to occur during the reverse martensitic transformation (in heating) [187].

Magnetization vs temperature curve in heating indicated, for low magnetic field applied, a reverse martensitic transformation occurring at approximately 297 K. Applying a magnetic field will move the structural transformation temperature within the estimated interval from -2.78 to -1.04 K/T [182]. Thus, under the 1.2 T applied field, this transformation temperature is expected to shift to a value approximately between 296 K and 294 K, which is where we observe the MCE occurs with highest

magnitude value of ΔT exhibited by the material in calculations performed after the measurements provided by the IR camera. This means that the SQUID thermometer's calibration agrees with the thermocouple's calibration and MCE measurements performed with the IR camera and the M(T) results are thus consistent. In cooling, during the magnetically stable austenitic phase, MC effect values are always positive and do not vary significantly until temperature reaches the approximate value of 293 K. At this temperature, MCE values present a slow decrease. When temperature reaches 284 K, MCE values stabilize at very low values. This is also consistent with the information provided by the M(T) measurements. The hysteresis observed in the heating and cooling M(T) curves ranges from 305.1 K to 259.4 K.

7.2.4 – Mapping and analysis of temperature values at the microscopic scale in NCMG279, with and without applied magnetic field

In the next set of figures (Figs. 7.28 to 7.44) we present series of images of the sample collected with the IR camera at different moments in time, while protocol B was beginning to be performed, thus before and after the magnetic field is applied to the sample for the first time, for different T_{sample} values.

Each pixel in the images corresponds to an area of about 85x85µm^2, and there are 0.04 ms between consecutive frames.

The temperature scales for these images can be determined either automatically by the IR camera software or manually by the user. In this case, they were selected by the user. This choice is key regarding which information we want to visually discern in the image provided by the IR camera. Subtle changes in the temperature of the sample require an appropriate temperature scale, sometimes with quite narrow temperature intervals. In those cases, differences in temperature occurring in the surroundings of the sample will become indistinguishable, since the temperature scale is not sensitive to such changes or may even not include the temperature values in question.

Fig. 7.28 shows the occurrence of the MCE on the exposed surface of the sample when the magnetic field is applied after the sample was heated to the temperature of 288,4 K. The average inverse MCE observed is of about -0,15 K (Fig. 7.24). The first image on the top row shows the uncovered area of the sample without applied magnetic field. In the following images, as the field is applied, it is quite clear that different areas of the sample respond differently to the presence of the magnetic field. There seems to be an area between most of the sample on the left and a small portion on the right part of the sample that does not contribute to the effect in an observable way. 0,680 s after the beginning of the magnetic field application (and while the field is still being applied), the sample is relaxing into equilibrium, though a different one from before the magnetic field was applied. Fig. 7.29 shows a plot of the average of temperatures of all the pixels at all instants (corresponding to each frame, which for this measurement means a 0.040 s difference between consecutive points) of the measurement when the sample is at 288,4 K (in heating). In the same plot, we can also see for each instant the temperature of the pixel that, at that specific instant, registered the minimum/maximum temperature amongst all pixels being measured. This means that, for each instant, we may very well be providing the temperature of different pixels, since certainly it is not always the same pixel that shows the maximum (or minimum) temperature at all times. This plot provides an idea of quantification of the effect. Fig. 7.28 makes it harder for us to quantify the effect when the data is thus presented, but it allows us to observe the phenomena semi-quantitatively pixel-by-pixel. Further along in this chapter we will show that resorting to MATLAB software, we can quantify the information concerning temperature variation for each pixel, at each instant, and handle the available data systematically to map the phenomena occurring microscopically over the whole sample. For now, it is reasonable to accept the type of representation in Fig. 7.28 to discuss qualitative aspects of the phenomena occurring on the sample.

Fig. 7.30 shows a close-up of the plot in Fig. 7.29 focusing on the instants featured in Fig. 7.28, and the due correspondence between instants and plot points is established. Fig. 7.31 provides the temperature distributions corresponding to the

maps represented in Fig. 7.28, when the MCE was studied after the NCMG279 sample was heated to 288.4 K. Such temperature distributions are known for other studied sample temperatures and Table 7.3 contains this information systematized for such sample temperatures. In this table, $T_{(center\ of\ distribution)}$ +(-) δT informs on the highest (lowest) pixel temperature value registered by the IR camera, and $T_{(highest\ number\ of\ events)}$ represents the temperature value most pixels presented, for each considered sample temperature at a given time.

Fig. 7.28 - IR camera images over time of sample NCMG279 after it was heated to the temperature of 288,4 K, before and after a magnetic field was applied.
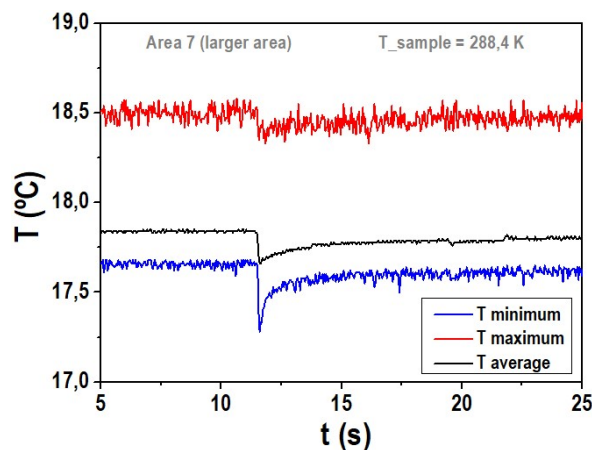
Fig. 7.29 - Plot of the average of temperatures of all the pixels for all instants of a given period of the measurement (T_{sample}=288,4 K, in heating), and the temperature of the pixels that, at a specific instant, registered the minimum/maximum value amongst all pixels being measured.

218
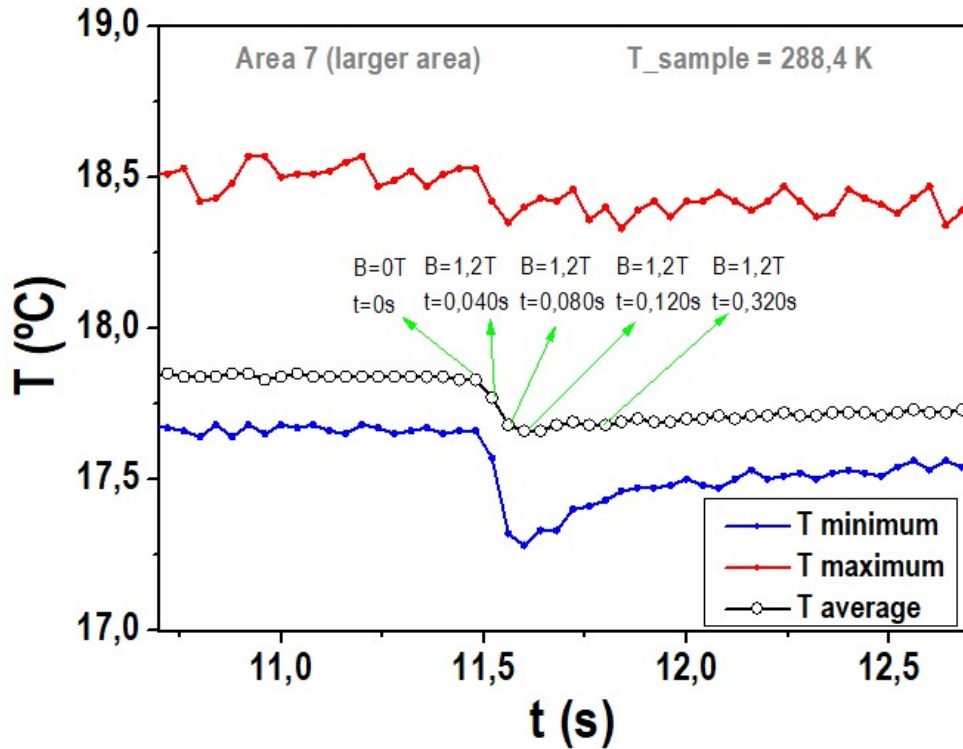
Fig. 7.30 - Close-up of Fig. 7.28 for the instants around the first field application; correspondence with the instants depicted in Fig.7.27 is established.

Fig. 7.32 shows that, when the sample is heated to 289,9 K, it shows a behavior quite like the one presented in the previous figure. The regions where the MCE is triggered are roughly the same, only the image resolution is slightly better due to the higher magnitude of the effect at this temperature ($\Delta T_{average}$ = -0,29 K).

In Fig. 7.33, the MCE is show for T = 292,8 K, where it has $\Delta T_{average}$ = -0,43 K. The regions where the effect manifests more intensely are the same, but the higher magnitude of the effect provides better image resolution and allows us to discern more vividly visual nuances as to how more precisely the changes in temperature in the affected areas evolve over time with the applied magnetic field. We can also notice that, until now, the effect seemed to be more intense on the left area of the sample, whereas for this temperature, the narrower area on the right seems to reach lower temperature values in the presence of the magnetic field.
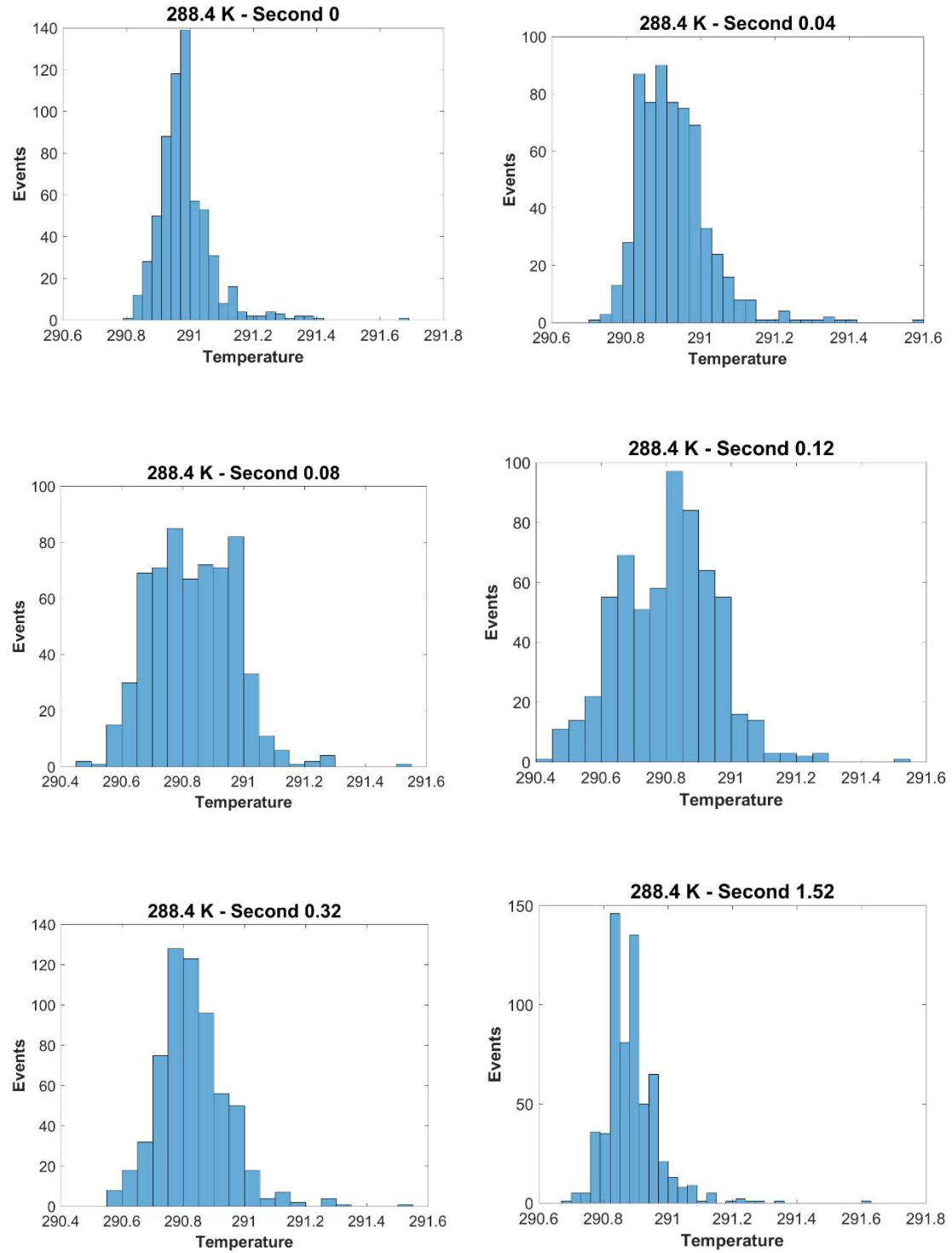
Fig. 7.31 – Pixel temperature distributions corresponding to the maps represented in Fig. 7.27, when the MCE was studied after the NCMG279 sample was heated to 288.4 K.
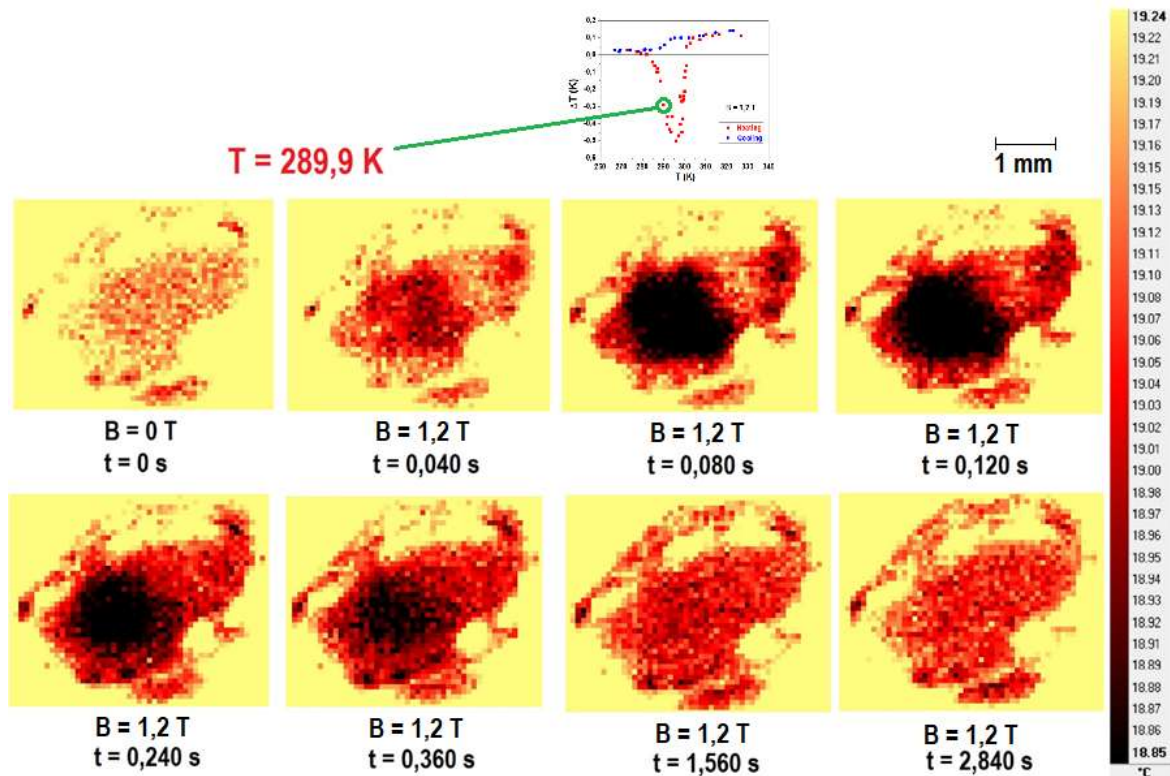
Fig. 7.32 - IR camera images over time of sample NCMG279 after it was heated to the temperature of 289,9 K, before and after a magnetic field was applied.

Fig. 7.34 shows a plot of the average of temperatures of all the pixels at all instants (corresponding to each frame, which for this measurement means a 0.040 s difference between consecutive points) of the measurement when the sample is at 292,8 K (in heating). In the same plot, we can also see for each instant the temperature of the pixel that, at that specific instant, registered the minimum/maximum temperature amongst all pixels being measured.

Fig. 7.35 shows a close-up of the plot in Fig. 7.34 focusing on the instants featured in Fig. 7.33, and the due correspondence between instants and plot points is established.
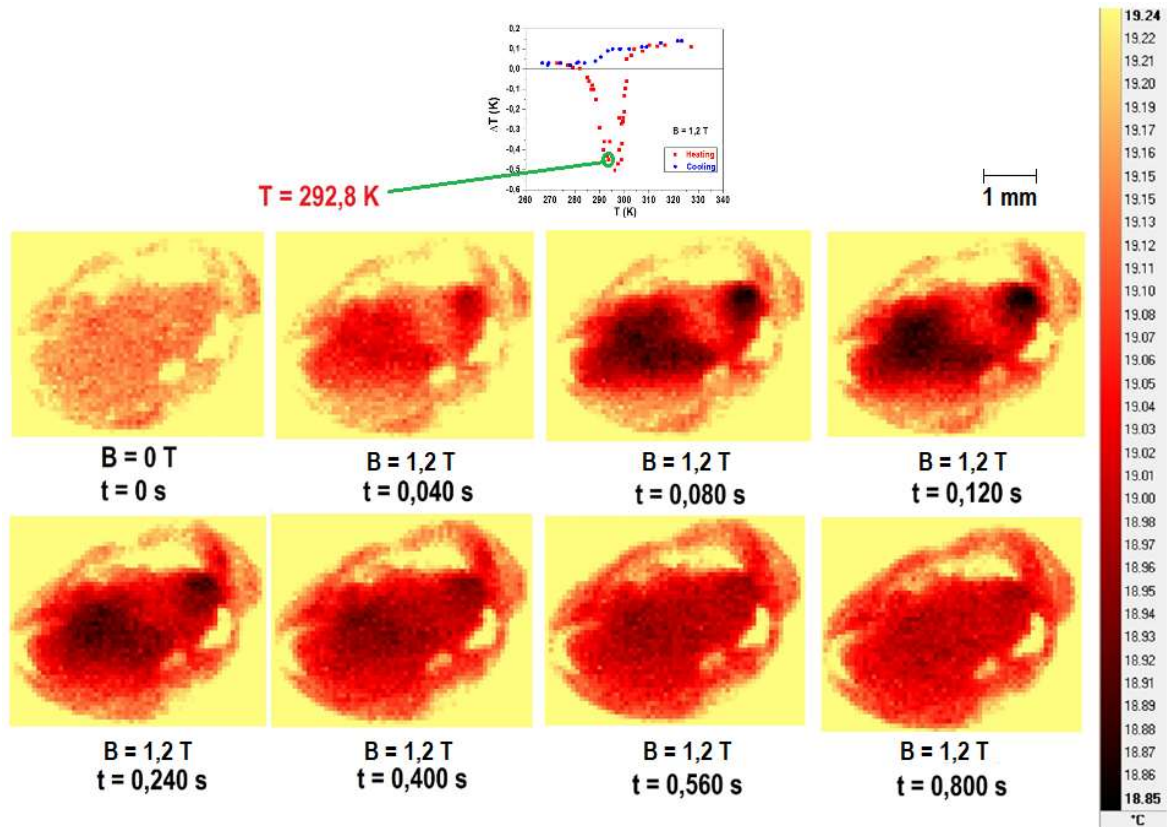
Fig. 7.33 - IR camera images over time of sample NCMG279 after it was heated to the temperature of 292,8 K, before and after a magnetic field was applied.

Fig. 7.34 - Plot of the average of temperatures of all the pixels for all instants of a given period of the measurement (T_{sample}=292,8 K, in heating), and the temperature of the pixels that, at a specific instant, registered the minimum/maximum value amongst all pixels being measured.
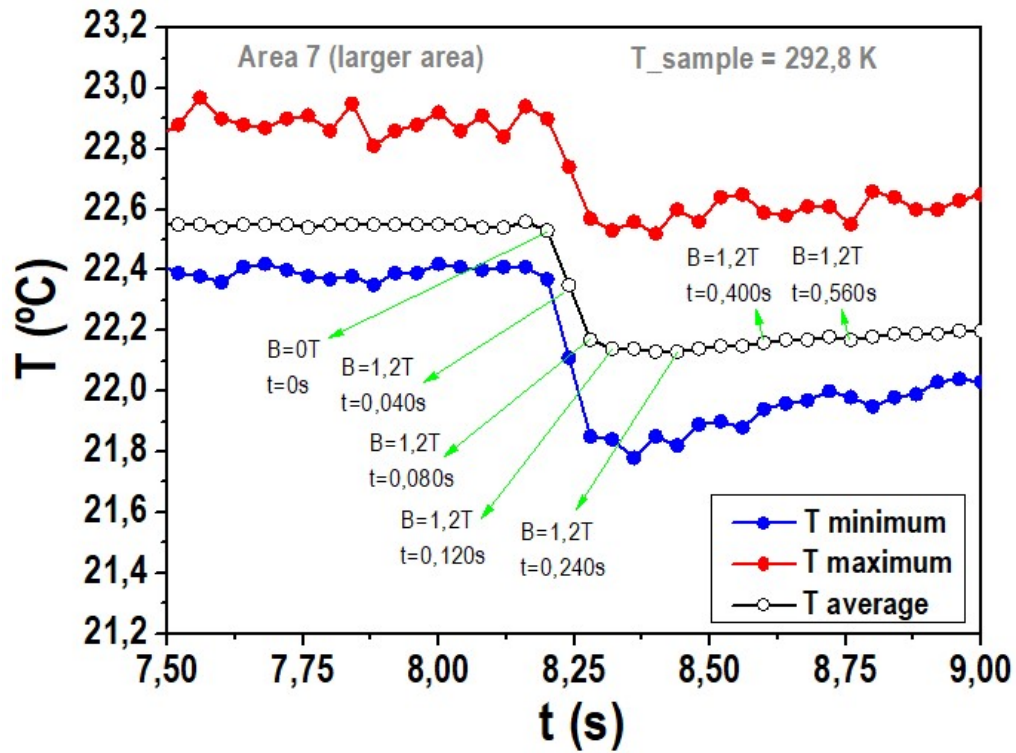
Fig. 7.35 - Close-up of Fig. 7.34 for the instants around the first field application; correspondence with the instants depicted in Fig. 7.33 is established.

Fig. 7.36 shows the MCE after the sample was heated to the temperature of 294,7 K.For all measured temperatures, this is where the MCE is more intense ($\Delta T_{average}$ = -0,54 K). This is also the first measured temperature (in heating) where we expect the sample to undergo (even if partially) the reverse martensitic transformation. In fact, here, the areas where the MCE is triggered by the presence of the magnetic field change. There are still significant portions of the sample which seem to be less affected than others by the presence of the magnetic field, but there is not such a marked distinction between regions as we had observed so far.

From Fig. 7.36 to Fig. 7.43 (for 294,7 K $\leq$ T $\leq$ 300,0 K, or, as from around the temperature of the reverse martensitic transformation to about 300 K), we clearly see the regions of the sample most affected by the presence of the magnetic field and thus, mostly responsible for the occurrence of the inverse MCE, gradually shifting predominantly to the right side of the exposed surface of the sample.
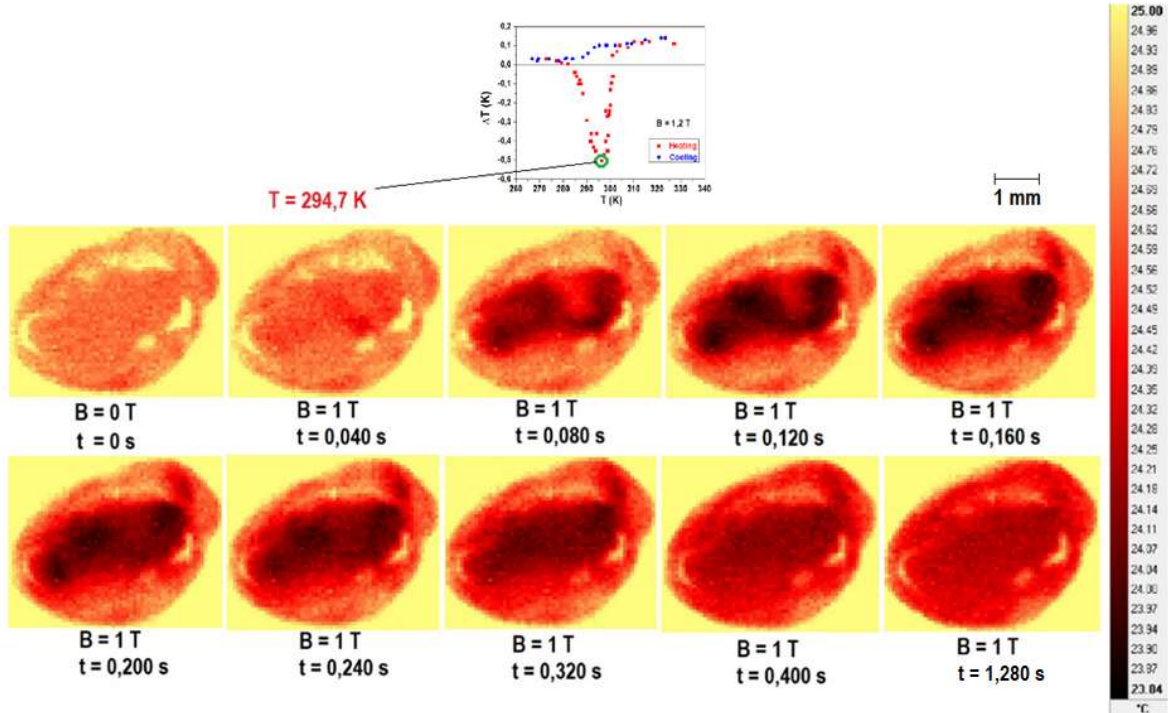
Fig. 7.36 - IR camera images over time of sample NCMG279 after it was heated to the temperature of 294,7 K, before and after a magnetic field was applied.

For temperatures above roughly 300 K, the sample starts to exhibit the direct MCE, with quite low magnitudes, with the sample showing a quite repetitive and consistent behavior in terms of the homogeneity with which the exposed surface of the sample reacts to the presence and subsequent removal of the applied magnetic field. One of the highest magnitudes ($\Delta T_{average}$ = 0,11 K) measured for the direct MCE, for T = 310,1 K, allows for the presentation of the clearest IR images as a representative example of such behavior (Fig. 7.44).

Fig. 7.40 shows a plot of the average of temperatures of all the pixels at all instants (corresponding to each frame, which for this measurement means a 0.040 s difference between consecutive points) of the measurement when the sample is at 299 K (in heating). In the same plot, we can also see for each instant the temperature of the pixel that, at that specific instant, registered the minimum/maximum temperature amongst all pixels being measured.
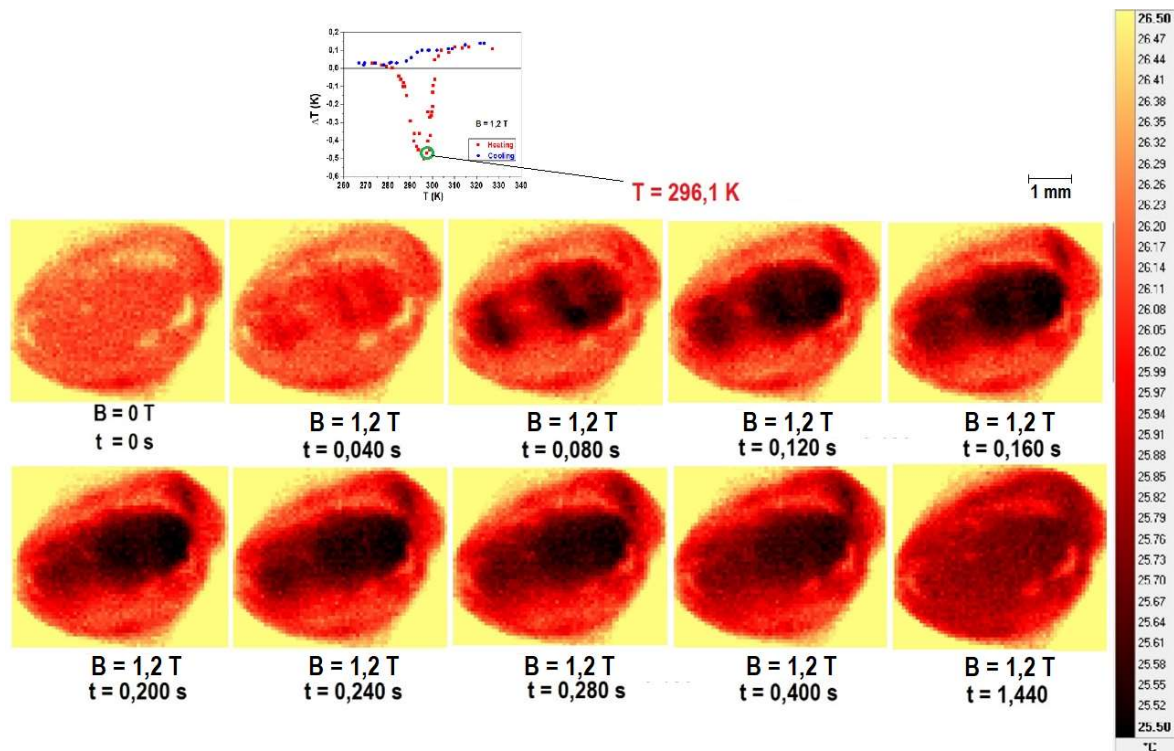
Fig. 7.37 - IR camera images over time of sample NCMG279 after it was heated to the temperature of 296,1 K, before and after a magnetic field was applied.
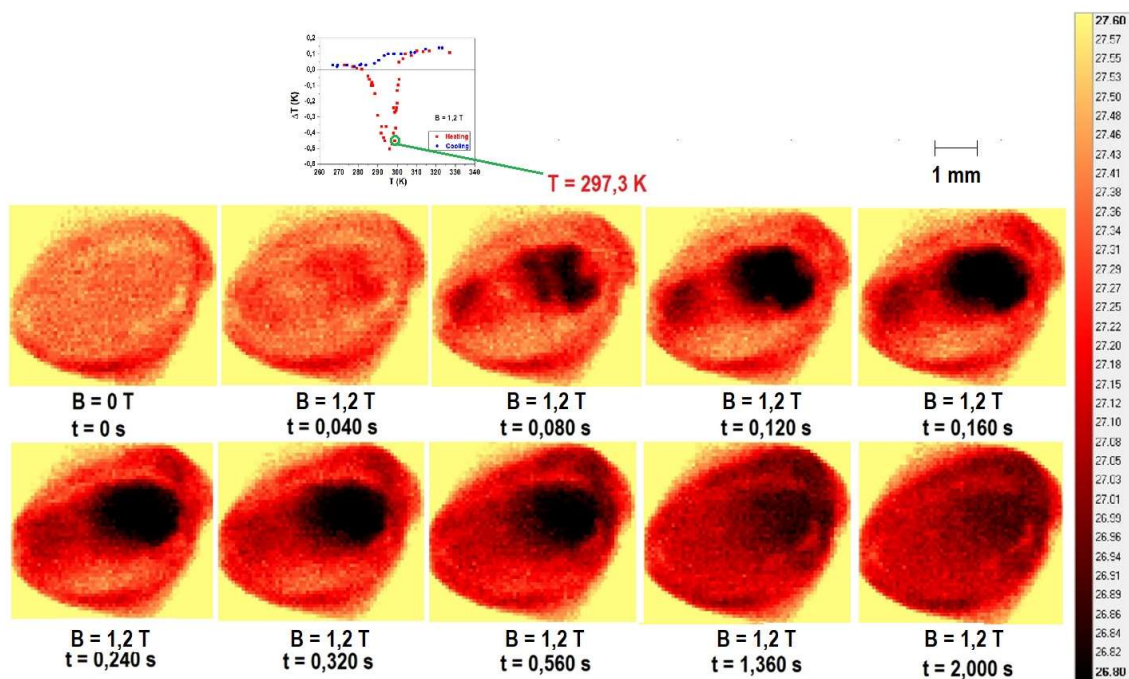
Fig. 7.38 - IR camera images over time of sample NCMG279 after it was heated to the temperature of 297,3 K, before and after a magnetic field was applied.
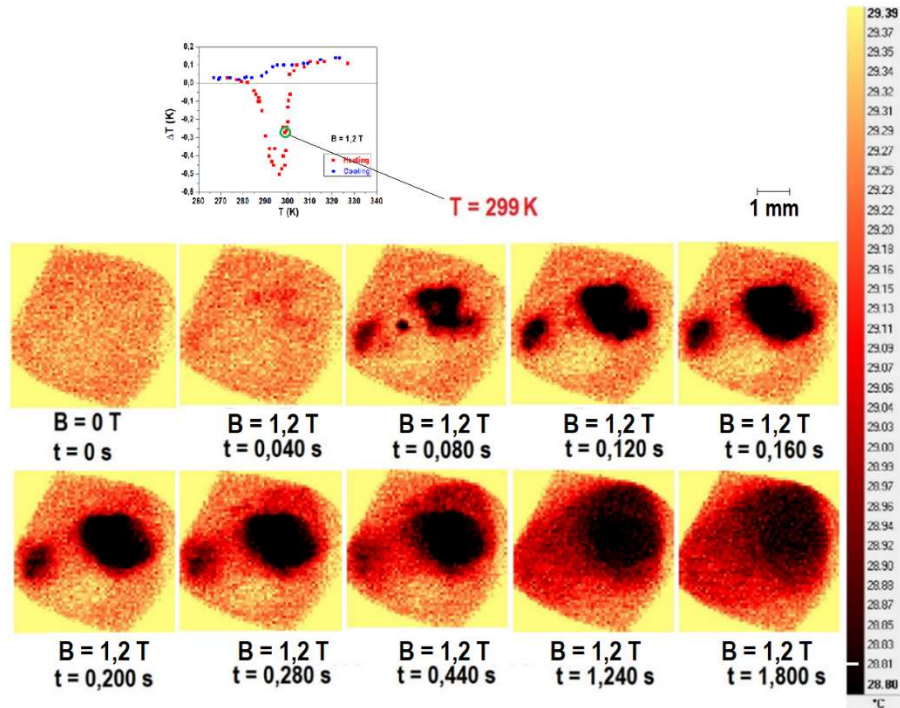
Fig. 7.39 - IR camera images over time of sample NCMG279 after it was heated to the temperature of 299 K, before and after a magnetic field was applied.

Fig. 7.41 shows a close-up of the plot in Fig. 7.40 focusing on the instants featured in Fig. 7.39, and the due correspondence between instants and plot points is established.
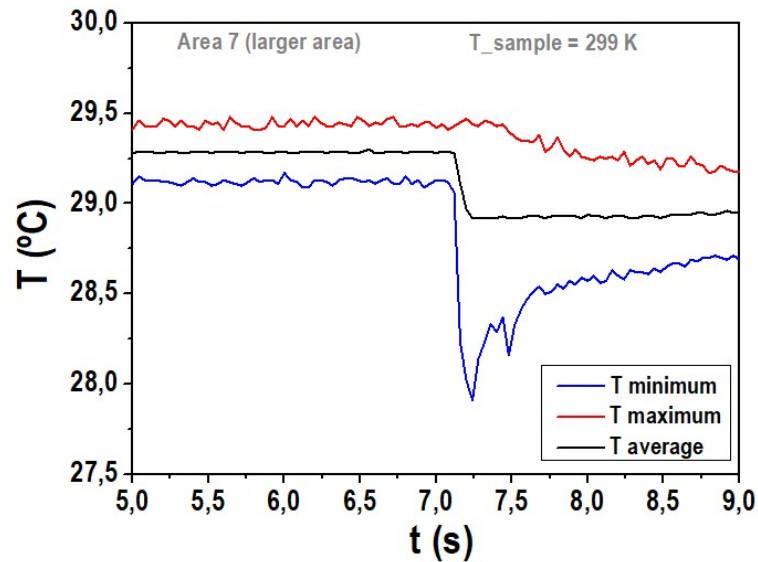
Fig. 7.40 - Plot of the average of temperatures of all the pixels for all instants of a given period of the measurement (T_{sample}=299 K, in heating), and the temperature of the pixels that, at a specific instant, registered the minimum/maximum value amongst all pixels being measured.
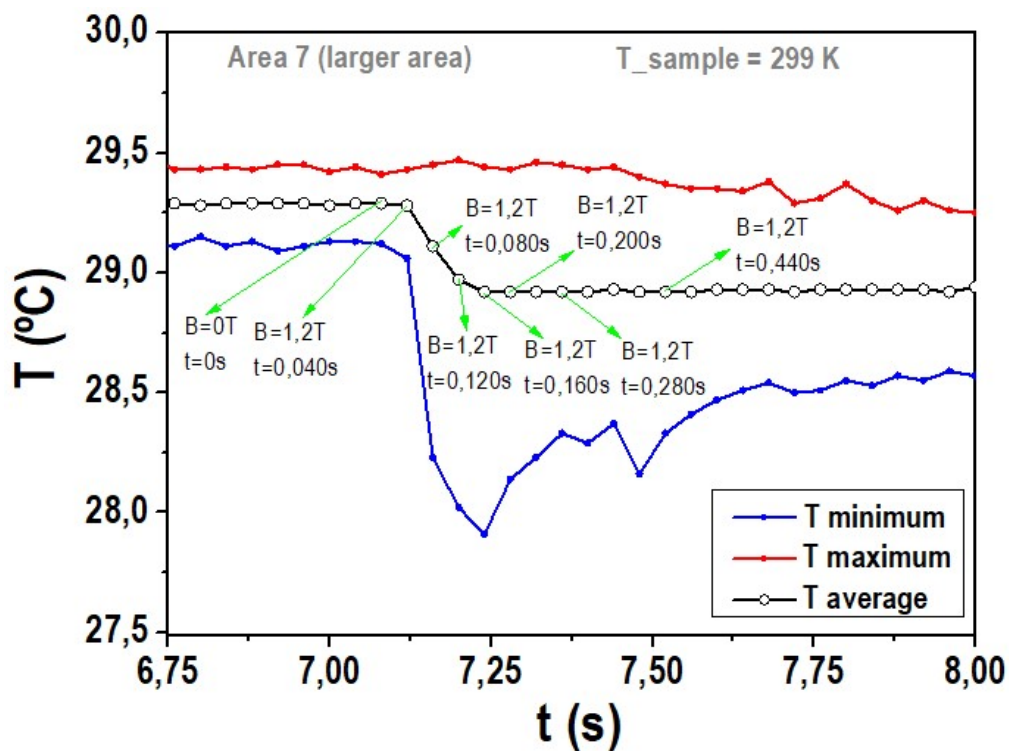
Fig. 7.41 - Close-up of Fig. 7.40 for the instants around the first field application; correspondence with the instants depicted in Fig. 7.39 is established.
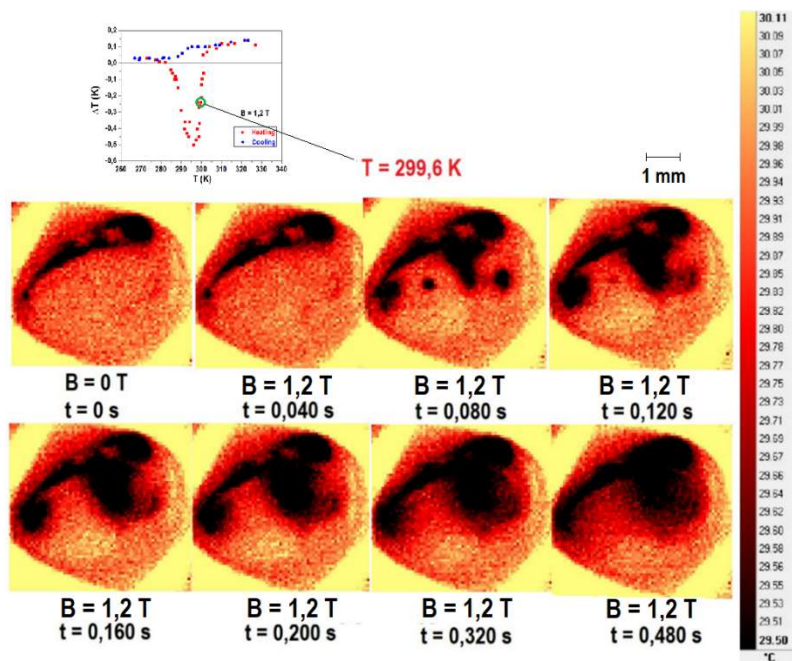
Fig. 7.42 - IR camera images over time of sample NCMG279 after it was heated to the temperature of 299,6 K, before and after a magnetic field was applied.
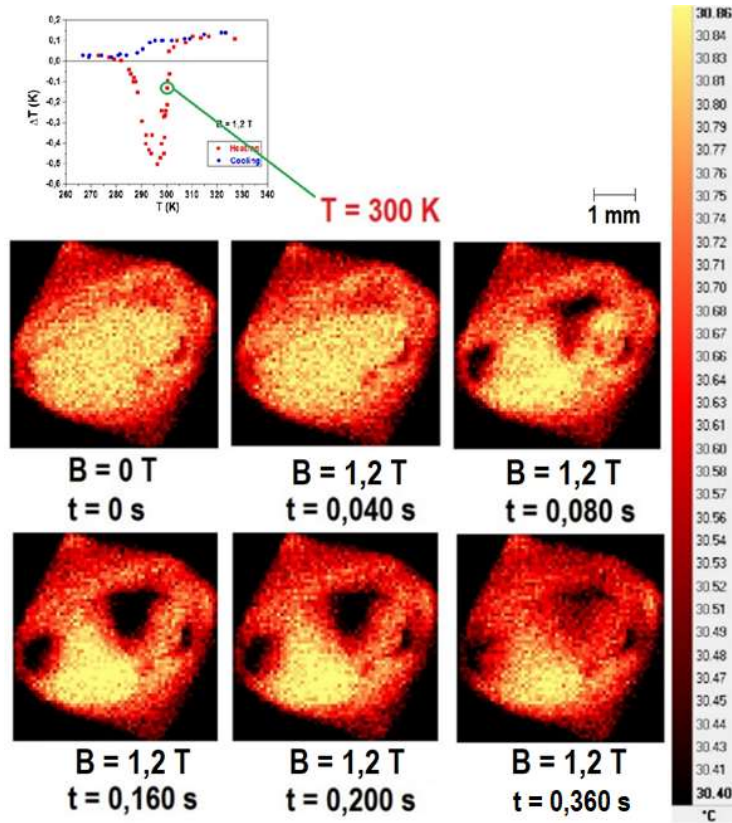
Fig. 7.43 - IR camera images over time of sample NCMG279 after it was heated to the temperature of 300 K, before and after a magnetic field was applied.
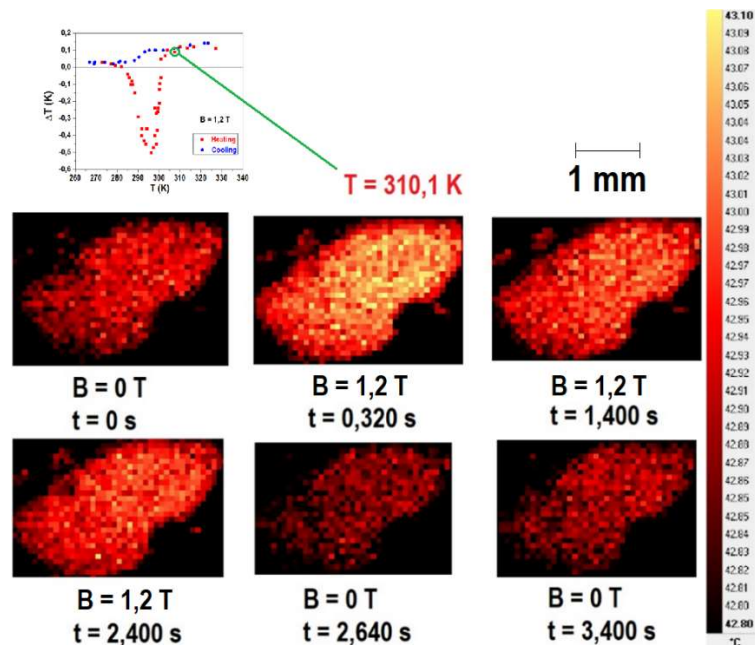
Fig. 7.44 - IR camera images over time of sample NCMG279 after it was heated to the temperature of 310,1 K, before and after a magnetic field was applied.

As well as for heating, we present Figs. 7.46 and 7.47 for the cooling process, depicting series of images of the sample collected with the IR camera at different moments in time, while protocol B was beginning to be performed, thus before the magnetic field is applied and after its removal. Unlike what happens in heating, with the reverse martensitic transformation, the cooling process has revealed itself rather uneventful in terms of the way in which the MCE occurs.

Fig. 7.45 shows the plot of the average temperature value of the selected surface area 7 (largest area) of the NCMG279 sample as a function of time, with the sample brought to 314,8 K from 340 K as a magnetic field is consecutively applied to and removed from the sample. It is very clear that the successive field applications cause a very similar effect on the sample, in terms of magnitude of the effect and the homogeneity of the values of temperature involved.

Figs. 7.46 and 7.47 to 7.55 are shown as representative examples of the consistently homogeneous response of the whole surface of the sample to the application and removal of the magnetic field verified for all studied temperatures.
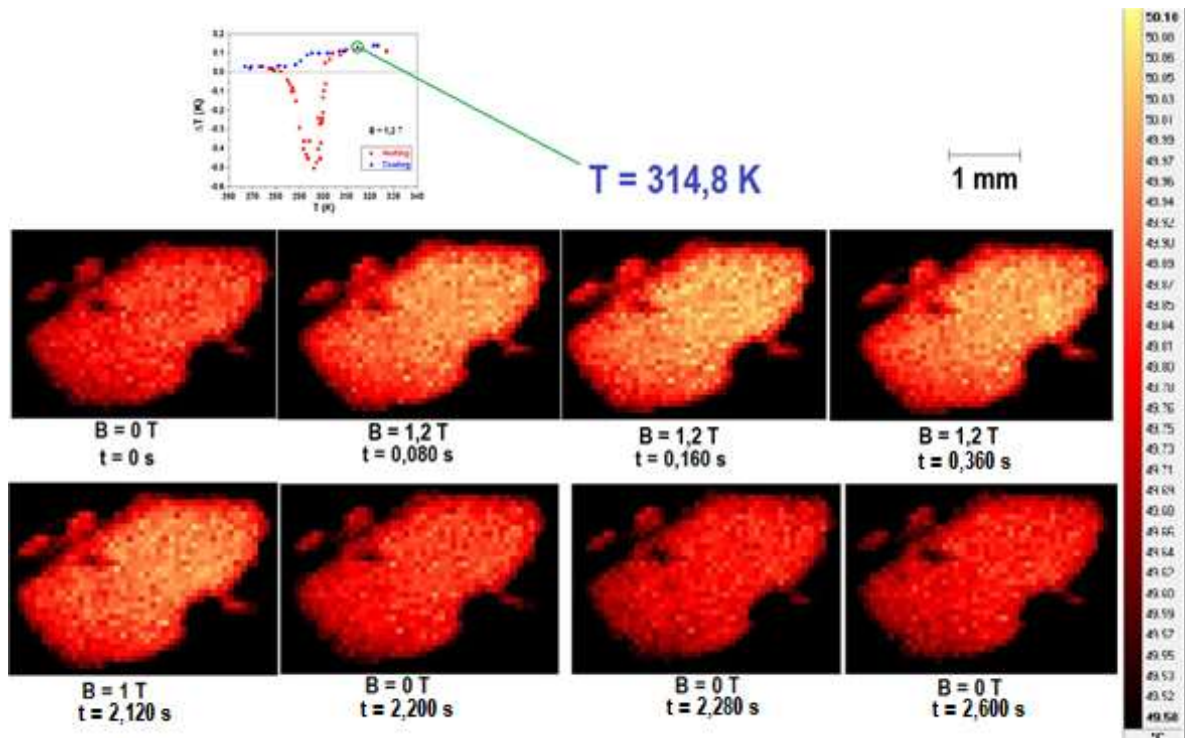
Fig. 7.45 - IR camera images over time of sample NCMG279 after it was cooled to the temperature of 314,8 K, before a magnetic field was applied, after the magnetic field was applied and after the magnetic field was removed.

Fig. 7.46 - Plot of the average temperature value of selected surface area 7 (largest area) of the NCMG279 sample as a function of time, with the sample cooled from 340 K to the temperature of 314,8 K, showing the temperature behaviour as a magnetic field is consecutively applied to and removed from the sample.
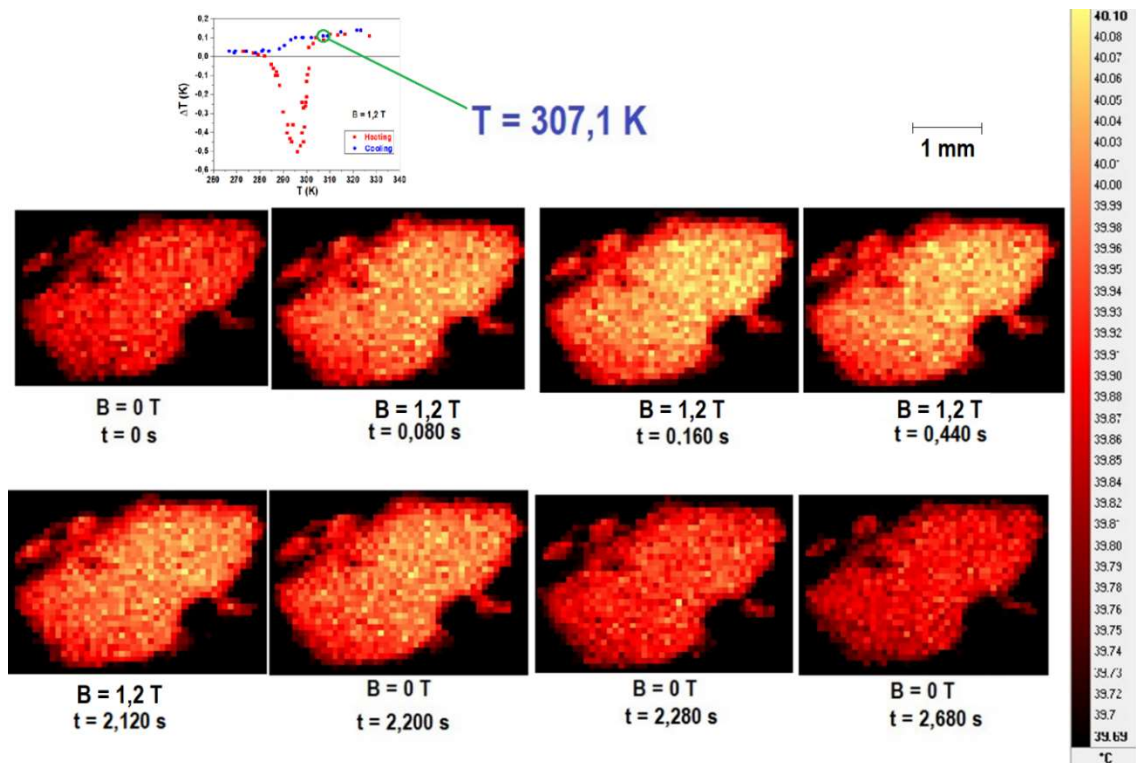
Fig. 7.47- IR camera images over time of sample NCMG279 after it was cooled to the temperature of 307,1 K, before a magnetic field was applied, after the magnetic field was applied and after the magnetic field was removed.
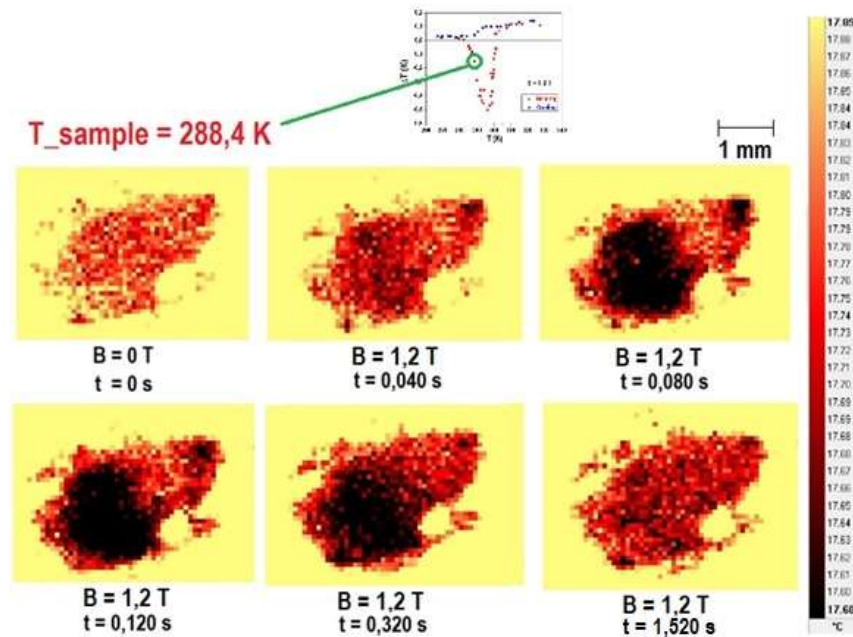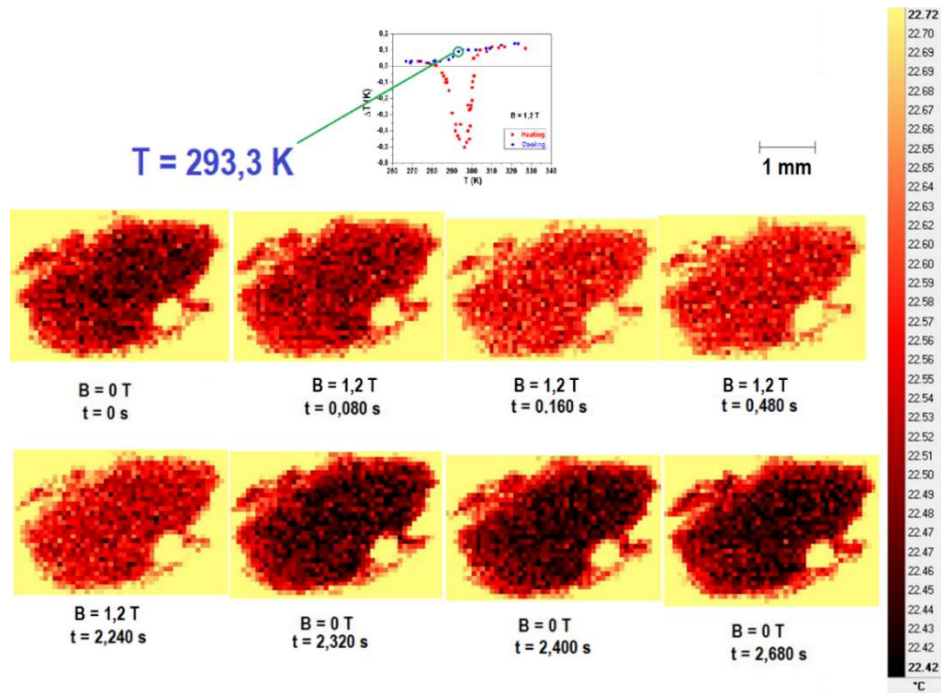
Fig. 7.48 - IR camera images over time of sample NCMG279 after it was cooled to the temperature of 293,3 K, before a magnetic field was applied, after the magnetic field was applied and after the magnetic field was removed.
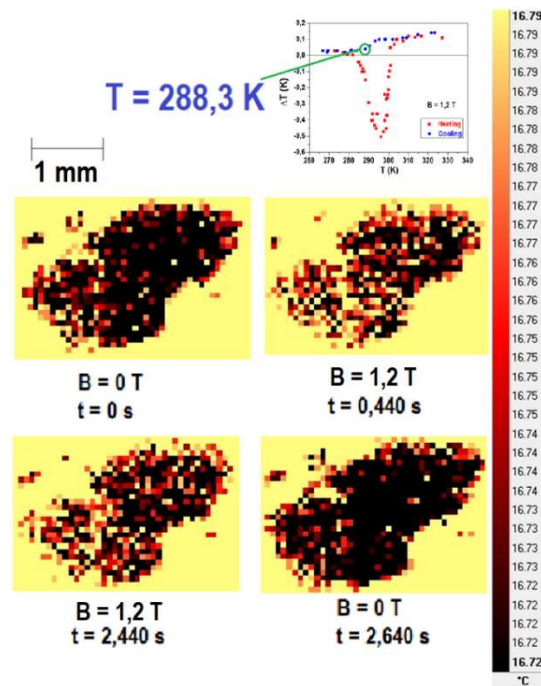
Fig. 7.49 - IR camera images over time of sample NCMG279 after it was cooled to the temperature of 288,3 K, before a magnetic field was applied, after the magnetic field was applied and after the magnetic field was removed.

Table 7.3 - Temperature distribution values for the different sample temperatures in heating (red) and cooling (blue) and temperature value observed in higher number of pixels; information collected from histograms like the ones presented in Fig. 7.31

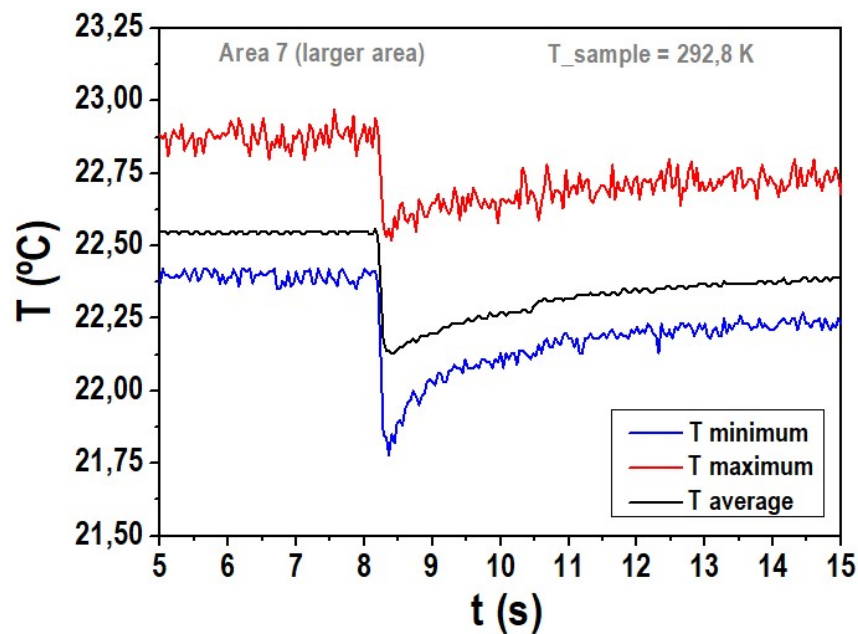| T_{sample}	t (s)									
	$T_{(center\ of\ distribution)} \pm \delta T$ (K)									
	$T_{(highest\ number\ of\ events)}$ (K)									
288.4	0.000	0.040	0.080	0.120	0.320	1.520	-	-	-	-
	291.1 ±0.3	291.1 ±0.3	290.9 ±0.4	290.8 ±0.4	291.0 ±0.4	291.4 ±0.7	-	-	-	-
	291.0	290.9	290.8	290.8	290.8	290.8	-	-	-	-
289.9	0.000	0.040	0.080	0.120	0.240	0.360	1.560	2.840	-	-
	295.2 ±0.3	292.3 ±0.4	292.1 ±0.5	292.2 ±0.5	292.2 ±0.4	292.2 ±0.4	292.3 ±0.3	292.4 ±0.3	-	-
	292.3	292.2	292.1	292.2	292.0	292.1	292.2	292.2	-	-
292.8	0.000	0.040	0.080	0.120	0.240	0.400	0.560	0.800	-	-
	295.7 ±0.2	295.6 ±0.3	295.4 ±0.4	295.3 ±0.3	295.2 ±0.3	295.3 ±0.3	295.4 ±0.3	295.4 ±0.3	-	-
	295.6	295.5	295.2	295.2	295.2	295.3	295.4	295.3	-	-
294.7	0.000	0.040	0.080	0.120	0.160	0.200	0.240	0.320	0.400	1.280
	297.9 ±0.2	297.8 ±0.2	297.6 ±0.4	297.4 ±0.4	297.4 ±0.4	297.4 ±0.4	297.4 ±0.4	297.3 ±0.2	297.4 ±0.3	297.5 ±0.2
	297.8	297.8	297.4	297.2	297.2	297.2	297.2	297.2	297.4	297.4
296.1	0.000	0.040	0.080	0.120	0.160	0.200	0.240	0.280	0.400	1.440
	299.3 ±0.1	299.2 ±0.2	299.0 ±0.5	299.0 ±0.4	298.9 ±0.4	298.9 ±0.4	298.9 ±0.4	298.9 ±0.3	298.9 ±0.3	299.0 ±0.3
	299.3	299.2	299.0	298.8	298.8	298.8	298.8	298.8	298.8	298.9
297.3	0.000	0.040	0.080	0.120	0.160	0.240	0.320	0.560	1.360	2.000
	300.5 ±0.1	300.5 ±0.2	300.3 ±0.4	300.2 ±0.6	300.1 ±0.5	300.2 ±0.4	300.1 ±0.4	300.2 ±0.4	300.2 ±0.2	300.2 ±0.2
	300.5	300.5	300.4	300.3	300.2	300.2	300.2	300.2	300.2	300.2
299.0	0.000	0.040	0.080	0.120	0.160	0.200	0.280	0.440	1.240	1.800
	302.4 ±0.1	302.4 ±0.2	301.9 ±0.6	301.8 ±0.8	301.8 ±0.8	301.8 ±0.6	302.0 ±0.6	302.0 ±0.6	302.0 ±0.3	302.1 ±0.3
	302.4	302.4	302.3	302.2	302.2	302.3	302.2	302.2	302.2	302.0
299.6	0.000	0.040	0.080	0.120	0.160	0.200	0.320	0.480	-	-
	303.0 ±0.2	303.1 ±0.2	302.8 ±0.4	302.6 ±0.6	302.6 ±0.6	302.6 ±0.6	302.7 ±0.6	302.8 ±0.4	-	-
	303.1	303.1	303.0	303.0	303.0	303.0	302.9	302.9	-	-
300.0	0.000	0.040	0.080	0.160	0.200	0.360	0.400	1.440	-	-
	304.0 ±0.2	303.9 ±0.2	303.7 ±0.2	303.6 ±0.4	303.6 ±0.4	303.8 ±0.3	298.9 ±0.3	299.0 ±0.2	-	-
	304.0	304.0	304.0	304.0	304.0	303.8	298.8	298.9	-	-
310.1	0.000	0.320	1.400	2.400	2.640	3.400	-	-	-	-
	315.7 ±0.5	315.8 ±0.5	315.8 ±0.4	315.8 ±0.4	315.6 ±0.4	315.6 ±0.4	-	-	-	-
	316.0	316.1	316.1	316.1	316.0	316.0	-	-	-	-
314.8	0.000	0.080	0.160	0.360	2.120	2.200	2.280	2.600	-	-
	322.6 ±0.7	322.6 ±0.7	322.6 ±0.6	322.6 ±0.6	322.5 ±0.6	322.5 ±0.6	322.4 ±0.6	322.4 ±0.6	-	-
	323.1	323.1	323.1	323.1	323.0	323.0	323.0	322.9	-	-
307.1	0.000	0.080	0.200	0.360	2.040	2.320	2.440	2.600	-	-
	312.9 ±0.4	312.9 ±0.4	312.9 ±0.4	312.9 ±0.4	312.9 ±0.4	312.8 ±0.4	312.8 ±0.4	312.8 ±0.4	-	-
	313.1	313.2	313.1	313.2	313.2	313.0	313.0	313.0	-	-
288.3	0.000	0.440	2.440	2.640	-	-	-	-	-	-
	290.0 ±0.4	290.1 ±0.3	290.1 ±0.4	290.0 ±0.4	-	-	-	-	-	-
	289.8	289.9	289.9	289.8	-	-	-	-	-	-

We have also analyzed in detail the behavior of three selected pixels in different areas of the sample. As previously mentioned, each pixel corresponds to an area of about 85x85 µm^2. The change in temperature experienced by each pixel when the 1.2 T magnetic field is applied to the sample for the first time is plotted in Figs. 7.51 to 7.53, and the data for the three pixels is plotted in Fig. 7.54. ΔT values for each pixel were calculated in the same way that was previously described for obtaining the values of the variation in average temperature for the smallest selected area (2) (values presented in Fig. 7.24), with the aid of Figs. 7.25 and 7.26.

These plots describe how dramatically different these microscopic areas of the sample experience the MCE (especially through the reverse martensitic transformation) for the several studied temperatures, depending on the region of the sample where they can be found.
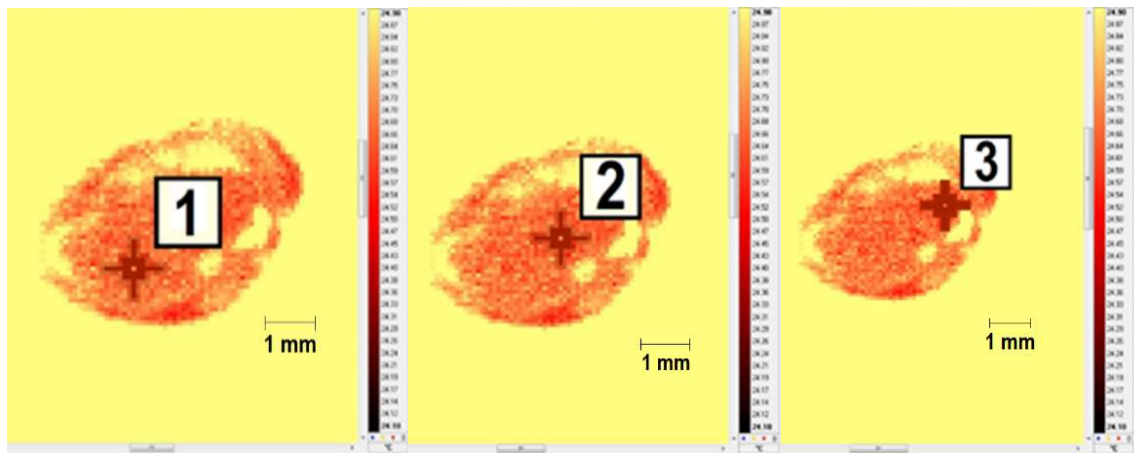
Fig. 7.50 - IR camera image of the sample's exposed surface showing the location of selected pixels 1, 2 and 3
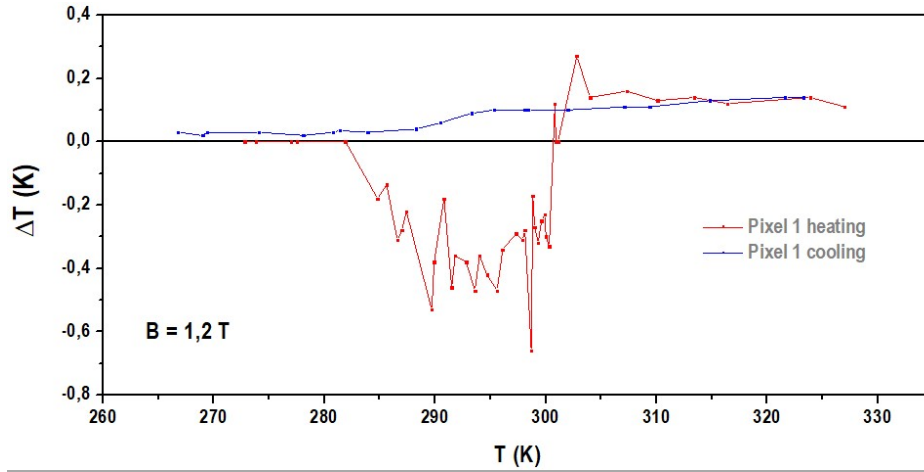
Fig. 7.51 - ΔT experienced by pixel 1 as a function of temperature when 1.2 T is applied to the NCMG279 sample.
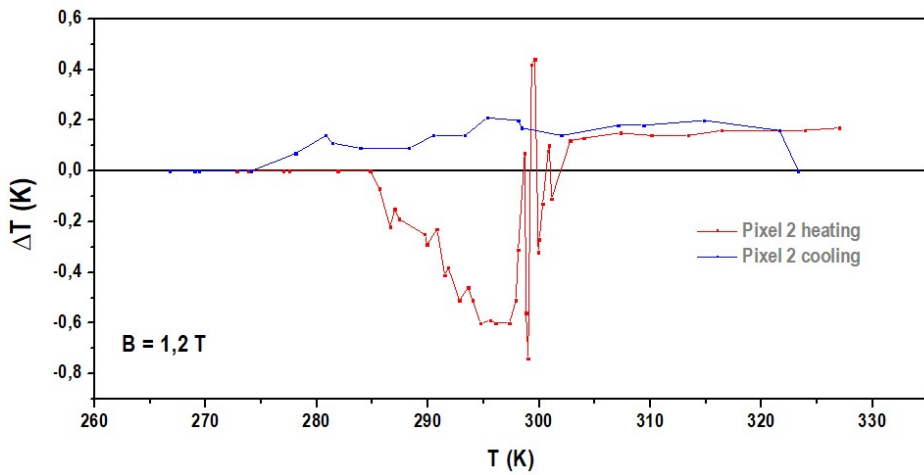
Fig. 7.52 - ΔT experienced by pixel 2 as a function of temperature when 1.2 T is applied to the NCMG279 sample.
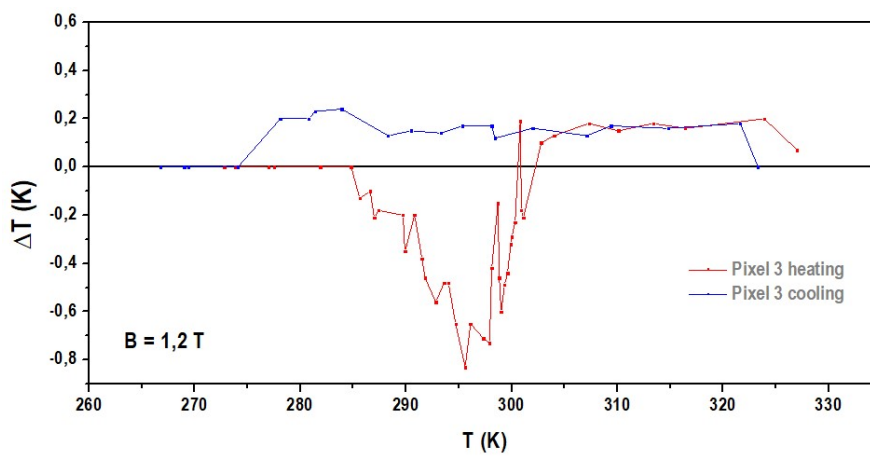
Fig. 7.53 - ΔT experienced by pixel 3 as a function of temperature when 1.2 T is applied to the NCMG279 sample.
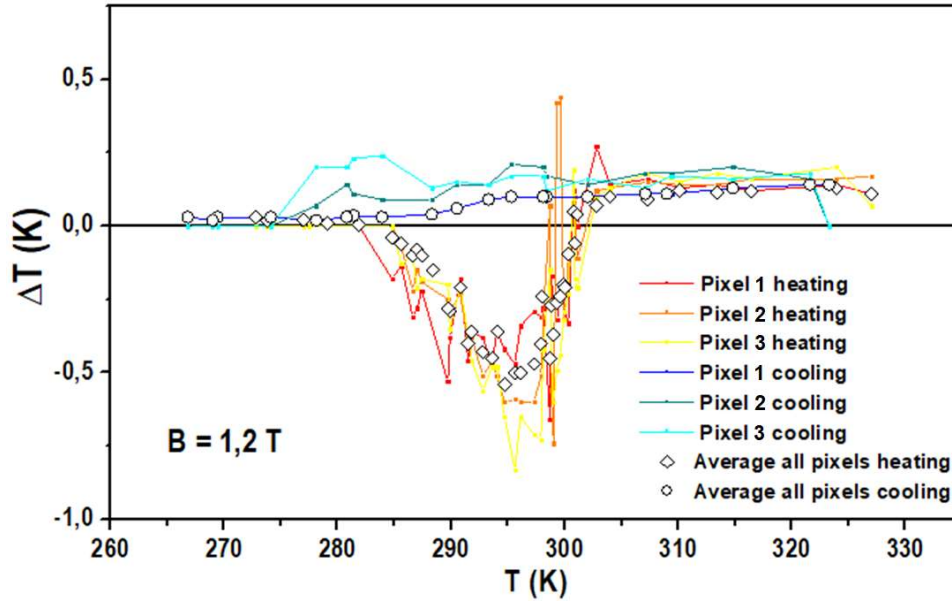
Fig. 7.54 - ΔT experienced by the three pixels as a function of temperature when 1.2 T is applied to the NCMG279 sample. The average ΔT for all pixels already presented in Fig. 7.24 was added for comparison purposes.

To sum up, in heating, from 273 K to 327 K, we see low magnitude direct MCE while the sample is in the martensitic phase. As the sample is being heated and sets out to approach the temperature at which its reverse martensitic transformation is expected to happen, the sample experiences the reverse MCE and the magnitude of the effect increases with temperature. Under such circumstances, the left area of the sample is predominantly engaged in the occurrence of the MCE. Once the expected temperature for the sample's reverse martensitic transformation is reached, the inverse MCE's magnitude peaks and there is no longer a clear predominance of one side of the sample engaging in the MCE effect. As we increase the temperature, the MCE is still inverse, its magnitude decreases, and the effect gradually manifests itself more evidently on the opposite side of the sample. Above 300 K, where under B = 1.2 T the sample is expected to have fully transformed to the austenitic phase (according to M vs T measurements, Figs. 7.2 and 7.3), the MCE is direct, presents low magnitudes, and manifests homogeneously throughout the sample's surface.

In cooling, from 327 K to 267 K, the MCE is always direct and shows very low magnitudes for all temperatures. The sample always responds homogeneously to

the application and removal of the magnetic field, and, unlike during the heating process until about 300 K, the MCE manifests in the same way independently if the magnetic field is being applied for the first time or not.

7.2.5 – MCE behavior for successive applications of the magnetic field

To end the analysis of our results this is precisely the aspect left to address: what happens after the magnetic field is first applied to the sample in heating, from 273 K to 327 K, for the several studied temperatures?

The responses are diverse, according to the temperatures under consideration.

Plots in Figs. 7.55 to 7.64 show that for temperatures up to 294,7 K (when the inverse MCE magnitude for the first field application peaks) the MCE almost always changes from inverse to direct when the magnetic field is first removed and that after the second magnetic field removal, the MCE is always direct. The main exception to this behavior happens for T = 292,8 K, where only the inverse MCE is repeatedly observed. From Fig. 7.24 we have learned that when the sample is at temperatures in the vicinity of the reverse transformation temperature, where we are likely to have a coexistence of both martensitic and austenitic phases, the first reaction of the sample to the magnetic field is to manifest the inverse MCE. The observation of the direct MCE after a few consecutive applications of the magnetic field would lead us to believe that the magnetic field is inducing the sample to either transform "back" to the martensitic or "forward" to the austenitic phase. Given the incredibly small magnitude of the direct MCE observed, and reporting back to Fig. 7.24, the former hypothesis should be considered more likely to be accurate. For temperatures higher than 294,7 K and until around 300 K, the behavior of the sample is consistent: only the first field application shows the inverse MCE, after which only the direct MCE is observed. As temperature increases between these two values, the magnitude of the direct MCE observed also increases, which leads us to believe that 294,7 K represents a turning point when subsequent applications of the field induced the sample to transform towards the austenitic phase. At 310,1 K, the

sample being fully transformed to the austenitic state, only direct MCE is observed,
and it manifests in the same way, no matter how many times the field is being applied
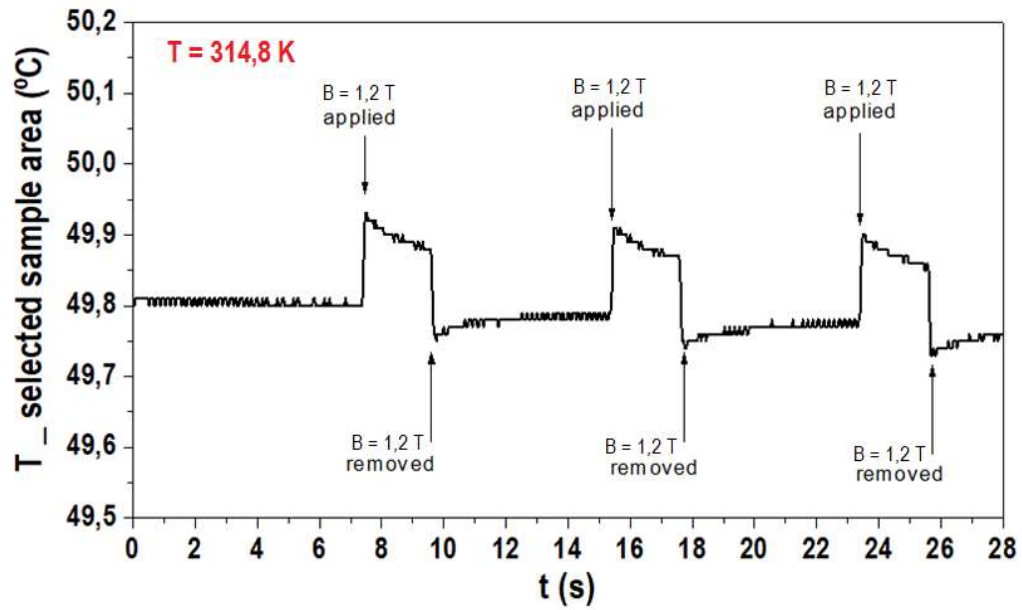to the sample.
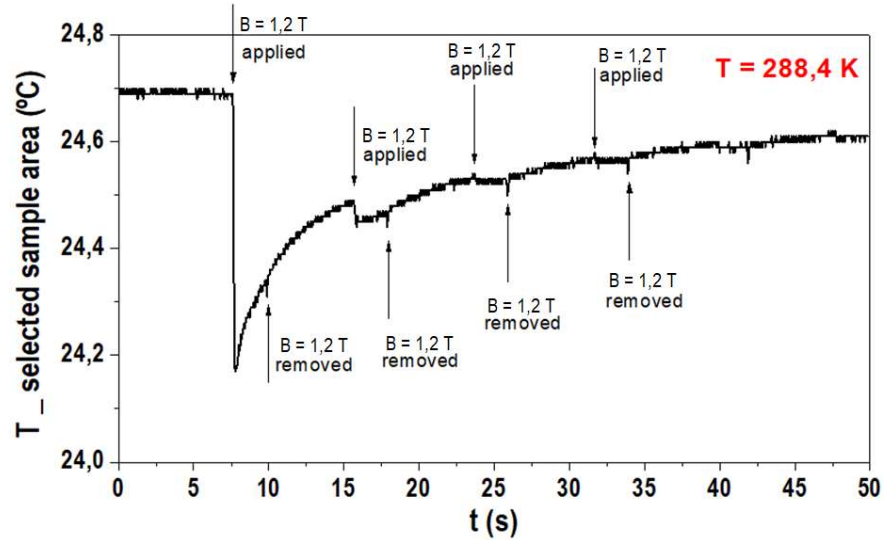
Fig. 7.55 - Plot of the average temperature value of selected surface area 7 (largest area) of the
NCMG279 sample as a function of time, as the sample was heated to the temperature of 288,4 K, as
a magnetic field is consecutively applied and removed.
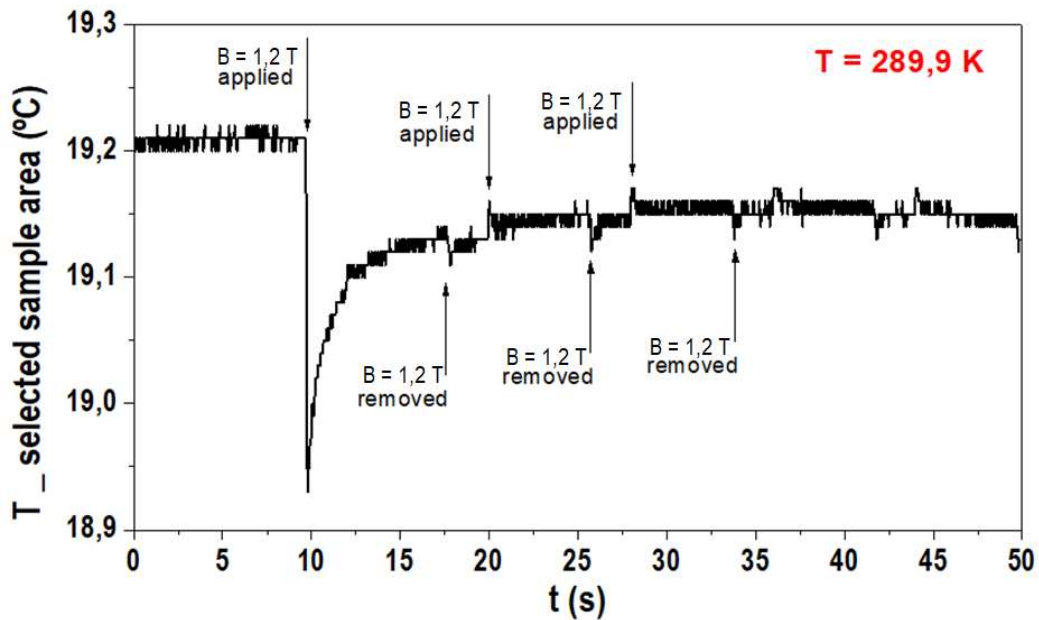
Fig. 7.56 - Plot of the average temperature value of selected surface area 7 (largest area) of the
NCMG279 sample as a function of time, as the sample was heated to the temperature of 289,9 K, as
a magnetic field is consecutively applied and removed.
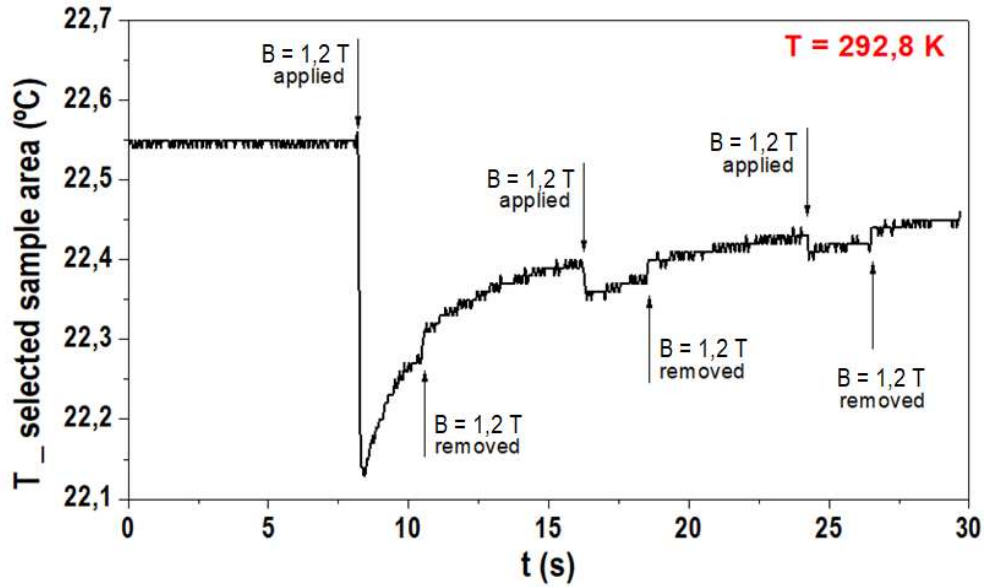
Fig. 7.57 - Plot of the average temperature value of selected surface area 7 (largest area) of the NCMG279 sample as a function of time, as the sample was heated to the temperature of 292,8 K, as a magnetic field is consecutively applied and removed. It depicts an exceptional behavior amongst all plots representing successive field applications.
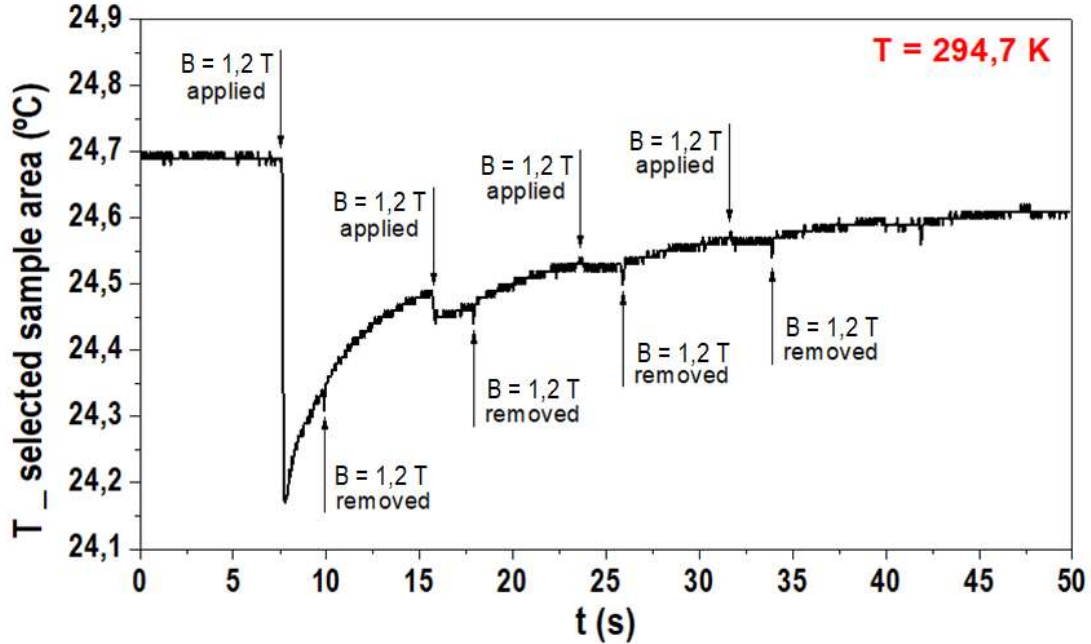
Fig. 7.58 - Plot of the average temperature value of selected surface area 7 (largest area) of the NCMG279 sample as a function of time, as the sample was heated to the temperature of 294,7 K, as a magnetic field is consecutively applied and removed.
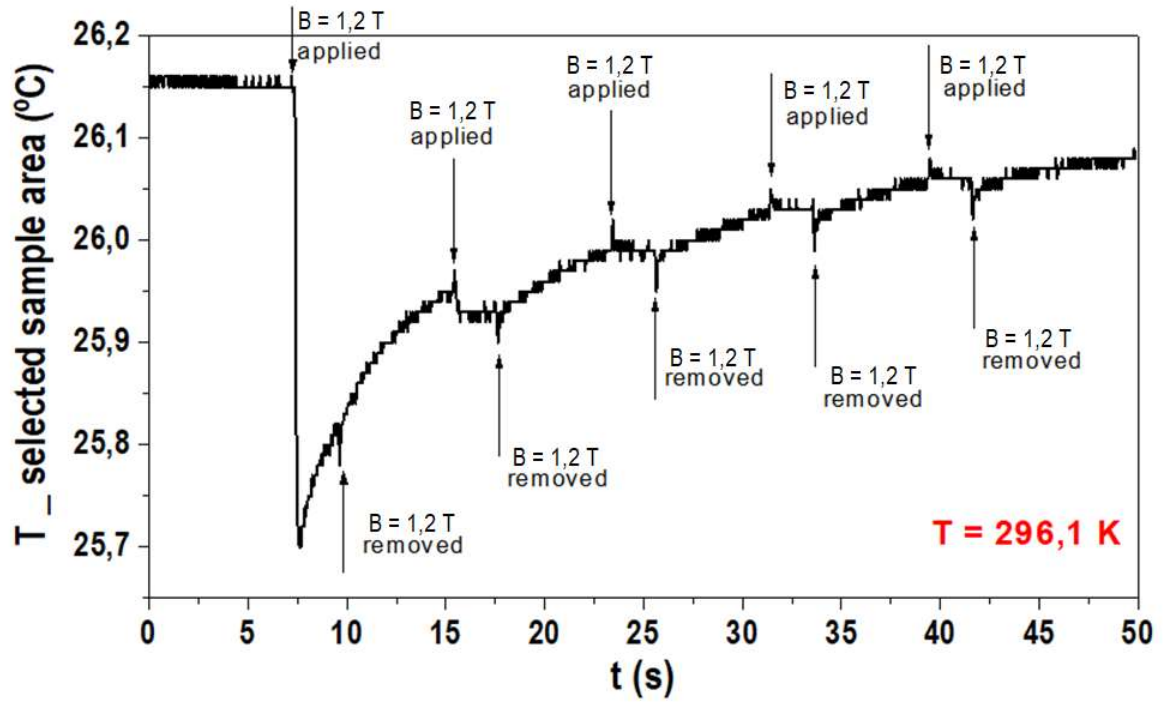
Fig. 7.59 - Plot of the average temperature value of selected surface area 7 (largest area) of the NCMG279 sample as a function of time, as the sample was heated to the temperature of 296,1 K, as a magnetic field is consecutively applied and removed.
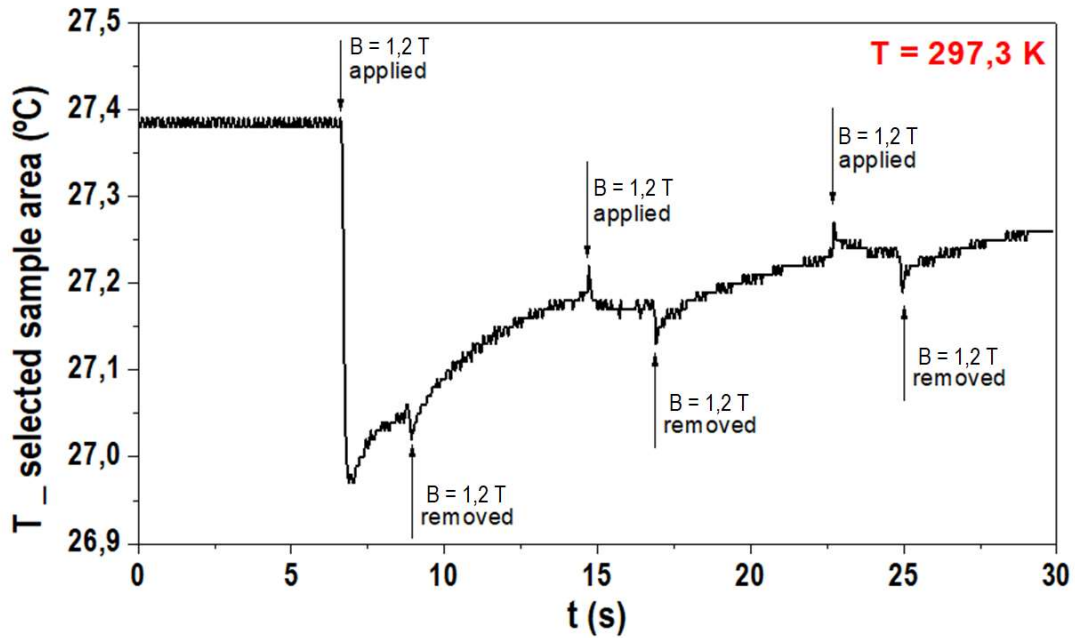
Fig. 7.60 - Plot of the average temperature value of selected surface area 7 (largest area) of the NCMG279 sample as a function of time, as the sample was heated to the temperature of 297,3 K, as a magnetic field is consecutively applied and removed.
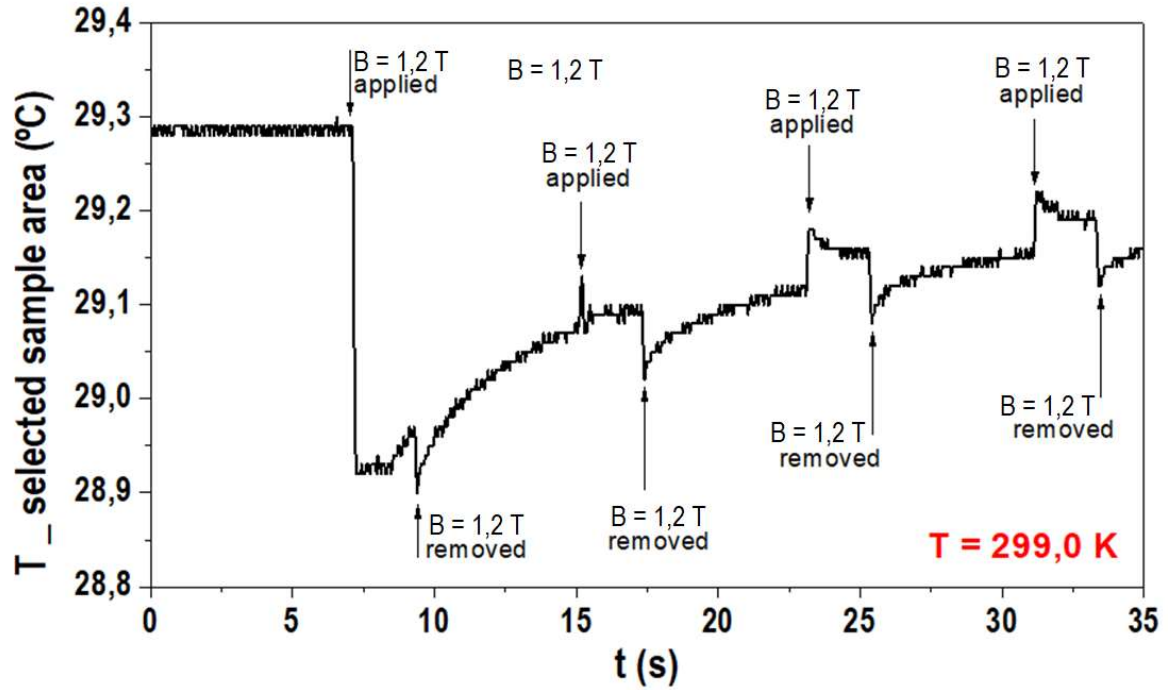
Fig. 7.61 - Plot of the average temperature value of selected surface area 7 (largest area) of the NCMG279 sample as a function of time, as the sample was heated to the temperature of 299,0 K, as a magnetic field is consecutively applied and removed.
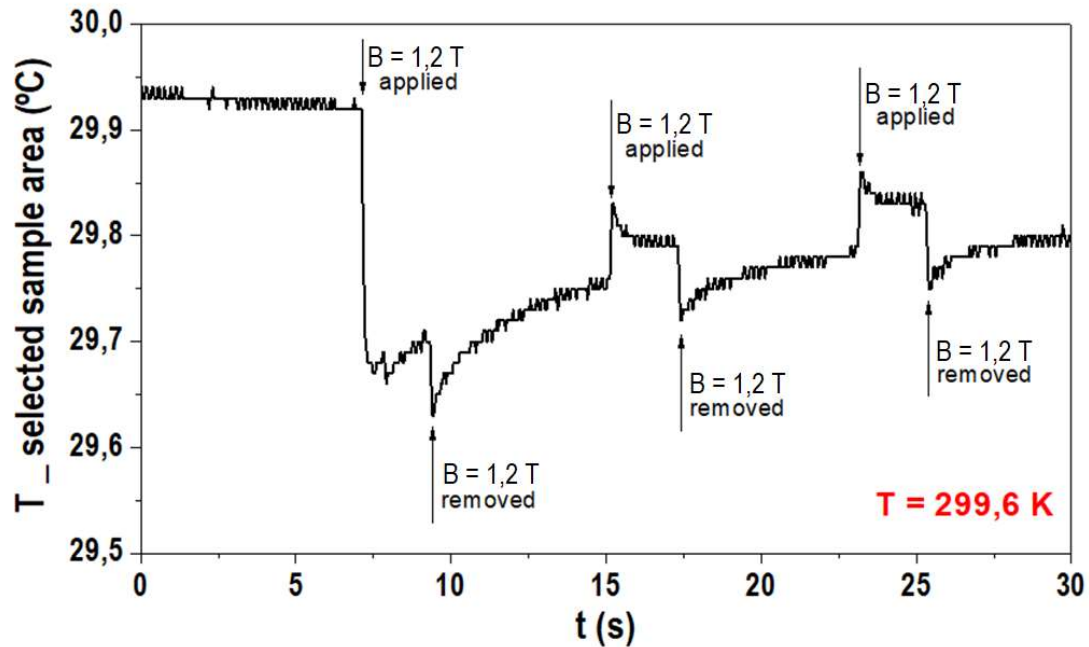
Fig. 7.62 - Plot of the average temperature value of selected surface area 7 (largest area) of the NCMG279 sample as a function of time, as the sample was heated to the temperature of 299,6 K, as a magnetic field is consecutively applied and removed.
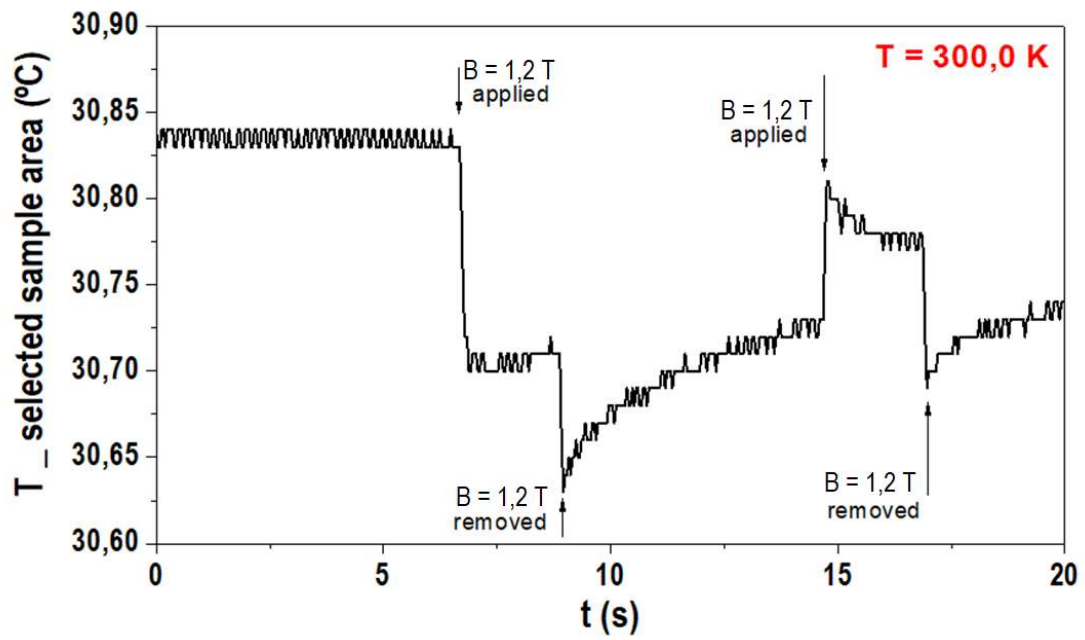
Fig. 7.63 - Plot of the average temperature value of selected surface area 7 (largest area) of the NCMG279 sample as a function of time, as the sample was heated to the temperature of 300,0 K, as a magnetic field is consecutively applied and removed.
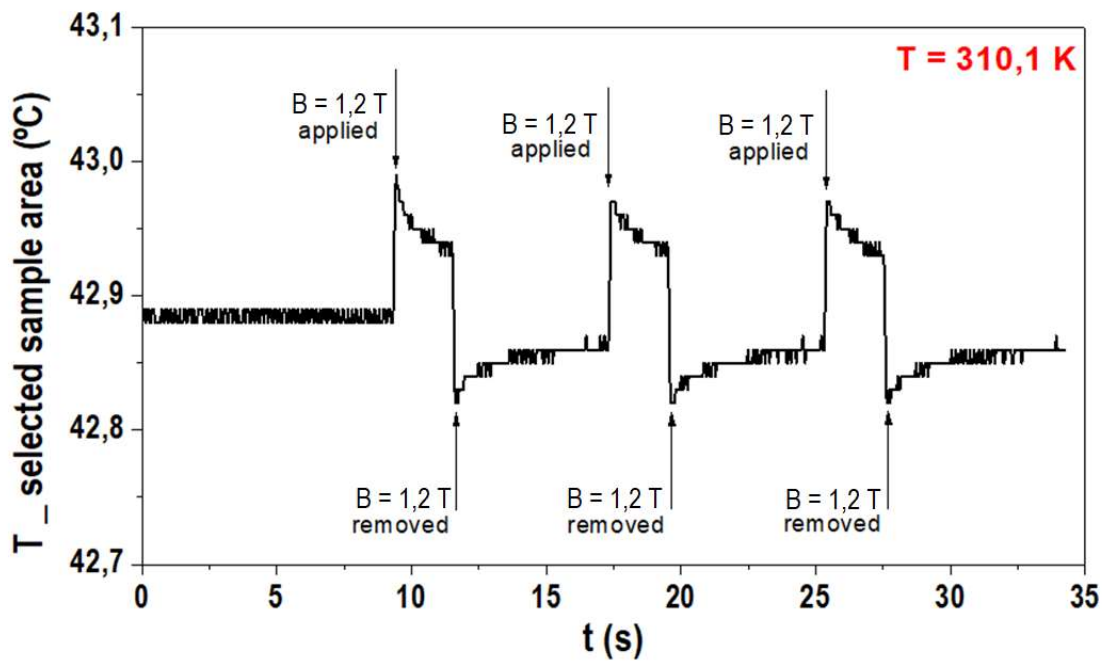
Fig. 7.64 - Plot of the average temperature value of selected surface area 7 (largest area) of the NCMG279 sample as a function of time, as the sample was heated to the temperature of 310,1 K, as a magnetic field is consecutively applied and removed.

7.3 – Mapping the MCE at the microscale

As previously mentioned, we used MathWorks MATLAB Software to handle the available data more systematically and ultimately map the MCE at the microscale.

Figs. 7.65 shows the result for the difference between the average temperature of the sample surface right after the magnetic field was applied and the average temperature of the sample surface just before the magnetic field was applied, when the sample is at different temperatures in heating and cooling. The distribution of the values of the MCE occurring at different sample temperatures, both in the heating (on the left) and in the cooling (on the right) processes can be seen in Fig. 7.66.
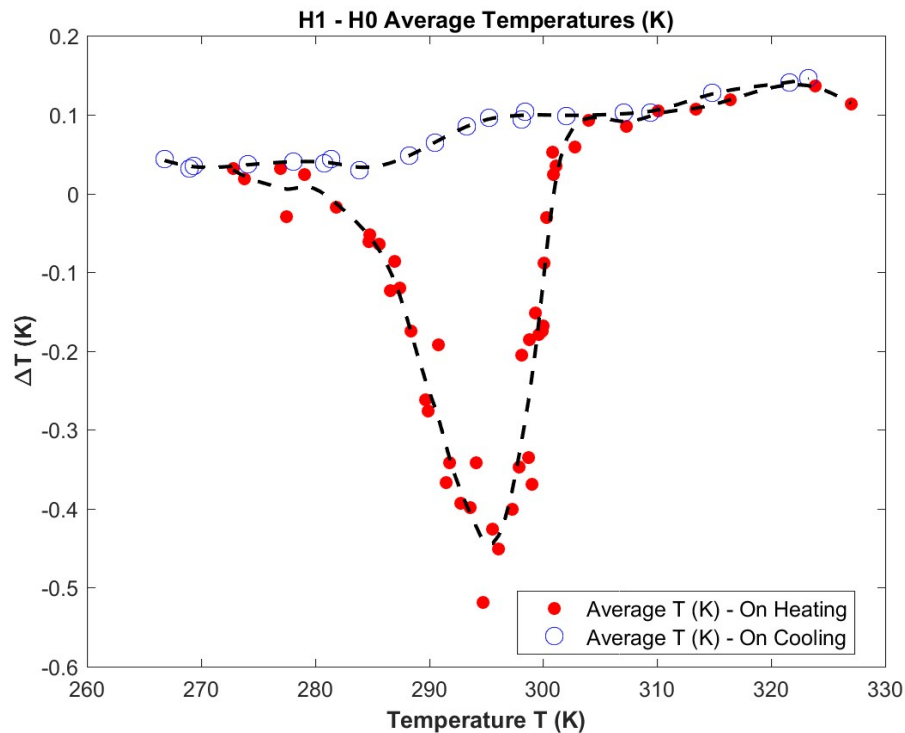
Fig. 7.65 - Difference between the average temperature of the sample surface right after the magnetic field was applied and the average temperature of the sample surface just before the magnetic field was applied, for different sample temperatures in heating and cooling.
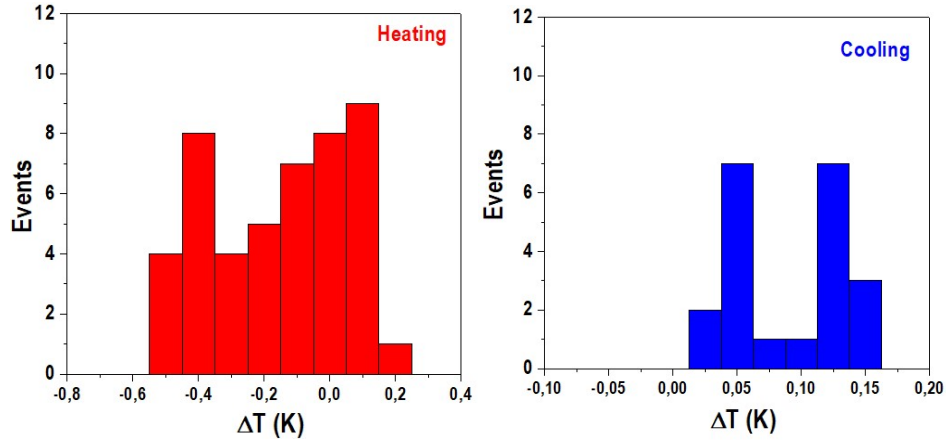
Fig. 7.66 - Distribution of the MCE values in heating and cooling for sample NCMG279.

Fig. 7.67a and 7.67b show, for heating and cooling, respectively, the plot of the difference between the temperature right after and just before the magnetic field was applied for the sample location which registers the maximum and the minimum value of the MCE for each sample temperature (T_{sample}) in heating (this location usually varies from one T_{sample} to the next). The values for the difference in the average temperature of the sample surface in the same conditions are also presented for comparison.
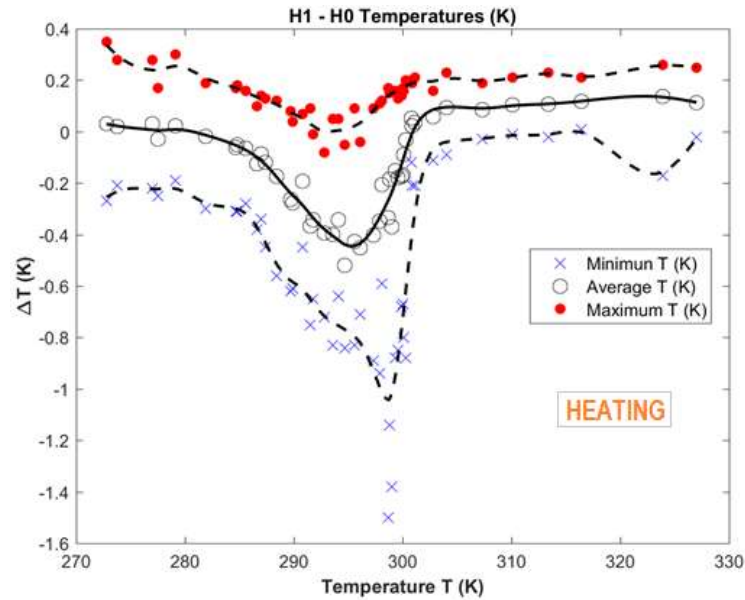
Fig. 7.67a - Plot of $\Delta T = T(H \neq 0) - T(H=0)$ vs T_{sample} in heating for three different situations: minimum, maximum and average calculated ΔT.
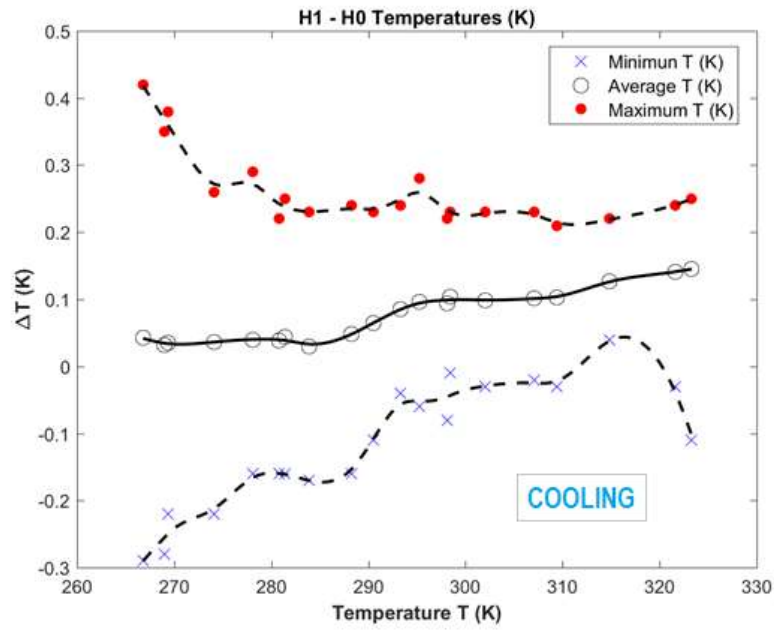
Fig. 7.67b - Plot of $\Delta T = T(H{\neq}0) - T(H{=}0)$ vs T_{sample} in cooling for three different situations: minimum, maximum, and average calculated ΔT.

Fig. 7.68 plots the difference between the maximum and minimum values of the MCE, which occur in different locations (pixels) of the NCMG279 sample for each considered sample temperature, both in heating and cooling procedures.
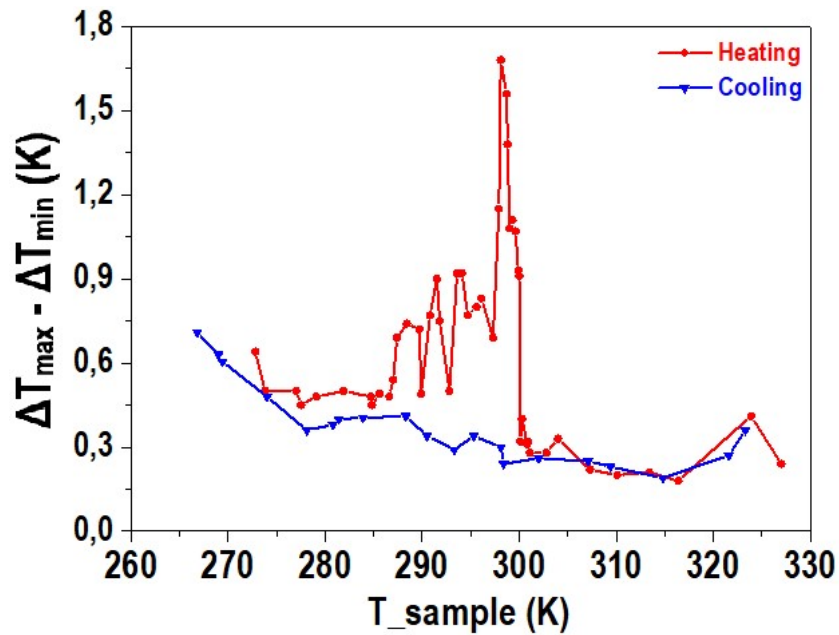
Fig. 7.68 - Difference between the maximum and minimum values of the MCE (naturally registered in different locations of the NCMG279 sample) at each considered sample temperature.

To properly present the inhomogeneity effects, we prepared the mapping of the MCE across all the measured area. Thus, Figs. 7.69 and 7.70 present the sample surface with a color scale depicting the MCE amplitude provided by the IR camera at all measured locations of the sample surface, for all the different sample temperatures considered, for the first magnetic field application, and while the sample is in the heating and cooling process, respectively. All maps in both figures have the same color scale, with limits determined by the highest and lowest values measured throughout the whole experiment. In every map there is a white and a black cross, signaling the location where the maximum and minimum ΔT values occur. For a more dynamic presentation of the changes, videos were prepared with the images presented in Figs. 7.69 and 7.70 . In these videos (links below), we can see the evolution of the phenomena in the whole sample as the studied temperatures increase (a) and then decrease b):

a) https://youtu.be/Q1pquw_2cIE

b) https://youtu.be/WmZBCmeCnIA
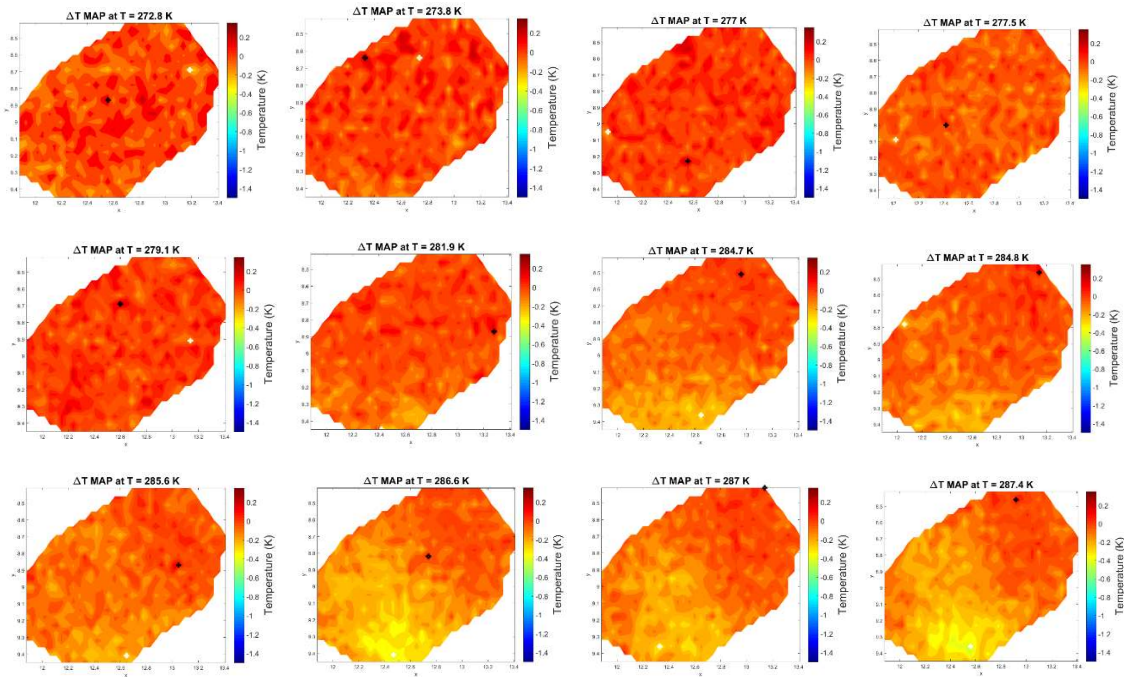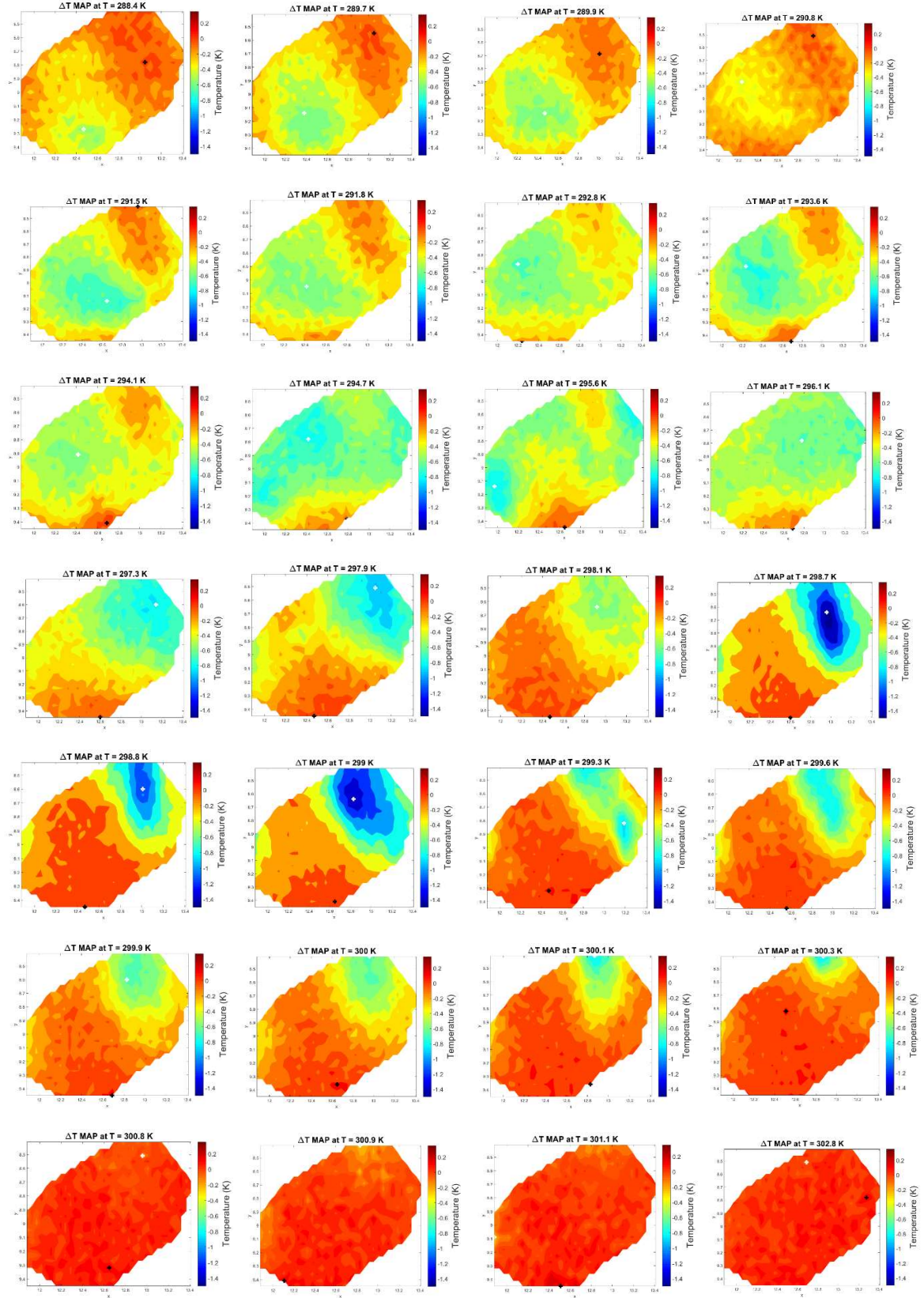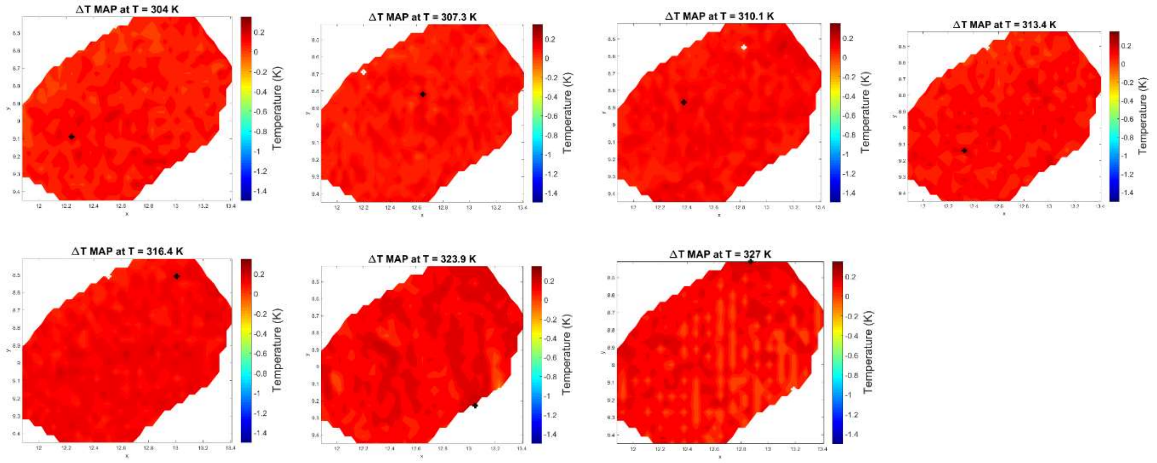
Fig. 7.69 - MCE amplitude measured by the IR camera at different locations of the surface of the sample for different temperatures while the sample is in the heating process.
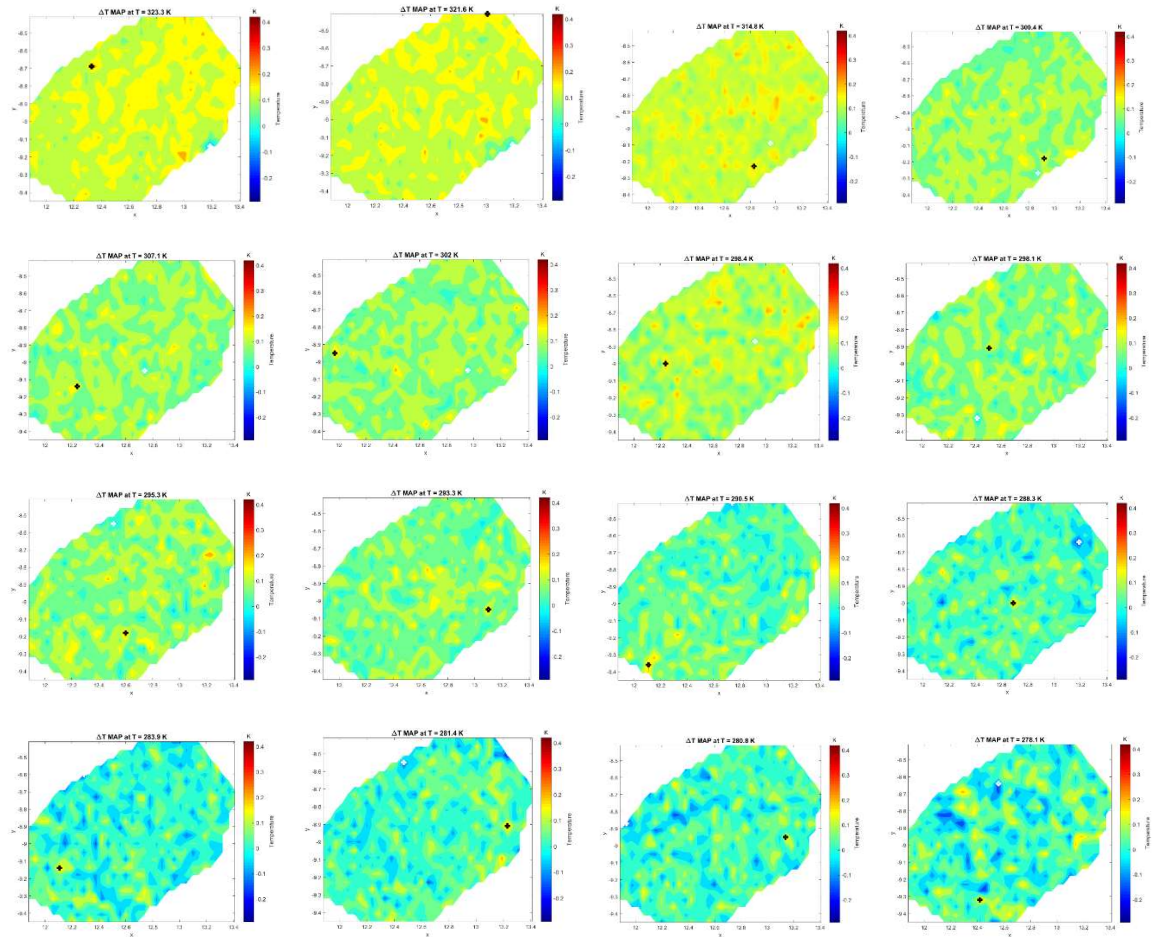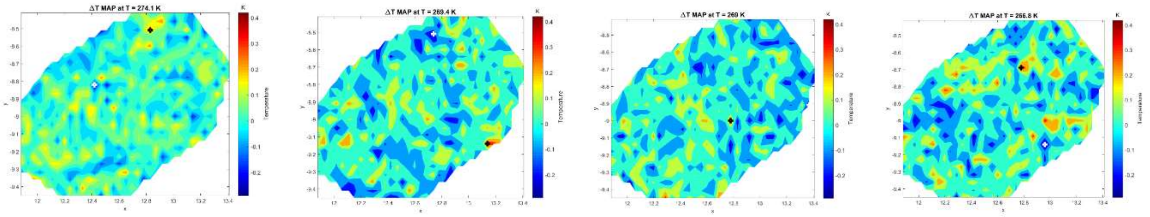
Fig. 7.70 - MCE amplitude measured by the IR camera at different locations of the surface of the sample for different temperatures while the sample is in the cooling process.

Any set of (x,y) coordinates from the maps in Figs. 7.69 and 7.70 can be strategically elected to plot the MCE results in the way that is presented in Figs. 7.71 to 7.74. As an example, we have elected three temperatures of interest according to the observation of the plot in Fig. 7.67, showing the difference between the average temperature of the sample surface right after the magnetic field was applied and the average temperature of the sample surface just before the magnetic field was applied: 277 K (well before the transformation), 298.7 K (within the transformation) and 316.4 K (well after the transformation). For each of these three sample temperatures, we have identified the locations where the ΔTs resulting from the MCE are maximum (highest positive value or negative value with lowest modulus) and minimum (lowest positive value or negative value with highest modulus) on heating. These six different locations were thus selected and their ΔT vs T$_{sample}$ behavior was plotted on heating and cooling in Figs. 7.71 to 7.74.
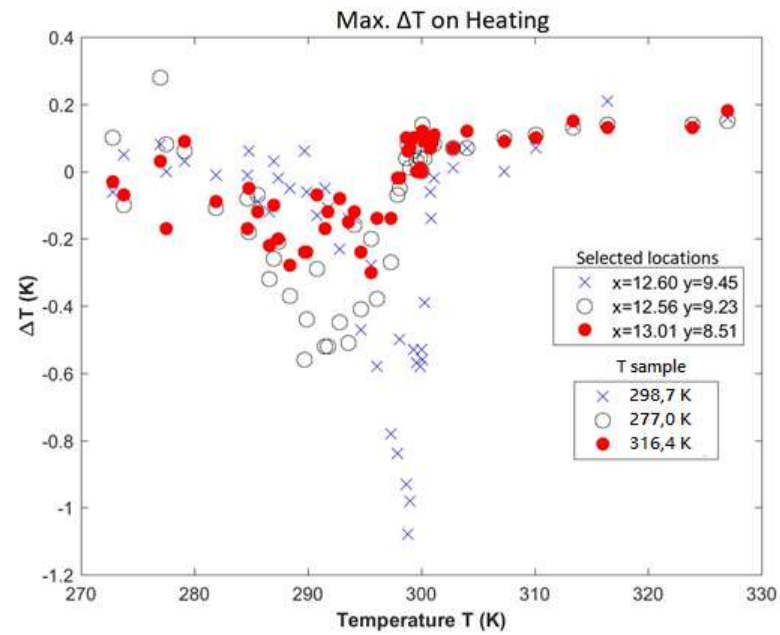
Fig. 7.71 - ΔT vs T$_{sample}$ for selected locations where ΔT max is observed on heating.
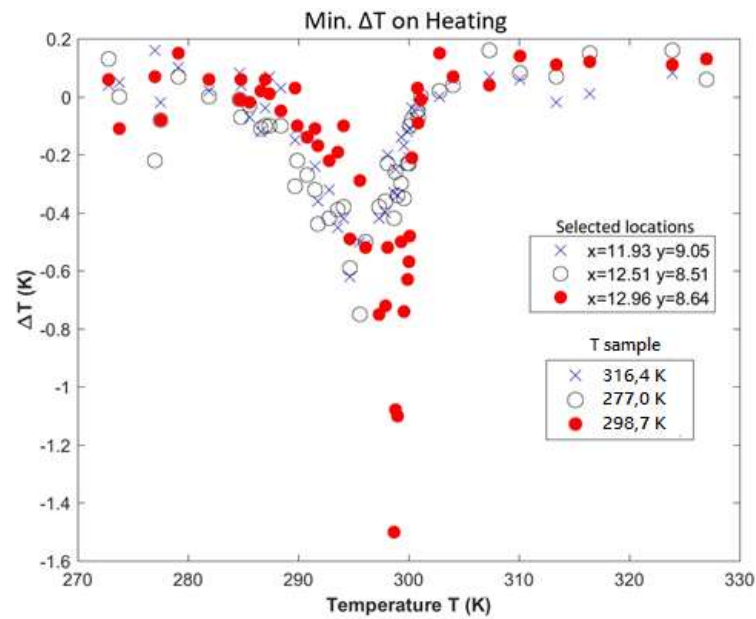
Fig. 7.72 - ΔT vs T$_{sample}$ for selected locations where ΔT min is observed on heating.
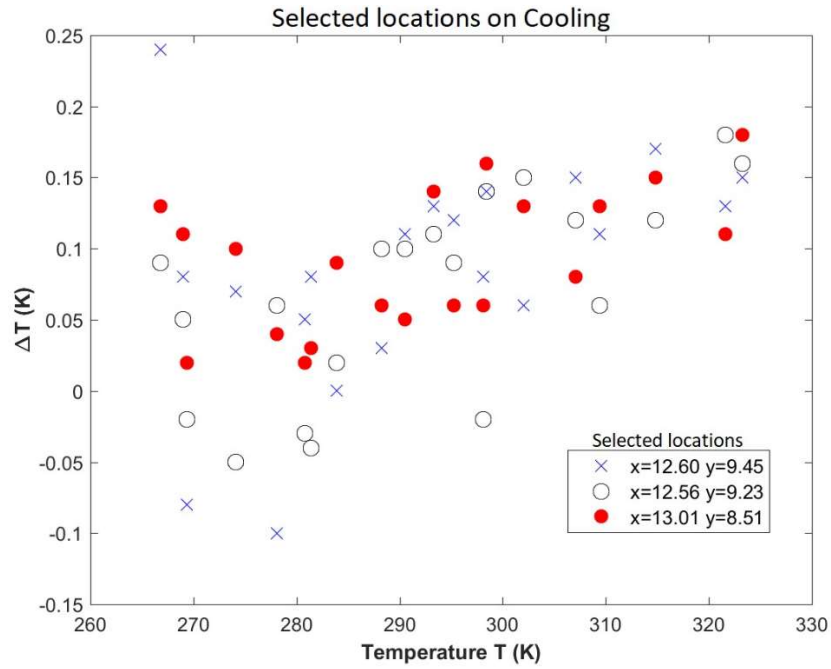
Fig. 7.73 - ΔT vs T$_{sample}$ for same locations from Fig. 7.71, now on cooling.
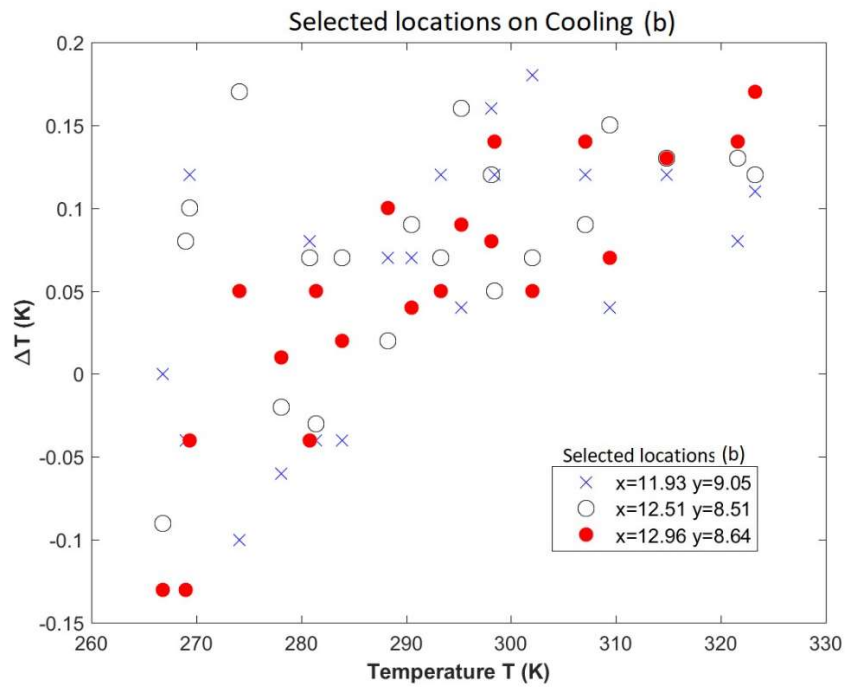
Fig. 7.74 - ΔT vs T$_{sample}$ for same locations from Fig. 7.72, now on cooling.

After this study was performed, as the cleaning of the sample and its removal was attempted, we have observed that, immediately after the removal of the black

paint, some cracks were visible on the surface (Fig. 7.75 left) and eventually there was some removal of material from the cracked surface (Fig. 7.7 right).

Fig. 7.75 - Cracks on the surface of the sample (left) and removal of material from the surface (right).

7.4 – Final remarks

The study reveals substantial novelty in the manifestation of the MCE at the microscopic scale, associated with phase inhomogeneity dynamics, showing clear behavioral differences in heating and cooling (from 273 K to 327 K and then to 267 K) of a FSMA around the martensitic transformation. Mapping of the relative contribution of each microscopic area to the effect during the martensitic transformation was presented.

In 2012, Titov *et al.* [188] discussed the effect of magnetic field-cycling and the conventional and inverse magnetocaloric effect at the macroscale in two systems of the Heusler family: Ni-Mn-In and Ni-Mn-Sn. Their study consisted mainly in measuring adiabatic temperature changes (ΔT_{ad}) as a function of temperature and the effect of field cycling at each temperature of measurement ($T_{measurement}$).

They started with $Ni_{50.0}Mn_{35.3}In_{14.7}$ in the martensitic phase and heat the sample to different values of $T_{measurement}$. For $T < T_{As}$ (T_{As}, starting temperature for reverse martensitic transformation), reversible MCE appears on the first field application and removal. For $T_{As} < T_{measurement} < T_{Af}$, ($T_{Af}$, finish temperature for reverse martensitic transformation), inverse MCE was observed on the first application and removal of

the field, irreversible for further field applications and removals due to hysteresis losses. When the sample initial state was the austenitic phase and it was then cooled to a mixed austenite/martensite phase ($T_{Mf} < T_{measurement} < T_{Ms}$), a reversible inverse MCE was observed.

The $Ni_{48.6}Mn_{34.9}Sn_{16.5}$ sample was cooled to the martensitic state (T = 100 K) and then heated to $T_{measurement}$. For $T_{measurement} < 125$ K, conventional MCE happens when the field is applied and removed. When the sample is on the reverse path of the thermal hysteresis of the M(T) curve, the inverse and conventional MCE are observed, respectively, when the field is applied and removed. For $T_{measurement} > 160$ K, the sample is in the austenitic phase and the conventional MCE is observed. The sample was then taken, for another set of measurements, to the initial state of T = 180 K, and then cooled to the $T_{measurement}$ desired. Only conventional MCE was observed on first field application and removal (no field cycling reported).

They concluded that the occurrence of hysteresis around the transition causes limitations on adiabatic temperature changes and that the reversibility of such changes are linked to the reversibility of the proportion of the structural phases present in the sample at the moment of field application.

The results obtained by Titov *et al.* [188] share common ground with what was here shown in Figs. 7.55 to 7.64. When we consider increasing $T_{measurement}$ values which are set reasonably above the reverse martensitic transformation temperature, a reversible, conventional MCE is observed, with regular $|\Delta T_{ad}|$ values observed in subsequent field applications and removals. When $T_{measurement}$ values are in the vicinity of the reverse martensitic transformation temperature, we also observe a $|\Delta T_{ad}|$ of the first field application higher than the $|\Delta T_{ad}|$ of the first field removal. Still in this vicinity we observe inverse MCE for the first field application and conventional MCE for the first field removal. For three different $T_{measurement}$ values (288.4 K, 294.7 K, and 296.1 K), this also happens for the second field application and removal. For all other $T_{measurement}$ values (except one), subsequent field applications and removals exhibit the conventional MCE. The exception is $T_{measurement} = 292.8$ K, for which only the inverse MCE is observed in every field application and removal.

The compatibility between the macroscopic studies of magnetic field cycling in the MCE of other shape memory alloys and the average ΔT_{ad} results directly obtained by the infrared camera for the whole area of the sample is an indicator of the instrument's reliability for measuring phenomena at smaller scales. It also sets the need of the detailed information for the optimization of magneto-thermal cyclings.

8 – CLOSING REMARKS AND FUTURE WORK

The main goals of this work consist in the study of local thermomagnetic and thermoelastic phenomena at the micrometric and nanometric scale of nanostructured systems of Ni-Mn-Ga (FSMA), Ni-Ti (SMA) and ferroelectric $BaTiO_3$ using infrared thermography and scanning thermal microscopies. These techniques provide resolutions of 3 µm/pixel and 50nm/pixel, respectively, in a wide temperature range.

The study of such phenomena included performing thermal maps of the responses at a micro/nanoscale of the samples under external applied fields and local heating.

We studied the thermal effect of locally induced structural transformations by a combined temperature dependent cantilever deflection in two Ni-Mn-Ga thin films (400 nm and a 100 nm) and compared it to what happens when the transformation is overall induced. The great novelty of this work was finding that locally transforming the sample translates into much wider T_M intervals than for overall structural transformation inducing, within a same micrometric area of the material. Perhaps even more impressive were the local T_Ms maps obtained for the probed areas, which allow an extremely direct and effective visual comparison between locally vs overall structural transformation inducing in terms of its impact on T_M values and transformation progression. Here, SThM, with its simultaneously heated and temperature measuring tip, successfully undertook the role of thermal actuator by locally inducing the transformation. It was disclosed as a relevant tool to locally study and act at a nanometric scale on shape memory alloys exhibiting martensitic twinning on their surface. In the case when changes in the SMA's structure during the transformation do not occur near the surface and/or in a direction in which the cantilever can properly sense them, the described method does not prove successful, as demonstrated for the NiTi wire sample probed. On a

macroscopic scale the SMA transformations and their irreversibility interval were analyzed by electrical and magnetic properties.

The exact reasons why we observed such diversity of local structural transformation behavior in the probed Ni-Mn-Ga films are yet to be fully understood and correlation with further studies must be attempted.

Electrical resistivity is perhaps one of the properties we can measure which is more susceptible to local "inhomogeneties" of the material. Reported "anomalous behaviors" of the electrical resistivity as a function of temperature during the martensitic transition in Ni-Mn-Ga led to further studies which are a good match for the endeavor of trying to understand the martensitic transformation mechanism from a local point of view. We have found in the vicinity of the martensitic transition of a Ni-Mn-Ga thin film deposited onto a Si/SiO_2 avalanche effects (both jumps and depressions) in resistivity vs temperature measurements which are independent of the applied electrical current and aren't eliminated by sample saturating magnetic field values. The reasonable explanation for these phenomena is the occurrence of changes in avalanches in domain walls. Thermal return point memory phenomena are also observed.

It will be important in future work to resort to computational modeling to get further insight on the mechanisms responsible for the differences in the local behavior of the transformation.

The direct measurement of the EC effect in thin films at micro/nanoscale has been proven so challenging that very few attempts are documented. Once more, SThM takes the leading role in performing the task, followed by infrared microscopy. MLCs are a consensual starting point for the unravelling of the strengths and pitfalls of this often-complex task. We have not deviated from the conventional approach and attempted to contribute with our insights on the matter, by realizing that SThM does allow direct measurement at the nanoscale of a ΔT in electrocaloric materials under an electrical field. However, the main conclusion drawn from our study, in conjugation with those by Kar Narayan and Shan is that, ascertaining the true impact of collateral effects on the measurement of ΔT in order to filter them and obtain the most reliable value of ΔT resulting from the EC effect is not straightforward at all and

there is a lot to take into account and clarify before we can safely state that SThM, or infrared thermography (following the same line of thought) are directly measuring the actual EC effect. We show that there is an effect of the electrical field on the SThM probe's cantilever, strongly compromising the control of distance between probe and sample. It is crucial that this effect is carefully dissected and a solution for better control over the probe position in relation to the sample must be devised. Studying this effect by inverting the polarization of the voltage applied would be an interesting follow up in this context. Other aspects to address would be the feasibility of electrical contacts on the thin films while ensuring that mounting of the sample allows proper electrical insulation of the equipment on the sample holder. Clear access for the SThM tip to the area of the sample where the effect is to be measured is also, obviously, a requisite that must be filled.

For the study of the MCE at the microscale, we resorted to a Co-doped Ni-Mn-Ga bulk sample and infrared thermography. The novelty of the study resides in the presentation of large differences of the MCE in heating and cooling, at the microscopic scale, in the vicinity of the structural transformation, due to phase inhomogeneity dynamics. Mapping of the contribution of each microscopic area of the sample to the effect during the structural transformation was performed. The definite follow up is to design, plan and execute a setup for the study of the MCE inhomogeneities with SThM, in order to take these studies a step further into the nanoscale.

The aim of this thesis was to explore and obtain a higher degree of knowledge and phenomenological understanding on the selected caloric effects at the micro/nanoscale, while simultaneously developing currently non-existent routes in the realm of micro/nano-thermal characterization. We have here demonstrated how SThM and infrared thermography enable direct observation and mapping of thermal properties at the nano and micro scales, unveiling what will hopefully in the future become a mere glimpse of how powerful these techniques can prove to be, if properly acknowledged, in several fields, from material science to device thermal management.

It is the author's firm belief that the thesis initial ambition to contribute towards innovative solutions in heat management in different technological fields shall be accomplished and the research presented will hopefully motivate the study of other materials and the exploration of further study routes which are relevant in the context of the considered caloric effects.

9 – REFERENCES

[1] A. Kitanovski, J. Tušek, U. Tomc, U. Plaznik, M. Ozbolt, and A. Poredoš. *Magnetocaloric Energy Conversion: From Theory to Applications.* Springer International Publishing, 2015.

[2] A. Saxena and A. Planes. *Mesoscopic Phenomena in Multifunctional Materials: Synthesis, Characterization, Modeling and Applications.* Springer Series in Materials Science, 2015.

[3] X. Moya, E. Stern-taulats, S. Crossley,D. González-Alonso, S. Kar-narayan, A. Planes, L. Mañosa, and N. D. Mathur. Giant Electrocaloric Strength in Single-Crystal $BaTiO_3$. *Adv. Mat.,* 25(9): 1360–1365, 2013.

[4] K. Otsuka, and C. M. Wayman. *Shape Memory Material.* Cambridge University Press, 1998.

[5] C. Bechtold, C. Chubla, R. L. de Miranda and E. Quandt. High cyclic stability of the elastocaloric effect in sputtered TiNiCu shape memory films. *Appl. Phys. Lett.,* 101:091903, 2012.

[6] J. Cui, Y. Wu, J. Muehlbauer, Y. Hwang, R. Radermacher, S. Fackler, M. Wuttig, and I. Takeuchi. Demonstration of high efficiency elastocaloric cooling with large DT using NiTi wires. *Applied Physics Letters,* 101:073904, 2012.

[7] A. Sozinov, A. Likhachev, N. Lanska, and K. Ullakko. Giant magnetic-field-induced strain in NiMnGa seven-layered martensitic phase. Appl. Phys. Lett., 80: 1746, 2002.

[8] F. Albertini, L . Pareti, and A. Paoluzi. Composition and temperature dependence of the magnetocrystalline anisotropy in $Ni_{2+x}Mn_{1+y}Ga_{1+z}$ (x+y+z=0) Heusler alloys. *Appl. Phys. Lett.,* 81:4032, 2002.

[9] L. Pareti, M. Solzi, F. Albertini, and A. Paoluzi. Giant entropy change at the co-occurrence of structural and magnetic transitions in the Ni Mn Ga Heusler alloy. *Eur. Phys. J. B,* 32:307, 2003.

[10] K.A. Gschneidner Jr., V. K. Pecharsky, and O. Tsokol. Recent developments in magnetocaloric materials. *Rep. Prog. Phys.,* 68:1479, 2005.

[11] L. Mañosa, D. Gonzàlez-Alonso, A Planes, E. Bonnot, M.Barrio, J. L. Tamarit, S. Aksoy, and M. Acet. Giant solid-state barocaloric effect in the Ni−Mn−In magnetic shape-memory alloy. *Nature Mater.*, 9(6): 478−481, 2010.

[12] Sindhunil Barman Roy, *Handbook of Magnetic Materials.* Elsevier, 2014.

[13] A. Sozinov, N. Lanska, A. Soroka, and W. Zou. 12% magnetic field-induced strain in Ni-Mn-Ga-based non-modulated martensite. *Appl. Phys. Lett.*, 102, 021902 (2013)

[14] F. Bernard, P. Delobelle, C. Rousselot, and L. Hirsinger. Microstructural, mechanical and magnetic properties of shape memory alloy $Ni_{55}Mn_{23}Ga_{22}$ thin films deposited by radio-frequency magnetron sputtering. *Thin Solid Films*, 518(1): 399–412, 2009.

[15] P. J. Webster. Heusler alloys. *Contemporary Physics*, 10(6):559-577, 2006.

[16] A. Planes, L. Mañosa, and A. Saxena. *Magnetism and Structure in Functional Materials*. Springer Series in Materials Science, 2005.

[17] J. Dubowik, I. Gościańska, A. Szlaferek, and Y. V. Kudryavtsev. Films of Heusler alloys. *Materials Science*, 25(2):583-598, 2007.

[18] B. I. Bleaney. *Electricity and Magnetism: Volume 2*. Oxford University Press, 2013.

[19] T. Correia and Q. Zhang. *Electrocaloric Materials.* Springer-Verlag Berlin Heidelberg, 91–105, 2014.

[20] J. F. Scott. Electrocaloric Materials. *Annual Review of Materials Research*, 41(1):229-240, 2011.

[21] A. S. Mischenko, Q. Zhang, J. F. Scott, R. W. Wathmore, and N. D. Mathur. Giant Electrocaloric Effect in Thin-Film $PbZr_{0.95}Ti_{0.05}O_3$. *Science* 311:1270, 2006.

[22] M. J. Pereira, A. A. C. S. Lourenço, and V. S. Amaral. Structural and Electromagnetic Properties of Ni-Mn-Ga Thin Films Deposited on Si Substrates. *EPJ Web of Conferences*, 75:03006, 2014

[23] D. Ercolani and L. Sorba. Transport properties of InGaAs based devices. *PhD Thesis*, 2020.

[24] Rede Nacional de Microscopia Eletrónica. http://rnme.up.pt/in3/rnme_pr_3sem_en.htm (2020)

[25] Gomes, L. Transição martensítica em filmes finos de Ni$_{2+x+y}$Mn$_{1-x}$Ga$_{1-y}$. *Masters Thesis*, 2014.

[26] C. Zimm, A. Jastrab, A. Sternberg, V. Pecharsky, K. Gschneidner Jr., M. Osborne, and I. Anderson. Description and Performance of a Near-Room Temperature Magnetic Refrigerator. (1998) In: Kittel P. (eds) Advances in Cryogenic Engineering. Advances in Cryogenic Engineering, vol 43. Springer, Boston, MA.

[27] Sindhunil Barman Roy. Handbook of Magnetic Materials, Edited by K.H.J. Buschow, Elsevier, Volume 22, 2014, Page 206.

[28] J. R. Gómez, J. F. Garcia, R. D. M. Catoira, and M. R. Gómez. Magnetocaloric effect: A review of the thermodynamic cycles in magnetic refrigeration. *Renewable and Sustainable Energy Reviews*, 17:74-82, 2013.

[29] D. C. Wang, Y. H. Li, D. Li, Y. Z. Xia, and J. P. Zhang. A review on adsorption refrigeration technology and adsorption deterioration in physical adsorption systems. *Renewable and Sustainable Energy Reviews,* 14:344–53, 2010.

[30] S. A. Thompson. An overview of nickel-titanium alloys used in dentistry. *International Endodontic Journal*, 33:297-310, 2000.

[31] E. Bonnot, R. Romero, L. Mañosa, E. Vives, and A. Planes. Elastocaloric effect associated with the martensitic transition in shape-memory alloys. *Physical review letters*, 100:125901, 2008

[32] A. M. Tishin, Y. I. Pichkin, V. I. Zverev, and P. W. Egolf. A review and new perspectives for the magnetocaloric effect: new materials and local heating and cooling inside the human body. *International Journal of Refrigeration*, 68:177-186, 2016

[33] http://magnetocaloric.web.ua.pt/mce.html (2020)

[34] A. M. Tishin and Y. I. Spichkin, *The Magnetocaloric Effect and its Applications,* Institute of Physics, CRC Press (2016)

[35] J. Y. Law, V. Franco, L. M. Moreno-Ramírez, A. Conde, D. Y. Karpenkov, I. Radulov, K. P. Skokov, and O. Gutfleisch. A quantitative criterion for determining the order of magnetic phase transitions using the magnetocaloric effect. *Nat. Commun.,* 9:2680, 2018.

[36] E. Warburg. Magnetische untersuchungen. *Ann. Phys.* 13:141-164, 1881.

[37] P. Weiss and A. Piccard. Sur un nouveau phénomène magnétocalorique. *Compt Rend Ac Sci,* 166:352, 1918

[38] S. A. Niktin, G. Myalikgulyev, A. M. Tishin, M. P. Annaorazov, K. A. Asatryan, A, and L. Tyurin. Magnetocaloric effect in FeRh compound. *Phys. Lett. A,* 148:363-366, 1990

[39] W. F. Giauque. A thermodynamic treatment of certain magnetic effects. A proposed method of producing temperatures considerably below 1° absolute. *J. Am. Chem. Soc.*, 49(8):1864–1870, 1927.

[40] G. V. Brown. Magnetic heat pumping near room temperature. *Journal of Alloys and Compounds*, 47:3673-80, 1976.

[41] A. M. Tishin and Y. I. Spichkin. Recent progress in magnetocaloric effect: Mechanisms and potential applications. *International Journal of Refrigeration*, 37:223-229, 2014.

[42] C. Felser and A. Hirohata. *Heusler Alloys: Properties, Growth, Applications.* Springer International Publishing, 2015.

[43] R. C. O'Handley, *Modern Magnetic Materials: Principles and Applications*. John Wiley & Sons, 2000.

[44] P. J. Webster, K. R. A. Ziebeck, S. L. Town and M. S. Peak. Magnetic order and phase transformation in Ni2MnGa. *Philosophical Magazine B*, 49(3):295-310, 1984

[45] J. Pons, V. A. Chernenko, R. Santamarta, and E. Cesari. Crystal structure of martensitic phases in Ni-Mn-Ga shape memory alloys. *Acta Mater,* 48:3027–3038, 2000.

[46] A. N. Vasil'ev, V. D. Buchel'nikov, T. Takagi, V. V. Khovailo, and E. I. Estrin. Shape memory ferromagnets. *Phys Uspekhi,* 46:559–588, 2003.

[47] L. Righi, l., F. Albertini, L. Pareti, A. Paoluzi, and G. Calestani. Commensurate and incommensurate "5M" modulated crystal structures in Ni–Mn–Ga martensitic phases. *Acta Mater,* 55:5237–5245, 2007.

[48] C. P. Opeil, B. Mihaila, R. K. Schulze, L. Mañosa, A. Planes, W. L. Hults, R. A. Fisher, P. S. Riseborough, P. B. Littlewood, J. L. Smith, and J. C Lashley.

Combined experimental and theoretical investigation of the premartensitic transition in Ni_2MnGa. *Phys Rev Lett* 100:165703, 2008.

[49] A. Planes, L. Mañosa, and M. Acet. Magnetocaloric effect and its relation to shape-memory properties in ferromagnetic Heusler alloys. *J Phys Condens Matter*, 21:233201, 2009.

[50] V. V. Khovaylo, V. D. Buchelnikov, R. Kainuma, V. V. Koledov, M. Ohtsuka, V. G. Shavrov, T. Takagi, S. V. Taskaev, and A. N. Vasiliev. Phase transitions in $Ni_{2+x}Mn_{1-x}Ga$ with a high Ni excess. *Physical Review B,* 72:224408/1-224408/10, 2 005.

[51] V. A. Chernenko, A. R. Lopez, M. Kohl, J. M. Barandiaran, M. Ohtsuka, I. Orue, and S. Besseghini. Structural and magnetic characterization of martensitic Ni–Mn–Ga thin films deposited on Mo foil. *Acta materialia*, 20:5461-5467, 2006.

[52] R. Honeycombe, and H. Bhadeshia. *Steels: microstructure and properties*. Butterworth-Heinemann, 1995.

[53] L. Righi, F. Albertini, G. Calestani, L. Pareti, A. Paoluzi, C. Ritter, P. A. Algarabel, L. Morellon, and I. M. Ricardo. Incommensurate modulated structure of the ferromagnetic shape-memory Ni_2MnGa martensite. *Journal of Solid State chemistry,* 179(11):3525-3533, 2006.

[54] A. Ayuela, J. Enkovaara, K. Ullakko, and R. M. Nieminen. Structural properties of magnetic Heusler alloys. *J. Phys.: Condens. Matter* 11:2017–2026, 1999.

[55] Z. Y. Zhang, Z. W. Du, B. L. Shao, A. S. Liu, and Z. M. Sun. Characterization of Ni–Mn–Ga alloy with Gd addition. *Materials Characterization*, 8:1041-1045, 2008.

[56] V. N. Murray. *Progress in Ferromagnetism Research*. Nova Science Pub Inc, 2006.

[57] M. V. McLeod, D. Bayer, Z. Turgut, A. K. Giri, and B. S. Majumdar. Significant enhancement of magnetocaloric effect in a NiMnCuGa Heusler alloy through textural modification. *J. Appl. Phys.,* 127:223906, 2020.

[58] M. Pasquale, C. P. Sasso, L. H. Lewis, L. Giudici, T. Lograsso, and D. Schlagel. Magnetostructural transition and magnetocaloric effect in $Ni_{55}Mn_{20}Ga_{25}$ single crystals. *Phys. Rev. B,* 72:094435, 2005.

[59] L. Zhenzhuang, I. Zongbin, B. Yang, Y. Yang, Y. Zhang, C. Esling, X. Zhao, and L. Zuo. Large low-field magnetocaloric effect in directionally solidified $Ni_{55}Mn_{18+x}Ga_{27-x}$ (x=0, 1, 2) alloys. *Journal of magnetism and magnetic materials*, 445:71-76, 2018.

[60] J. Liu, T. Gottschall, K. P. Skokov, J. D. Moore, and O. Gutfleisch. Giant magnetocaloric effect driven by structural transitions. *Nat Mater.*, 11(7):620-626, 2012

[61] G. Porcari, F. Cugini, S. Fabbrici, C. Pernechele, F. Albertini, M. Buzzi, M. Mangia, and M. Solzi, Convergence of direct and indirect methods in the magnetocaloric study of first order transformations: The case of Ni-Co-Mn-Ga Heusler alloys. *Phys. Rev. B,* 86:104432, 2012.

[62] S. Fabbrici, F. Albertini, A. Paoluzi, A., F. Bolzoni, R. Cabassi, M. Solzi, L. Righi, and G. Calestani. Reverse magnetostructural transformation in Co-doped NiMnGa multifunctional alloys. *Applied Physics Letters*, 95:022508, 2009.

[63] S. Fabbrici, J. Kamarad, Z. Arnold, F. Casoli, A. Paoluzi, F. Bolzoni, R. Cabassi, M.Solzi, G. Porcari, C. Pernechele, and F.Albertini., From direct to inverse giant magnetocaloric effect in Co-doped NiMnGa multifunctional alloys, *Acta Materialia,* 59 412–419, 2011

[64] L. Mañosa, A. Planes, E. Vives, E. Bonnot, and R. Romero. The use of shape-memory alloys for mechanical refrigeration. *Funct. Mater. Lett.,* 2:73–78, 2009.

[65] A. Ziolkowski. *Pseudoelasticity of Shape Memory Alloys: Theory and Experimental Studies.* Butterworth-Heinemann, 2015.

[66] K. Yamauchi, I. Ohkata, K. Tsuchiya, and S. Miyazaki. *Shape Memory and Superelastic Alloys Applications and Technologies.* Woodhead Publishing, 2011.

[67] E. Bonnot, R. Romero, X. Illa, L. Mañosa, A. Planes, and E. Vives. Hysteresis in a system driven by either generalized force or displacement variables: Martensitic phase transition in single-crystalline Cu−Zn−Al. *Phys. Rev. B,* 76:064105, 2007.

[68] W. Buehler, J. V. Gilfrich, and R. C. Wiley. Effect of Low-Temperature Phase Changes on the Mechanical Properties of Alloys near Composition TiNi. *Journal of Applied Physics*, 34:1475, 1963.

[69] M. A. Ferreira, M. A. Luersen, and P. C. Borges. Nickel-titanium alloys: A systematic review. *Dental Press J. Orthod.*, 17(3):71-82, 2012.

[70] N. A. Zarkevich n.a. and D. D. Johnson. What is the stable atomic structure of NiTi austenite? *Phys. Rev. B*, 90:060102, 2014.

[71] K. Otsuka and X. Ren. Physical Metallurgy of Ti-Ni-based Shape Memory Alloys. *Progress in Materials Science,* 50(5):511–678, 2005.

[72] http://www.biancogianfranco.com/It%2020Mio%20sito%20Materiali%20e%20 trattamenti.html (2017)

[73] H. Ossmer, C. Chluba, B. Krevet, E. Quandt, M. Rohde, and M. Kohl. Elastocaloric cooling using shape memory alloy films. *Journal of Physics: Conference series*, 476:012138, 2013.

[74] H. Ossmer, C. Chluba, M. Gueltig, E. Quandt, M. Kohl. Local evolution of the elastocaloric effect in TiNi-Based Filme. *Shape Memory Superelasticity*, 1(2):142–152, 2015.

[75] J. P. Garrett, E. Ertekin, and H. Sehitoglu. Elastocaloric cooling potential of NiTi, Ni_2FeGa, and CoNiAl, *Acta Materialia* 96:420–427, 2015.

[76] P. Kobenko and J. Z. Kurtschatov. Dielektrische eigenschaften der seignettesalzkristalle. *Physik*, 66:192, 1930.

[77] G. G. Wieseman and J. K. Kuebler. Electrocaloric effect in ferroelectric Rochelle salt. *J. Phys. Rev.*, 131:2023, 1963.

[78] M. Anoufa, J. M. Kiat, and C. Bogicevic. Electrocaloric effect in core-shell ferroelectric ceramics: Theoretical approach and practical conclusions. *Appl. Phys. Lett.*, 107:172902, 2015.

[79] H. Maiwa. *Electrocaloric Properties of (Pb,La)(Zr,Ti)O3 and BaTiO3 Ceramics*, Advanced Ceramic Processing, Mohamed, A.M.A (Ed.), InTech (2015)

[80] B. Neese, B. Chu, S.-G. Lu, Y. Wang, E. Furman, and G. M Zhang. Large electrocaloric effect in ferroelectric polymers near room temperature. *Science,* 321:821, 2008.

[81] Y. Bai, K. Ding, G. P Zheng, S. Q Shi, L. J. Qiao, and D. Guo. The Electrocaloric Effect in BaTiO$_3$ Thick Film Multilayer Structure at High Electric Field. *Key Engineering Materials*, 512-515:1304-1307, 2012.

[82] M. Ožbolt, A. Kitanovski, J. Tušek, A. Poredoš. Electrocaloric refrigeration: Thermodynamics, state of the art and future perspectives. *International Journal of Refrigeration*, 40:174-188, 2014.

[83] G. H. Kwei, A. C. Lawson, S. J. L. Billinge, and S. W. Cheong. Structures of the ferroelectric phases of barium titanate. *J. Phys. Chem.,* 97(10):2368–2377, 1993.

[84] www.materialsdesign.com/system/files/appnotes/BaTiO3_1.pdf (2017)

[85] P. Geeta, P. Sarita, and D. K. Rao. Synthesis, structure, properties, and applications of barium titanate nanoparticles. *International Journal of Advanced Technology in Engineering and Science*, 4(1), 2016.

[86] S. Nayak, B. Sahoo, T. K. Chaki, and D. Khastgir. Facile preparation of uniform barium titanate (BaTiO3) multipods with high permittivity: impedance and temperature dependent dielectric behavior. *RSC Adv.*, 4:1212-1224, 2014.

[87] S. A. Hayward and E. Salje. The pressure-temperature phase diagram of BaTiO$_3$: A macroscopic description of the low-temperature behaviour. *Journal of Physics: Condensed Matter,* 14:L599, 2002.

[88] G. Akcay, S. P. Alpay, J. V. Mantese, and G. A. Rossetti. Magnitude of the intrinsic electrocaloric effect in ferroelectric perovskite thin films at high electric fields. *Appl. Phys. Lett.*, 90:252909, 2007.

[89] J. H. Qiu and Q. Jiang. Grain size effect on the electrocaloric effect of dense BaTiO$_3$ nanoceramics. *J. Appl. Phys.,* 105:034110, 2009.

[90] Y. Bai, G. Zheng, and S. Shi. Direct measurement of giant electrocaloric effect in BaTiO$_3$ multilayer thick film structure beyond theoretical prediction. *Appl. Phys. Lett,* 96:192902, 2010.

[91] S. Kar-Narayan and N. D. Mathur. Direct and indirect electrocaloric measurements using multilayer capacitors, *J. Phys. D: Appl. Phys.,* 43:032002, 2010.

[92] C. Dekker. Carbon nanotubes as molecular quantum wires. *Phys Today* 52**:**22–30, 1999.

[93] L. Shi and A. Majumdar. *Micro-nano scale thermal imaging using scanning probe microscopy,* Applied Scanning Probe Techniques, Bhushan, B., Fuchs, H. & Hosaka, S. (Eds.), 327–362. Berlin: Springer-Verlag Berlin. (2004)

[94] B. Cretin, S. Gomès, N. Trannoy, and P. Vairac. *SThM in Microscale and Nanoscale Heat Transfer,* Volz, S. (Ed.), 181–238. Berlin: Springer-Verlag Berlin. (2007).

[95] C. D. Brites, P. P. Lima, N. J. Silva, A. Millán, V. S. Amaral, F. Palacio and L. D. Carlos. Thermometry at the nanoscale. *Nanoscale*, 4(16):4799–4829, 2012.

[96] P. Tovee, M. Pumarol, D. Zeze, K. Kjoller, O. Kolosov. Nanoscale spatial resolution probes for SThM of solid stat materials. *J Appl Phys*, 112(11):114317, 2012.

[97] Y. Yue, and X. Wang. Nanoscale thermal probing. *Nano Rev*, 3:11586, 2012.

[98] S. Kar-Narayan, S. Crossley, X. Moya, V. Kovacova, J. Abergel, A. Bontempi, N. Baier, E. Defay, and N. D. Mathur. Direct electrocaloric measurements of a multilayer capacitor using SThM and infra-red imaging. *Appl Phys Lett,* 102:032903, 2013.

[99] A. Kaźmierczak-bałata, J. Bodzenta, M. Krzywiecki, J. Juszczyk, J. Szmidt, and P. Firek. Application of scanning microscopy to study correlation between thermal properties and morphology of $BaTiO_3$ thin films. *Thin Solid Films*, 545:217–221, 2013.

[100] E.-S. Lee, S. Cho, H.-K Lyeo, and Y.-H. Kim. Seebeck effect at the atomic scale. *Phys Rev Lett,* 112:136601, 2014.

[101] G. Wielgoszewski, M. Babij, R. F. Szeloch, T. Gotszalk. Standard-based direct calibration method for SThM nanoprobes. *Sens Actuators A* 214:1–6, 2014.

[102] F. Menges, A. Stemmer, H. Riel, and B. Gotsmann. Quantitative thermometry of nanoscale hot spots, *Nano Lett*, 12:596, 2012.

[103] G. Hwang, J. Chung, and O. Kwon. Enabling low-noise nullpoint SThM by the optimization of scanning thermal microscope probe through a rigorous theory of quantitative measurement. *Rev Sci Instrum*. 85(11):114901, 2014.

[104] A. Majumdar, SThM. *Annu Rev Mater Sci*, 29:505–585, 1999.

[105] U. Wischnath, J. Welker, M. Munzel, and A. Kittel. The near-field scanning thermal microscope. *Rev Sci Instrum*, 79:073708, 2008.

[106] M. Mcconney, D. Kulkarni, H. Jiang, T. Bunning, and V. Tsukruk. A new twist on SThM. *Nano Lett*, 12(3):1218, 2012.

[107] F. Menges, A. Stemmer, H. Riel, and B. Gotsmann. Thermal transport into graphene through nanoscopic contacts. *Phys Rev Lett*, 111:205901, 2013.

[108] S. Gomès, A. Assy, and P. Chapuis. SThM: A review. *Phys Status Solidi A*, 212:477–494, 2015.

[109] J. Lee and Y. Gianchandani. High-resolution scanning thermal probe with servocontrolled interface circuit for microcalorimetry and other applications. *Rev Sci Instrum*, 75:1222, 2004.

[110] H. M. Pollock and A. Hammiche. Micro-thermal analysis: Techniques and applications. *J Phys D: Appl Phys*., 34:R23–R53, 2001.

[111] S. Cho, S. D. Kang, W. Kim, E.-S. Lee, S.-J. Woo, K.-J. Kong, I. Kim, H.-D. Kim, T. Zhang, J. A. Stroscio, Y. Kim, and H.-K. Lyeo. Thermoelectric imaging of structural disorder in epitaxial graphene. *Nat Mater,* 12(10):913–918, 2013.

[112] T.-H. Fanga and W.-J. Chang. Microthermal machining using SThM. *Appl Surf Sci*, 240:312–317, 2005.

[113] D. M. Price (2008). Micro-thermal analysis and related techniques. In Handbook of Thermal Analysis and Calorimetry Vol 5 Chapter 3, Brown, M. E., Gallagher, P. K. (Eds.), pp. 55-92. Amsterdam: Elsevier.

[114] J. Bodzenta, J. Juszczyk, and M. Chirtoc. Quantitative scanning thermal microscopy based on determination of thermal probe dynamic resistance. *Review of Scientific Instruments*, 84:093702, 2013.

[115] L. David, S. Goḿes, and M. Raynaud. Application of scanning thermal microscopy for thermal conductivity measurements on meso-porous silicon thin films. *Journal of Physics D: Applied Physics,* 40:4337–46, 2007.

[116] B. Gotsmann and M. A. Lantz. Quantized thermal transport across contacts of rough surfaces. *Nature Materials,* 12:59-65, 2012.

[117] https://cordis.europa.eu/project/id/604668/reporting (2020)

[118] M. Reading and D. Price. (2003) US Pat. Appl. 20030004905

[119] P. G. Royall, D. Q. M. Craig, and D. B. Grandy. The Use of Micro-Thermal Analysis as a means of in-situ characterization of a Pharmaceutical Tablet Coat. *Thermochim. Acta,* 380:165, 2001.

[120] https://www.kntnano.com/probes/ (2020)

[121] S. Gomès, L. David, V. Lysenko, A. Descamps, T. Nychyporuk, and M. Raynaud. Application of scanning thermal microscopy for thermal conductivity measurements on meso-porous silicon thin films. *J. Phys. D: Appl. Phys.,* 40:6677-6683, 2007.

[122] Ref. Manual Park

[123] G. Meyers, A. Pastzor, (n.d.) Correlation between nanoscale and bulk Thermal Analysis, Retrieved from http://www.anasysinstruments.com/an10.pdf

[124] H. Fischer. Calibration of micro-thermal analysis for the detection of glass transition temperatures and melting points. *Journal of Thermal Analysis and Calorimetry,* 92(2):625–630, 2008.

[125] S. Gomès, P. Newby, B. Canut, K. Termentzidis, O. Marty, L. Fréchette, P. Chantrenne, V. Aimez, J.-M. Bluet, and V. Lysenko. Characterization of the thermal conductivity of insulating thin films by scanning thermal microscopy. *Microelectronics Journal,* 44:1029–1034, 2013.

[126] N-A. Gotzen and G. Van Assche. Nano-Thermal Analysis: Application to Studies of Polymer Blends*. Imaging & Microscopy* 9(2):33–34, 2007.

[127] V. V. Tsukruka, V. V. Gorbunova, and N. Fuchigamia. Microthermal analysis of polymeric materials. *Thermochimica Acta,* 395:151–158, 2003.

[128] A. Dawson, M. Rides, A. S. Maxwell, A. Cuenat, and A. R. Samano. Scanning thermal microscopy techniques for polymeric thin films using temperature contrast mode to measure thermal diffusivity and a novel approach in conductivity contrast mode to the mapping of thermally conductive particles. *Polymer Testing,* 41:198-208, 2015.

[129] https://www.engineeringtoolbox.com/thermal-conductivity-d_429.html (2020)

[130] https://www.professionalplastics.com/professionalplastics/ThermalProperties ofPlasticMaterials.pdf (2020)

[131] https://www.engineeringtoolbox.com/thermal-conductivity-metals-d_858.html (2020)

[132] https://periodictable.com/Properties/A/ThermalConductivity.v.html (2020)

[133] Y. K. Kuo, K. M. Sivakumar, H. C. Chen, J. H. Su and C. S. Lue. Anomalous thermal properties of the Heusler alloy $Ni_{2+x} Mn_{1-x}Ga$ near the martensitic transition. *Physical Rev. B,* 72:054116, 2005.

[134] R. W. Ruddock. *Basic Infrared Thermography Principles.* Reliabilityweb.com, 2010.

[135] G. Gaussorgues. *Infrared Thermography.* London, Chapman Hall, 1994.

[136] A. Rogalski. History of infrared detectors. *Opto-Electronics Review*, 20(3):279-308, 2012.

[137] R. Berz and H. Sauer. *The Medical Use of Infrared-Thermography-History and Recent Applications,* Thermografie-Kolloquium, Lecture 04, 1-12 (2007)

[138] A. Kouba and S. Willard. *What is new and hot in zoo technology: thermography,* Communiqué (American Zoo & Aquarium Association) March 10–13 (2005).

[139] A. F. Boonstra, L. Germeroth, E. J. Boekema. Structure of the light harvesting antenna from Rhodospirillum molischianum studied by electron microscopy. *Biochim. Biophys. Acta,* 1184:227–234, 1994.

[140] D. J. McCafferty. The value of infrared thermography for research on mammals: previous applications and future directions. *Mammal Rev.,* 37(3):207–223, 2007.

[141] R. Usamentiaga, P. Venegas, J. Guerediaga, L. Veja, J. Molleda, F. G. Bulnes. Infrared thermography for temperature measurement and non-destructive testing. *Sensors-Basel*, 14(7):12305-48, 2014.

[142] G. J. Tattersall. Infrared thermography: A non-invasive window into thermal physiology. *Comparative biochemistry and physiology. Part A, Molecular & integrative physiology*, 202:78-98, 2016.

[143] B. Subramainam, B. B. Lahiri, T. Saravanan, and T. Jayakumar. Infrared Thermography for Condition Monitoring- A Review. *Infrared Physics & Technology*, 60:35–55, 2013.

[144] Y. Q. Fu, S. Zhang, M. J. Wu, W. M. Huang, H. J. Du, J. K. Luo, A.J. Flewitt, and W.I. Milne. On the lower thickness boundary of sputtered TiNi films for shape memory application. *Thin Solid Films,* 515:80-86, 2006.

[145] A. Ishida, M. Sato. Thickness effect on shape memory behavior of Ti-50.0at.%Ni thin film. *Acta Mater*, 51(18):5571-5578, 2003.

[146] J. Ye, R. K. Mishra, A. R. Pelton, and A. M. Minor. Direct observation of the NiTi martensitic phase transformation in nanoscale volumes. *Acta Materialia,* 58(2): 490–498, 2010.

[147] T. Waitz, V. Kazykhanov, and H. P. Karnthaler. *Acta Mater*, 52:137, 2004.

[148] J. W. Dong, J. Q. Xie, J. Lu, C. Adelmann, C. J. Palmstrøm, J. Cui, Q. Pan, T. W. Shield, R. D. James, and S. McKernan. Shape memory and ferromagnetic shape memory effects in single-crystal Ni_2MnGa thin films. *Journal of Applied Physics,* 95(5):2593-2600, 2004.

[149] https://www.nanoandmore.com/AFM-Probe-PPP-CONTR (2020)

[150] S. Kaufmann, U. K. Roessler, O. Heczko, M. Wuttig, J. Buschbeck, L. Schultz, and S. Fahler. Adaptive Modulations of Martensites. *Phys. Rev. Lett.,* 104:145702, 2010.

[151] S. Kaufmann, R. Niemann, T. Thersleff, U. K. Rößler, O. Heczko, J. Buschbeck, B. Holzapfel, L. Schultz, and S. Fähler. Modulated martensite: why it forms and why it deforms easily. *New J. Phys.,* 13:053029, 2011.

[152] A. Diestel, A. Backen, V. Neu, L. Schultz, and S. Fähler. Magnetic domain structure of epitaxial Ni-Mn-Ga films. *Scripta Materialia,* 67:423-6, 2012.

[153] X. Jin, D. Bono, C. Henry, and J. Feuchtwanger. Relaxation in Ni–Mn–Ga ferromagnetic shape memory alloys. *Philos. Mag.*, 83(28):3193, 2003.

[154] A. N. Vasil'ev, A. D. Bozhko, and V. V. Khovailo. Structural and magnetic phase transitions in shape-memory alloys $Ni_{2+x}Mn_{1-x}Ga$. *Pys Rev B,* 59:1113, 1999.

[155] Y. K. Kuo, K. M. Sivakumar, H. C. Chen, J. H. Su, and C. S. Lue. Anomalous thermal properties of the Heusler alloy $Ni_{2+x}Mn_{1-x}Ga$ near the martensitic transition. *Physical Review B*, 72:054116, 2005.

[156] V. V. Khovailo, K. Oikawa, C. Wedel, T. Takagi, T. Abe, and K. Sugiyama. Influence of intermartensitic transitions on transport properties of $Ni_{2,16}Mn_{0,84}Ga$ alloy. Journal of Physics Condensed Matter, 16(12): 1951-1961, 2004.

[157] F. Zuo, X. Su, and P. Zhang. Magnetic and transport properties of the $Ni_{2-x}Mn_{1+x}Ga$. *J. Phys. Condens. Matter,* 11:2821-2830, 1999.

[158] V.V. Khovailo, V. Takagi, A.D. Bozhko, and M. Matsumoto. Premartensitic transition in $Ni_{2+x}Mn_{1-x}Ga$ Heusler alloys. *J. Phys. Condens. Matter*, 13(42):9655, 2001.

[159] Tickle R., James R. D., Journal of magnetism and Magnetic Materials, 195 (1999) 627-638 Magnetic and magnetomechanical properties of Ni2MnGa

[160] J. Dubowik and I. Goscianska. Martensitic transformations in Ni-Mn-Ga sputtered films. *Journal of Magnetism and Magnetic materials,* 316(2):e599-e602, 2007.

[161] JCPDS file no. 65-5328

[162] F. Figueiras, E. Rauwel, and V. S. Amaral. Study of Ni_2-Mn-Ga phase formation by magnetron sputtering film deposition at low temperature onto Si substrates and $LaNiO_3/Pb(Ti,Zr)O_3$ buffer. *Journal of Vacuum Science & Technology A*, 28(1):6, 2010.

[163] J. Dubowik, I. Gościańska, Y. V. Kudryavtsev, Y. P. Lee, P. Sovák, and M. Konĉ. Magnetic properties of Ni-Mn-Ga Heusler alloy films. 3(1):143-146

[164] J. Ortín and L. Delaey. Hysteresis in shape-memory alloys. *International Journal of Non-Linear Mechanics,* 37(8):1275-1281, 2002.

[165] X. B. Wang, B. Verlinden, and J. Van Humbeeck. R-phase transformation in NiTi alloys. *Materials Science and Technology,* 30(13):1517-1529, 2014.

[166] J. Uchil, K. Ganesh Kumara, and K. K. Mahesh. Effect of thermal cycling on R-phase stability in a NiTi shape memory alloy. *Materials Science and Engineering: A,* 332(1-2):25–28, 2002.

[167] PDF 04-004-8472, International Centre for Diffraction Data

[168] PDF 04-014-2533, International Centre for Diffraction Data

[169] W. Brantley, D. Berzins, M. Iijima, E. Tufekçi, and Z. Cai. *Structure/property relationships in orthodontic alloys.* In book *Orthodontic Applications of Biomaterials,*

[170] N. A. Zarkevich and D. D. Johnson. Stable Atomic Structure of NiTi Austenite. *Physical Review B,* 90(6): 060102(R), 2014.

[171] R. J. Wasilewski, S. R. Butler, and J. E. Hanlon. On the Martensitic Transformation in TiNi. Met. Sci. J., 1(1):104–110, 1967.

[172] F. E. Wang, B. F. DeSavage, W. J. Buehler, and W. R. Hosler. The Irreversible Critical Range in the TiNi Transition. *J. Appl. Phys.,* 39(5):2166–2175, 1968.

[173] M. A. Mitchell, F. E. Wang, and J. R. Cullen. Electronic density of states in TiNi II and TiNi III. *J. Appl. Phys.,* 45(8):3337–3339, 1974.

[174] S. E. Kulkova, V. E. Egorushkin, and V. V. Kalchikhin. The electron structure of NiTi martensite. *Solid State Commun.,* 77(9):667–670, 1991.

[175] T. Fukuda, T. Kakeshita, H. Houjoh, S. Shiraishi, and T. Saburi. Electronic structure and stability of intermetallic compounds in the Ti–Ni System. *Mater. Sci. Eng. A,* 273–275:166–169, 1999.

[176] A. Kyianytsia. Magnetic and magnetoelastic properties of NiTi shape memory alloy and NiTi/Ni bilayer. Physics [physics]. Université de Lorraine, 2019. English. NNT:2019LORR0299 tel-02559546

[177] N. Botterill, D. Grant, J. Zhang, and C. Roberts. A new approach to characterization of the transition temperatures of thin film NiTi shape memory alloys. *Journal of Materials Research*, 19(6):1762-1767, 2004.

[178] S. Crossley, T. Usui, B. Nair, S. Kar-Narayan, X. Moya, S. Hirose, A. Ando, and N. D. Mathur. Direct electrocaloric measurement of 0.9Pb(Mg1/3Nb2/3)O3-0.1PbTiO3 films using scanning thermal microscopy. *Appl. Phys. Lett.*,108: 32902, 2016.

[179] D. Shan, K. Pan, Y. Liu, and J. Li. High fidelity direct measurement of local electrocaloric effect by scanning thermal microscopy. *Nano Energy*, 67(104203):2211-2855, 2020

[180] B. Nair, T. Usui, S. Crossley, S. Kurdi, G. G. Guzmán-Verri, X. Moya, S. Hirose, and N. D. Mathur. Large electrocaloric effects in oxide multilayer capacitors over a wide temperature range. *Nature*, 575:468–472, 2019.

[181] https://pt.rs-online.com/web/p/mlccs-condensadores-ceramicos-multicapa/ 1364047/ (2020)

[182] "Atomic Force Microscopy: Understanding Basic Modes and Advanced Applications",Greg Haugstad, John Wiley & Sons, 04/09/2012, page 143

[183] J. I. Pérez-Landazábal, V. Recarte, V. Sánchez-Alarcos, C. Gómez-Polo, and E. Cesari. Magnetic properties of the martensitic phase in Ni-Mn-In-Co metamagnetic shape memory alloys. *Appl. Phys Lett.*, 102:101908, 2013.

[184] J. I. Pérez-Landazábal, V. Recarte, V. Sánchez-Alarcos, J. J. Beato-López, J. A. Rodríguez-Velamazán, J. Sánchez-Marcos, C. Gómez-Polo, and E. Cesari. Giant direct and inverse magnetocaloric effect linked to the same forward martensitic transformation. *Sci. Rep.*, 7:13328, 2017.

[185] https://www.igus.eu/info/drive-technology-toothed-belt-axes-drylin-zlw (2020)

[186] https://www.igus.pt/info/drive-technology-dryve-motor-control-system (2020)

[187] T. Krenke, E. Duman, M. Acet, E. F. Wassermann, X. Moya, L. Mañosa, A. Planes, E. Suard, and B. Ouladdiaf. Magnetic superelasticity and inverse magnetocaloric effect in Ni-Mn-In. *Phys. Rev. B*, 75:104414, 2007

[188] I. Titov, M. Acet, M. Farle, D. González-Alonso, L. Mañosa, A. Planes, T. Krenke. Hysteresis effects in the inverse magnetocaloric effect in martensitic Ni-Mn-In and Ni-Mn-Sn. *J. Appl. Phys.*, 112:073914, 2012.

APPENDIX I
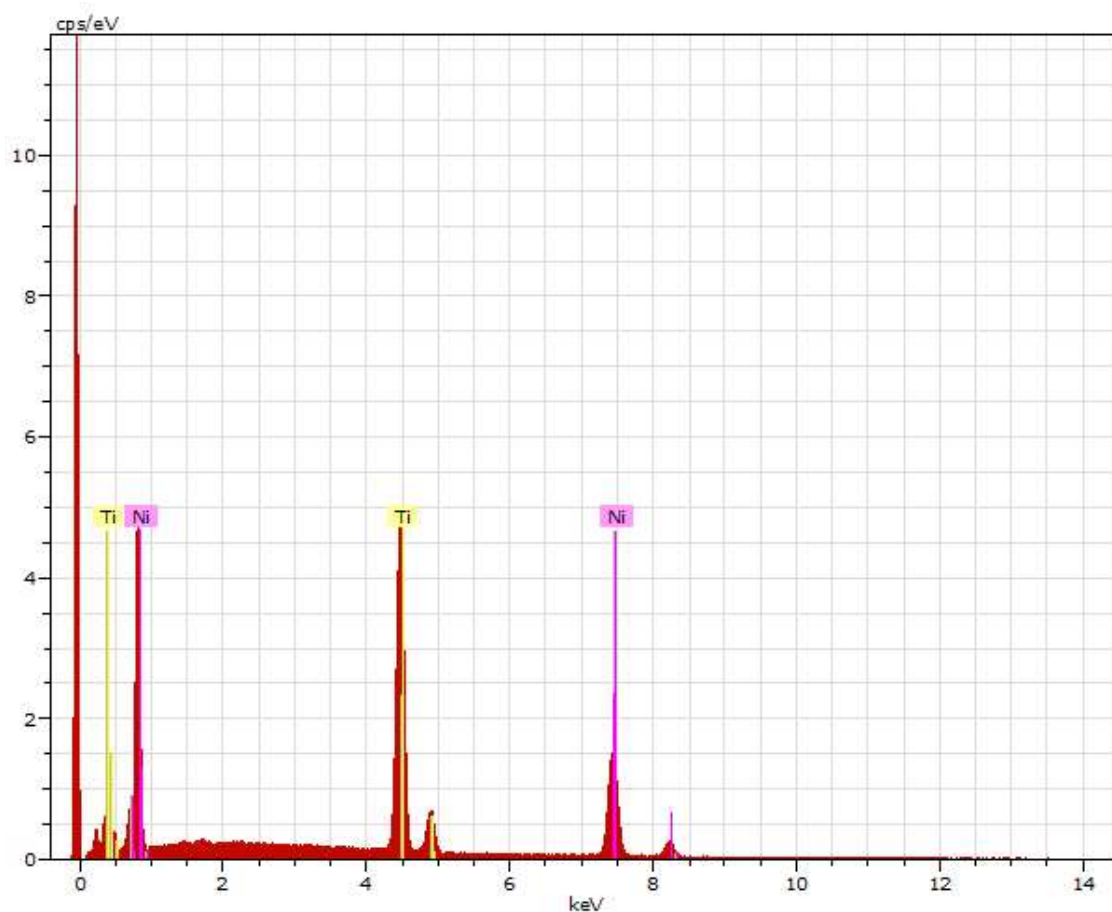
Fig. I.1 - EDS Spectrum of area 2 of sample NiTi_1.

```
Spectrum: 3.spx

Element    Series  unn. C norm. C Atom. C Error (3 Sigma)
                   [wt.%]  [wt.%]  [at.%]          [wt.%]
-------------------------------------------------------------
Nickel    K-series  49.91   55.92   50.86            4.87
Titanium  K-series  39.34   44.08   49.14            3.55
-------------------------------------------------------------
          Total:    89.25  100.00  100.00
```
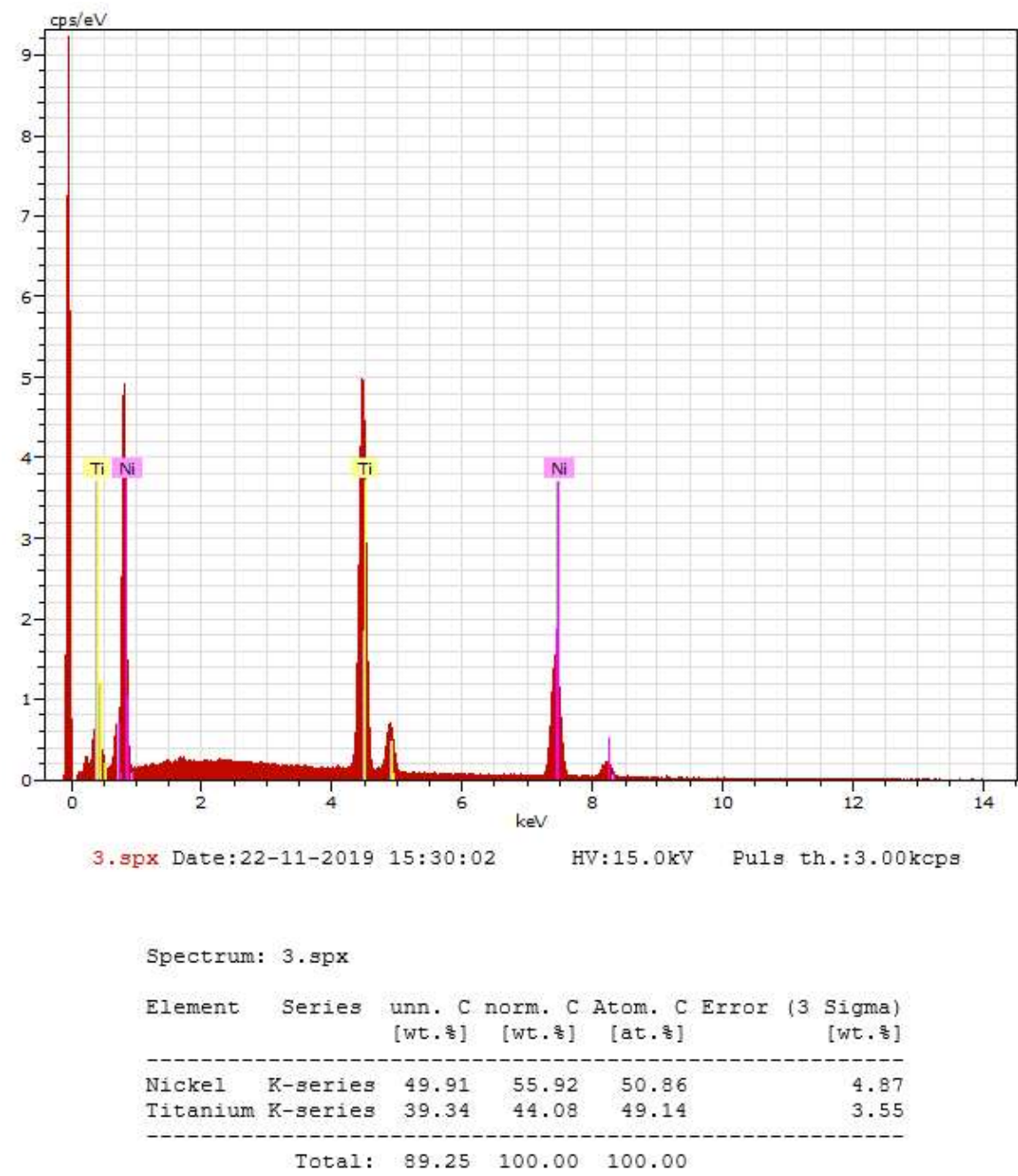
Fig. I.2 - EDS Spectrum of area 3 of sample NiTi_1.
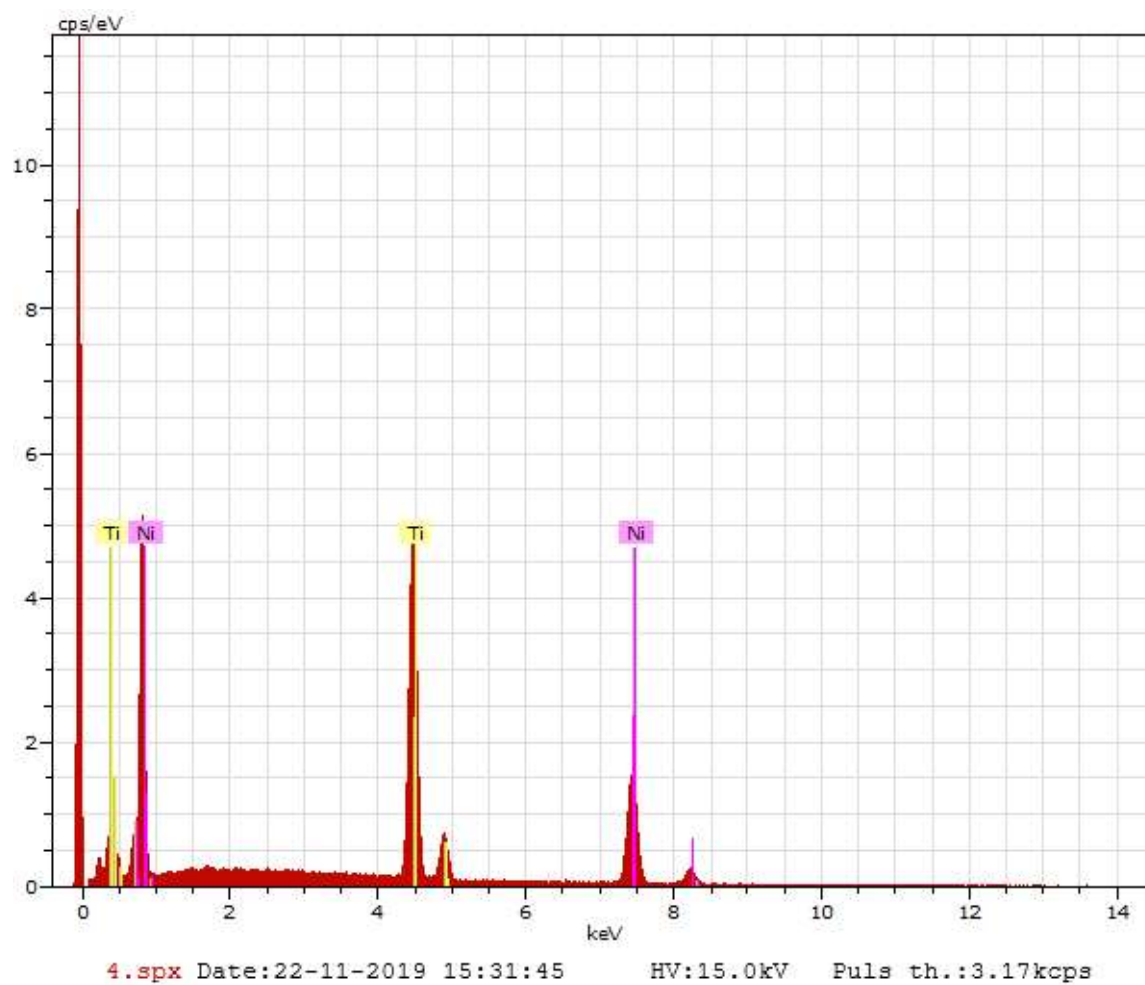
Fig. I.3 - EDS Spectrum of area 4 of sample NiTi_1.

APPENDIX II
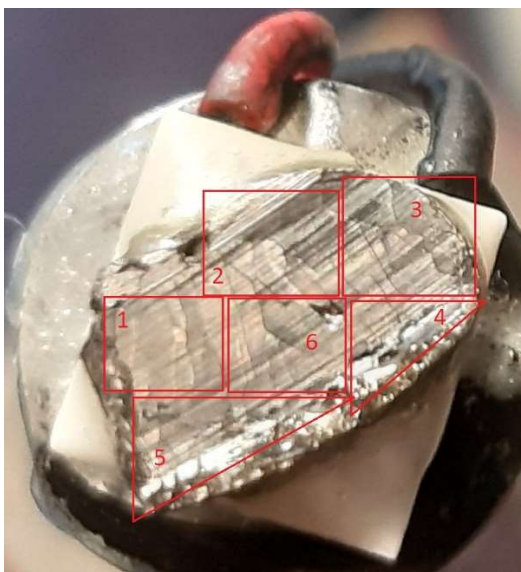
Fig. II.1 - Image of sample NCMG279 with different areas analyzed by EDS signaled.

Fig. II.2 - SEM image of area corresponding approximately to area 1 defined in Fig. II.1.
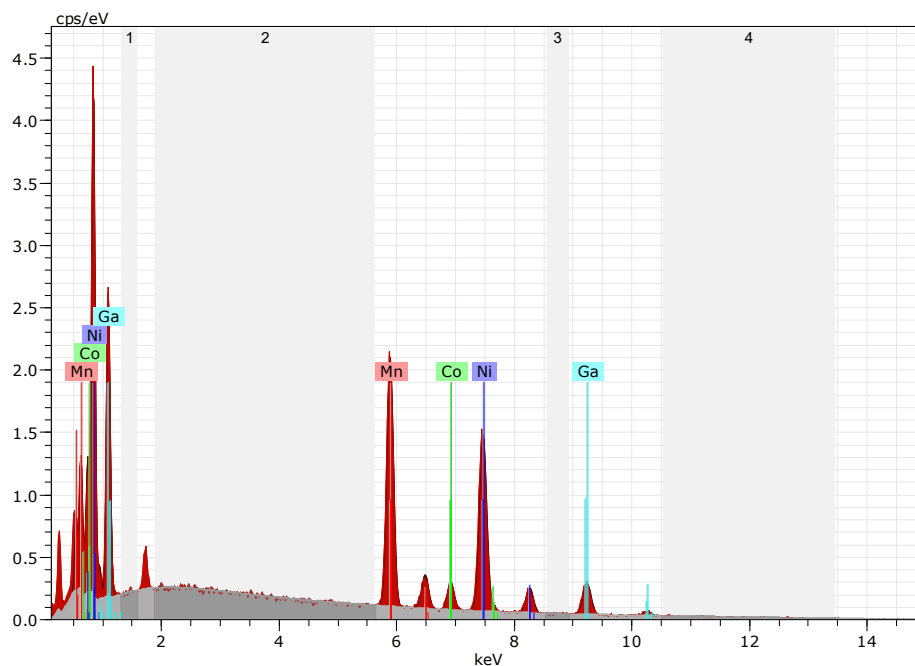
Spectrum: area 1.spx

Element	Series	unn. C [wt.%]	norm. C [wt.%]	Atom. C [at.%]	Error (3 Sigma) [wt.%]
Manganese	K-series	25,90	27,46	29,89	2,41
Cobalt	K-series	5,17	5,49	5,57	0,68
Nickel	K-series	41,25	43,73	44,54	4,04
Gallium	K-series	22,01	23,33	20,01	2,83
	Total:	94,33	100,00	100,00	

Fig. II.3 - EDS spectrum of area 1 shown on SEM image in Fig. II.2.
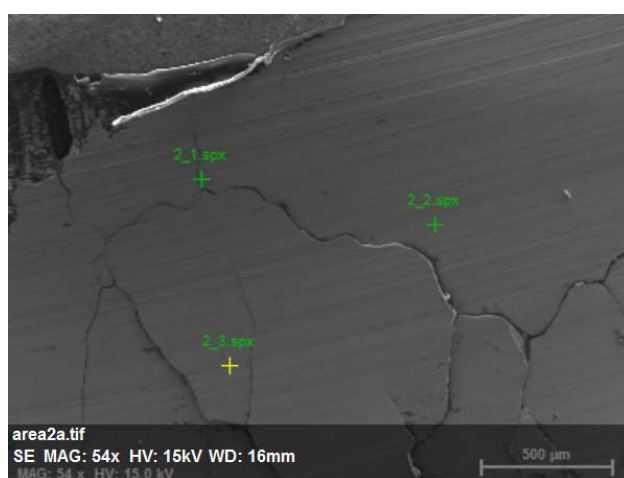
Fig. II.4 - SEM image of area corresponding approximately to area 2 defined in Fig. II.1.

Spectrum: area 2.spx

Element	Series	unn. C [wt.%]	norm. C [wt.%]	Atom. C [at.%]	Error (3 Sigma) [wt.%]
Manganese	K-series	24,94	26,17	28,56	2,34
Cobalt	K-series	5,44	5,71	5,81	0,71
Nickel	K-series	41,57	43,63	44,57	4,08
Gallium	K-series	23,33	24,49	21,06	3,03
	Total:	95,28	100,00	100,00	

Fig. II.5 - EDS spectrum of area 2 shown on SEM image in Fig. II.4.
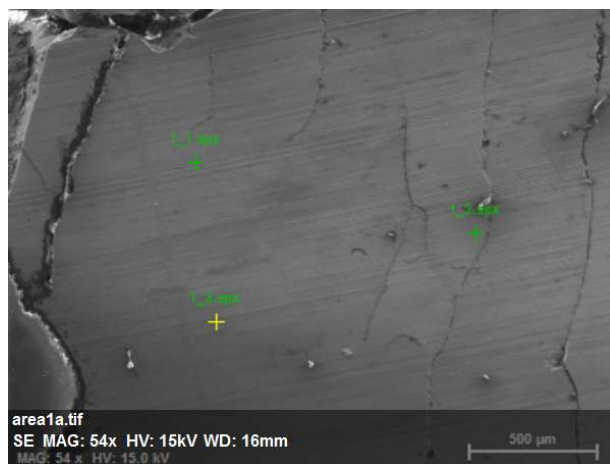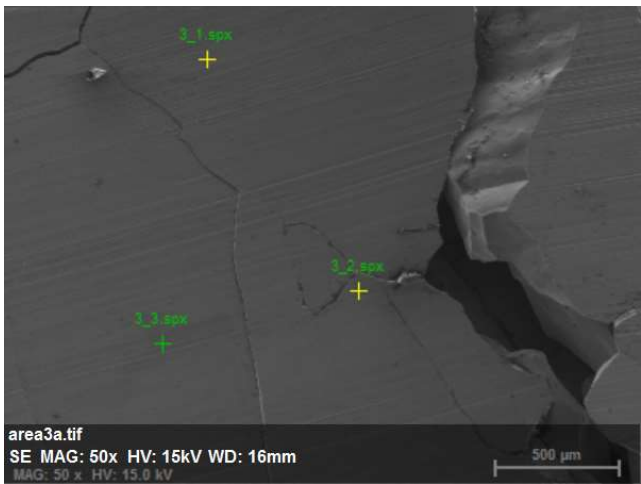

Fig. II.6 - SEM image of area corresponding approximately to area 3 defined in Fig. II.1.

279

```
Spectrum: area 3.spx

Element     Series  unn. C norm. C Atom. C Error (3 Sigma)
                    [wt.%]  [wt.%]  [at.%]          [wt.%]
-----------------------------------------------------------
Manganese K-series  24,75   26,64   29,05            2,35
Cobalt    K-series   5,52    5,94    6,04            0,75
Nickel    K-series  40,00   43,05   43,96            3,99
Gallium   K-series  22,65   24,37   20,95            3,04
-----------------------------------------------------------
          Total:    92,92  100,00  100,00
```
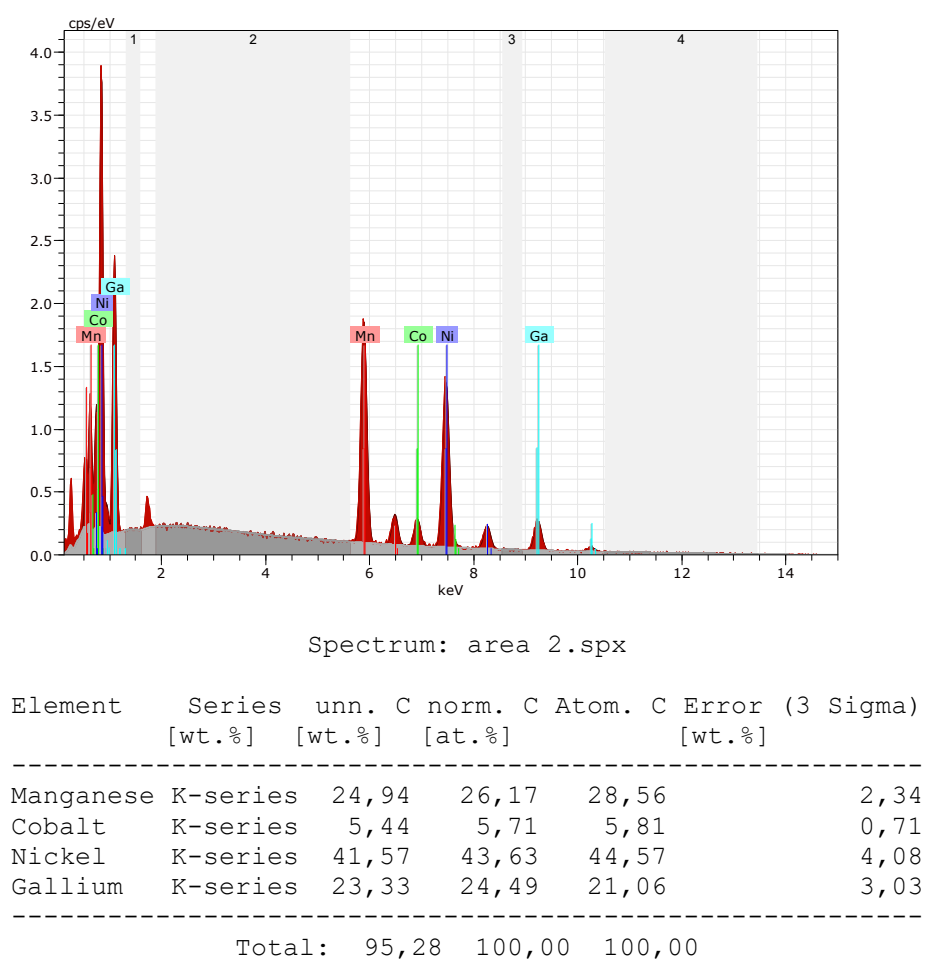
Fig. II.7 - EDS spectrum of area 3 shown on SEM image in Fig. II.6.
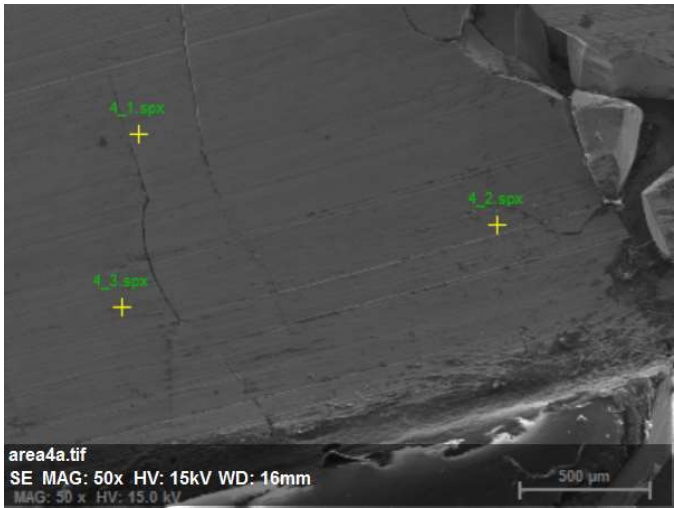
Fig. II.8 - SEM image of area corresponding approximately to area 4 defined in Fig. II.1.

```
Spectrum: area 4.spx

Element     Series   unn. C norm. C Atom. C Error (3 Sigma)
                     [wt.%]  [wt.%]  [at.%]           [wt.%]
-------------------------------------------------------------
Manganese K-series   25,13   28,40   30,78             2,37
Cobalt    K-series    5,33    6,02    6,08             0,71
Nickel    K-series   39,39   44,50   45,14             3,90
Gallium   K-series   18,65   21,07   17,99             2,51
-------------------------------------------------------------
            Total:   88,50  100,00  100,00
```

Fig. II.9 - EDS spectrum of area 4 shown on SEM image in Fig. II.8.

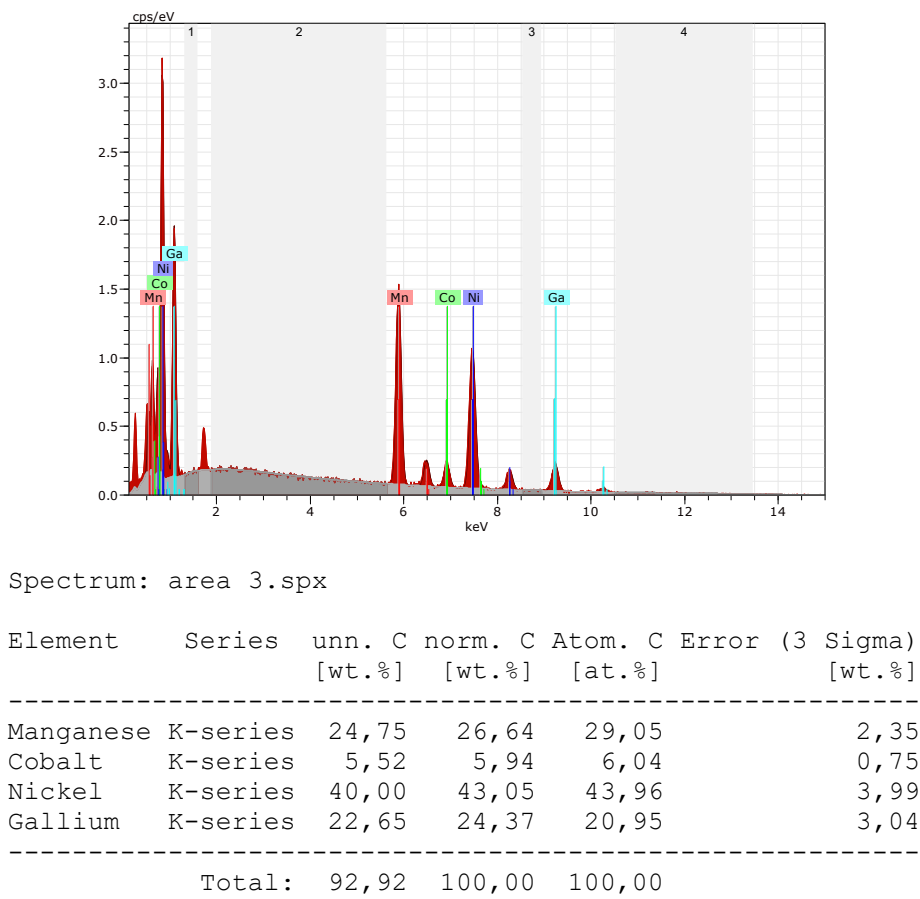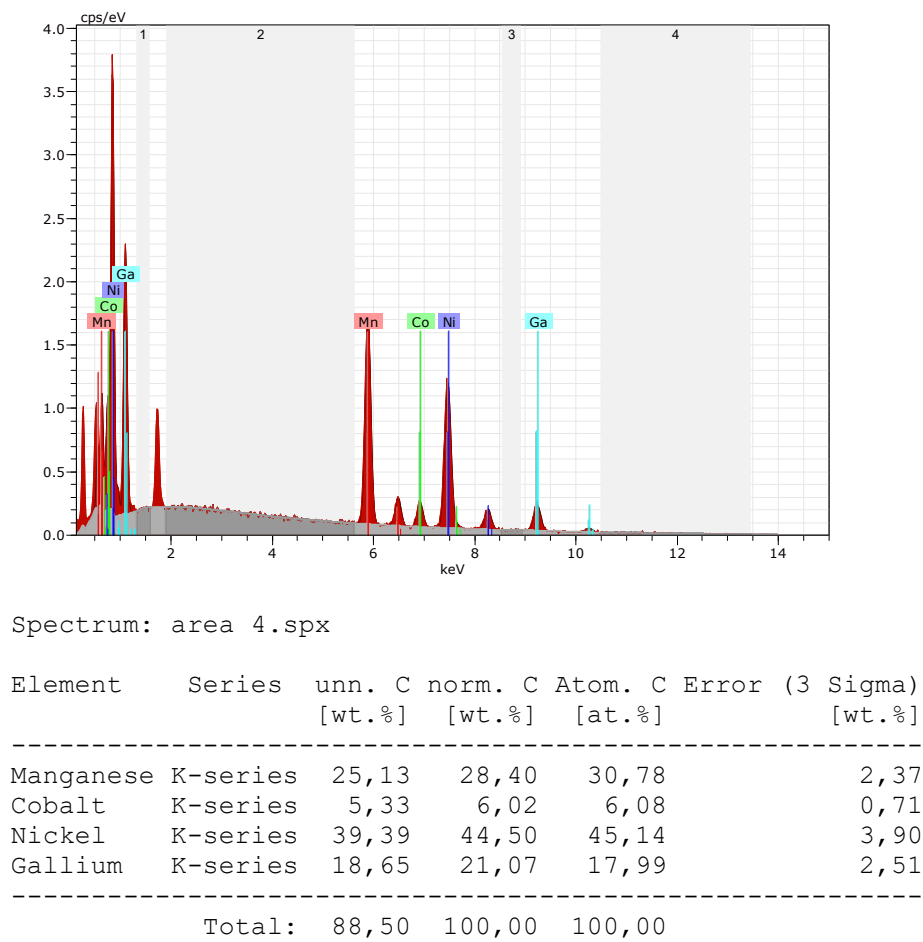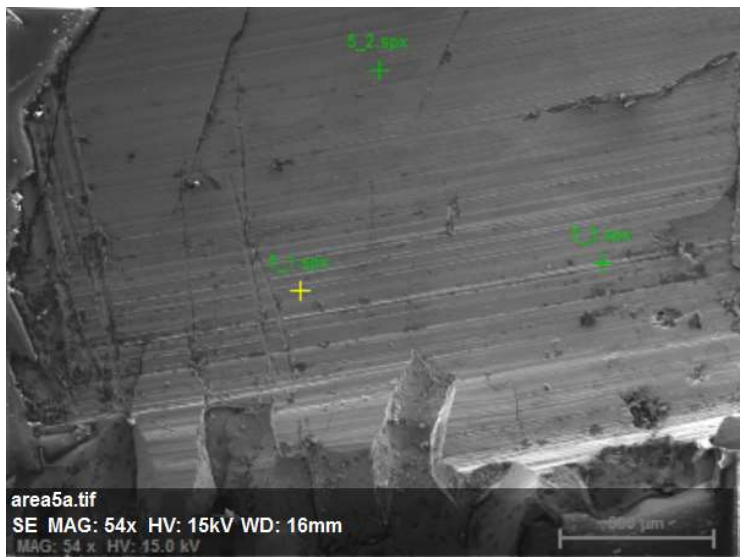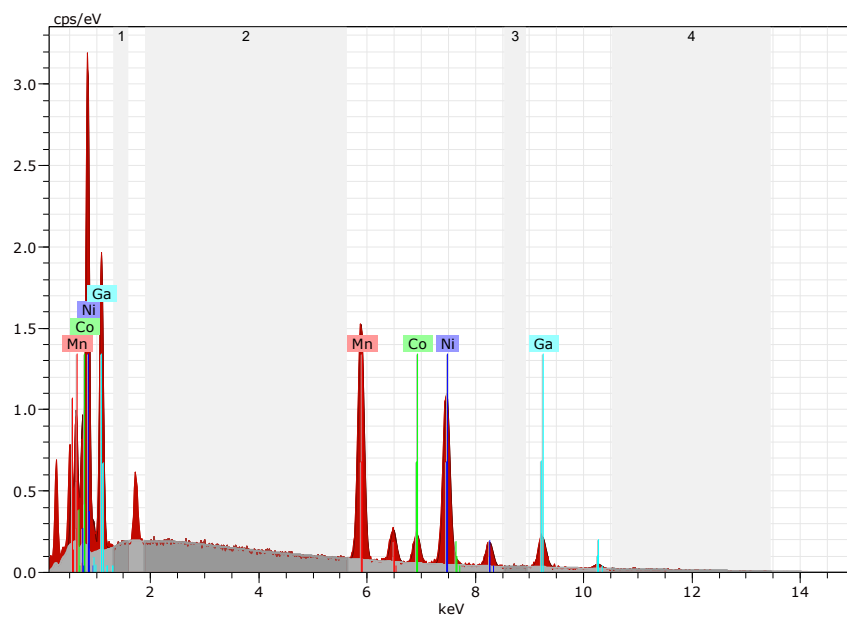Fig. II.10 - SEM image of area corresponding approximately to area 5 defined in Fig. II.1.

```
Spectrum: area 5.spx

Element     Series   unn. C norm. C Atom. C Error (3 Sigma)
                     [wt.%]  [wt.%]  [at.%]           [wt.%]
-----------------------------------------------------------
Manganese K-series   24,98   26,74   29,04             2,37
Cobalt    K-series    5,79    6,20    6,27             0,78
Nickel    K-series   42,43   45,42   46,17             4,22
Gallium   K-series   20,22   21,65   18,52             2,74
-----------------------------------------------------------
            Total:   93,41  100,00  100,00
```

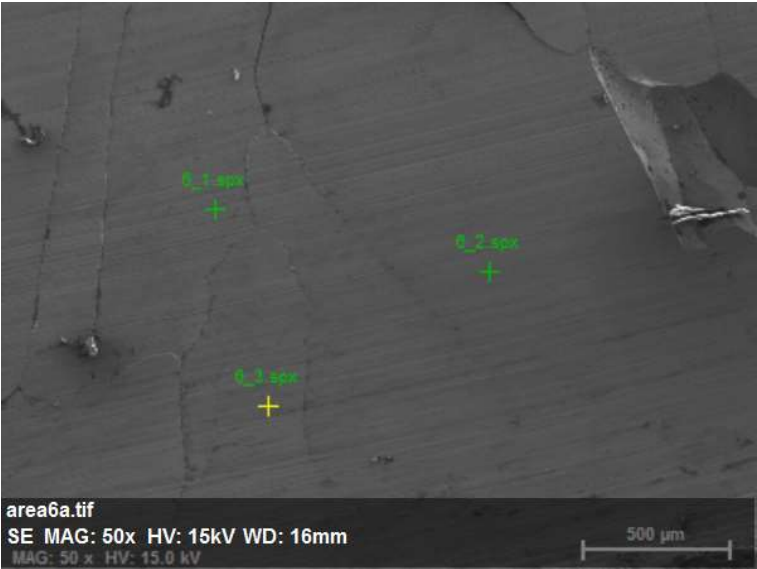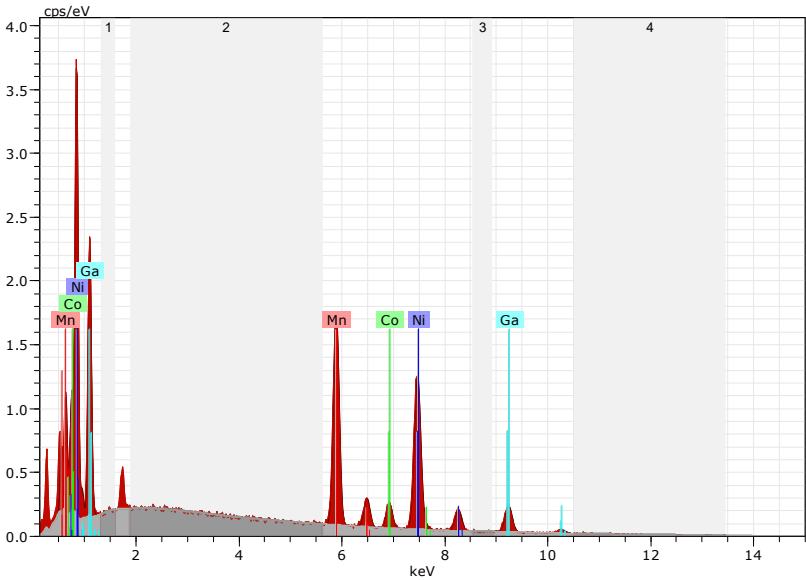Fig. II.11 - EDS spectrum of area 5 shown on SEM image in Fig. II.10.

Fig. II.12 - SEM image of area corresponding approximately to area 6 defined in Fig. II.1.


```
Spectrum: area 6.spx

Element     Series  unn. C norm. C Atom. C Error (3 Sigma)
                    [wt.%]  [wt.%]  [at.%]           [wt.%]
-------------------------------------------------------------
Manganese K-series   25,08   26,68   28,97             2,36
Cobalt    K-series    5,61    5,97    6,04             0,74
Nickel    K-series   42,89   45,61   46,37             4,23
Gallium   K-series   20,44   21,74   18,61             2,72
-------------------------------------------------------------
          Total:     94,02  100,00  100,00
```

Fig. II.13 - EDS spectrum of area 5 shown on SEM image in Fig. II.12.